THE UNIVERSITY OF WARWICK

Capacitive Imaging Technique For Non-destructive Evaluation (NDE)

By

Xiaokang Yin   B.Eng. M.Sc.

Submitted for the degree of

Ph.D. in Engineering

to the

University of Warwick

Describing research conducted in the

School of Engineering

Submitted February 2011

Table of Contents

List of Figures

Chapter 3

Chapter 7

List of Tables

Acknowledgements

First of all, I am infinitely grateful to my supervisor, Professor David Hutchins, who has endlessly supported me in the development and writing of this thesis with his patience, excellent supervision and seemingly limitless knowledge. He also significantly contributed to all my publications that originated at Warwick and supplied the much needed encouragement and optimism at the tough times. One simply could not wish for a better supervisor. I also greatly appreciate his financial support throughout my Ph.D. course. I would also like to thank Dr. Duncan Billson for his caring discussions and advice on this research.

I would like to thank Dr. Geoff Diamond for his timely advice, discussions and novel ideas at the early stage of this research. My thanks also go to Dr. Lee Davis for his assistance with computers, printers, experimental setups, and numerous devices, apparatus that had to be brought to life over the years in the lab. I would like to express my thanks to the team of technicians of the School of Engineering, especially Mr. Huw Edwards, Mr. Frank Courtney, Mr. Ian Griffith and Mr. Colin Banks, for manufacturing some of the components or specimens used during this research. I would also like to thank former members of the AIM Lab and my fellow PhD students: Dr. Chuan Li, Dr. Eddie Ho, Dr. Prakash Pallav, Mrs. Celine Canal, Mr. Aamer Saleem and Mr. Vipin Seetohul for their companionship and cooperation.

I would especially like to thank my parents, Zhenxian Yin and Ruiyun Meng, who have provided extensive and continuous support throughout my study abroad. Finally, I would like to express my gratitude and love to my wonderful fiancée Yaning, who makes it all worthwhile, for her love, devoted support and encouragement.

Declaration

The work described in this thesis was conducted by the author, except where stated otherwise, in the School of Engineering, University of Warwick between the dates of March 2007 and February 2011. No part of this work has been previously submitted to the University of Warwick or any other academic institution for admission to a higher degree. All publications to date arising from this thesis are listed after the bibliography.

Xiaokang Yin, Feb 28th 2011.

Summary

This thesis describes the development and characterization of a novel NDE method-the Capacitive Imaging (CI) technique. The CI technique employs a pair of (or multiple) electrodes to form a co-planar capacitor, and uses the fringing quasi-static electric field established across the electrodes to investigate specimens of interest. In general, the CI probe is sensitive to surface and hidden defects in insulating materials, and surface features on conducting materials. The CI technique is advantageous for its non-contact and non-invasive nature, and the capacitive coupling allows the CI technique to work on a wide variety of material properties.

The theoretical background to the CI technique has been developed. It is shown that in the frequency range of operation (10 kHz to 1 MHz), the quasi-static approximation is valid and the Maxwell's Equations describing the general electromagnetic phenomena can be simplified. The practical implementation of the CI system is based on this analysis, and it is shown that the CI technique has features that can complement techniques such as eddy current methods that are already established in NDE.

The design principles of the CI probes that are required for an optimum imaging performance have been determined, by considering the key measures of the performance including the depth of penetration, the measurement sensitivity, the imaging resolution and the signal to noise ratio (SNR). It has been shown that the operation frequency is not an influential factor - the performance of the CI probe is determined primarily by the geometry of the probe (*e.g.* size/shape of the electrodes, separation between electrodes, guard electrodes etc.). Symmetric CI probes with triangular-shaped electrodes were identified as a good general purpose design. Finite Element (FE) models were constructed both in 2D and 3D in COMSOL^{TM} to predict the electric field distributions from CI probes. Effects of thickness of specimen, lift-off distance and relative permittivity value etc were examined using the 2D models. The sensitivity distributions of different CI probes were obtained from the 3D models and were used to characterize the imaging ability of the given CI probes.

The fundamental concepts of the CI technique have been experimentally validated in a series of scans where the defects were successfully imaged in insulating (Perspex) and conducting (*e.g.* Aluminium, Steel and carbon fibre composite) specimens. The detection of corrosion under insulation (CUI) has also been demonstrated. The imaging abilities were assessed by investigating various standard specimens under different situations. The CI technique was then successfully applied to various practical specimens, including glass fibre laminated composites and sandwich structures, laminated carbon fibre composites, corroded steel plate and pipe, and concrete specimens. Further measurements were also conducted using modified CI probes, to demonstrate the wide range of applications of the CI technique.

Chapter 1   Introduction

1.1   Introduction

Non-destructive Evaluation (NDE), which is also sometimes referred to as Non-destructive testing (NDT) or Non-destructive Inspection (NDI), has been defined as comprising those test methods used to evaluate the properties of a material, component or system without causing damage. NDE techniques has found numerous industrial applications such as the inspection of pipelines, rails, pressure tanks, aircraft, bridges and many other components, where the risks are high and precautions are required. The main functions of NDE are [1]:

- To ensure the system freedom from defects likely to cause failure.

- To ascertain the dimensions of a component or structure.

- To determine the physical and structural properties of materials of interest.

NDE techniques have developed rapidly in recent years. A variety of physical principles are used, and there is no single method around which a "black box" may be built to satisfy all requirements in all circumstances. Some examples include dye penetrant testing, ultrasonic testing, and acoustic emission. Electromagnetic techniques cover almost all the frequency spectrum, starting from DC (potential drop methods and magnetic leakage detection), through the radio frequency (RF) region (eddy current) and microwave region (ground penetrating radar), also covering the THz (THz or millimetre-wave imaging) and the infrared region (IR imaging and themorgraphy). Ionizng techniques occur at even higher frequencies (X-ray and γ-ray radiography). This thesis is primarily concerned with the radio frequency region, as the capacitive imaging (CI) technique to be discussed mainly operates at frequencies of up to 1 MHz.

This chapter begins with a brief review of the electrical and magnetic methods of NDE that operate in the RF region. This is then followed by a review of various

capacitive sensors. The final section gives the objectives of the research and an overview of the remaining chapters of this thesis.

1.2 Electrical and magnetic methods of NDE

The physical and structural properties of a specimen can be related to the electrical and magnetic properties (including electrical conductivity, electrical permittivity and magnetic permeability) of the material. By assessing the electrical and magnetic property variations, defects within the specimen can be detected. In this section, a brief review of these electrical and magnetic methods is presented.

1.2.1 Eddy current methods

The eddy current method works on the principles of electromagnetic induction and can be applied to electrically conducting and/or magnetically permeable materials. In the eddy current technique, a current carrying coil (typically sinusoidal AC) is used to excite a time varying magnetic field in the material under test. The time varying magnetic field will induce conduction currents (if the material is conducting) and magnetization currents (if the material is permeable) in the specimen. According to Lenz's Law, both kinds of currents can generate a secondary magnetic field in the opposite direction and contribute to the total magnetic field, as shown in Figure 1.1.
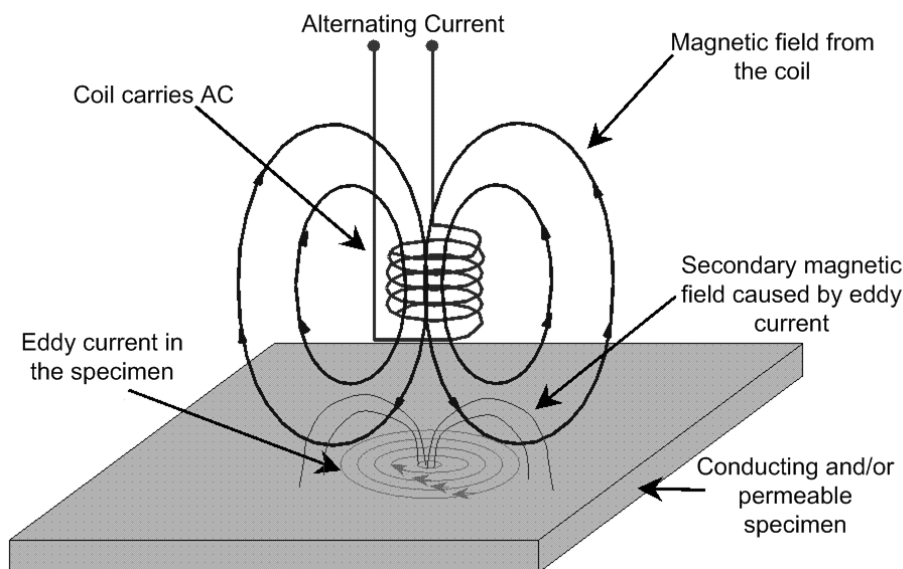
Figure 1.1: *The induction of eddy current.*

The total magnetic field, which contains the effects of the specimen, is then sensed by either the excitation coil or a separate sensing coil. If there is a defect, the coil impedance will be changed, which can be measured and correlated with the defect. As a vector quantity, the impedance change has both amplitude and phase angle. The amplitude provides information about the severity of the defect (e.g. the size). For the phase angle, as the generation of eddy currents can be considered as a time dependent process, meaning that the eddy currents below the surface take a little longer to form than those at the surface. This provides information about the defect location or depth if comparison is made to a known reference (lift-off).

The density of the eddy current is non-uniform and decays through the thickness of the specimen, due to the skin effect. To characterize the penetration depth, the term "standard depth of penetration" is defined as the depth at which the eddy current density is 37% of its value at the surface and commonly used in eddy current inspections. The standard depth of penetration δ can be calculated from the following equation:

$$\delta = \frac{1}{\sqrt{\pi f \mu \sigma}} \, , \tag{1.1}$$

where f is the excitation frequency of the current, μ is the magnetic permeability and σ is the electrical conductivity. It can be seen from Equation (1.1) that for a given material the depth of penetration is inversely proportional to the square root of the frequency. Therefore, high frequencies can be to used to detect very shallow defects (cracks, flaws) in a material, and low frequencies can be used to detect sub-surface buried defects and to test highly conductive materials [2].

In the past few decades, the basic eddy current sensors have evolved into many more sophisticated types, such as sensors with planar coils [3], sensors using giant magnetoresistive (GMR) magnetometers to detect the secondary magnetic field [4], and sensors using pulsed excitation [5].

Although widely used in various NDE applications, the limitations of the eddy current methods have been recognized [6]. A few key limitations are:

- It works only on conducting materials.

- Penetration thickness for complete volumetric eddy-current inspection is limited.

- Inspection of ferromagnetic materials is difficult if the saturation method is not applicable.

- Operator skill is necessary for meaningful testing and evaluation.

1.2.2 Potential drop methods

The basic principle for the potential drop method is the use a pair of electrodes to inject a steady current through a conducting specimen, and another pair to measure the resultant potential difference across a small distance (a few millimeters) [7]. There are two basic types of potential drop methods, namely the DC potential drop (DCPD) and AC potential drop (ACPD). Figure 1.2 shows the arrangement for both the DCPD and the ACPD measurements. Four electrodes (A, B, C and D) are in contact with the conducting specimen. A current I (DC or AC) is passed through the specimen between electrode A and B, the potential difference between electrodes C and D, V, is measured.
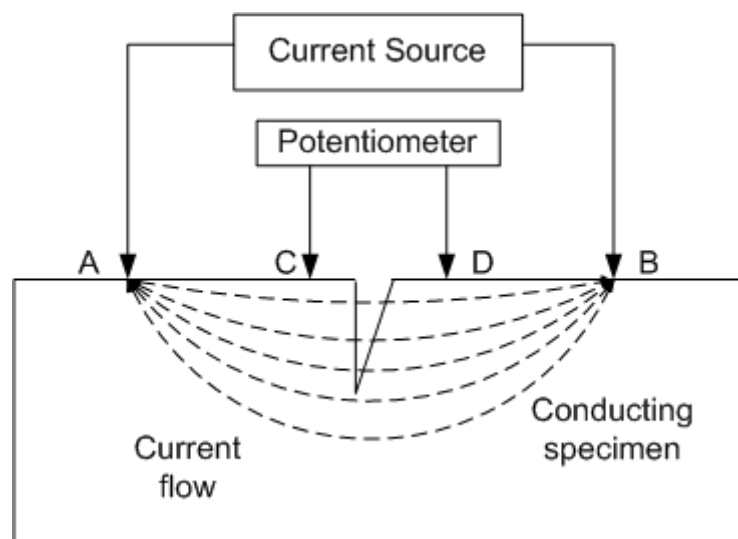
Figure 1.2: *Arrangement for potential drop measurements.*

The ratio *V/I* contains information on the specimen and can be used to determine wall thickness or size and position of cracks [8]. The DCPD methods are usually used to measure depth of surface breaking cracks after they have been detected by other techniques, by comparing the measured potentials from both a normal area and the area surrounding the crack. For ACDP methods, unlike the DCPD where a large uniform direct current is throughout the whole volume of the material, the alternating current can only be carried near the conducting surface due to the "skin effect".

In both DCPD and ACPD methods, intimate contact is needed between the electrodes and the specimen to establish good electrical contact, and sometimes the current will heat the specimen and cause safety problems.

1.2.3   Magnetic methods

For magnetic methods, a magnetic field is applied to the specimen under test and the resultant changes of magnetic flux associated with defects in the targeting region are observed. A review of the magnetic methods can be found in [9, 10]. Figure 1.3 shows how discontinuities of magnetic permeability (e.g. a surface slot) affect the lines of induced magnetic flux.
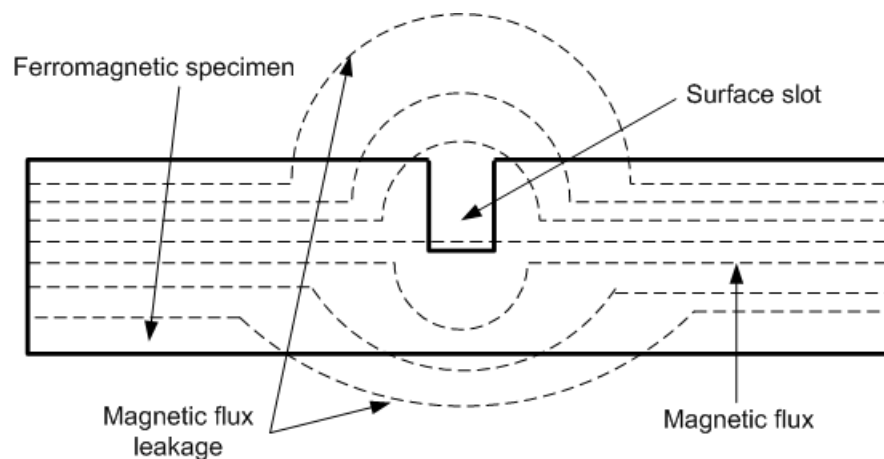
Figure 1.3: *Magnetic flux leakage at a slot cut into a magnetized specimen.*

It can be seen from Figure 1.3 that there is magnetic flux leakage normal to the surface due to the presence of the slot. North and south magnetic poles will appear on the opposite sides of the slot [1]. Flux leakage also takes place at the opposite surface with a lower density, but over a wider region.

The magnetic field in the specimen can be generated by placing a magnetized yoke in contact with the specimen, passing a current through the specimen, or using magnetic induction using a coil or a threading bar. The flux leakage associated with possible defects can then be detected by magnetic particles, magnetic tape (magnetography) or sensing coils and other sensors (e.g. Hall sensors, magnetoresistive sensors or the superconducting quantum interface device (SQUID). Magnetic methods are confined to ferromagnetic materials and sometimes contact with specimen is required (e.g. metal clamps for the current injection).

1.2.4   Capacitive methods

Traditional capacitive methods rely on the capacitive coupling between the active electrode pairs, and utilize the electric field as the probing field to interrogate specimens. Capacitive techniques have not been widely used for NDE, in contrast to say eddy current methods. This is partially due to the historic use of conducting materials (which are suitable for eddy current inspections) in critical components. Secondly, for some capacitive methods, the specimen is often sandwiched between two electrodes so that the specimen is exposed to a uniform electric field, which is only practical for specimens in a relatively thin plate shape and requires access to both sides of the specimen. However, in recent years with the ever increasing use of non-conducting materials (*i.e.* polymers and glass fibre composites) in manufacturing and the development of co-planar capacitive sensors, the number of NDE applications for which the capacitive methods may be appropriate has been expanding.

Most capacitive sensors have historically been used for measurements that are not considered routinely in mainstream NDE. For instance, they are used to characterize the property of a specimen, such as its dielectric constant, from the measured capacitance. Amongst these sensors, the most extensively studied are planar fringing field sensors (also referred to as dielectrometry sensors [11]). They require only single side access to the specimen due to the co-planar electrodes and can provide measurements of the electrical properties (such as dielectric permittivity and electrical conductivity) of the specimen in the proximity of the sensor surface [12-14]. These are typically then correlated to other properties of interest [15], such as the cure state [16], moisture content [17], temperature [18], coating thickness [19], porosity and

thermal conductivity [20], etc. In most of the cases, such a measurement is taken by an LCR meter or a basic impedance measurement circuit with a single frequency excitation, and the measured capacitance is then correlated to the measured property via models [21] or databases [22] generated prior to the measurement. However sometimes, the measurement is taken over a range of frequencies and the frequency dependent effective permittivity can be determined via an impedance analysis. Inter-digital fringing field sensors (see Figure 1.4) are the most commonly-seen design, because of the increased output capacitance between the electrodes due to the spatially periodic structure [23] [24].
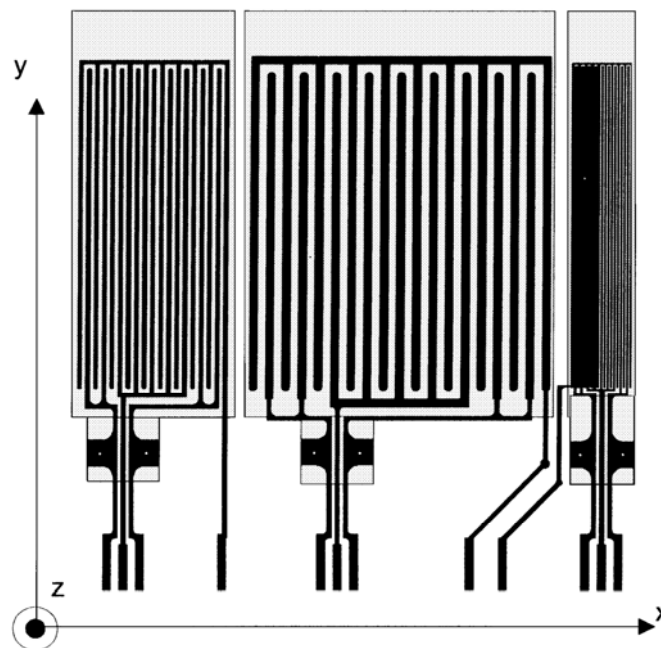
Figure 1.4: *Diagram of a three-wavelength interdigital sensor with spatial periodicities of 2.5 mm, 5.0 mm, and 1.0 mm [25] (the term wavelength refers to the spatial periodicity of the interdigital structure that equals to the distance between neighbouring fingers of the same electrode).*

Other types of capacitive sensor have been used for the detection of inhomogeneities. For example, capacitive array sensors with differential output have been used to precisely define the edges of surface and subsurface slots in dielectrics and surface slots in conductors [21], rectangular capacitive sensors are used for the detection of water intrusion [26] and voids [27] in composite structures, and concentric capacitive sensors are used for the detection of a localized anomaly in a multi-layered structure, such as an aircraft radome [28]. In addition, capacitive sensor arrays with multi

7

sensing electrodes (shown in Figure 1.5) have also been used to image buried objects, such as landmines and unexploded ordnance (UXO) [29].
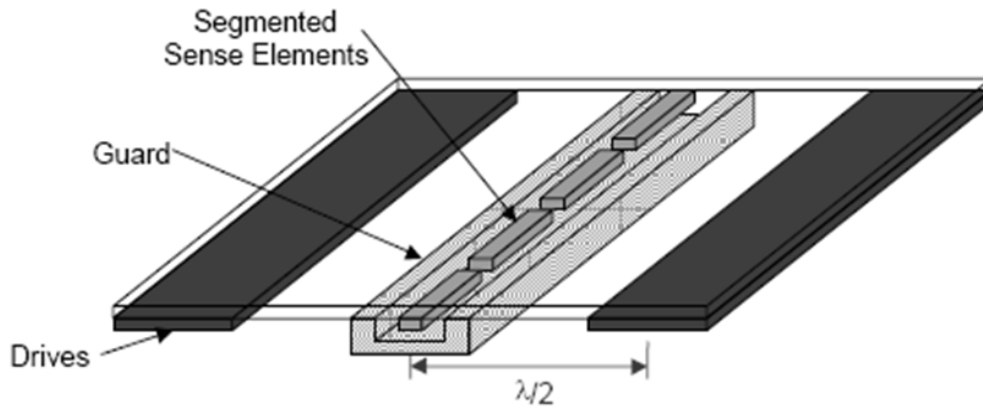
Figure 1.5: *Capacitive sensor with single driving and multi sensing electrodes [29].*

In this thesis, the above methods are extended by using capacitive techniques for a wide-ranging investigation into possible NDE applications.

1.2.5 Other electromagnetic methods

There are also techniques that operate in the RF region but do not fall into any of the categories mentioned in Section 1.2.1 to Section 1.2.4.

The first one is called the electric potential (displacement current) sensor (EPS) [30], which can be used for the inspection of conducting specimens. These sensors have ultra-high input impedance (10^{17} Ω) and can detect small electric potentials with high sensitivity. Basically, by scanning the EPS over the surface of a specimen, the electric potential map of the scanned plane (in the vicinity of the surface) can be obtained. EPS was initially designed for the non-invasive detection of the weak electrical signals generated by the human body, for example, the electrocardiogram (ECG) and the electroencephalogram (EEG), and the feasibility for NDE has been demonstrated by the inspection of carbon fibre composite [30] and stainless steel [31]. The EPS approach can be used in both voltage and current mode. In the voltage mode, the conducting specimen is connected to an AC voltage via an electrode attached to the specimen. This creates an equipotential surface on the sample. If there is any flaw on

the surface, there will be a drop of the measured potential in the plane parallel to the surface of the specimen, as shown in Figure 1.6(a). The voltage mode only works for surface features, as the equipotential surface blankets everything underneath it. For hidden flaws, the current mode is need. In the current mode, a finite current is injected through the specimen by two electrodes at both ends of the specimen. This creates a voltage gradient along the length of the sample which should be uniform in the absence of defects. If a flaw exists in the path of the current (on the surface or within the skin depth), it will be reflected as local changes in conductivity (resistivity) and will be made manifest through the surface electric potential map above the sample (e.g. registered (locally) as relatively steep gradients, as shown in Figure 1.6(b)).
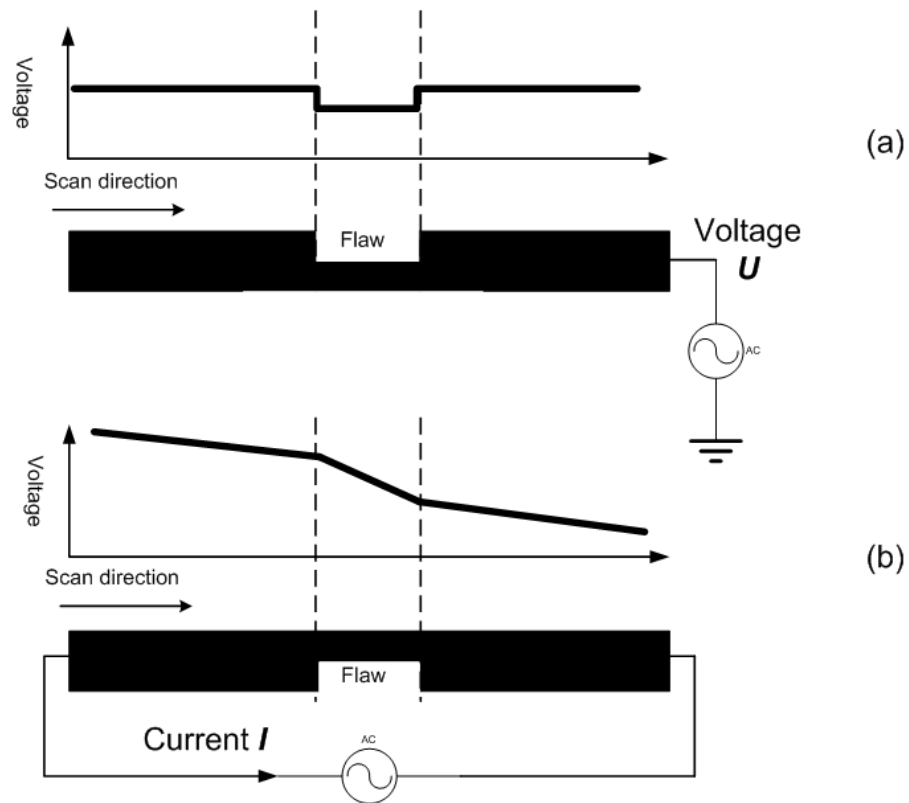
Figure 1.6: *Schematic diagram for EPS in (a) voltage mode and (b) current mode.*

The second technique is called capacitive resistivity (CR) technique [32], which is a geographical technique for the non-intrusive characterization of the shallow subsurface of the earth's surface. Fundamentally, the CR technique has evolved from the DC resistivity (potential drop) method (shown in Figure 1.7(a)) by changing the resistive coupling (direct contact between the electrodes and ground) into capacitive

coupling (non-contact), as shown in Figure 1.7(b). In a similar way to the DC resistivity method, the measurement circuit of the CR technique can be divided into two parts: a transmitter circuit used to energise the ground, and a receiver part to measure a potential. In practice, the sensors are usually in the form of "line-antenna" or "plate-wire combination". Recently, the CR sensor with an inductive source has also been reported [33].
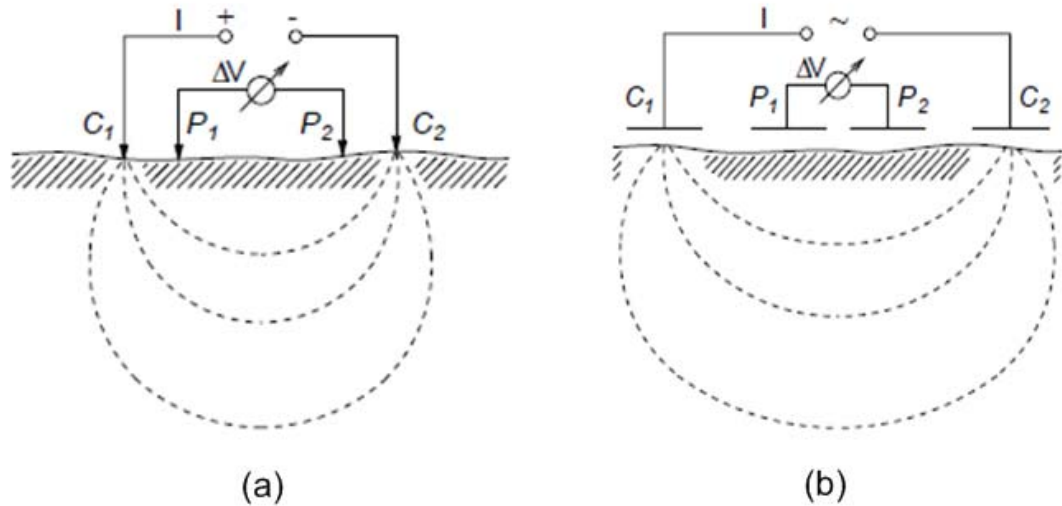
Figure 1.7: *Schematic diagram for (a) the DC resistivity method and (b) the capacitive resistivity method[32].*

1.3 A general review on capacitive sensors

In addition to the above, many other different kinds of capacitive sensors have been designed, which are all based on the same physical phenomenon. A review of these capacitive sensors will help to understand the CI technique presented in this thesis.

The first reference to capacitive sensors is found in *Nature*,1907 [34], and the capacitive sensors have been developing since then. Fundamentally, most of the capacitive sensors are based on extremely simple physical concepts-the simple parallel capacitor model [35]. In this model, the capacitance, C, is related to other parameters by a simple relationship:

$$C = \varepsilon A / d \,, \tag{1.2}$$

10

where d is the plate separation, A is the plate area and ε is the dielectric constant of the material sandwiched between the plates. Nowadays, capacitive sensors have a wide variety of uses. Typical applications of capacitive sensors can be loosely placed into the following categories:

Proximity sensing- Capacitive proximity sensors sense distances to nearby targets without requiring contact. There are basically two types. In the first, the sensor itself forms one plate and the object to be measured forms the other. For theses sensors, the target object has to be conducting. The second type uses the principle of fringing capacitance, and the target object could either be a conductor or an insulator. The application of proximity sensors includes personnel protection (alarm will be triggered if the operator's hand is too close to the machine) [36, 37], light switches (light will be switched on for an approaching person) and vehicle detection.

Measurement - Capacitive coupling between electrodes can be used to measure physical quantities such as displacement [38], thickness [39], rotation [40], movement [41], pressure [42], humidity [43], properties of substance [44], etc. The measured physical quantity can change one (or some) of the three parameters (ε, A and d) mentioned in Equation (1.2) and hence a measurable capacitance change. For example, in a capacitive humidity sensor, it is the change in the dielectric constant of the material (humidity in air), ε, that changes the capacitance. There are many examples in the literature [45-47], e.g. for multi-interface detection between air/liquid.

Fingerprinting - Capacitive sensor arrays with extremely small (~ 0.05 mm) sensing pair are used to acquire tiny surface features (such as ridges and valleys on human skin), and prototypes of fingerprint acquisition systems [48, 49] have been reported in the literature.

IT applications - In some devices, data are capacitively-coupled across a small gap. Typical applications in this category is the capacitive card reader [50]. Capacitive sensor arrays can also be used to detect the motion of fingers or eyebrows [51] [52]. Some of the touch screens on mobile phones and computers are also examples in this category.

Flow Tomography - Electrical Capacitance Tomography (ECT) offers a method for measuring the physical properties of solids, liquids and gasses [32]. ECT systems usually operate under the 2D assumption and image the material properties across the cross-section area (e.g. a section of pipeline). The cross-section to be imaged (say of flow in a pipe) is surrounded by a set of capacitive electrodes which are mounted inside (conducting walls) or outside (insulating walls) of the vessels, as shown in Figure 1.8. The changes in capacitance between all possible combinations of electrode pair (for a 12 electrodes system, as shown in Figure 1.8, the number is 66) which occur when material with different electrical properties is introduced to the imaging cross-section are measured. The image of the cross-section is then reconstructed with these measured capacitances via various reconstruction algorithms. It is an excellent method for analyzing multi-phase flow in oil and gas pipelines.
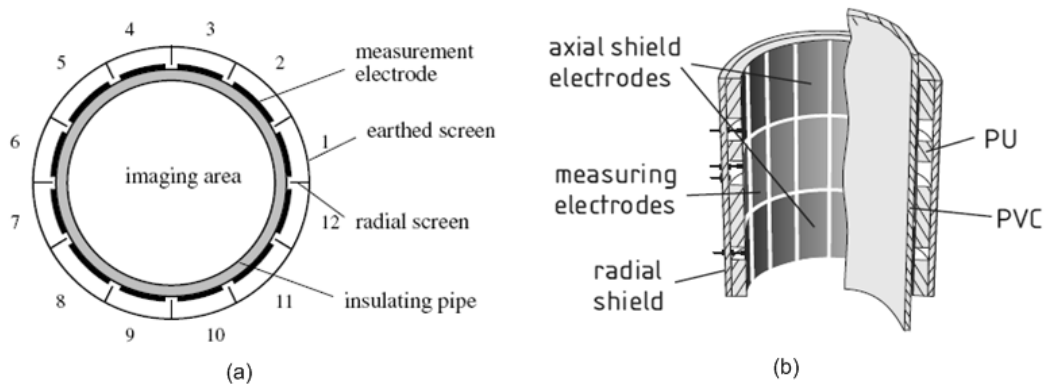
Figure 1.8: *(a) Cross-sectional view and (b) 3D schematic diagram of a typical ECT sensor with 12 electrodes[53].*

1.4 Objectives of the research and outline of the thesis

The thesis describes the work conducted on the development and characterisation of the capacitive imaging (CI) technique, which has the potential to overcome some of the problems that may be encountered by other electrical and magnetic NDE approaches. Although the idea of using the capacitive coupling between active electrodes to measure physical quantities has existed for some time, the imaging ability of capacitive sensors for NDE purposes has yet to be studied in any great detail. As a general aim, this thesis seeks to investigate this aspect by presenting a full

appraisal of all aspects of the proposed CI technique. The scope of the research and the main objectives are:

- To investigate the fundamental concepts of CI, and to provide a unified description of the physical principles that dictate its practical implementation.

- To study the design principles of CI probes, and provide recommendations for probe design and selection.

- To characterize fabricated CI probes and evaluate their imaging ability.

- To identify influential system parameters, and to study the effects of variations in these parameters on the results obtained in an NDE measurement.

- To prove the practical validity of the CI technique by experimentation, and to evaluate the use of CI in a range of different applications.

These objectives are reflected in the following thesis structure:

Chapter 2 gives a detailed introduction of the proposed CI technique, beginning with a description of the CI concept and fundamentals. This is followed with a brief review of the theoretical background, including the Maxwell equations, the quasi-static approximation, the electrical properties of the specimens under test and the calculation of capacitance. The modes of operation are then classified depending on the electrical conditions of the specimens along with the corresponding equivalent circuits. The instrumentation of the CI system is subsequently presented followed with some preliminary results - images formed by amplitude variation and phase difference from scans conducted on Perspex and steel plate. Finally, the proposed CI technique is compared with the widely used eddy current technique and conventional capacitive sensors.

Chapter 3 discusses the general design principles of the CI probes. Firstly, measures for the evaluation of the CI probe performance are presented. The concept of volume of influence is then raised, to evaluate the imaging ability of a given CI probe. Examples of CI probe designs are then provided, namely symmetric and concentric

geometries. Design factors, such as separation between electrodes, guard electrodes, and electrode shapes are also discussed and examined experimentally.

In Chapter 4, Finite Element (FE) models are constructed in COMSOL^{TM} and used to model the CI technique. Firstly, the 2D models are used to demonstrate how the electric fields from a CI probe interact with different specimens. Effects of specimen thickness, lift-off distance and relative permittivity values on the CI probe response are carried out, together with simulations of flaw detection. Subsequently, 3D models were constructed, to provide a more accurate prediction of the probe performance. The measurement sensitivity of CI is then studied based on the 3D models. Firstly, the perturbation method is used and a rather coarse sensitivity map is obtained from the 3D model. A detailed derivation of the sensitivity distribution function is then presented, based on which a more refined sensitivity map can be obtained. Finally, the sensitivity maps of probes with different geometries are obtained and compared, providing an overview of the CI probe performance and an assessment for the influences of the sensor design parameters.

In Chapter 5, a series of basic experiments to validate the concept of the CI technique is described. The results of these experiments are used to verify the predictions of the probe performances discussed in Chapters 3 and 4. Firstly, some instrumentation-related issues are considered. Secondly, typical results including the detection of surface and hidden defects in non-conducting specimens, and surface features on conducting specimens, are presented. Thirdly, practical CI measurements are undertaken with various samples under different situations and using different probes, through which the defect detection ability of the CI technique is assessed. Subsequently, surface features on metals are successfully detected through a relatively thick insulation layer, indicating a possible application for the detection of the Corrosion under Insulation (CUI). Finally, the responses of the CI probes to features smaller in size comparing to the probe sensing area are examined.

In Chapter 6, the CI technique is used as an NDE tool to investigate various practical samples, including glass-fibre laminated composites and sandwich structures, laminated carbon-fibre composites, corroded steel plate, and pipes. A set of

preliminary experiments to image buried objects (both conducting and non-conducting) using the CI technique is also presented.

Chapter 7 examines how the CI technique can be used on the inspection of concrete specimens. The introductory part of this chapter provides a brief review of the commonly used methods for concrete inspection. 2D FE models are then used to predict how the electric field interacts with concrete structures. The results of experiments conducted on different concrete specimens are also presented, including samples with surface cracks, hidden air voids and rebars. Finally, the limitations encountered in the concrete inspection using the CI technique are discussed.

In Chapter 8, modified CI probes, including probes using two pins or two coils as active electrodes and using a high impedance oscilloscope probe as sensing electrode, are proposed and investigated. It is shown that this extends the range of applications of CI methods.

Finally, Chapter 9 draws conclusions from this research, and outlines suggestions for further work which have arisen from the findings of this thesis.

1.5   References

[1]   J. Blitz, "Electrical and Magnetic Methods og Non-destructive Testing (Second Edition)," Chapman and Hall, 1997, p. 44.

[2]   H. Yamada, T. Hasegawa, Y. Ishihara, T. Kiwa, and K. Tsukada, "Difference in the detection limits of flaws in the depths of multi-layered and continuous aluminum plates using low-frequency eddy current testing," *NDT & E International,* vol. 41, pp. 108-111, 2008.

[3]   R. J. Ditchburn and S. K. Burke, "Planar rectangular spiral coils in eddy-current non-destructive inspection," *NDT & E International,* vol. 38, pp. 690-700, 2005.

[4]   J.-T. Jeng, G.-S. Lee, W.-C. Liao, and C.-L. Shu, "Depth-resolved eddy-current detection with GMR magnetometer," *Journal of Magnetism and Magnetic Materials,* vol. 304, pp. e470-e473, 2006.

[5]   G. Y. Tian and A. Sophian, "Reduction of lift-off effects for pulsed eddy current NDT," *NDT & E International,* vol. 38, pp. 319-324, 2005.

[6]   G. Van Drunen and V. S. Cecco, "Recognizing limitations in eddy-current testing," *NDT International,* vol. 17, pp. 9-17, 1984.

[7]   R. Ghajar, "An alternative method for crack interaction in NDE of multiple cracks by means of potential drop technique," *NDT & E International,* vol. 37, pp. 539-544, 2004.

[8]   H. Sun, "Electromagnetic methods for measuring material properties of cylindrical rods and array probes for rapid flaw inspection," PhD Thesis, Iowa State University, 2005.

[9]   D. C. Jiles, "Review of magnetic methods for nondestructive evaluation: 39145 Jiles, D.C. NDT International, Vol. 21, No. 5, pp. 311-319 (Oct. 1988)," *NDT International,* vol. 22, pp. 54-54, 1989.

[10]   D. C. Jiles, "Review of magnetic methods for nondestructive evaluation (Part 2)," *NDT International,* vol. 23, pp. 83-92, 1990.

[11]   A. V. Mamishev, "Interdigital dielectrometry sensor design and parameter estimation algorithms for non-destructive materials evaluation," in *Electrical Engineering and Computer Science* Cambridge: PhD thesis, Massachusetts Institute of Technology, 1999.

[12]   E. Bozzi and M. Bramanti, "A planar applicator for measuring surface dielectric constant of materials," *Instrumentation and Measurement, IEEE Transactions on,* vol. 49, pp. 773-775, 2000.

[13]   P. A. von Guggenberg and M. C. Zaretsky, "Estimation of one-dimensional complex-permittivity profiles: a feasibility study," *Journal of Electrostatics,* vol. 34, pp. 263-277, 1995.

[14]   A. V. Mamishev, A. R. Takahashi, Y. Du, B. C. Lesieutre, and M. Zahn, "Parameter estimation in dielectrometry measurements," *Journal of Electrostatics,* vol. 56, pp. 465-492, 2002.

[15]   D. S. Schlicker, Yanko; Washabaugh, Andrew and Goldfine, Neil "Capacitive Sensing Dielectrometers for Noncontact Characterization of Adhesives and Epoxies," in *Society Plastics Engineers (SPE)* ANTEC, 2002.

[16]   K. G. Bang, J. W. Kwon, D. G. Lee, and J. W. Lee, "Measurement of the degree of cure of glass fiber-epoxy composites using dielectrometry," *Journal of Materials Processing Technology,* vol. 113, pp. 209-214, 2001.

[17]   X. Li, A.S.Zyuzin, and A. V. Mamishev, "Measuring moisture content in cookies using dielectric spectroscopy," *Electrical Insulation and Dielectric Phenomena, 2003. Annual Report. Conference on* , vol., no., pp. 459- 462, 19-22 Oct. 2003

[18]   B. Oertel, T. Hübert, D. Heinze, and U. Banach, "Capacitive sensor system for measurement of temperature and humidity," *Fresenius' Journal of Analytical Chemistry,* vol. 349, pp. 391-393, 1994.

[19]   M. C. Zaretsky, P. Li, and J. R. Melcher, "Estimation of thickness, complex bulk permittivity and surface conductivity using interdigital dielectrometry," *Electrical Insulation, IEEE Transactions on,* vol. 24, pp. 1159-1166, 1989.

[20]   J. T. L. Neil J. Goldfine, Yanko Sheiretov, Paul J. Zombo, "Dielecirometers and magnetometers, suitable for in-situ inspection of Ceramic and Matellic Coated Components," *SPIE proc,* vol. 2459, pp. 164-174, 1995.

[21]   M. Gimple and B. A. Auld, "Variable geometry capacitive probes for multipurpose sensing," *Research in Nondestructive Evaluation,* vol. 1, pp. 111-132, 1989.

[22]   D. E. Schlicker, "Imaging of absolute electrical properties using electroquasistatic and magnetoquasistatic sensor arrays," PhD thesis, Massachusetts Institute of Technology 2005.

[23]   Y. Sheiretov and M. Zahn, "Modeling of spatially periodic dielectric sensors in the presence of a top ground plane bounding the test dielectric," *Dielectrics and Electrical Insulation, IEEE Transactions on,* vol. 12, pp. 993-1004, 2005.

[24]   A. V. Mamishev, K. Sundara-Rajan, Y. Fumin, D. Yanqing, and M. Zahn, "Interdigital sensors and transducers," *Proceedings of the IEEE,* vol. 92, pp. 808-845, 2004.

[25]   A. V. Mamishev, S. R. Cantrell, Y. Du, B. C. Lesieutre, and M. Zahn, "Uncertainty in multiple penetration depth fringing electric field sensor measurements," *Instrumentation and Measurement, IEEE Transactions on,* vol. 51, pp. 1192-1199, 2002.

[26]   A. A. Nassr, W. H. Ahmed, and W. W. El-Dakhakhni, "Coplanar capacitance sensors for detecting water intrusion in composite structures," *Measurement Science and Technology,* vol. 19, p. 075702, 2008.

[27]   A. A. Nassr and W. W. El-Dakhakhni, "Non-destructive evaluation of laminated composite plates using dielectrometry sensors," *Smart Materials and Structures,* vol. 18, p. 055014, 2009.

[28]   T. Chen and N. Bowler, "Analysis of a concentric coplanar capacitive sensor for nondestructive evaluation of multi-layered dielectric structures," *Dielectrics and Electrical Insulation, IEEE Transactions on,* vol. 17, pp. 1307-1318, 2010.

[29]   D. Schlicker, A. Washabaugh, I. Shay, and N. Goldfine, "Inductive and capacitive array imaging of buried objects," *Bindt Insight,* vol. 48, pp. 02-306, 2006.

[30]   W. Gebrial, R. J. Prance, C. J. Harland, P. B. Stiffell, H. Prance, and T. D. Clark, "Non-contact imaging of carbon composite structures using electric potential (displacement current) sensors," *Measurement Science and Technology,* vol. 17, pp. 1470-1476, 2006.

[31]   R. Prance, W. Gebrial, and C. Antrobus, "Depth profiling of defects in stainless steel using electric potential sensors and a non-contact AC potential drop method," *Insight,* vol. 50, pp. 95-97, 2008.

[32]   O. Kuras, "The capacitive resistivity technique for electrical imaging of the shallow subsurface," PhD thesis, The university of Nottingham, 2002.

[33]   C. H. Adams, "Capacitive Array Resistivity with an Inductive Source," in *School of Applied Science*: PhD thesis, RMIT University, 2008.

[34]   L. K. Baxter, *Capacitive Sensors: Design and Applications*: Wiley-IEEE Press, 1996.

[35]   A. Stuart and J. A. Allocca, "Transducers: Theory and Applications," Reston Publishing, 1984, p. 89.

[36]   P. Malcovati, A. Baschirotto, A. d'Amico, C. Natale, M. Norgia, and C. Svelto, "Capacitive Proximity Sensor for Chainsaw Safety," in *Sensors and Microsystems*. vol. 54: Springer Netherlands, 2010, pp. 433-436.

[37]   N. A. C. Rolando and et al., "Design and empirical investigation of capacitive human detectors with opened electrodes," *Measurement Science and Technology,* vol. 21, p. 015802, 2009.

[38]   F. Zhu, J. W. Spronck, and W. C. Heerens, "A simple capacitive displacement sensor," *Sensors and Actuators A: Physical,* vol. 26, pp. 265-269, 1991.

[39]   H. Carr and C. Wykes, "Diagnostic measurements in capacitive transducers," *Ultrasonics,* vol. 31, pp. 13-20, 1993.

[40]   Y. Xu, T. Zhang, H. Wang, and D. Chen, "Smart floating element flowmeter based on a capacitive angular displacement transducer," *Flow Measurement and Instrumentation,* vol. 16, pp. 1-6, 2005.

[41]   J. C. Lotters, W. Olthuis, P. H. Veltink, and P. Bergveld, "Design, realization and characterization of a symmetrical triaxial capacitive accelerometer for medical applications," *Sensors and Actuators A: Physical,* vol. 61, pp. 303-308, 1997.

[42]   W. H. Ko and Q. Wang, "Touch mode capacitive pressure sensors," *Sensors and Actuators A: Physical,* vol. 75, pp. 242-251, 1999.

[43]   Y. Kim, B. Jung, H. Lee, H. Kim, K. Lee, and H. Park, "Capacitive humidity sensor design based on anodic aluminum oxide," *Sensors and Actuators B: Chemical,* vol. 141, pp. 441-446, 2009.

[44]   N. Kirchner, D. Hordern, D. Liu, and G. Dissanayake, "Capacitive sensor for object ranging and material type identification," *Sensors and Actuators A: Physical,* vol. 148, pp. 96-104, 2008.

[45]   H. Caniere and et al., "Horizontal two-phase flow characterization for small diameter tubes with a capacitance sensor," *Measurement Science and Technology,* vol. 18, p. 2898, 2007.

[46]   G. Meng, A. J. Jaworski, and J. C. S. Kimber, "A multi-electrode capacitance probe for phase detection in oil-water separation processes: design, modelling and validation," *Measurement Science and Technology,* vol. 17, pp. 881-894, 2006.

[47]   A. Jaworek and A. Krupa, "Phase-shift detection for capacitance sensor measuring void fraction in two-phase flow," *Sensors and Actuators A: Physical,* vol. 160, pp. 78-86, 2010.

[48]   L. Jeong-Woo, M. Dong-Jin, K. Jiyoun, and K. Wonchan, "A 600-dpi capacitive fingerprint sensor chip and image-synthesis technique," *Solid-State Circuits, IEEE Journal of,* vol. 34, pp. 469-475, 1999.

[49]   A. Bevilacqua, A. Gherardi, and R. Guerrieri, "In Vivo Quantitative Evaluation of Skin Ageing by Capacitance Image Analysis," in *Application of Computer Vision, 2005. WACV/MOTIONS '05 Volume 1. Seventh IEEE Workshops on*, 2005, pp. 342-347.

[50]   M. Rehman, A. Abu_Al_Aish, and K. Lee Bee, "A simple capacitive security card system," in *Mechatronics and Its Applications, 2008. ISMA 2008. 5th International Symposium on*, 2008, pp. 1-4.

[51]   V. Rantanen, P.-H. Niemenlehto, J. Verho, and J. Lekkala, "Capacitive facial movement detection for human–computer interaction to click by frowning and lifting eyebrows," *Medical and Biological Engineering and Computing,* vol. 48, pp. 39-47, 2009.

[52]   J. Smith, T. White, C. Dodge, J. Paradiso, N. Gershenfeld, and D. Allport, "Electric field sensing for graphical interfaces," *Computer Graphics and Applications, IEEE,* vol. 18, pp. 54-60, 1998.

[53]   W. Yang, "Design of electrical capacitance tomography sensors," *Measurement Science and Technology,* vol. 21, pp. 1-13, 2009.

Chapter 2   The Capacitive Imaging (CI) technique

2.1   Introduction

It can be seen from the review presented in Chapter 1 that all electromagnetic NDE methods require some form of coupling between a sensor and the specimen under test. Depending on the nature of the source field, frequency and type of sensor, the coupling mechanism can be resistive, inductive or capacitive. Capacitive Imaging (CI) uses capacitive coupling to a sample. In this chapter, the concepts of the CI technique and the approach of the measurement will be discussed in an attempt to provide a unified description of this technique. Firstly, the fundamentals of the CI probe are described, together with some theoretical background. A classification of the modes of operation is then given, and the measurement techniques used in CI are discussed. Preliminary results are also presented, and the technique is compared to other approaches such as the eddy current technique.

2.2   Capacitive imaging fundamentals

The basic design of a typical capacitive imaging probe can be thought of as a parallel-plate capacitor whose electrodes are unfolded into the same plane, as shown in Figure 2.1.
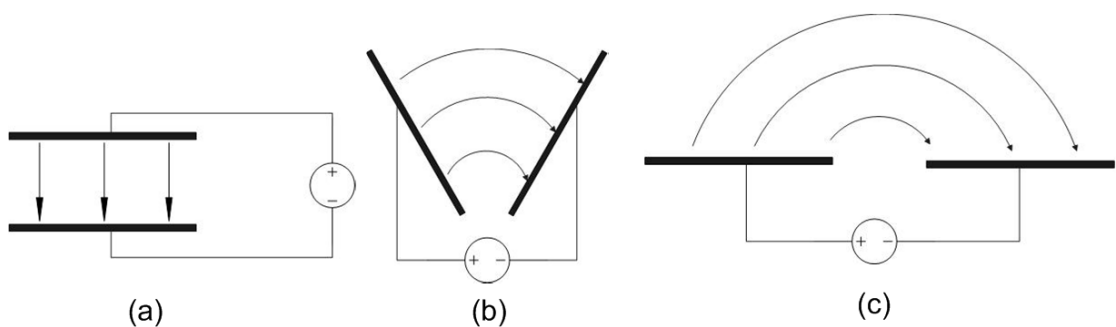
Figure 2.1: *Schematic diagram of the electric field distribution as electrodes change from being in a conventional parallel-plate capacitor geometry (a) to become co-planar (c).*

A schematic diagram of the capacitive imaging approach is shown in Figure 2.2. The co-planar probe, which contains two or more metal electrodes, generates a non-linear

electric field distribution within the test material when a potential difference is applied between the driving and sensing electrodes. The presence of the sample under test will affect the resultant electric field pattern, and furthermore, any property change in the sample (such as the presence of a defect) within the volume covered by the electric field distribution will also have an effect, as shown in Figure 2.2. The resultant electric field distortion will then result in a change in the charge induced at the sensing electrode, and this change in signal can be detected. Scanning such an electrode pair across a surface and measuring the resultant change in stored charge for a given voltage would then create a map of changes in electrical properties within the specimen under test.
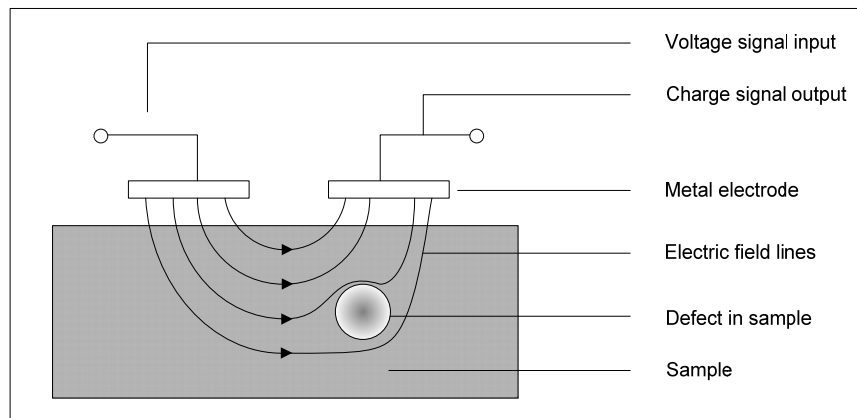
Figure 2.2: *The schematic diagram of the capacitive imaging approach.*

Fundamentally, the behaviour of the probing electric field differs with the sample being insulator or conductor. If the testing sample is a dielectric material or possesses very low conductivity, the electric field generated from the capacitive imaging probe will have a certain volume of influence in the testing sample. Any defect presented in the volume will distort the electric field, and change the amount of induced charges on the sensing electrode, as shown in Figure 2.3(a).

If the testing specimen is a conductor, the electric field will penetrate through both any insulation coating and the air gap, and reach the surface of the conductor. Due to the high conductivity, charges can move freely and will accumulate on the conducting surface. As a result, instead of going further into the conductor, the electric field will create an equal potential surface on the conductor, as shown in Figure 2.3(b). Therefore, only the surface features of the conductor (such as pitting, crack, corrosion,

etc.) will change the pattern of the local electric field and consequently change the amount of induced charge on the sensing electrode, while the interior features under the conducting surface are blanketed. Note that this CI approach is a non-contact technique and the air gap between the electrodes and the sample can be quite large (on the order of millimetres). Thus, sample surface preparation is often not required. In addition, the approach only requires single-sided access to the test sample.

(a)　　　(b)
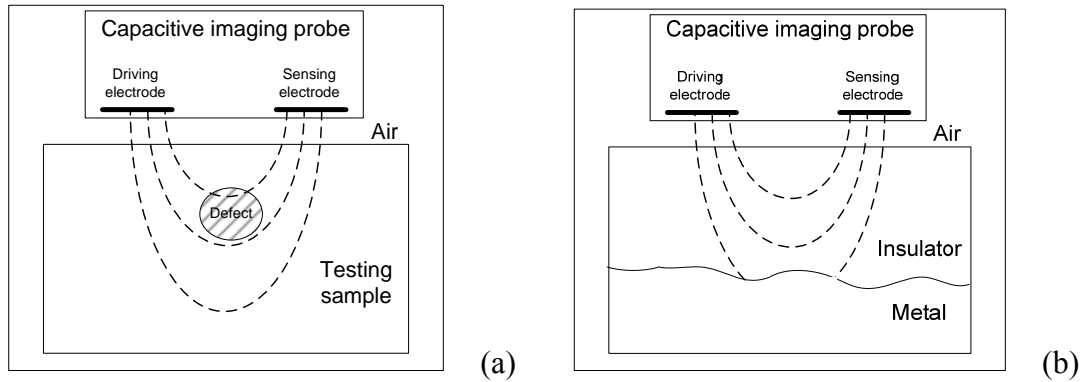
Figure 2.3: *The schematic diagrams of the sensing mechanisms for (a) a non-conducting specimen and (b) a conducting specimen with insulation coating.*

A typical capacitive imaging probe is shown in Figure 2.4. The co-planar triangular imaging electrodes, plus the grounded guard electrodes (used for shielding the two electrodes electrically from each other) are fabricated by etching a printed circuit board (PCB) substrate. The PCB was also coated in copper on its rear surface and mounted in a metal box to shield the electrodes from electrical noise interference, and to enhance the radiated electric field magnitude in the direction of the sample surface. For an accurate evaluation, the electrode geometry must be designed with some care. General design principles will be discussed in detail in Chapters 3 and 4.
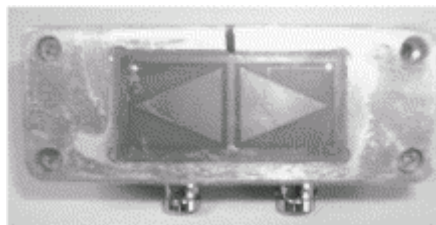
Figure 2.4: *Photograph of a pair of triangular electrodes, mounted in a shielded metallic container.*

2.3   General theoretical background

2.3.1   Maxwell equations

The most general formulation of the laws of electromagnetic fields is due to Maxwell who unified the observations of Faraday, Gauss and Ampere in four equations which relate the electromagnetic field to its sources. The vectors that constitute the electromagnetic field are the electric field density $\boldsymbol{E}$, the magnetic induction $\boldsymbol{B}$, the dielectric displacement $\boldsymbol{D}$ and the magnetic field intensity $\boldsymbol{H}$. The sources are the spatial distributions of electric charge density ρ and electric current density $\boldsymbol{J}$. In the space-time domain Maxwell equations are typically described as:

$$\nabla \times \boldsymbol{E} = -\frac{\partial \boldsymbol{B}}{\partial t} \qquad (Faraday's\,law) \tag{2.1}$$

$$\nabla \times \boldsymbol{H} = \boldsymbol{J} + \frac{\partial \boldsymbol{D}}{\partial t} \qquad (Ampere's\,law) \tag{2.2}$$

$$\nabla \bullet \boldsymbol{D} = \rho \qquad (Gaussian\,law) \tag{2.3}$$

$$\nabla \bullet \boldsymbol{B} = 0 \qquad (Gaussian\,law) \tag{2.4}$$

In order to solve the electromagnetic problems, a further set of relations among the field quantities $\boldsymbol{D}$, $\boldsymbol{E}$, $\boldsymbol{B}$ and $\boldsymbol{H}$ must be established, as there are more variables than equations contained within the Maxwell equations. These additional equations are known as constitutive relations, and can be written simply as:

$$\boldsymbol{D} = \varepsilon_0 \varepsilon \boldsymbol{E} \tag{2.5}$$

$$\boldsymbol{B} = \mu_0 \mu \boldsymbol{H} \tag{2.6}$$

$$\boldsymbol{J} = \sigma \boldsymbol{E} \tag{2.7}$$

where ε is the relative electric permittivity, μ is the relative magnetic permeability and σ is the material's electrical conductivity (in S/m). In free space, ε_0 =8.85 pF/m and μ_0 =4π·10^{-7} H/m. Note that, ε and μ can be complex quantities representing

complex permittivity and complex permeability respectively (which are more appropriate to be denoted as ε and μ) and will be discussed later.

2.3.2 The quasi-static approximation

It can be seen from the previous section that Maxwell's equations (which relate electric and magnetic fields) are needed for an accurate analysis of an electromagnetic problem. However, under certain conditions, a simplifying approximation which ignores magnetic fields is possible without significant loss of accuracy. Systems in which this approximation is reasonable are defined as quasi-static systems. Quasi-static in electrodynamics refers to a regime where "the system is smaller compared with the electromagnetic wavelength associated with the dominant time scale of the problem.[1]". More details of the quasi-static problem can be found in [2]. In the proposed CI technique, the frequency used is typically in the range 10 kHz - 1 MHz. Hence, the corresponding wavelength is in the range 300 m – 30 km, which is much greater than the dimensions of the probe. Therefore, the CI technique is comfortably in the quasi-static regime. In this regime, the magnetic field varies so slowly that it can be considered to be decoupled from the electric field and ignored. Therefore, simplified versions of Maxwell's equations can be used, namely

$$\nabla \times \boldsymbol{E} \approx 0 \tag{2.8}$$

$$\nabla \times \boldsymbol{H} \approx 0 \tag{2.9}$$

$$\nabla \bullet \boldsymbol{D} = \rho \tag{2.10}$$

$$\nabla \bullet \boldsymbol{B} = 0 \tag{2.11}$$

These simplified equations imply that the electric field $\boldsymbol{E}$ produced by a given charge density distribution ρ is irrotational, and the magnetic field intensity $\boldsymbol{H}$ is approximated by zero. Furthermore, it is possible to express the electric field $\boldsymbol{E}$ as the gradient of a scalar function φ, called the electric potential or voltage, as:

$$\boldsymbol{E} = -\nabla \varphi \tag{2.12}$$

With the simplified equations, the analysis of the CI system can be considered as an electrostatic analysis and the problem can be simplified to the prediction of the

electric field produced by various charge distributions (from different probe geometries) within different materials and specimens under test. This uses Poisson's equation, which takes the form:

$$\nabla(\varepsilon_0\varepsilon\nabla\varphi) = \rho \qquad (2.13)$$

In most of the CI applications, there is no free charge in the volume where the probing field exists (with the specimens being dielectrics). Thus the charge density distribution ρ equals to zero, and the Poisson's Equation (Equation (2.13)) reduces to the Laplace's Equation, which is written as:

$$\nabla(\varepsilon_0\varepsilon\nabla\varphi) = 0 \qquad (2.14)$$

The electric potential distribution φ can then be obtained by solving the Laplace's Equation. This will be further discussed in the Finite Element modelling in Chapter 4 where a more general form is presented.

2.3.3   Electrical properties of specimens under test

For the proposed CI technique, it is important to have knowledge of how the electrical properties such as the conductivity and permittivity affect the measured signal. For good conductors, as mentioned in section 2.2, the probing quasi-static electric field will terminate at the conducting surface, and thus the electrical properties (primarily conductivity) have minimal effects on the measured signal. Conversely, for insulators and poor conductors, a certain interior volume of the specimen is probed by the electric field, and the electrical properties (primarily permittivity) have significant effects on the measured signal and need to be discussed in detail.

When an external electric field is applied to a dielectric material in which the amount of free charge is very small (*i.e.* approximates to zero in Laplace's Equation), the material will be polarized and the atom or molecule of the material forms an electric dipole that maintains an electric field which tends to oppose the applied field. For a linear and isotropic material, the polarization density $\boldsymbol{P}$ is related to the external electric field intensity $\boldsymbol{E}$ as follows:

$$\boldsymbol{P} = \varepsilon_0\chi_e\boldsymbol{E}, \qquad (2.15)$$

where again ε_0 is the permittivity of free space and χ_e is the electric susceptibility of the material. The electric displacement $\boldsymbol{D}$ is then related to the polarization density $\boldsymbol{P}$ in the following way:

$$\boldsymbol{D} = \varepsilon_0 \boldsymbol{E} + \boldsymbol{P} = \varepsilon_0 (1 + \chi_e) \boldsymbol{E} = \varepsilon_0 \varepsilon \boldsymbol{E} \qquad (2.16)$$

where ε is the static relative permittivity of the material and given by:

$$\varepsilon = 1 + \chi_e \qquad (2.17)$$

It is worth noting that the constitutive relation described in Equation (2.16) is for the static case. In a time varying electric field the polarization is frequency-dependent and the frequency domain response of a dielectric material can be written in terms of the complex permittivity $\boldsymbol{\varepsilon}$ as:

$$\boldsymbol{\varepsilon} = \varepsilon' - j\varepsilon'' , \qquad (2.18)$$

where the real part ε' is the commonly called permittivity which describes the ability of a material to support an electrical field (*i.e.* a measure of energy storage) and the imaginary part ε'' is the loss factor which represents the losses in the material (*i.e.* relaxation, resonant effect, or loss by ionic conduction). Since all media invariably posses a finite (although, possibly, very small) conductivity σ, a more general form of the effective permittivity $\boldsymbol{\varepsilon}_{eff}$ can be written as:

$$\boldsymbol{\varepsilon}_{eff} = \varepsilon' - j\left(\varepsilon'' + \frac{\sigma}{\omega \varepsilon_0} \right), \qquad (2.19)$$

where ω is the angular frequency of the applied electric field. It can be seen from Equation (2.19) that the dielectric response of an insulating material is frequency-dependent. Several mechanisms are associated with this phenomenon and represent a field of study in itself (a detailed description on these phenomena can be found in [3-5]). However, such phenomena are not subject to this particular study, as in the quasi-static regime the dielectric losses are $\varepsilon'' = 0$ and $\varepsilon' = \varepsilon$ (static relative permittivity). Equation (2.19) can then be written as:

$$\varepsilon_{eff} = \varepsilon = \varepsilon - j\frac{\sigma}{\omega\varepsilon_0}.$$ (2.20)

As the conductivity values of insulating materials are usually very small, the static relative permittivity ε is a good approximation with which to characterize such materials, and will be used in the remaining part of the thesis.

2.3.4 Capacitance

Capacitance is the ability of a structure to hold electrical charge. It is also a measure of the amount of the stored electrical energy for a given electric potential. By the standard definition, the capacitance of conductor i due to a conductor j is the ratio between the charge on the conductor i (denoted as Q_i) and the voltage between the conductor j and a reference. Because of the linearity of all the equations involved, the total charge on conductor i induced by all other conductors is the sum of the separately induced charges [6]. For the parallel geometry, as shown in Figure 2.1(a), a voltage V can be applied across the two plates to produce a total flux Ψ. Then the amount of flux in coulombs produced by V is:

$$\Psi = Q = CV$$ (2.21)
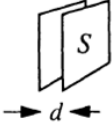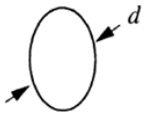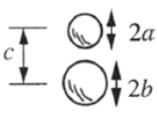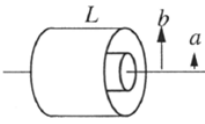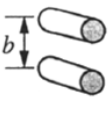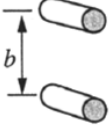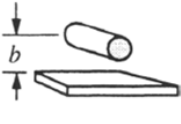
The symbol C is the capacitance of the plates in Farads (coulomb/volt).

2.3.5 Calculating capacitance

Capacitances for some typical capacitors have been calculated by researchers [7] and are summarized in Table 2-1. Aside from the easy symmetric cases presented in Table 2-1, many other useful electrode configurations have been solved analytically, among which the mostly discussed one is the coplanar capacitor. To calculate the capacitance of a planar capacitor, it is customary to use conformal mapping [8, 9]. This has been used to calculate the capacitance for capacitors with two coplanar strips [10], comb-finger capacitors [11], interdigital capacitors [12], multilevel metal capacitors [13], capacitor with a cylindrical dielectric [14], and capacitors with arbitrary cross section [15]. However, conformal mapping is only applicable to 2D cases (in the cross-section plane). Other methods, such as Green functions [16] and method of moments [17] have also been reported. However, these methods are only

29

suitable for geometries which have the correct symmetry (e.g. concentric geometries). To characterize co-planar capacitive imaging probes (such as that shown in Figure 2.4) a 3D analysis is required. It is thus necessary to use a numerical method. Finite Element modelling is used in this work, and will be discussed in detail in Chapter 4.

Table 2-1: *Capacitances for some typical capacitors.*

Geometry	Capacitance	
	Two parallel plates; S is the area of the surface; d is the separation; fringing flux lines at the edges are ignored.	$C = \dfrac{\varepsilon_0 \varepsilon S}{d}$
	Single thin disk with a diameter *d*; capacitance to a ground at infinity	$C = 35.4 \times 10^{-12} \varepsilon \times d$
	Sphere with a diameter *d*; capacitance to a ground at infinity	$C = 55.6 \times 10^{-12} \varepsilon \times d$
	Two spheres with diameters 2a and 2b; separation c; A good approximation if a and b are much lesser than 2c	$C \approx \dfrac{4\pi\varepsilon_0\varepsilon}{\dfrac{a+b}{ab} - \dfrac{1}{c}}$
	Two concentric cylinders with diameters 2a and 2b; length L;	$C = \dfrac{2\pi\varepsilon_0\varepsilon}{\ln\left(b/a\right)} L$
	Two parallel cylinders with diameters 2a and separation b; length L;	$C = \dfrac{\pi\varepsilon_0\varepsilon}{\ln\left(\dfrac{b+\sqrt{b^2-4a^2}}{2a}\right)} L$
	Two parallel cylinders with diameters 2a and separation b; length L; If b>>a	$C \approx \dfrac{\pi\varepsilon_0\varepsilon}{\ln\dfrac{b}{a}} L$
	A cylinder with diameter *2a* and length L above an infinite plane; separation b	$C = \dfrac{2\pi\varepsilon_0\varepsilon L}{\ln\left(\dfrac{b+\sqrt{b^2-a^2}}{a}\right)}$

2.4 Modes of operation

Depending on the nature of the specimens under test, the CI technique operates in different modes as shall be demonstrated in this section.

2.4.1 The CI probe with a non-conducting specimen under test

The first mode of the sensing mechanism is the CI probe with a non-conducting specimen, as shown in Figure 2.5.
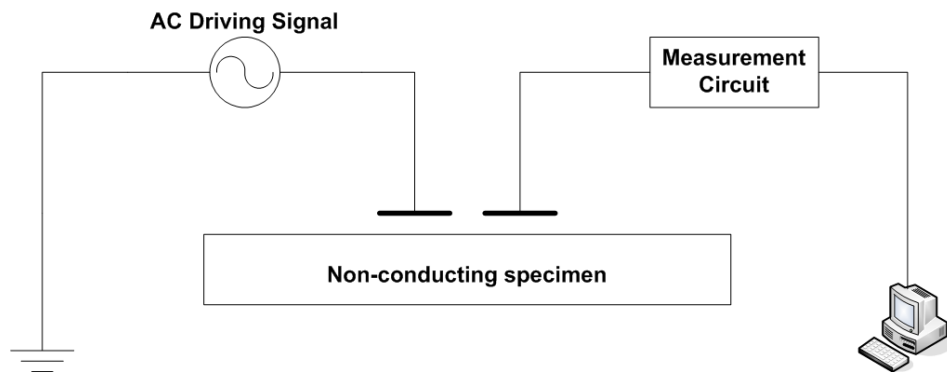
Figure 2.5: *Schematic diagram of the CI probe with a non-conducting specimen under test.*

In this case, the proximity of the non-conducting specimen and the air gap between the specimen and probe surface will act as the dielectric media between the two electrodes of the equivalent variable capacitor, as shown in Figure 2.6. Permittivity variations within the volume sampled by the probing field (such as a varying lift-off distance, a dent on the surface, a void under the surface or other forms of defects) will result in a capacitance change.
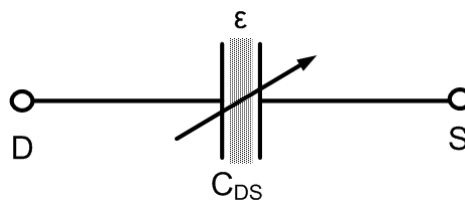
Figure 2.6: *Equivalent circuit of the CI probe with a non-conducting specimen under test.*

31

2.4.2 A non-conducting specimen between the CI probe and a grounded substrate

The second mode of the sensing mechanism is a non-conducting specimen between the CI probe and a grounded substrate, as shown in Figure 2.7.
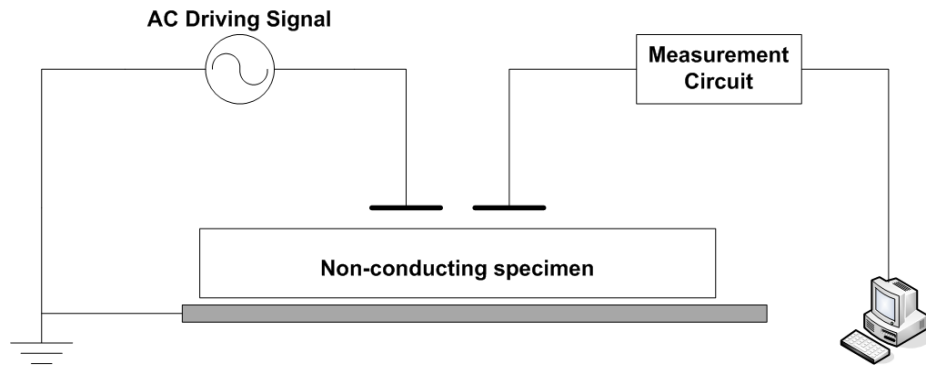
Figure 2.7: *Schematic diagram of a non-conducting specimen between the CI probe a grounded substrate.*

In this case, if the non-conducting specimen is not too thick for the grounded substrate to have an impact, the grounded substrate will act as a third parallel-placed counter electrode, as shown in Figure 2.8. It will create an additional parallel-plate capacitor from each electrode to the grounded substrate, denoted as C_{DG} and C_{SG}. As parallel plate capacitors, these two capacitors will not be sensitive to the position of the specimen and the possible defects (if the distance between the probe surface and the grounded substrate is fixed). However, the capacitance between the driving and sensing electrode, denoted as C_{DS}, will still be sensitive to lift-off distance and the position/size of the possible defects.
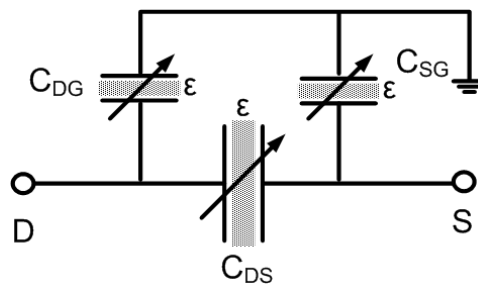
Figure 2.8: *Equivalent circuit of a non-conducting specimen between the CI probe a grounded substrate.*

2.4.3 The CI probe with a grounded conducting specimen under test

The third mode of the sensing mechanism is the CI probe with a grounded conducting specimen, as shown in Figure 2.9.
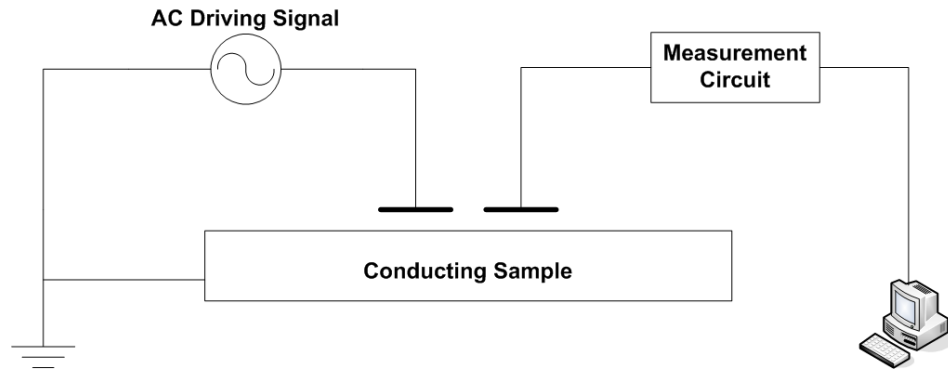
Figure 2.9: *Schematic diagram of the CI probe with a grounded conducting specimen under test.*

In this case, the proximity of a conducting and grounded specimen surface will act as a third, parallel counter electrode and again will create an additional parallel-plate capacitor from each electrode to the grounded surface, denoted as C_{DG} and C_{SG} (As shown in Figure 2.10). The variations of the distance between the electrodes and the grounded surface (lift-off distance variations and/or surface features) will change the capacitances. For the capacitance between the driving and sensing electrode (denoted as C_{DS}), due to the so-called shielding effect [18], as the grounded surface approaching the probe, more and more fringing electric field lines from the driving electrode will rather terminate on the grounded metal surface than cross to the sensing electrode. Therefore, C_{DS} is also sensitive to the distance between the electrodes and the grounded surface (lift-off distance).
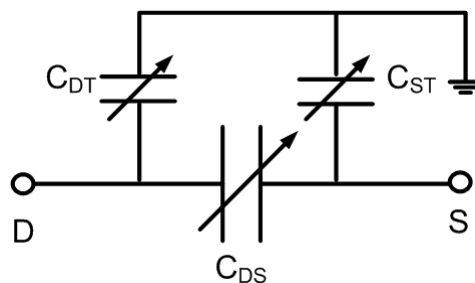
Figure 2.10: *Equivalent circuit of the CI probe with a grounded conducting specimen under test.*

2.4.4 The CI probe with a floating conducting specimen under test

The fourth mode of the sensing mechanism is the CI probe with a floating (*i.e.* non-grounded) conducting specimen, as shown in Figure 2.11.
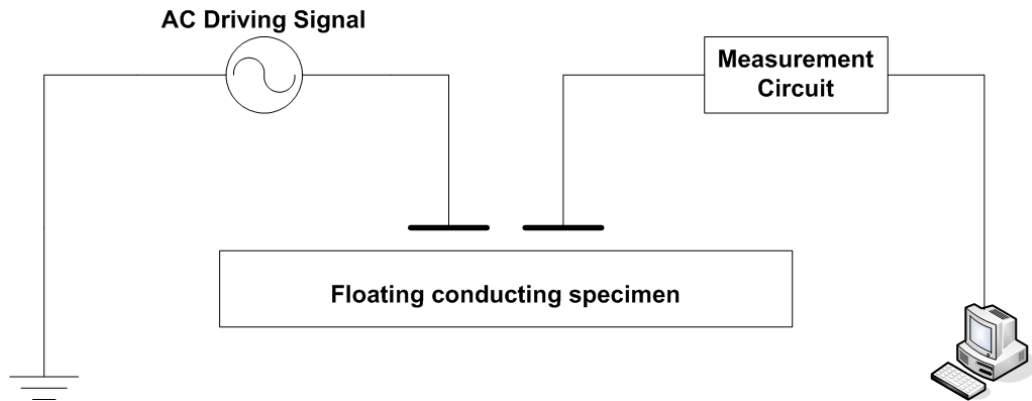
Figure 2.11: *Schematic diagram of the CI probe with a floating conducting specimen under test.*

In this case, the proximity of the conductive and electrically floating surface will create a parallel-plate capacitance from each electrode of the probe to the floating conducting surface as shown in Figure 2.12. Comparing Figure 2.10 and Figure 2.12, the shielding effect of the floating surface can be seen as the shield effect of a grounded surface coupled with a variable parasitic capacitor (denoted as C_{TG}) from the floating surface to ground.
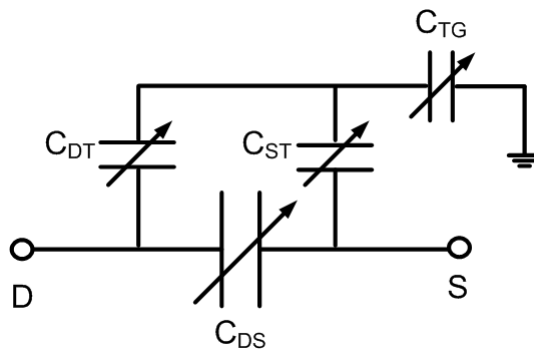
Figure 2.12: *Equivalent circuit of the CI probe with a floating conducting specimen under test.*

2.4.5 Discussions on the modes of operation

Due to the non-linearity of the fringing electric field from the planar CI probe and the complexity of the influential factors, it is difficult to find a comprehensive overview in the literature for obtaining some insight into the expected probe response to different defects in different operation modes. One paper has described ways of possibly finding the effect of distance from different conducting surfaces for capacitive position sensors [18], but this is insufficient for imaging applications. A method based on sensitivity distribution analysis has thus been developed and will be discussed in detail in later chapters.

2.5 Measurement method

Some of the capacitive sensors reported in literature use LCR meters to measure the capacitance changes [19-22]. This approach is not used in the present CI technique, as sometimes the sensitivity provided by LCR meters is not high enough to distinguish very small variations. In theory, the measurements of capacitance are usually taken either in the harmonic regime or in the static regime between at least two electrostatic equilibria [23]. To proceed such a measurement, the electrodes of the capacitive probe can be connected to the driving voltage, left floating or grounded. The voltage of driven and grounded electrodes is imposed (to the driving voltage or 0) at any time but the amount of charge on the electrode can vary. In contrast, the voltage on the floating electrode can vary but the amount of the charge cannot. The measurement can be taken from the driving, the grounded or the floating electrode and the measured signal can be either a charge, or a voltage [23]. For the proposed CI technique, the probe usually comprises two active electrodes: one of the electrodes is driven by a known voltage, and the measurement is taken from the other electrode. For instance, theoretically the sensing electrode can be connected to ground through an ammeter in order to obtain the charge (current) directly, or connected to a voltmeter to measure the voltage.

From the above discussions, it can be seen that the capacitance measurement is practically an impedance measurement (*i.e.* apply an electrical stimulus (a known voltage or current) to the driving electrode and observe the response (the resulting

current or voltage) from the sensing electrode). Commonly, in terms of types of stimulus, there are three different methods which are used for impedance measurements [24].

1) To measure impedance by applying a single-frequency voltage and measuring the amplitude and phase shift of the resulting current at that frequency.

2) To apply a transient voltage, e.g. a pulse or a step function, and to measure the resulting time-varying current. Both input and output signals are Fourier-transformed into the frequency domain, yielding frequency-dependent impedance.

3) To apply a voltage signal composed of random (white) noise and measure the resulting current. By calculating the power density spectra of input and output signals, the frequency-dependent impedance can be obtained.

The latter two approaches are broadband measurements and they need rather complex signal generation and processing, which make them very difficult for high speed measurement. Therefore, the single frequency approach is more suitable for the work in this thesis.

Independent of the type of stimulus, there also exist several techniques for impedance measurement such as bridge method, resonant method, current-voltage method, network analysis method, auto-balancing bridge methods, etc. The selection of the techniques depends on frequency range, required accuracy, measurement range, and system complexity. More details of the current measuring techniques can be found in the Agilent impedance measurement handbook [25]. Since in this thesis the low-frequency range is of particular interest, the very basic current-voltage approach, which is suitable for low-frequency measurement, was used and is briefly described below.

In the four operation modes mentioned in the previous section, the sensing mechanisms (probe and specimens under test) can be considered as variable capacitors (denoted as C). If the input impedance of the measuring circuit (denoted as R) is taken into account, the measurement system can be considered as an RC series

circuit, and the voltage is measured from one electrode of the capacitor, as shown in Figure 2.13:
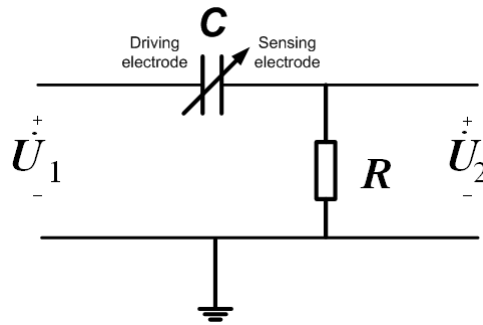
Figure 2.13: *Equivalent circuit of the measurement circuit.*

The relationship between the measured voltage $\dot{U}_2$ and the driving voltage $\dot{U}_1$ can be expressed as:

$$\dot{U}_2 = \frac{j\omega RC}{1 + j\omega RC} \cdot \dot{U}_1,$$

(2.22)

where ω is the angular frequency of the driving voltage. From the vector diagram of this circuit, the amplitude of the output voltage $\left|\dot{U}_2\right|$ can be calculated as:

$$\left|\dot{U}_2\right| = \left|\dot{U}_1\right| \cdot \left(\frac{\omega R}{\sqrt{\dfrac{1}{C^2} + \omega^2 R^2}} \right),$$

(2.23)

and the phase shift ϕ between $\dot{U}_2$ and $\dot{U}_1$ can be calculated as:

$$\phi = tg^{-1}\left(\frac{1}{\omega RC}\right).$$

(2.24)

The system described by Equation (2.22) is a high pass filter. If a typical capacitance of the CI probe (C=1 pF) and the input impedance of the charge amplifier (R= 100Ω (> 10 kHz)) were selected as examples, the cut-off frequency of this system is 1.6×10^9 Hz and the Bode diagram of the measurement system is shown in Figure 2.14.
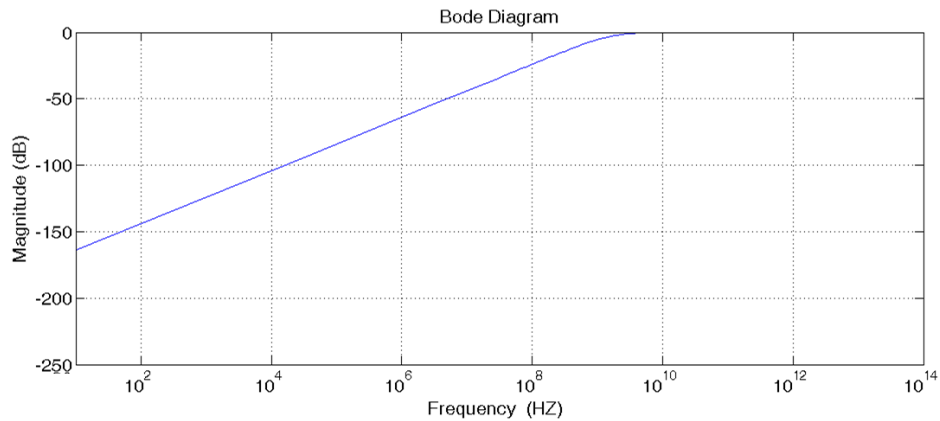
Figure 2.14:*The Bode diagram of the measurement circuit described by Equation (2.22)*

It can be inferred from Figure 2.14 that the excitation frequency should be smaller than the cut-off frequency (1.6×10^9 Hz in this case) to ensure the measurement circuit is sensitive to the targeting capacitance change (on the slope of the plot), and the frequency range (10 kHz to 1MHz) used in this work is thus suitable.

In addition, from Equation (2.23) and Equation (2.24), it is evident that with the excitation amplitude $\left| \dot{U}_1 \right|$, excitation frequency ω and the input impedance R being constant, the amplitude of the measured voltage is positively correlated with the variable capacitance of the sensing mechanism, while the phase shift is negatively correlated.

2.6   Instrumentation

2.6.1   Instrumentation description

A schematic diagram of the basic instrumentation is shown in Figure 2.15. The CI probe was held and manipulated by an X-Y scanning stage, which could be used to scan the probe across the sample surface. To measure the signal at any particular location, a single frequency AC signal was applied as the driving voltage to one of the electrodes. The frequency of operation could be adjusted from 10 kHz to 1 MHz. The drive voltage waveform was obtained from a Turlby Thandar Instruments TG120 signal generator. The capacitance across the electrodes was not measured directly, as

this would not be sufficiently sensitive. Instead, a Cooknell CA/6 charge amplifier was used to convert the charge signal on the sensing electrode to an AC voltage signal, which could then be recorded if desired. However, greater sensitivity was obtained by using a lock-in amplifier, which converts the AC voltage signal into a DC voltage proportional to the amplitude of the received AC signal. The DC output was then recorded using a Tektronix TDS 430 oscilloscope, and transferred to the PC for storage. The PC also controlled the X-Y scanning stage, and the signal recorded in specified locations so as to build up an image.
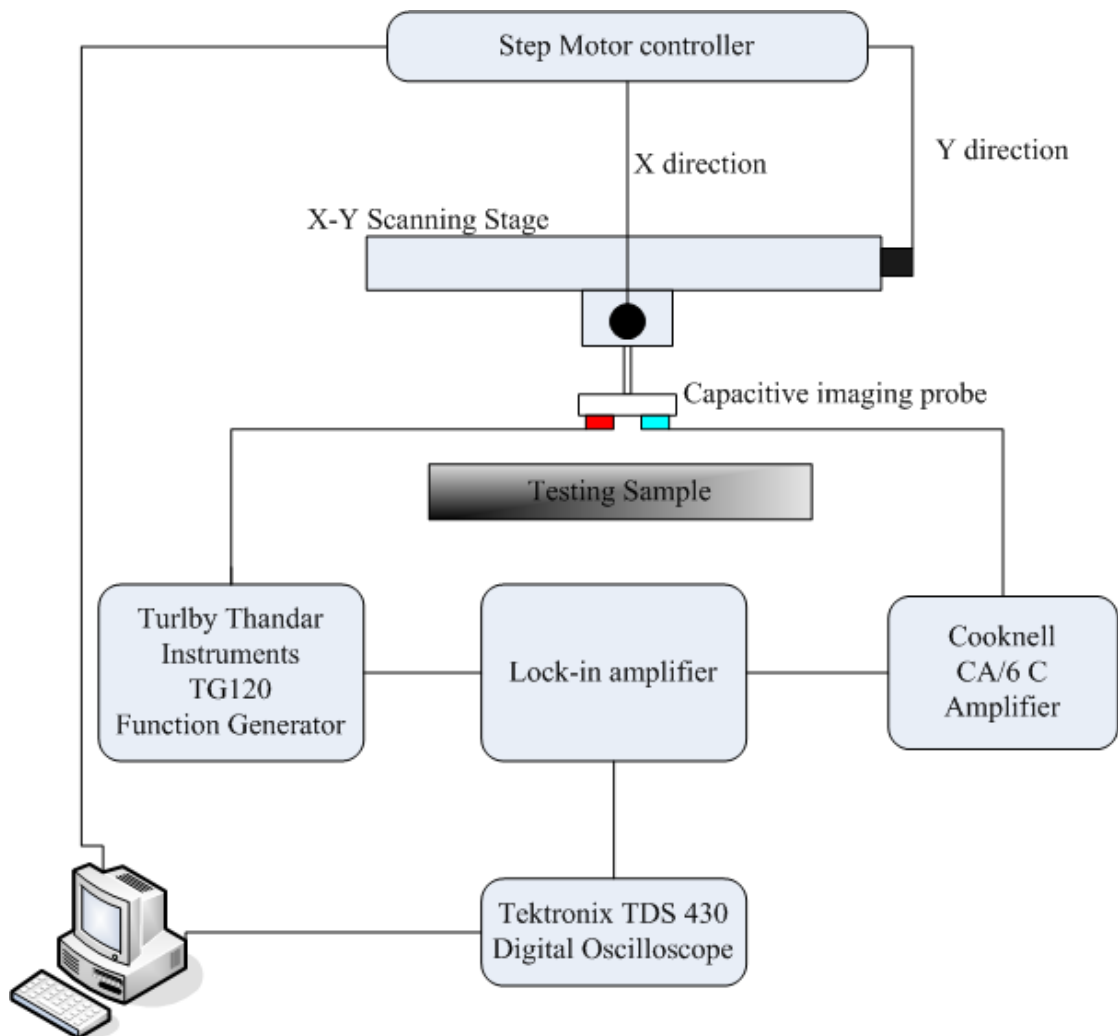
Figure 2.15: *System block diagram of capacitive imaging system.*

2.6.2 Explanatory notes on the instrumentation

The CI probe is the core part of the system and must be designed according to particular applications, details on probe design and characterization will be presented in Chapter 3 and Chapter 4.

The lock-in amplifier employed in the system is an example of phase-sensitive detection, and allows a high degree of noise suppression in small signal measurements. A Scitec 441 lock-in amplifier was used initially for preliminary tests and a SR850 lock-in amplifier was then used for most of the results, as shall be demonstrate in later chapters. Note that, the SR 850 lock-in amplifier has an internal oscillator, which can provide both an adjustable-amplitude sine wave output and a synchronous, fixed-amplitude reference output. The sine wave amplitude can be set from 4mV to 1 V rms (2 mV resolution). The oscillator frequency can be adjusted between 1 mHz and 100 kHz. Sometimes, in a practical scan, the signal generator can be removed from the system and the sine wave output from the SR 850 is used to excite the driving electrode of the CI probe, while the reference output provides a frequency reference to the lock-in.
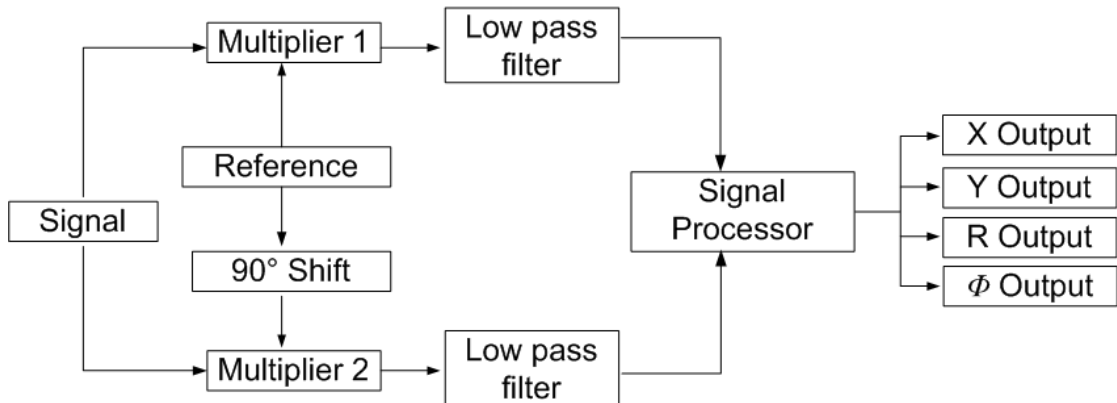
Figure 2.16: *Block diagram of the lock-in amplifier.*

Both of the lock-in amplifiers used in this work are dual-channel. Figure 2.16 shows the schematic diagram of a dual-channel lock-in amplifier. The Signal (output from the charge amplifier) is in the form of a sine wave with noise:

$$V_{signal}(t) = V_{signal} \sin(\omega t + \theta_{signal}) + N(t) \tag{2.25}$$

The Reference signal is with the same frequency of the Signal, as:

$$V_{reference}(t) = V_{reference} \sin(\omega t + \theta_{reference}) \tag{2.26}$$

With a 90° phase shift the Reference signal becomes:

$$V'_{reference}(t) = V_{reference} \cos(\omega t + \theta_{reference}) \tag{2.27}$$

The output from Multiplier 1 is:

$$
\begin{aligned}
& V_{signal}(t) \cdot V_{reference}(t) \\
&= V_{signal}V_{reference} \sin(\omega t + \theta_{signal}) \sin(\omega t + \theta_{reference}) + N(t)V_{reference} \sin(\omega t + \theta_{reference}) \\
&= \frac{1}{2}V_{signal}V_{reference} \cos(\theta_{signal} - \theta_{reference}) - \frac{1}{2}V_{signal}V_{reference} \cos(2\omega t + \theta_{signal} - \theta_{reference}) \\
&\quad + N(t)V_{reference} \sin(\omega t + \theta_{reference})
\end{aligned} \tag{2.28}
$$

After the low pass filter, the X output can be obtained:

$$X = \frac{1}{2}V_{signal}V_{reference} \cos(\theta_{signal} - \theta_{reference}) \tag{2.29}$$

Accordingly, the Y output from the other channel can be obtained:

$$Y = \frac{1}{2}V_{signal}V_{reference} \sin(\theta_{signal} - \theta_{reference}) \tag{2.30}$$

The X output and Y output are then processed, and the R output and Φ output can be obtained respectively:

$$R = \sqrt{X^2 + Y^2} = \frac{1}{2}V_{signal}V_{reference} \tag{2.31}$$

$$\phi = \tan^{-1}\frac{Y}{X} = (\theta_{signal} - \theta_{reference}) \tag{2.32}$$

From Equations (2.31) and (2.32), it can be seen that the noise has been removed successfully. The R output represents the amplitude of the Signal while the Φ output represents the phase angle of the Signal. Both of the R output and Φ output can be used as parameters to form images, as shall be demonstrated.

2.7   Preliminary results

Preliminary experiments were conducted to illustrate how this approach would work in practice, and the results are presented in this section. The first specimen was a 21 mm thick Perspex plate containing four 20 mm by 20 mm square flat-bottomed holes (3 mm, 7 mm, 11 mm and 15 mm deep respectively). A 40 mm by 20 mm CI probe with two triangular electrodes (as shown in Figure 2.4) was scanned 1 mm above the surface with the holes. Both the amplitude and the phase were used to form images as shown in Figure 2.17. In the amplitude plot (Figure 2.17(a)), the square holes were detected as darker areas and in the phase plot (Figure 2.17(b)) the holes were detected as lighter areas. (In all the images presented hereafter, dark areas are low measured values and light areas are high values.)
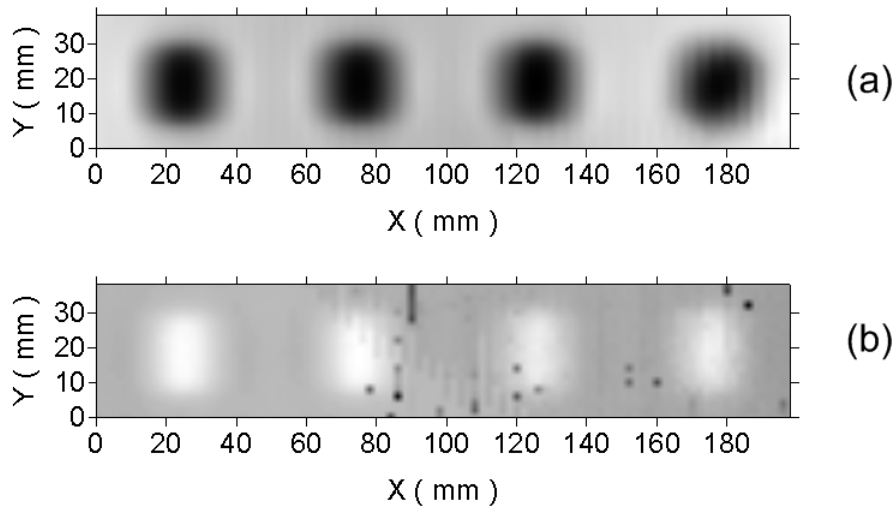
Figure 2.17: *Capacitive images of a Perspex plate with four flat bottomed holes. (a) Amplitude plot and (b) phase difference plot.*

The second specimen was a 10 mm thick steel plate containing four 20 mm in diameter circular flat-bottomed holes (2 mm, 4 mm, 6 mm and 8 mm deep respectively). The same 40 mm by 20 mm CI probe with two triangular electrodes was scanned 1 mm above the surface with the holes and during the scan, the steel specimen was grounded. Again, both the amplitude and the phase were used to form images as shown in Figure 2.18. In the amplitude plot (Figure 2.18(a)), the square holes were detected as lighter areas and in the phase plot (Figure 2.18(b)) the holes were detected as darker areas. In addition, the depth information of the holes can be obtained in the amplitude plot from the intensity variations of the lighter areas.
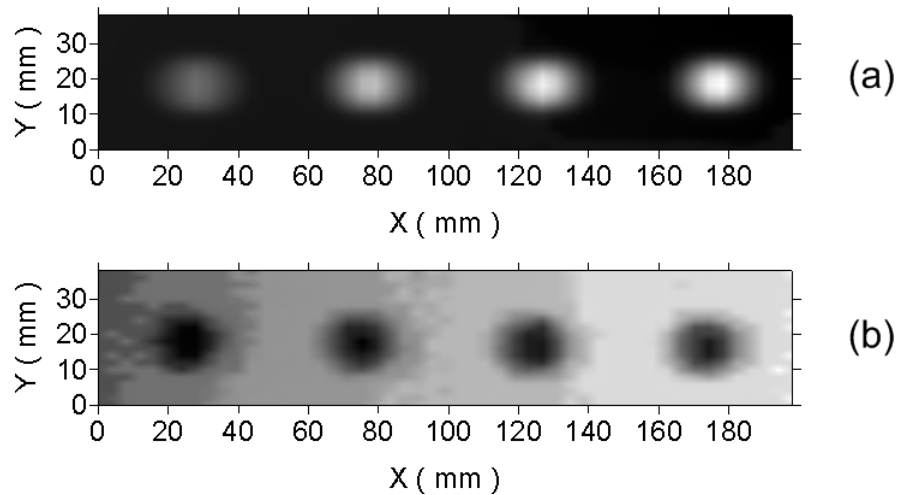
Figure 2.18: *Capacitive images of a steel plate with four flat bottomed holes. (a) Amplitude plot and (b) phase difference plot.*

It can be seen from Figure 2.17 and Figure 2.18, the CI probe is sensitive to surface features on both non-conducting and conducting specimens. It is also evident that the amplitude plots (Figure 2.17(a) and Figure 2.18(a)) provided higher contrast than the phase plots (Figure 2.17(b) and Figure 2.18(b)). Note that, differs from the eddy current approach, the phase different in the CI approach is caused purely by capacitance change in the measured circuit (shown in Figure 2.13) and does not contain information about the depth of the defect, as the probing electric field is considered to be established in the whole probed volume instantaneously in each scan position. Detailed experiment settings and more experiments will be presented in later chapters.

2.8   Discussion and conclusions

In this chapter, the theory background of the CI technique has been presented. The sensing mechanism, the measurement methods and the instrumentation of the CI system have also been explained, which provided an overview of the proposed CI technique. In order to gain a better understanding, the CI technique is compared with eddy current technique and other capacitive approaches.

2.8.1 Comparison with eddy current techniques

At first sight, the CI technique may seem similar to eddy current methods, with the coils simply replaced by flat electrodes. However, the modes of operation are completely different.

Consider first the sensing mechanism: for eddy current techniques, the coil is used to maximise the creation of an induced current within the material, caused principally by maximizing the oscillating magnetic field generated by the coil at the sample surface. Eddy currents are then generated which circulate within the material in closed loops, and these are detected by the same or a separate coil. However, the CI technique differs in that it maximises the electric field component and hence induces an electrostatic field. The absence of a coil minimizes the magnetic field component, and the air gap stops a direct ohmic current that would be generated by intimate contact between the electrodes of the device and any metallic/conducting specimen. Hence eddy current generation is discouraged, whereas a quasi-static electric field is established between the two electrodes, which can be used for imaging.

In addition, eddy current techniques rely on current circulating within the materials, thus the materials need to have reasonably high conductivity values. The induced eddy currents are running on the surface of the conducting specimens and penetrating to a certain depth depending on the frequency and the nature of the specimen (permeability and conductivity), therefore the eddy current techniques are sensitive to surface features and near surface features within the penetration depth. However, the CI technique relies on the electric field between the driving and sensing electrodes, which has a certain volume influence in non-conducting specimen and can also be disturbed by a conducting surface. Therefore, the CI technique is sensitive to both surface and subsurface features in non-conducting specimens and surface features on conducting specimens.

There is also a difference in the imaging performance. For the eddy current techniques, the penetration depth is determined by the frequency of the driving current and the nature of the conducting specimen (magnetic permeability and conductivity) due to the skin effect, and the ultimate imaging resolution, which primarily determined by the dimension of the eddy current probe, can also be affected by the frequency, as for

lower frequencies, the eddy current penetrates deeper into the material and also spreads a little wider in the radial direction. However, for the CI technique, there is no natural skin depth in non-conducting materials. The penetration depth and the imaging resolution are determined by the nature of the probing quasi-static electric field, which is primarily determined by the sensor geometry, and irrelevant to the frequency of the driving voltage.

2.8.2   Comparison with other capacitive sensors

It can be seen from the review presented in Chapter 1 that planar capacitive sensors have been widely used for a wide range of applications, such as proximity/ thickness/ displacement measurement, material characterization and NDE applications. In most of the NDE applications, the capacitive sensor systems are for non-imaging purposes, and the property changes in the specimens (e.g. water intrusion, buried objects or the presence of defects) are estimated based on the relation between the capacitance change and the property change. While for the CI technique, the actual image of the possible defects is sought.

Capacitive sensors for imaging applications can be categorised into direct imaging, model based imaging and tomographic imaging [26]. The CI technique is a direct imaging method, in which a direct mapping from a set of measurement to an image is sought. Other direct imaging methods have also been reported sporadically, but they were either designed as array (and sometimes works in a differential mode for edge detection [27]) or with multi sensing elements. Most capacitive sensors for imaging applications fall into the latter two categories. In the model based imaging method, a model of the image and the imaging system is constructed (usually in the form of measurement grids or look-up tables), and this framework is then used to infer information that is not directly available [28, 29]. In the tomographic imaging methods, the sensitivity distribution of a sensor is obtained by solving the forward problem and then the image is reconstructed by solving the inverse problem.

In past work, capacitive sensors have been designed for other applications and sensing methods [18, 27-32], while the CI probes used in this thesis are optimised for imaging performance. The electrodes in the CI probes are usually in triangular shape and

separated by a grounded guard electrode, and this has been found to be a good geometry for co-planar imaging, an aspect that has not been reported in the literature.

2.8.3   Conclusions

The theory behind the basic operation of capacitive imaging systems has been described, including the possible electrical arrangements and the basis behind the quasi-static approximation. The following chapters give more detail of the actual experimental arrangements and the way in which the expected fields can be modelled using Finite Element (FE) approaches.

2.9 References

[1]   J. D. Jackson, *Classical Electrodynamics*, Third ed. New York: Wiley, 1999.

[2]   J. Larsson, "Electromagnetics from a quasistatic perspective," *American Journal of Physics,* vol. 75, pp. 230-239, 2007.

[3]   A. K. Jonscher, *Dielectric relaxation in solids*. London: Chelsea Dielectric Press, 1983.

[4]   C. J. F. Böttcher, *Theory of electric polarization*. Amsterdam, New York: Elsevier Scientific Pub. Co.

[5]   G. G. Raju, *Dielectrics in Electric Fields*: CRC Press, 2003.

[6]   R. M. Fano, R. B.Adler, and L. J. Chu, *Electromagnetic Fields, Energy, and Forces*. New York: John Wiley & Sons, 1960.

[7]   L. K. Baxter, *Capacitive Sensors: Design and Applications*: Wiley-IEEE Press, 1996.

[8]   E.S.Kochanov, *Radiotekhnika,* vol. 7, p. 82, 1967.

[9]   R. Schinziger and P. A. A. Laura, *Conformal mapping: methods and applications*. Amsterdam: Elsevier, 1991.

[10]   O. Vendik, S. Zubko, and M. Nikol'skii, "Modeling and calculation of the capacitance of a planar capacitor containing a ferroelectric thin film," *Technical Physics,* vol. 44, pp. 349-355, 1999.

[11]   P. Bruschi, A. Nannini, F. Pieri, G. Raffa, B. Vigna, and S. Zerbini, "Electrostatic analysis of a comb-finger actuator with Schwarz-Christoffel conformal mapping," *Sensors and Actuators A: Physical,* vol. 113, pp. 106-117, 2004.

[12]   R. Igreja and C. J. Dias, "Analytical evaluation of the interdigital electrodes capacitance for a multi-layered structure," *Sensors and Actuators A: Physical,* vol. 112, pp. 291-301, 2004.

[13]   B. Aditya, C. P. Bipul, and R. Kaushik, "An Analytical Fringe Capacitance Model for Interconnects Using Conformal Mapping," *Computer-Aided Design of Integrated Circuits and Systems, IEEE Transactions on,* vol. 25, pp. 2765-2774, 2006.

[14]   K. A. Bergmanis and I. G. Matis, "Calculation of the electric field of a capacitor with a cylindrical dielectric," *Mechanics of Composite Materials,* vol. 7, pp. 461-464, 1971.

[15]   M. Goano, F. Bertazzi, P. Caravelli, G. Ghione, and T. A. Driscoll, "A general conformal-mapping approach to the optimum electrode design of coplanar waveguides with arbitrary cross section," *Microwave Theory and Techniques, IEEE Transactions on,* vol. 49, pp. 1573-1580, 2001.

[16]   T. Chen and N. Bowler, "Analysis of a concentric coplanar capacitive sensor for nondestructive evaluation of multi-layered dielectric structures," *Dielectrics and Electrical Insulation, IEEE Transactions on,* vol. 17, pp. 1307-1318, 2010.

[17]   E.-W. Bai and K. E. Lonngren, "Capacitors and the method of moments," *Computers & Electrical Engineering,* vol. 30, pp. 223-229, 2004.

[18]   J. Zoethout, A. Boletis, and H. Bleuler, "High Performance Capacitive Position Sensing Device for Compact Active Magnetic Bearing Spindles," *JSME International Journal Series C Mechanical Systems, Machine Elements and Manufacturing,* vol. 46, pp. 900-907, 2003.

[19]   A. W. H. Nassr A A and E.-D. W. W, "Coplanar capacitance sensors for detecting water intrusion in composite structures," vol. 19, p. 075702, 2008.

[20]   A. A. Nassr, W. H. Ahmed, and W. W. El-Dakhakhni, "Coplanar capacitance sensors for detecting water intrusion in composite structures," *Measurement Science and Technology,* vol. 19, p. 075702, 2008.

[21]   A. A. Nassr and W. W. El-Dakhakhni, "Non-destructive evaluation of laminated composite plates using dielectrometry sensors," *Smart Materials and Structures,* vol. 18, p. 055014, 2009.

[22]   K. Sundara-Rajan, L. Byrd, II, and A. V. Mamishev, "Moisture content estimation in paper pulp using fringing field impedance spectroscopy," *Sensors Journal, IEEE,* vol. 4, pp. 378-383, 2004.

[23]   Jérôme Lucas, Stéphane Holé, and Christophe Bâtis, "Analytical capacitive sensor sensitivity distribution and applications," *Measurement Science and Technology,* vol. 17, pp. 2467-2478, 2006.

[24]   M. J. d. Silva, "Impedance Sensors for Fast Multiphase Flow Measurement and Imaging," PhD thesis, Technische Universität Dresden, 2008.

[25]   "Agilent impedance measurement handbook," Agilent Technologies, Application Note2009.

[26]   Xiaohui Hu and W. Yang, "Planar capacitive sensors -Designs and Applications," *Sensors Review,* vol. 30, pp. 24-39, 2010.

[27]   P. J. Shull, A. V. Clark, P. R. Heyliger, J. C. Moulder, and B. A. Auld, "Characterization of capacitive array for NDE applications," *Research in Nondestructive Evaluation,* vol. 2, pp. 11-27, 1990.

[28]   D. E. Schlicker, "Imaging of absolute electrical properties using electroquasistatic and magnetoquasistatic sensor arrays." PhD thesis, Massachusetts Institute of Technology 2005.

[29]   D. Schlicker, A. Washabaugh, I. Shay, and N. Goldfine, "Inductive and capacitive array imaging of buried objects," *Bindt Insight,* vol. 48, pp. 302-306, 2006.

[30]   L. Jeong-Woo, M. Dong-Jin, K. Jiyoun, and K. Wonchan, "A 600-dpi capacitive fingerprint sensor chip and image-synthesis technique," *Solid-State Circuits, IEEE Journal of,* vol. 34, pp. 469-475, 1999.

[31]   X. B. Li, S. D. Larson, A. S. Zyuzin, and A. V. Mamishev, "Design principles for multichannel fringing electric field sensors," *Sensors Journal, IEEE,* vol. 6, pp. 434-440, 2006.

[32]   B. A. Auld, A. V. Clark, S.R.Schaps, and P.R.Heyliger, "capacitive probe array measurement and limitations," in *Review of Progress in Quantitative Nondestructive Evaluation*, 1993, pp. 1063-1070.

Chapter 3   General design principles for CI probes

3.1   Introduction

Capacitive sensors have been used previously for a number of applications, with different designs of sensors being used to address specific measurement requirements. These can be generally grouped under three main application areas: proximity sensors, permittivity measurement and tomography in pipes containing multi-phase flow. Amongst all the design variables the electrode geometry is seen to be the most decisive factor [1-5]. As examples, circular geometry sensors have been used to estimate the permittivity of a sample [6], semi-cylindrical sensors were designed for examining hard rock core samples [7] and are also used within flow meters [8-11]. Multi-segment sensors have been used for many applications, including position measurement, the detection of interfaces and tomography [12-16]. Capacitive type sensors with other geometries have also been reported [17-23]. For capacitive tomography sensors (see Figure 1.8), where the electrodes are symmetrically mounted inside or outside the pipe wall, the effects of sensor structure [24, 25], electrode length [26], shape and position of guard electrode have been studied [15]. For planar capacitive sensors, in addition to the shape of the active electrodes, an added guard electrode has been proved to be beneficial to the designs [27]. For the commonly-used multichannel and interdigital sensors (see Figure 1.4), the spatial periodicity can multiply the sensors' sensing capacitance and thus increase sensitivity.

Studies have also been presented into developing design principles for planar sensors [1, 2, 28-31]. A review of these papers indicates that they were designed primarily for through-transmission or proximity sensing, with additional work for high accuracy permittivity measurement. The use of co-planar sensors for single-sided imaging and material inspection at depth within a solid has not been described in the literature in any detail. Hence, the probes used in the present measurements must be designed with some care, to address the requirements for the NDE of materials and the imaging of defects.

In this chapter, key measures of the performance of the CI probes used throughout the work presented in this thesis are discussed. The general design principles are discussed by consideration of two typical probe geometries - symmetric and concentric.

3.2   Measures for the evaluation of CI probe performance

One of the most common uses for capacitive sensors is as proximity sensors, where the sensor head is used to measure the air gap between sensor and measured surface. For subsurface imaging and bulk inspection, the requirements are different – it is necessary to design the probe so that the required field distribution within the sample under test is produced. To evaluate the performance of a given CI probe, depth of penetration, measurement sensitivity, signal to noise ratio (SNR) and imaging resolution could be considered as the fundamental measures. Each of the measures will be described in details in the following sections.

3.2.1   Depth of penetration

The depth of penetration, as the term implies, is a measure of how deep the electric field can penetrate into a sample. In CI applications, where the quasi-static assumption is valid, the penetration depth of the electric field into a given material is determined by two factors: the permittivity of the material and the electrode geometry. The electric field from a given driving electrode decays more quickly within materials with higher permittivity. However, the primary factor for a given material in determining depth of penetration is then the geometry of both the driving and receiving electrodes. For the purpose of defect detection using the CI technique, the depth of penetration is more suitably referred to as depth of interrogation, because we are interested in determining to what depth the change in electrical properties can be detected. Both the driving (source) electrode and the sensing electrode need to be considered.

There is no consensus on defining the penetration depth for planar capacitive sensors because of the complexity of the fringing electric field and the variety of the probe geometry. One way of accounting for both sensing and driving electrodes in evaluating the effective penetration depth is to position a sample under the probe, move it further away from the surface and measure the terminal capacitance across the driving and

sensing electrodes [1]. A threshold of 3 percent of the dynamic range (the difference between the capacitance with sample at $z = 0$ position and the asymptotic capacitance ($z = \infty$)) is then used to define the z distance as the penetration depth, as shown in Figure 3.1.
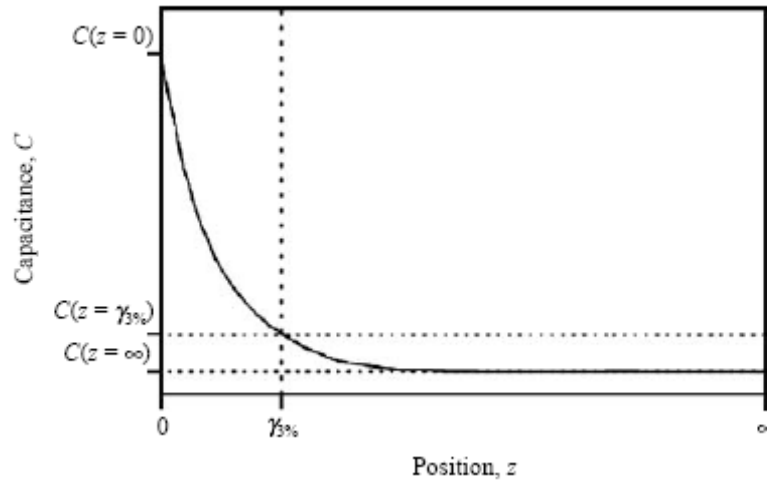
Figure 3.1: *Evaluation of the penetration depth of a planar capacitive sensor, where $\gamma_{3\%}$ is the effective penetration depth[1].*

A second way of defining the penetration depth is to consider the overall capacitance in terms of energy [32]. The general formula for capacitance calculated from energy is:

$$C = \frac{2}{V^2} \cdot \int W_e,$$
(3.1)

where V is the potential across the capacitor and W_e is the energy density. The penetration depth can then be defined as the depth at which 99% of the total capacitance is reached.

These approaches differ from those used for eddy currents, where the penetration depth can be controlled by varying the frequency. The penetration depth of CI probes depends largely on the geometry of both of the electrodes (size, shape and arrangement) and the separation between the driving and sensing electrodes for a given material. The control of penetration depth from changing probe geometries in capacitive sensors, sometimes called the artificial-skin effect or zoom effect, has been exploited in the *w-k* dielectrometry sensors [33]. For the interdigital sensors used, the penetration depth is

defined to be of the order of $\lambda / 2\pi$, where λ is the spatial periodicity of the electrode structure [28]. Such interdigital sensors are designed to have a high measurement sensitivity. In our case, it is signal change and not absolute value that is of primary interest. Hence the design of the measurement probe differs.

3.2.2 Measurement sensitivity

The measurement sensitivity is defined as the ratio between the change in output and the change of targeting physical parameter. For conventional capacitive sensors designed for measuring sample electric properties (non-imaging applications), such as measuring permittivity value or moisture content, the absolute value of the measurement sensitivity is enough as the whole sampled volume in a specimen is assumed to be homogeneous. For imaging applications, the distribution of sensitivity is also of interest, because the measurement sensitivity is position dependent for CI probes due to the non-uniformity of the electric field between the coplanar driving electrode and sensing electrode. The sensitivity distribution can be estimated using the tangential slope of the curve shown in Figure 3.1, and it can be seen that the sensitivity decreases with the distance increasing. The measurement sensitivity distribution is determined by the distribution of the electric field from the CI probe, which is primarily determined by the probe geometry. Generally, for a particular capacitive sensor, a local electric property change, such as the presence of a defect, will cause a bigger signal change if it is located in a position where the electric lines are more densely spaced (which is usually near the probe surface) as it will perturb more electric lines. It is worth noting that the imaginary electric lines emanate from the driving electrode, and can terminate at ground, infinity and the sensing electrodes. Only the electric lines which terminate at the sensing electrode take part in the measurement. Therefore, to be more accurate, the sensitivity is higher at a position where the electric lines which terminate at the sensing electrode are more densely packed. The sensitivity distribution of a CI probe can be predicted and subsequently used for probe design and optimization, and details will be discussed in the next chapter.

3.2.2 Imaging resolution

Imaging resolution refers to the smallest feature that can be detected from a scan. For NDE purposes, an image produced by a CI probe should have an appreciable spatial resolution to define the shape and size of a defect. In a 2D X-Y scan, each pixel in the obtained image corresponds to the result from a scan position, and the intensity of the pixel is a reflection on the local electric properties averaging over a certain volume. The sampled volume of each scan point is also determined by the geometry of the probe. Generally, for a fixed electrode size and shape, a bigger electrode separation means lower resolution as the probe effectively samples a bigger volume. Note that, imaging resolution of a given CI probe may vary when applied to samples of different electric properties (conductivity or permittivity), because the probing electric field behaves differently with the sample being conductor or insulator.

3.2.3 Signal to noise ratio (SNR)

The capacitive imaging technique employs the fringing electric field from the planar electrode pair, and hence the capacitive coupling between the driving and sensing electrode is relatively weak. This leads to a very low signal on the sensing electrode which can be easily disturbed by noise. In terms of probe design, the signal to noise ratio can be improved by increasing the signal level (e.g. using a bigger size electrode and smaller electrode separation) or by reducing the noise level (e.g. using grounded back plane and guard electrodes).

3.3 The definition of the volume of influence (VOI) of the CI probe

From the discussions of the major measures of probe performance, it can be concluded that the performance of the CI probe is determined by the geometry (including the shape, size and arrangement of the electrodes) in a complex way. It is difficult to optimize the probe design by accessing each of the design parameters separately, because one design parameter can influence the probe performance in different aspects, and several design parameters can be considered at the same time to achieve one design requirement. The volume of influence (VOI) is thus used to describe which part of the testing sample under the probe plays a significant role in the measurement.

55

The broken line in Figure 3.2 schematically shows the VOI of a CI probe. Only the defects presented in the VOI will cause a detectable signal change. The VOI of a CI probe determines the ability to image defects at particular locations (in the same way that radiation field patterns from ultrasonic transducers define image quality). Preferably, the volume of influence should have a small cross-section in the horizontal direction and a large depth in the vertical direction, to provide a better spatial resolution for the image and a deeper penetration depth.
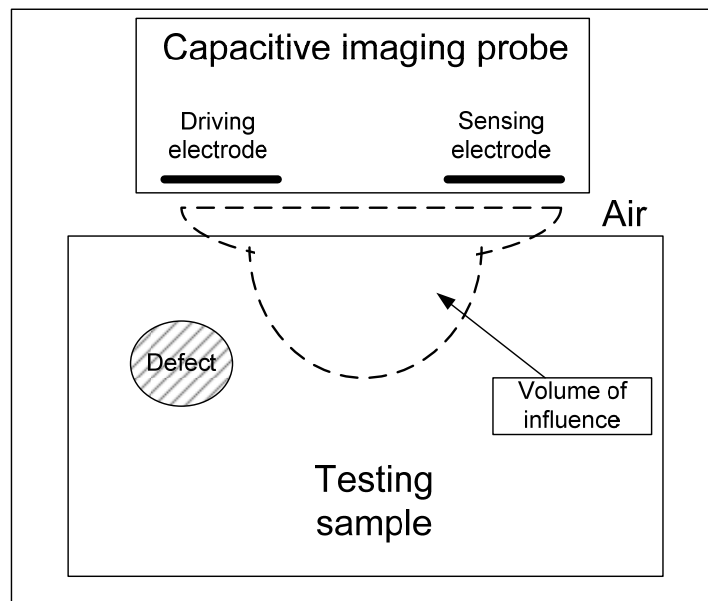
Figure 3.2: *Schematic diagram of the volume of influence (VOI) of the CI probe.*

Within the quasi-static electric field range, the VOI is primarily determined by the geometry of the CI probe. A common method based on the spatial distribution of energy was initially proposed [34] and used to determine the VOI for soil moisture content measurement using time domain reflectometry (TDR) probes [35] and capacitance probes [36]. In this thesis the determination of the VOI will be based on the analysis of the sensitivity distribution, which will be obtained through 3D Finite Element modelling in Chapter 4. The characterization for the volume of influence of CI probes will also be described in detail in chapter 4.

3.4 Examples of CI probe designs

To demonstrate the general relationship between the design variables and the probe performance, preliminary studies on two types of CI probe designs are presented here, namely symmetric probes and concentric probes.

3.4.1 Symmetric probes

The simplest symmetric capacitive probe is formed by a pair of rectangular metal plates, which acts as the positive and negative electrodes of the capacitor. To improve the performance of a symmetric CI probe, several design factors are considered. These factors are discussed in detail as follows:

a) Separation between electrodes:

For coplanar capacitive probes, the separation of a given shape of the electrodes is an important factor in controlling penetration depth. Figure 3.3(a) shows a pair of square electrodes. with d_1 being the separation between their centroids, and Figure 3.3(b) shows a second pair with an increased separation d_2 ($>d_1$). Figure 3.3(c) and Figure 3.3(d) are the cross-sectional views of the probes. The dashed lines indicate the electric field lines which effectively take part in the measurement. It can be seen that a probe design with a larger distance between the centroids of the two electrodes is to the detriment of the signal strength, as the field lines are spread over a larger volume of solid material. In this case, the coupling between the two electrodes is weaker and the electric field lines are more prone to travel further to reach the sensing electrode. This increases the penetration depth, and is hence useful for the detection of deeper features. Conversely, if the distance between the centroids is smaller (as shown in Figure 3.3(a)), the coupling between the two electrodes is stronger, and the electric field lines are more concentrated at the sample surface.
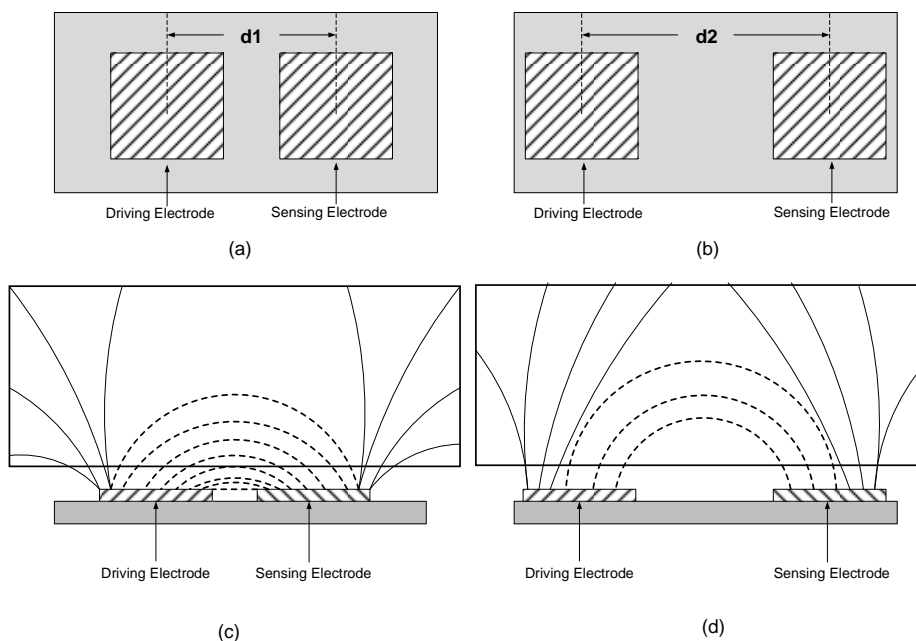
Figure 3.3: *Schematic diagrams for CI probes with different electrode separations. (a) Separation d_1, (b) Separation d_2, (c)Cross-section of the probe with d_1 separation and (d) Cross-section of the probe with d_2 separation.*

A six electrode array has been used to simulate electrode pairs with different separations experimentally. This is shown in Figure 3.4.
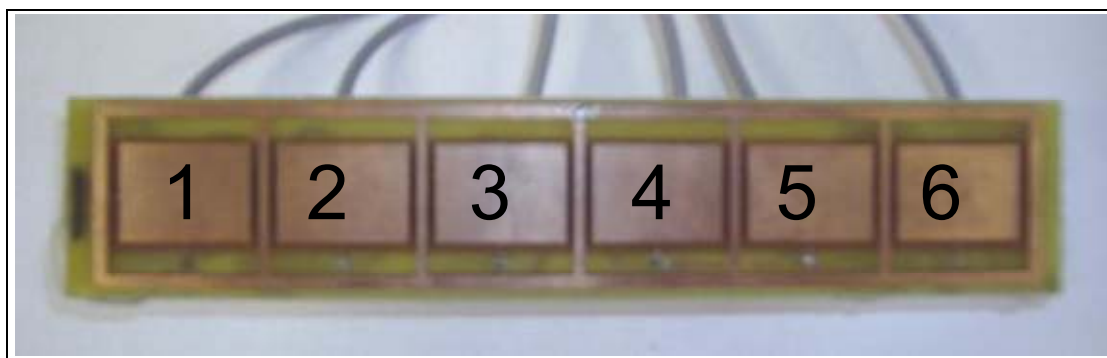
Figure 3.4: *Electrode array with each electrode numbered.*

The first electrode from left acted as the driving electrode and excited by a 10V peak-to-peak AC voltage, the second to the sixth electrode acted as sensing electrode in turn and the voltages on those sensing electrodes were measured. While one pair was selected other electrodes were left floating. The results are shown in Table 3-1 and Figure 3.5. It can be seen from the results that as the separation increases the voltage on sensing electrodes decreases which indicates a weaker capacitive coupling between

the electrode pair. Note that, the measured voltage did not tend to zero for the furthest pair because the guard electrodes surrounding each active electrodes in this electrode array were left floating during the experiment and coupled from both the driving and sensing electrodes.

Table 3-1: *Measured induced voltage for selected electrode pairs.*

	Pair	Measured induced Voltage (V)
1	1-2	2.90
2	1-3	1.43
3	1-4	1.08
4	1-5	1.03
5	1-6	1.00
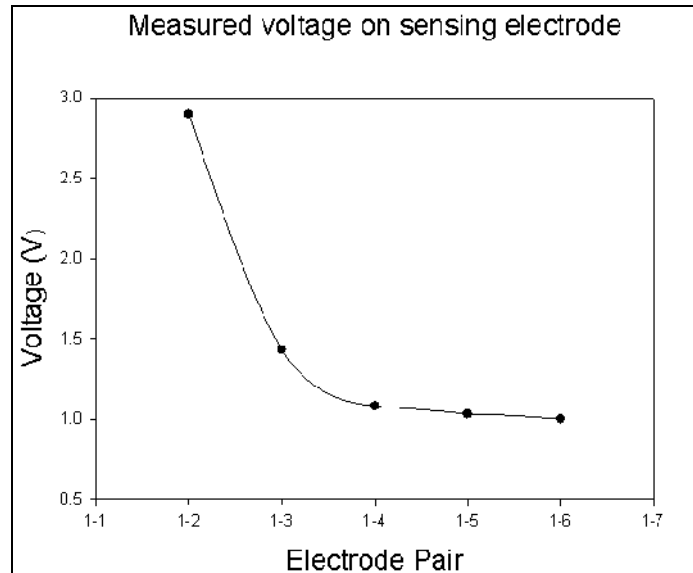
Figure 3.5: *Induced voltages of different electrode pairs.*

Another experiment aimed to find the relationship between the penetration depth and electrode separation using this six electrode array. The system diagram is shown in Figure 3.6. A grounded steel rod (5mm in diameter) was held and manipulated by the scanning stage. Electrode 1 in Figure 3.4 was driven by a 20 V peak-to-peak AC voltage and the induced voltage on electrode 2 to 6 was measured by an oscilloscope while the rod was moving away from the array surface along the central line for each selected pair.

59
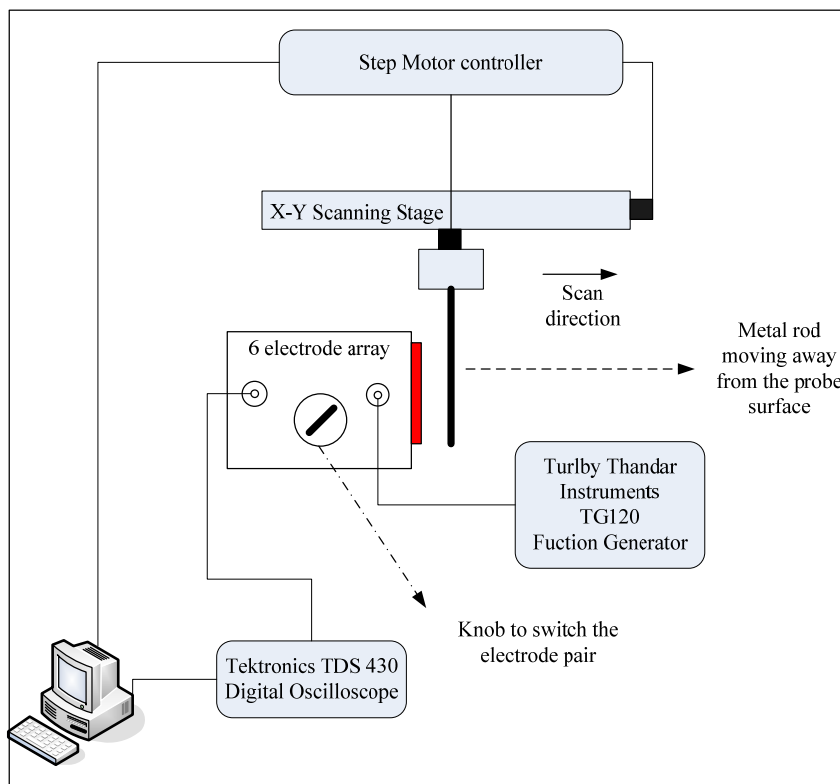
Figure 3.6: *Experimental arrangement for measuring the response of the electrode array to a grounded steel rod.*

Two of the results are shown here. For electrode pair 1-2, as shown in Figure 3.7(a), the voltage increases as the rod moving further till about 40 mm in this case, indicating the penetration depth is roughly 40 mm for pair 1-2. (Note that, the relatively big voltage (~3.7V) but small dynamic range of the measures signal was due to the floating guard electrodes and the absence of grounded back plane.) Similar results were expected for other pairs. However, as shown in Figure 3.7(b), even for pair 1-3, there was no such trend as in the pair 1-2 case. The reason is in the cases of pair 1-3 to 1-6 the separation between the driving and sensing electrode were too far and the coupling between the electrodes becomes too weak. In addition, the floating and guard electrodes drew more electric lines, which depleted the coupling further more. As a result, in the VOI of the 1-3 pair the sensitivity to the perturbation (the grounded rod) was too low to be measured with such equipment. Based on the results, a series of CI probes with gradually increased electrode separations are required. Alternatively, the effect of the electrode separation on the penetration depth for

symmetric CI probes can be examined from finite element models, and details will be shown in Chapter 4.

(a)   (b)
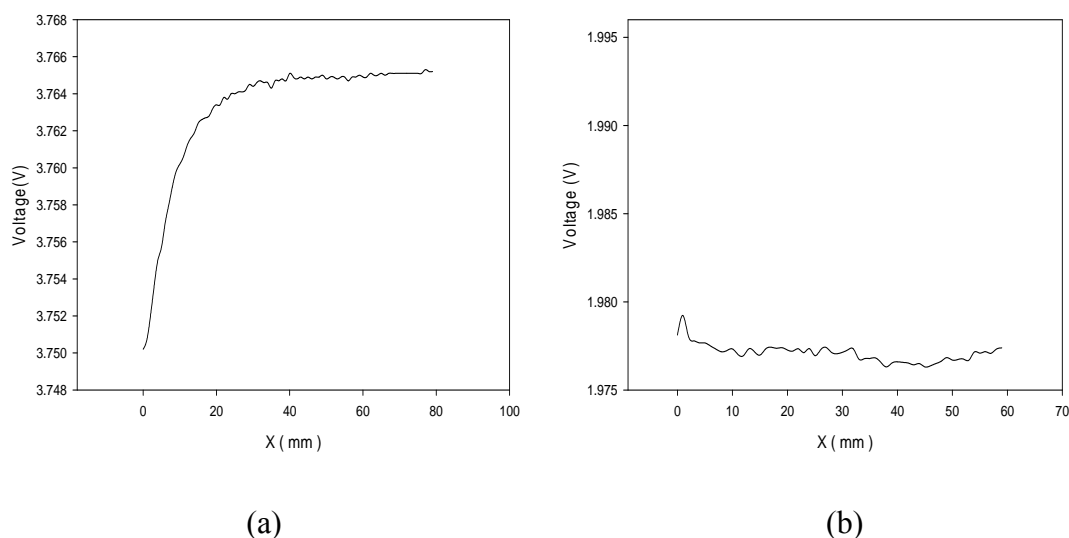
Figure 3.7: *Measured voltage with grounded rod moving away from array surface. (a) Electrode pair 1-2 and (b) electrode pair 1-3.*

b) Guard electrode:

When a voltage is applied to the driving electrode of a CI probe, the electric field emanates from all surfaces, including the side edges despite the fact that the electrode is usually very thin. The electric lines originated from the driving electrode are usually denser near the probe surface hence such devices are sensitive to very small unwanted surface features (such as surface roughness and dirt). In addition, if the thickness of the testing sample is small compared to the probe size, the effective regions of the measurement will be outside the sample. These factors are difficult to control in practical tests, so the results may become unreliable [27]. Guard electrodes are thus employed here to diminish these disadvantages as well as focus the electric field and eliminate noise from unwanted sources (e.g. ambient electromagnetic field). In capacitive imaging applications the guard electrodes are held at a "ground" potential.

61
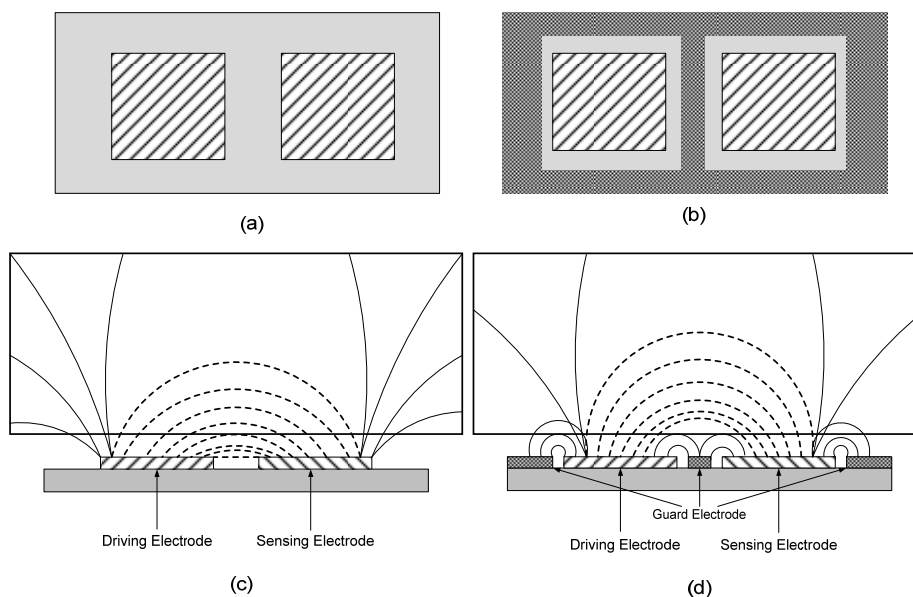
Figure 3.8: *Schematic diagrams for CI probes with and without guard electrodes. (a) Top view of the CI probe without guard electrodes, (b) Top view of the CI probe with guard electrodes, (c) Cross-section of the CI probe without guard electrodes and (d) Cross-section of the CI probe with guard electrodes.*

Figure 3.8(a) is a top view of a CI probe with the basic symmetric geometry - a pair of co-planar rectangular electrodes. The coplanar electrodes were patterned on an insulating substrate. Figure 3.8(b) shows an identical pair of electrodes with grounded guard electrodes – darker areas surrounded and between the electrodes. Figure 3.8(c) and figure 3.8(d) are the cross-sectional views of the two probes with the solid and dashed lines representing the schematic electric field lines. Again the dashed lines describe the regions that primarily affect the output.

The fringing electric field that originated from the driving electrode will travel through the air gap, penetrate into the sample and terminate on the sensing electrode. Without the guard electrodes, some of the electric lines travel directly from the driving electrode to the sensing electrode and they are more densely-spaced within the air gap, which makes the probe very sensitive to the small lift-off distance, as shown in Figure 3.8(c). The inner guard electrodes between the driving and sensing electrodes counteract this effect by blocking the direct path of the electric field line from the driving electrode to the sensing electrode and pushing more field lines towards the sample under test, as shown in Figure 3.8(d). Although the grounded

guard electrode between and surrounding the driving and sensing electrodes will reduce the signal strength, as some charge is lost in the parasitic coupling between the driving / sensing electrode and the grounded guard electrode, it will effectively increase the penetration depth of the probe and make the probe less sensitive to changes in the small lift-off distance. This is a drawback for displacement/distance measurement but an advantage for imaging purpose.

As mentioned earlier in this section, if the thickness of the non-conducting sample is small compared to the probe size, some of the electric lines will penetrate through the sample and emerge from the far side. The situation is illustrated by the solid electric lines in Figure 3.8(c). Although these lines are not in the high sensitivity region, they might cause errors in measurements. The outer guard electrodes counteract this effect by attracting some of the outer electric lines and make the probe less sensitive to the thickness of the sample, as shown in Figure 3.8(d).

Note that the situation shown in Figure 3.8(d) is a case in which the sensing electrode is floating, and hence there is a potential difference between the sensing electrode and the grounded guard. In practical CI applications, the charge signal (displacement current) on the sensing electrode is measured by charge amplifiers with low input impedance, which makes the sensing electrodes virtually grounded. Hence no charge is lost in the parasitic coupling between the sensing electrodes and grounded guard electrodes.

The influence of the guard electrodes was experimentally examined by measuring the electric field distribution in the vicinity of the CI probes. The system diagram for electric field measurements is shown in Figure 3.9. The driving electrode of the CI probe was stimulated by a signal generator (Turlby Thandar instruments TG120), and the sensing electrode was grounded. An oscilloscope probe (Tektronix P6139) was held and manipulated by an X-Y scanning stage, and the measured voltage in the vicinity of the probe is captured by the oscilloscope (Tektronix TDS430) and recorded by the computer. All the electric field distributions presented in this chapter were obtained with the oscilloscope probe scanned over the interested areas with a 1mm step.
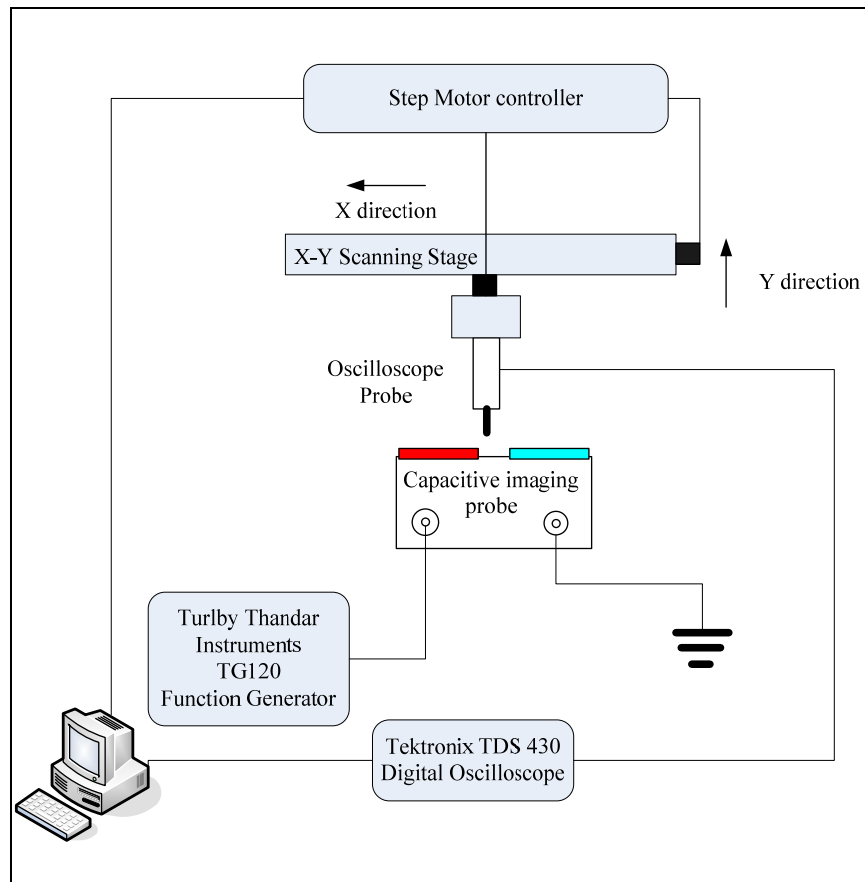
Figure 3.9: *Experimental arrangement for electric field mapping.*

The probe examined to investigate the effect of the guard electrode is shown in Figure 3.10.
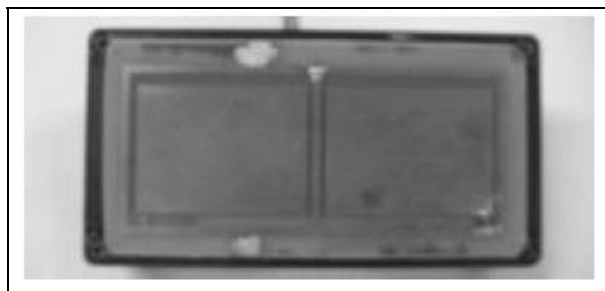
Figure 3.10: *Photograph of a CI probe with rectangular electrodes and guard electrodes.*

Scans of the electric field distribution were performed with the guard electrodes electrically isolated and grounded. The results are present in both a 2D intensity plot and a 3D wire frame plot, as shown in Figure 3.11(a) and 3.11(b).

64

(a)   (b)
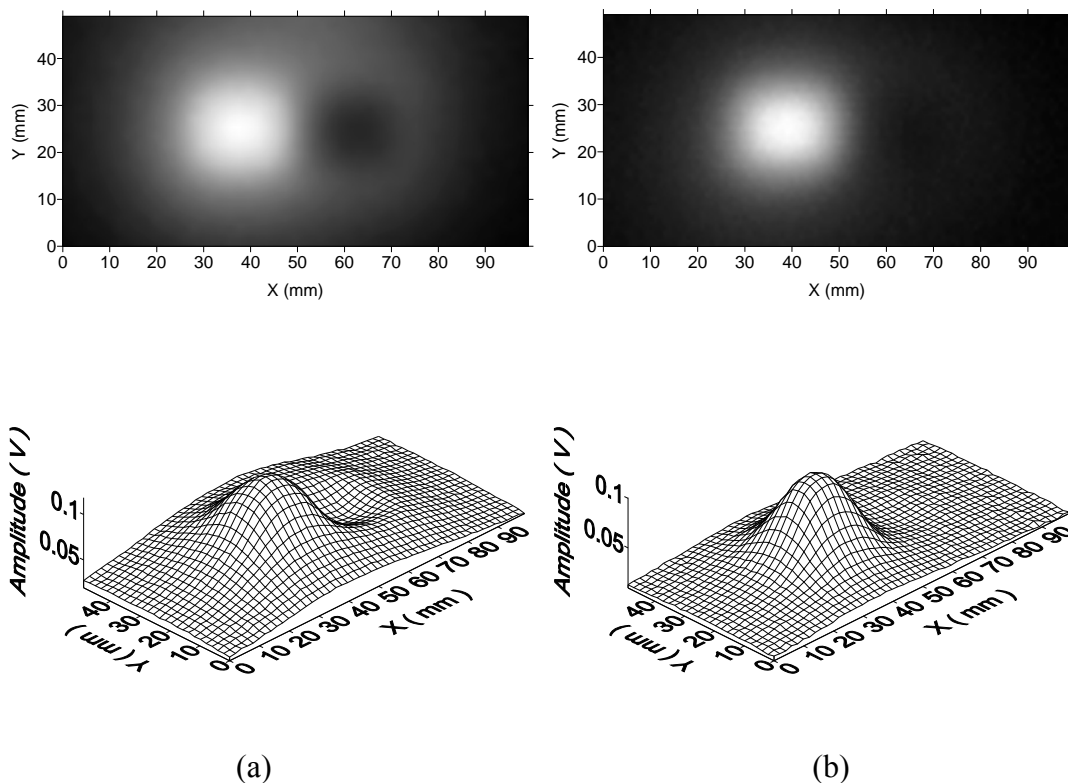
Figure 3.11: *Experimentally measured electric field maps below the square electrode pair shown in Figure 10, in a plane parallel to the electrodes and at a distance of 1 mm. Scans are shown for the guard electrode (a) electrically isolated and (b) grounded.*

The scans were taken from a parallel plane to the electrodes and at a distance of 1 mm. It can be seen that the grounded guard electrode confined the electrical field within a narrower spatial range and prevented the field lines going directly from driving electrode to sensing electrode. This forces the electric field going towards the material under test and increases the field penetration depth.

c) Choice of electrode shape:

Conventional capacitive sensors usually contain two rectangular shape electrodes [21] or two sets of interdigital electrodes, and the distance between the centres of the two adjacent electrodes determines the penetration depth of those sensors [28]. For probes with same overall electrodes area, to achieve a greater penetration depth, one can increase the distance between the electrodes but this will weaken the signal strength as the coupling between the driving and sensing electrodes are weaker and reduce the

image resolution as they are sampling a bigger area of the sample and more importantly it is physically disallowed if the size of the overall probe size is fixed.

Triangular electrodes can be used to balance these trade-offs, and can be positioned in two orientations: back-to-back or point-to-point. For back-to-back triangular electrodes, a comparison to rectangular electrodes of the same area (shown in Figure 3.12 (a) with a dashed line), demonstrates that the centroids P_t for the triangular electrodes are further apart than the centroids P_s for the rectangular electrodes. This will make the penetration depth greater when imaging bulk features in non-conductive samples.
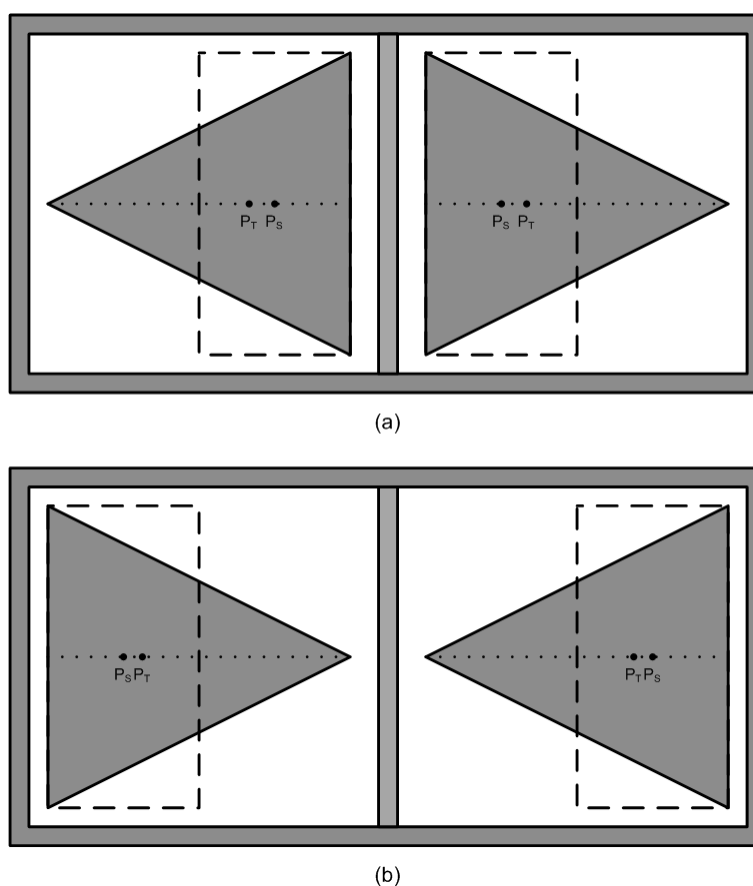
Figure 3.12: *Diagram for triangular pair probe (a) back-to-back (b) point-to-point.*

For a point-to-point triangular probe, Figure 3.12(b), the same comparison shows that the centroids for the triangular electrodes are more closely-spaced than the centroids for the equivalent rectangular ones. This will make the coupling between the two electrodes stronger which is good for surface feature imaging.
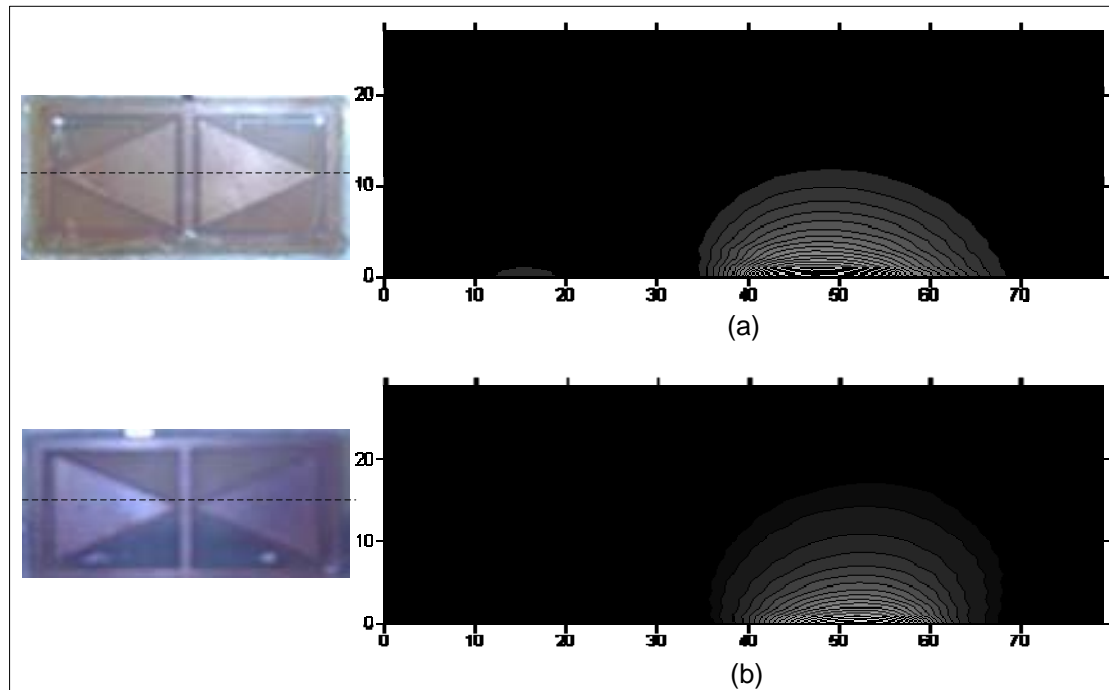
Figure 3.13: *Electric field plots along the dotted lines in each probe (a) back-to-back triangular electrodes (b) point-to-point triangular electrodes.*

The two arrangements have their own specialities and can be used in different situations. Figure 3.13 shows the electric field plots in air when scanning a probe along the dotted line and in a plane perpendicular to the page. From Figure 3.13(a), it can be seen that the electric field from a back-to-back triangular probe is converging towards the middle of the probe, while for a point-to-point triangular probe, the electric field is diverging towards the side of the probe as shown in Figure 3.13(b). It can then be concluded that the volume of influence of a back-to-back triangular probe is smaller than that of a point-to-point triangular probe if there is no sample under the probes. Note that, the plotted electric field maps (Figure 3.13) are in the form of equi-potential lines from the measured electric potential (voltage), although the figure suggested that the electric field lines are denser under the driving electrode, that doesn't mean that targeting features under the driving electrodes are more effective in the measurement, as only few of these field lines will terminate on the sensing electrode (and effective in the measurement). This is more appropriate to be explained in terms of the measurement sensitivity distribution, which will be discussed in Chapter 4.

When imaging a hidden feature in a non-conducting sample using symmetric probes, the whole volume of the fringing electric field will take part in the measurement. Therefore, with a smaller volume of influence, the back-to-back triangular probe will provide a better image resolution and will be capable of identifying defect with smaller size. On the contrary, the point-to-point triangular probe that has a bigger volume of influence will provide a deeper penetration depth and can be used to detect deeper buried defects. Conversely, when imaging a surface feature on a conducting sample using a symmetric probe, the fringing electric field between the nearest parts of the driving and sensing electrode will dominate. In the case of using point-to-point triangular electrodes, the volume of the fringing field between the two points of the two electrodes is very small and it will improve the sharpness of an image, which is an additional advantage of this kind of probe.

There is another advantage of the triangular electrode probes, in that the sharper corners will accumulate more charges and produce more electric lines in the corner which makes the signal stronger. The advantages of the triangular electrodes and the discussions on the selection of the two arrangements according to different applications will be further discussed based on the FE modelling results in chapter 4 and confirmed experimentally in chapter 5.

d) Back plane:

The electrodes of the CI probes can be made of a conductive material and there is usually a non-conducting substrate to mechanically support the electrodes. A grounded back plane is often used to shield unwanted electric field and ensure the radiated electric field emanated predominantly in the direction towards the sample. The CI probes described and used in this work were fabricated by etching a printed circuit board (PCB) substrate. The PCB was also coated in copper on its back surface and connected to ground when the probe is in use. The effect of the grounded back plane was studied. Two back-to-back triangular electrode probes were investigated. The two probes were nominally identical except only one of them was with the grounded backplane. Figure 3.14 shows the electric field plots in air when scanning the probes along the dotted line and in a plane perpendicular to the page.
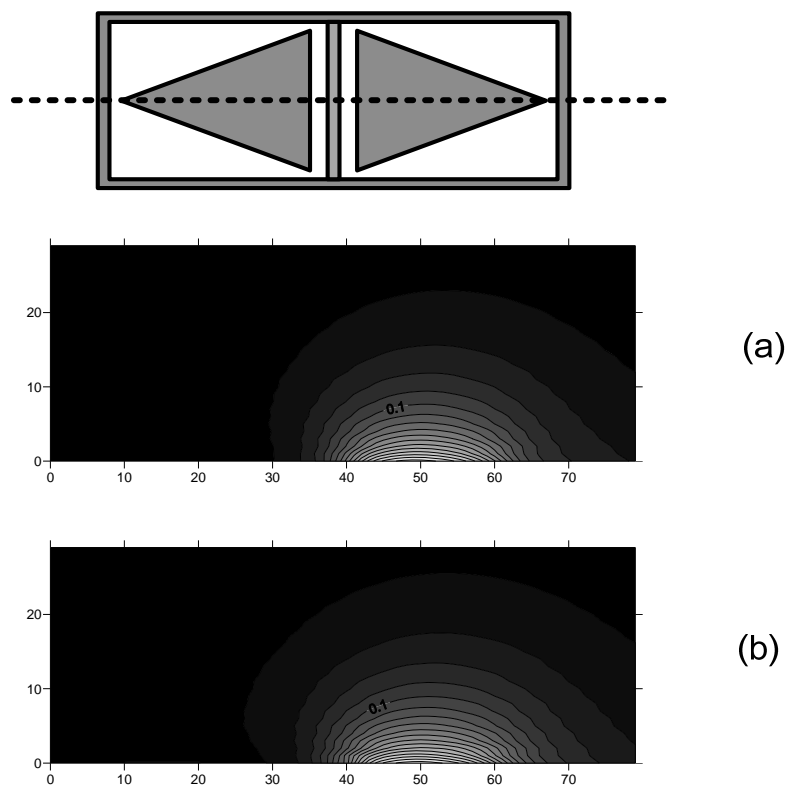
Figure 3.14: *Electric field plots along the dotted lines in each probe (a) with grounded backplane (b) without backplane.*

It can be seen by comparing Figures 3.14 (a) and (b) that the electric field decays more quickly with a grounded back plane. This is because the grounded back plane draws the electric lines from the front surface, which will result in a weaker signal level. However, compared to the case without the grounded back plane, the penetration depth will be increased. This can be explained by considering a practical measurement using a probe without the grounded backplane. In such situation, the "ground" potential will be at infinity (or at least on the grounded metal case), which will draw the electric lines further down compared to the case with a grounded back plane. Based on the comparison between the two cases, it can be seen that there again exists a trade-off between the penetration depth and signal strength.

3.4.2 Concentric probes

The second geometry of interest is shown in the photograph of Figure 3.15, namely that of using concentric electrodes, which could give better results under some circumstances [30].
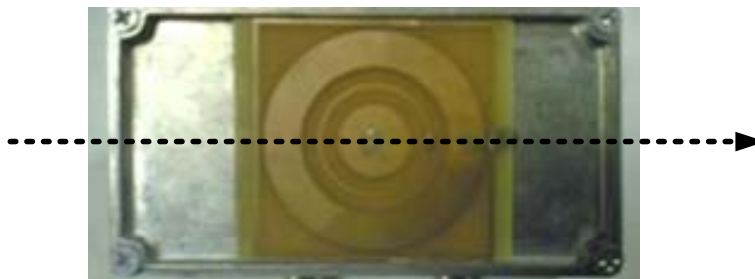
Figure 3.15: *Photograph of concentric electrode design. The outer annular electrode had inner and outer diameters of 32 mm and 48 mm respectively, and was separated from the inner disc electrode of 16 mm diameter by a thin grounded guard ring. An experimental scan was performed along the direction shown by the dotted line.*

A typical concentric probe has two active electrodes separated by a thinner guard ring. There are two modes of operation of this kind of concentric electrode design: either the central disc can be excited or the outer annulus can be used as the source. The electric field distribution that results from such a design has also been measured, as shown in Figure 3.16 for a plane across a diameter and perpendicular to the PCB surface. The field created by driving the outer annulus contains two lobes, as might be expected (Figure 3.16(a)). When the central disc is driven, Figure 3.16(b), a more suitable distribution is obtained, with a single central lobe.

(a)   (b)
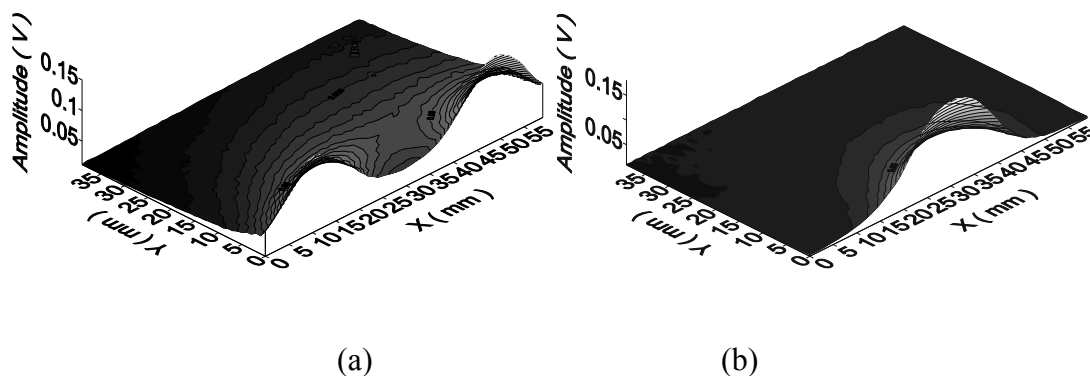
Figure 3.16: *Field plots of electric field distributions from concentric electrodes when (a) the outer annulus is excited, and (b) when the central disc is excited.*

The field in the latter case drops off fairly uniformly if measured in a perpendicular direction away from the driving electrode, as the plot of Figure 3.17(a) indicates. Conversely, the field drops off far more rapidly when the outer electrode is excited, as shown in Figure 3.17(b).
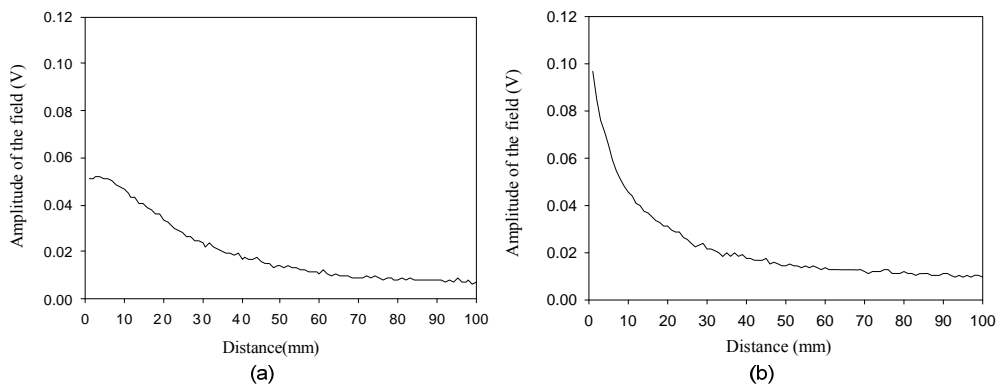
Figure 3.17: *Decay of electric field amplitude as a measurement probe is scanned in a perpendicular direction away from the PCB surface, starting from (a) the centre of the inner disc and (b) from within the outer electrode.*

From the analysis on the design variables for symmetric probes, it can be inferred that the width of the surrounding ring, the size of the inner disc and the gap between them are the factors that affect the performance of the probe with concentric geometry. Four concentric probes were made to evaluate the effects of geometry on concentric probe performance. The related parameters are labelled in the schematic diagrams shown in Figure 3.18.
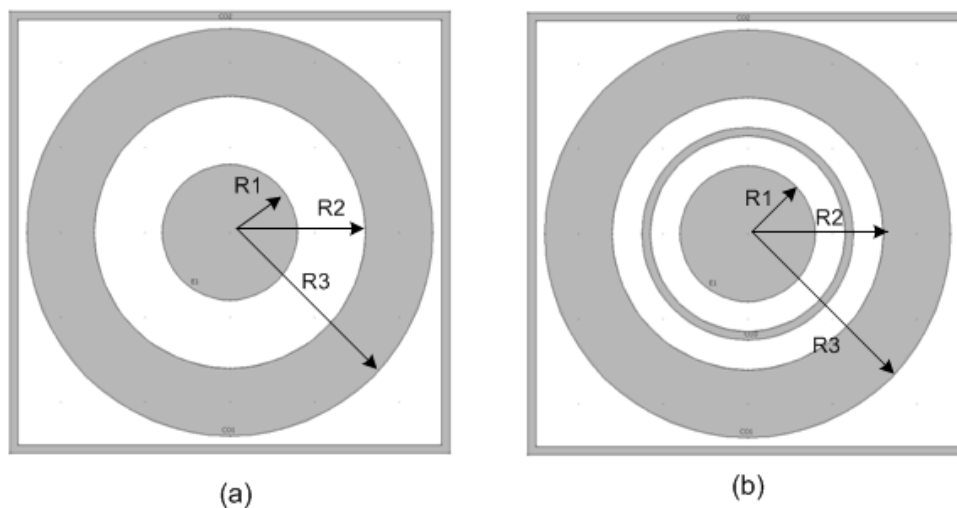
Figure 3.18: *Diagram for concentric probes. (a) Without inner guard electrode and (b) with an inner guard electrode.*

A similar experiment setup as shown in Figure 3.6 was used. A grounded rod (5mm in diameter) parallel to the probe surface was scanning away from the concentric probe surface for each probe. The specifications for each of the concentric probes and the corresponding results are shown in Figure 3.19.

The diameters of the inner discs for the four probes are identical and the outer rings were driven by the same voltage. Comparing Probes 1 and 2, with a wider separation and a thinner outer ring, Probe 2 has a bigger penetration depth (indicated by the dashed line) and lower measured values. Probe 3 has a similar penetration depth to Probe 2 but higher measured values. In addition, the grounded guard electrode in Probe 4 reduces the signal strength (lower measured values) but increased the penetration depth when compared to Probe 3. These results are in agreement with those of the triangular electrodes. However, note that the main difference of the concentric design is that its cylindrical geometry means that it is not sensitive to direction of the scan parallel to the measurement surface.

Although the measured field maps (Figure 3.16) and field drops (Figure 3.17) differed when either the outer annulus or central disc was excited, the two modes of operation will produce identical images for the same sample, as expected from reciprocity arguments (details will be discussed in Chapter 4). In addition, the inner disc can be replaced by an oscilloscope probe to act as a sensing tip, which will provide a very high image resolution. Note that, due to the high input impedance of the oscilloscope probe (10MΩ), this arrangement is not a pure capacitance measurement but measuring the distortion of the electric field from the outer ring.
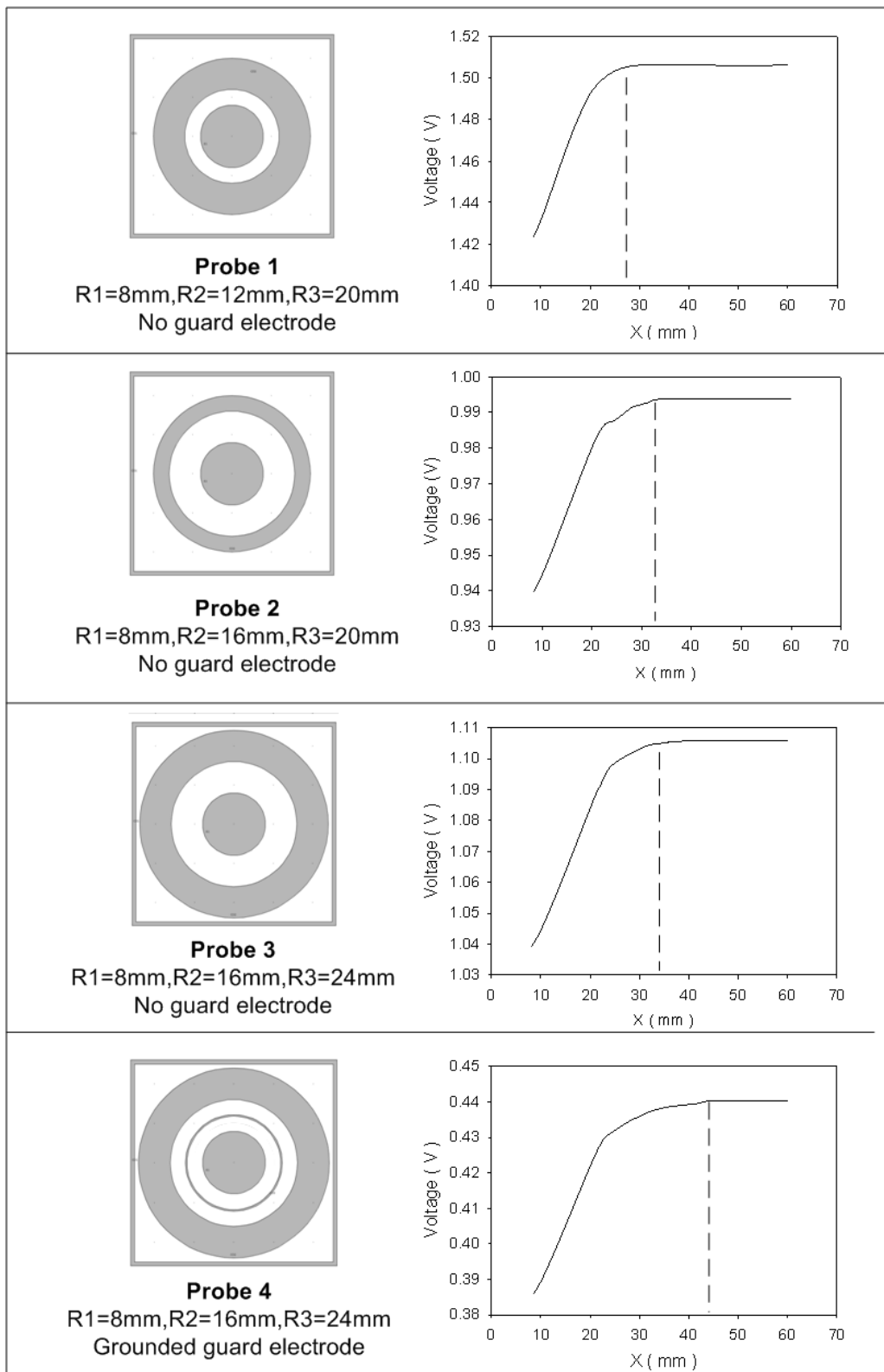
Figure 3.19: *Probe specifications (left column) and corresponding probe responses (right column).*

73

3.5   Discussion and conclusions

In common with other types of capacitive sensor, the geometry of the electrodes is a decisive factor for CI probe performance. For CI probes, the driving electrode and sensing electrode need not be of the same shape or size (e.g. the concentric geometry), and they can be arranged in different ways (e.g. point-to-point and back-to-back triangular electrodes). Therefore for CI probes with different design parameters, they will have different volumes of influence. The character of the volume of influence (size and shape) for a CI probe determined by the electrode geometry, decides the performance of this specific probe.

Generally, a bigger electrode area will provide a stronger signal but will trade off against the imaging resolution. Increased electrode separation and a grounded guard electrode will reduce the signal strength and spatial resolution at or near the surface but the overall performance of the probe will be compensated by a deeper penetration depth into the sample. Thus, ideally, to achieve an optimal design of the capacitive imaging probe, the geometry of the electrodes should be determined according to the desired penetration depth and imaging resolution for different applications. The electric field distributions in the examples shown in this chapter were measured in air and the design principles were derived based on the assumption that the sample under test is non-conducting. For surface features inspections on conducting samples, the probe performance will also be affected by the electrical condition of the conducting sample (e.g. sample being grounded or floating), details of which will be discussed in later chapters.

Amongst all the possible designs studied, the symmetric triangular pair probe, as shown in Figure 3.12 (a), balances the trade-offs to a certain extent and can be used as a good general-purpose probe for preliminary tests. However, the optimal probe design for a particular measurement can be achieved by a proper selection of the electrode size, shape and arrangement, depending on the application. Further discussions on probe design and quantitative analysis of probe performance will be presented in the next chapter.

3.6 References

[1]   X. B. Li, S. D. Larson, A. S. Zyuzin, and A. V. Mamishev, "Design principles for multichannel fringing electric field sensors," *Sensors Journal, IEEE,* vol. 6, pp. 434-440, 2006.

[2]   A. V. Mamishev, Y. Du, J. H. Bau, B. C. Lesieutre, and M. Zahn, "Evaluation of diffusion-driven material property profiles using three-wavelength interdigital sensor," *Dielectrics and Electrical Insulation, IEEE Transactions on,* vol. 8, pp. 785-798, 2001.

[3]   S. C. Mukhopadhyay, S. Yamada, and M. Iwahara, "Inspection of electroplated materials -- performance comparison with planar meander and mesh type magnetic sensor," *International Journal of Applied Electromagnetics and Mechanics,* vol. 15, pp. 323-329, 2002.

[4]   J. Hu, M. Jiang, X. Zhao, and Z. Lin, "Fringing Field Sensor Using a Circuit-Modulated Parameter for Measuring Water Content in a Soil Sample," *Journal of Irrigation and Drainage Engineering,* vol. 134, pp. 356-360, 2008.

[5]   X.Li, A.S.Zyuzin, and A. V. Mamishev, "Measuring moisture content in cookies using dielectric spectroscopy," in *Electrical Insulation and Dielectric Phenomena. Annual Report. ,* 2003, pp. 459- 462.

[6]   I. C. Shay and M. Zahn, "Cylindrical geometry electroquasistatic dielectrometry sensors," in *Electrical Insulation and Dielectric Phenomena, 2002 Annual Report Conference on*, 2002, pp. 126-129.

[7]   R. Marc and et al., "A guarded cylindrical capacitor for the non-destructive measurement of hard rock core samples," *Measurement Science and Technology,* vol. 17, p. 1390, 2006.

[8]   A. Jaworek, A. Krupa, and M. Trela, "Capacitance sensor for void fraction measurement in water/steam flows," *Flow Measurement and Instrumentation,* vol. 15, pp. 317-324, 2004.

[9]   A. Jaworek and A. Krupa, "Phase-shift detection for capacitance sensor measuring void fraction in two-phase flow," *Sensors and Actuators A: Physical,* vol. 160, pp. 78-86, 2010.

[10]   C.-T. Chiang and Y.-C. Huang, "A Semi-Cylindrical Capacitive Sensor with Signal Conditioner for Flow Meter Applications," in *Sensors, 2006. 5th IEEE Conference on*, 2006, pp. 1139-1142.

[11]   C. G. Xie and et al., "Design of capacitance electrodes for concentration measurement of two-phase flow," *Measurement Science and Technology,* vol. 1, p. 65, 1990.

[12]   X. J. Li, G. de Jong, and G. C. M. Meijer, "The application of the capacitor's physics to optimize capacitive angular-position sensors," *Instrumentation and Measurement, IEEE Transactions on,* vol. 46, pp. 8-14, 1997.

[13]   H. Wang and et al., "Optimum design of segmented capacitance sensing array for multi-phase interface measurement," *Measurement Science and Technology,* vol. 7, p. 79, 1996.

[14]   I. Ismail, J. C. Gamio, S. F. A. Bukhari, and W. Q. Yang, "Tomography for multi-phase flow measurement in the oil industry," *Flow Measurement and Instrumentation,* vol. 16, pp. 145-155, 2005.

[15]   W. Yang, "Design of electrical capacitance tomography sensors," *Measurement Science and Technology,* vol. 21, pp. 1-13, 2009.

[16]   W. Q. Yang and S. Liu, "Electrical capacitance tomography with square sensor," *Electronics Letters,* vol. 35, pp. 295-296, 1999.

[17]   J. E. Kenneth and S. R. Kamiel, "Void fraction measurements in gas - liquid flows using capacitance sensors," *Measurement Science and Technology,* vol. 7, p. 1153, 1996.

[18]   M. Zagnoni, A. Golfarelli, S. Callegari, A. Talamelli, V. Bonora, E. Sangiorgi, and M. Tartagni, "A non-invasive capacitive sensor strip for aerodynamic pressure measurement," *Sensors and Actuators A: Physical,* vol. 123-124, pp. 240-248, 2005.

[19]   E. Bozzi and M. Bramanti, "A planar applicator for measuring surface dielectric constant of materials," *Instrumentation and Measurement, IEEE Transactions on,* vol. 49, pp. 773-775, 2000.

[20]   Z. Chen and R. C. Luo, "Design and implementation of capacitive proximity sensor using microelectromechanical systems technology," *Industrial Electronics, IEEE Transactions on,* vol. 45, pp. 886-894, 1998.

[21]   N. Kirchner, D. Hordern, D. Liu, and G. Dissanayake, "Capacitive sensor for object ranging and material type identification," *Sensors and Actuators A: Physical,* vol. 148, pp. 96-104, 2008.

[22]   A. W. H. Nassr A A and E.-D. W. W, "Coplanar capacitance sensors for detecting water intrusion in composite structures," vol. 19, p. 075702, 2008.

[23]   A. A. Nassr and W. W. El-Dakhakhni, "Non-destructive evaluation of laminated composite plates using dielectrometry sensors," *Smart Materials and Structures,* vol. 18, p. 055014, 2009.

[24]   X. Dong and S. Guo, "Modelling an electrical capacitance tomography sensor with internal plate electrode," in *Test and Measurement, 2009. ICTM '09. International Conference on*. vol. 2, 2009, pp. 160-163.

[25]   A. M. Olmos, M. A. Carvajal, D. P. Morales, A. Garcia, and A. J. Palma, "Development of an Electrical Capacitance Tomography system using four rotating electrodes," *Sensors and Actuators A: Physical,* vol. 148, pp. 366-375, 2008.

[26]   Y.-P. Liu, G. Niu, and J. Wang, "Design of capacitance sensor system for void fraction measurement," *Journal of Zhejiang University - Science A,* vol. 6, pp. 1424-1429, 2005.

[27]   A. V. Bugrov, N. I. Dudkin, and I. M. Maslennikov, "One-sided capacitance transducer with a guard electrode," *Measurement Techniques,* vol. 19, pp. 967-969, 1976.

[28]   K. Sundara-Rajan, A. V. Mamishev, and M. Zahn, "Fringing Electric and Magnetic Field Sensors," in *Encyclopedia of Sensors*. vol. 4, 2005, pp. 89-100.

[29]   X. B. Li, C. Kato, A. S. Zyuzin, and A. V. Mamishev, " Design of multichannel fringing electric field sensors for imaging. Part I. General design principles," in *Electrical Insulation, 2004. Conference Record of the 2004 IEEE International Symposium on*, 2004, pp. 406- 409.

[30]   X. B. Li, C. Kato, A. S. Zyuzin, and A. V. Mamishev, "Design of multichannel fringing electric field sensors for imaging. Part II. Numerical examples," in *Electrical Insulation, 2004. Conference Record of the 2004 IEEE International Symposium on*, 2004, pp. 410-413.

[31]   A. V. Mamishev, B. C. Lesieutre, and M. Zahn, "Optimization of multi-wavelength interdigital dielectrometry instrumentation and algorithms," *Dielectrics and Electrical Insulation, IEEE Transactions on,* vol. 5, pp. 408-420, 1998.

[32]   R. W. Gamache, "Electromagnetic Material Properties Sensor," in *COMSOL Multiphysics User's Conference* Boston, 2005.

[33]   M. C. Zaretsky, L. Mouayad, and J. R. Melcher, "Continuum properties from interdigital electrode dielectrometry," *Electrical Insulation, IEEE Transactions on,* vol. 23, pp. 897-917, 1988.

[34]   J. H. Knight, "Sensitivity of time domain reflectometry measurements to lateral variations in soil water content," *Water resourses research,* vol. 28, 1992.

[35]   H. H. Nissen, P. Moldrup, T. Olesen, and O. K. Jensen, "Time Domain Reflectometry Sensitivity to Lateral Variations in Bulk Soil Electrical Conductivity," *Soil Science Society of America journal,* vol. 65, pp. 1351-1360, 2001.

[36]   H. Bolvin, A. Chambarel, and A. Chanzy, "Three-dimensional numerical modeling of a capacitance probe: Application to measurement interpretation," *Soil Science Society of America journal,* vol. 68, pp. 440-446, 2004.

Chapter 4   Finite element modelling of the CI probes

4.1   Introduction

As seen in Chapter 3, optimal probe design is essential for CI to operate properly. As discussed earlier in Chapter 2, it is only possible to obtain an analytical solution of the field equations for planar capacitors with the simplest geometries, *i.e.* a strip-shaped electrode pair. For NDE purposes, the absolute value of the calculated capacitance is insufficient to characterize the probe performance. Instead, the way in which the probing electric field is perturbed by the defects presented in the specimen is of more interest. From the discussions presented in Chapter 3, it can be seen that there are several variables that can be used to tailor the CI probe for an optimum performance, but the construction and testing of different physical prototypes are expensive and time consuming. It is thus useful to develop numerical models to efficiently and accurately represent the probe's performances.

In this chapter, finite element modelling (FEM) is used to calculate the electric field and predict the electric potential distribution near the CI probe. Results from 2D models are presented to demonstrate the range of applications of the CI technique and used to evaluate the non design-related parameters. Probe responses to typical flaws are also presented. The construction of 3D models is introduced, together with methods of obtaining the sensitivity distributions of the CI probes from the 3D models. A comparison of the sensitivity distributions of different CI probes in different situations is also made.

4.2   Finite element modelling applied to capacitive imaging probes

In Finite Element (FE) models, the problem domain is divided into series of small regions (called "elements") with simple geometries. The elements are then reconnected at discrete points (called "nodes"). The governing equations are applied to the sub-domain of a single element and the unknown variables at the nodes can be obtained. By connecting the elements together through the nodes, the behaviour over the entire domain can be determined.

To apply the FEM to the CI probes, the governing equations need to be considered first. Fundamentally, the electromagnetic phenomena are governed by the Maxwell's equations. In a general case of materials exhibiting both dielectric and conductive properties, the Maxwell-Ampere equation is considered.

$$\nabla \times \boldsymbol{H} = \boldsymbol{J} + \frac{\partial \boldsymbol{D}}{\partial t} \tag{4.1}$$

where $\boldsymbol{H}$ is the magnetic field intensity, $\boldsymbol{J}$ is the free current density and $\boldsymbol{D}$ is the electric flux density. To eliminate the magnetic field intensity $\boldsymbol{H}$, the divergence of both sides of Equation (4.1) is taken, as:

$$\nabla \bullet (\boldsymbol{J} + \frac{\partial \boldsymbol{D}}{\partial t}) = 0 \tag{4.2}$$

The frequencies used in capacitive imaging probes are generally in the region between 10 kHz and 1 MHz. As mentioned in Chapter 2, at such frequencies, inductive phenomena can be neglected and the electromagnetic field can be considered as a quasi-static electric field. It can then be assumed that the time-derivative of the magnetic flux density ($\boldsymbol{B}$) is negligible, and based on Faraday's Law the electric field ($\boldsymbol{E}$) is curl free,

$$\nabla \times \boldsymbol{E} = -\frac{\partial \boldsymbol{B}}{\partial t} = 0 \tag{4.3}$$

Based on Equation (4.3), the electric field ($\boldsymbol{E}$) can be described by an electric scalar potential distribution $\varphi(x, y, z)$, so the electric potential distribution $\varphi(x, y, z)$ can be introduced as:

$$\boldsymbol{E} = -\nabla \varphi(x, y, z) \tag{4.4}$$

and using the constitutive relationships:

$$\boldsymbol{J} = \sigma(x, y, z)\boldsymbol{E} \tag{4.5}$$

$$\boldsymbol{D} = \varepsilon(x, y, z)\boldsymbol{E} \tag{4.6}$$

Equation (4.2) can take the form:

80

$$\nabla \bullet \left[\sigma(x,y,z) \nabla \varphi(x,y,z) \right] + \nabla \bullet \left\{ \frac{\partial}{\partial t} \left[\varepsilon(x,y,z) \nabla \varphi(x,y,z) \right] \right\} = 0 \qquad (4.7)$$

Here, $\sigma(x,y,z)$ is the conductivity distribution and $\varepsilon(x,y,z)$ is the permittivity distribution. If the conductivity and permittivity distributions within the area of interest covered by the electric field are known, the electric potential distribution $\varphi(x,y,z)$ can be obtained by solving Equation (4.7). But in practice, due to the time-derivative coupling between the dielectric and conductive properties, solving Equation (4.7) is computationally prohibitive [1]. The practical way of solving this problem is to treat the system as either "predominantly dielectric" or "predominantly conductive" [1]. In the former case, Equation (4.7) can be simplified to be a Laplace's equation:

$$\nabla \bullet \left[\varepsilon(x,y,z) \nabla \varphi(x,y,z) \right] = 0 \qquad (4.8)$$

This equation is valid, for example, for Electrical Capacitance Tomography (ECT) applications [2, 3] and dielectrometry sensors [4]. In the latter case, the equation becomes

$$\nabla \bullet \left[\sigma(x,y,z) \nabla \varphi(x,y,z) \right] = 0 \qquad (4.9)$$

which is valid for Electrical Resistance Tomography (ERT) applications [5-7] and potential drop methods [8, 9].

Using the quasi-static assumption mentioned above, it is possible to use the Finite Element (FE) technique to solve the above equations, and to predict the potential distribution $\varphi(x, y, z)$ produced by the capacitive electrodes in a particular medium and geometry. The capacitive imaging probes satisfy the Dirichlet Boundary condition, as:

$$\varphi(x,y,z) = \begin{cases} V \big| (x,y,z) \in \Gamma_1 \\ 0 \big| (x,y,z) \in \Gamma_2 \\ 0 \big| (x,y,z) \in \Gamma_3 \end{cases} \qquad (4.10)$$

81

where, Γ_3 represent the external surface of the computational domains, and Γ_1 and Γ_2 are the surfaces enclosing the driving electrode and the sensing electrode respectively, V is the voltage applied on the driving electrode. Once Equation (4.7) is solved, Gauss's Law in a numerical integral form can be applied on the surface enclosing the sensing electrode to calculate the induced charge on that electrode that would result from the calculated electric potential distribution. Gauss's Law can be written as:

$$q = -\oiint_s \varepsilon(x,y,z)\nabla\varphi(x,y,z)d\mathbf{s} \qquad (4.11)$$

where $\mathbf{s}$ is the surface enclosing the sensing electrode.

The overall aims of the FE modelling are threefold:

1. To obtain the electric field distributions from the CI probe for specimens with different electrical properties.

2. To look at the electric field distortions due to the presence of defects within specimens and also examine the qualitative and quantitative changes from the calculated capacitance.

3. To back up the general design principles raised in Chapter 3, provide supplementary design suggestions and characterize particular CI probes.

In this thesis, a commercial FEM package, COMSOL^{TM} Multiphysics (version 3.3), is used for CI probe modelling. COMSOL^{TM} handles general static and quasi-static electromagnetic fields for both 2D and 3D geometries, and provides a convenient connection to MATLAB for further and more flexible analysis. In addition, the calculated capacitance for planar capacitor from models constructed in COMSOL^{TM} were proved to be with good agreement with other numerical methods [10] such as Methods of Moment (MOM) [11], Green's function methods [12] and Fourier transform methods [13].

The steps needed to construct a model in COMSOL^{TM} can be listed as follows:

1. Choose the right modelling mode.

2. Draw the model geometry (including the CI probe and the specimen) and define the computational domain.

3. Generate meshes with appropriate size and shape.

4. Set sub-domain properties (define the electrical properties)

5. Set boundary conditions.

6. Solve the model and find the electric field distribution.

7. Calculated desired physical quantities in the post-processing mode or export the data into MATLAB for further calculation.

4.3   2D FE models

2D models were constructed in COMSOL$^{\text{TM}}$ and the model geometry with the finite elements (meshes) is shown in Figure 4.1.

Figure 4.1: *2D Model geometry with elements.*

The simplest CI probe geometry (two rectangular shape electrodes) was used in the 2D models. It was assumed that the length of the rectangular electrode (perpendicular to the page) is much bigger than the width, so the electric field distributions along the length can be considered to be constant and won't be affected by end fields. Based on this assumption, the 3D geometry of the probe can be reduced to 2D and 2D models can be used to represent the whole probe. In addition, the electrodes were considered to be ideal with zero thickness and can be defined as boundaries in COMSOL$^{\text{TM}}$.

4.3.1   Field interaction with non-conducting materials

As an example of a field prediction, Figure 4.2 shows the electric field distribution predicted by the FE model for a non-conducting medium (the rectangular object) for both (a) a uniform sample and (b) a sample containing an air-filled elliptical void. It can be seen that the presence of the air-filled defect causes a distortion of the electric field, and this would lead to a detectable change in signal. This is caused by the different values of the relative permittivity, ε_r, (or dielectric constant) assumed for the solid sample (Perspex with relative permittivity $\varepsilon_r=3.3$) and air (relative permittivity $\varepsilon_r=1$). Thus, the model shows how the capacitive probe detects sub-surface defects due to a permittivity difference between the sample and air.
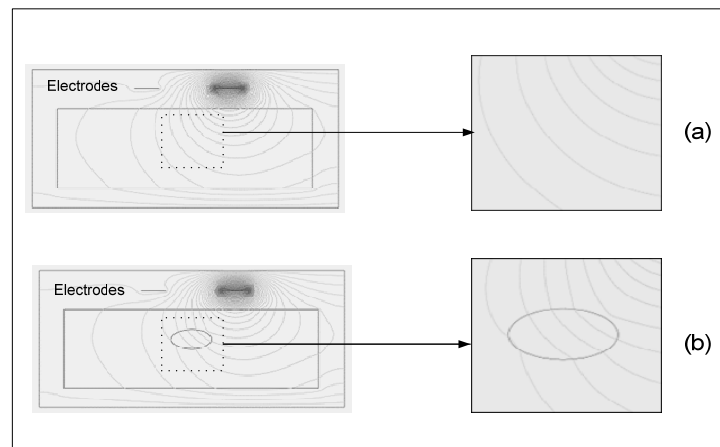
Figure 4.2: *The electric field distribution (equi-potential lines) inside an insulating specimen for (a) a uniform sample and (b) a sample containing an air-filled defect. The source electrode is on the right.*

4.3.2   Field interaction with conducting materials

The model is also useful in demonstrating the possibility of imaging conducting surfaces through an insulating barrier, as might exist in corrosion under insulation (CUI). Such a situation is shown in Figure 4.3. This represents a layer of insulation, of a thickness which is equal to air gap to the electrodes from the top surface of the sample (*i.e.* the lift-off distance). The electrodes were modelled at the relative sizes shown in the figure. Note that the field distribution predicted by these models is determined primarily by these geometric factors in the quasi-static model. The sample below the insulator is assumed to be a highly-conducting medium, such as a metal.
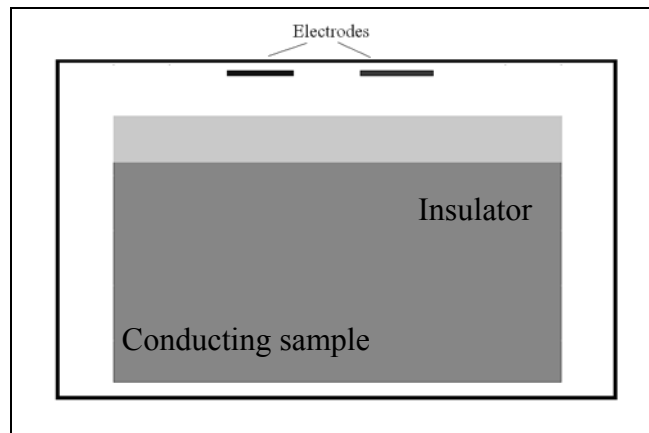
Figure 4.3: *Schematic diagram of a model to simulate corrosion under insulation (CUI).*

Assuming the geometry of Figure 4.3, the FE model predicts the field distribution in Figure 4.4 for (a) a uniform sample and (b) a sample with a notch on the surface. It can be seen that in the latter case, the electric field is seen to penetrate through the thick outer insulating layer, and then to be distorted by the simulated defect. This gives some indication that changes in the surface features of a metal hidden behind an insulator can be detected through this outer insulating coating.
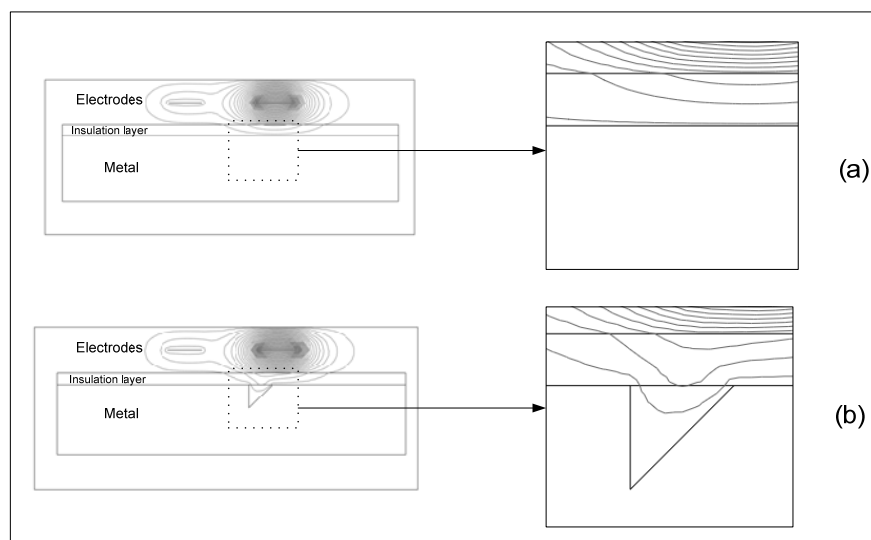
Figure 4.4: *Simulations of the electric field distribution for a metal sample covered with an insulator coating, for (a) a uniform metal surface, (b) a metal surface containing a notch.*

85

4.3.3　Non-dimensional modelling for the CI probe response

To obtain a general understanding on CI probe response from the 2D models, non-dimensional models were developed. The schematic diagram of the model is shown in Figure 4.5. The separation of the two electrodes, denoted by the letter B, was used as the characteristic length thought out the remainder of the session 4.2.3. The width of the electrode was 2B.
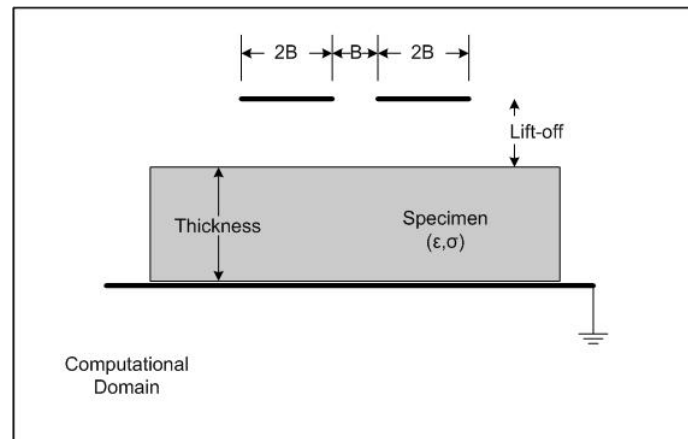
Figure 4.5: *Schematic diagram for 2D non-dimensional models.*

4.3.3.1　Parametric studies on the CI probe response

The effects of probe design parameters have been discussed in Chapter 3, and other non design-related parameters, such as thickness of specimen, lift-off distance and properties of specimen, remain to be studied. Non-dimensional models were used to examine the effects of these parameters and the results are presented in this section. Note that, the computational domain was 380B by 140B and the width of the specimens were 280B with their thicknesses changing in different models.

4.3.3.1.1　Effects of specimen thicknesses

The thickness of a specimen has a direct influence on CI probe response. For a non-conducting specimen, if the thickness of the specimen is small (thickness 1 in Figure 4.6), the electric field from the CI probe will penetrate through the specimen. If the thickness of the specimen increases, eventually the entire electric field will be within the specimen (thickness 2 in Figure 4.6), and the CI probe will be insensitive to the

thickness greater than this critical thickness. This critical thickness can reflect the penetration depth of the CI probe.
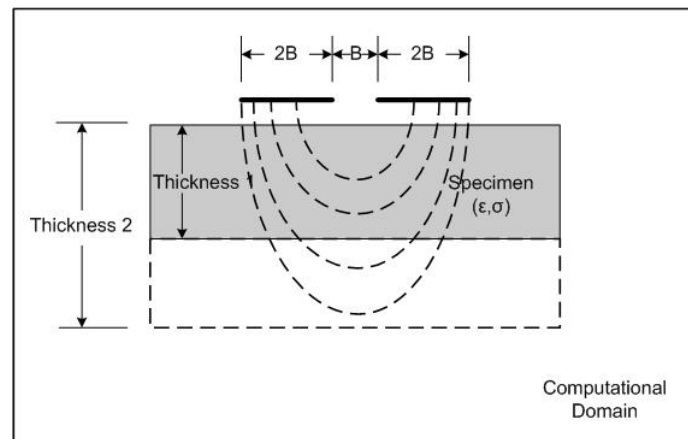
Figure 4.6: *Schematic diagram for models with specimens of different thickness.*

For non-conducting specimen a grounded substrate on the far side will greatly affect the results. The relative permittivity value of the specimen used to examine the effect of thickness and grounded substrate was chosen to be 4 and the lift-off distance was set to be 0.3B for all the thicknesses. The normalized capacitances were plotted against thickness (from 1B to 15B) for specimens with and without the grounded substrate, as shown in Figure 4.7.
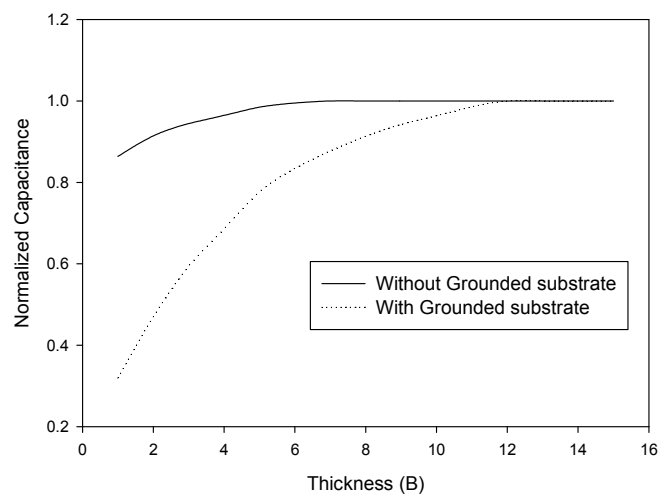
Figure 4.7: *Normalized capacitance against specimen thickness.*

It can be seen that with a grounded substrate, the critical thickness is bigger (12 B) than the case without grounded substrate (6B). This is because the grounded substrate will drag more electric field lines down. Another advantage for grounded substrate is the dynamic range of the probe response is also increased.

For conducting specimens, the equal potential surface on the conducting surface makes the CI probe insensitive to the thickness.

4.3.3.1.2   Effects of lift-off distances
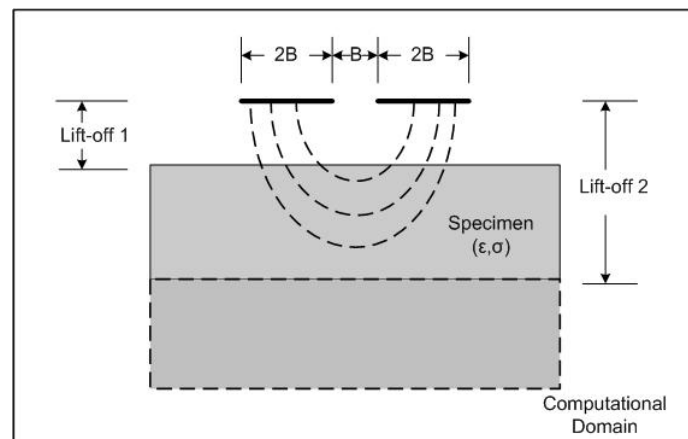
Figure 4.8: *Schematic diagram for models with different lift-offs.*

The effects of lift-off distances on the probe response are shown schematically in Figure 4.8. With lift-off 1, the specimen is within the reach of the probing field. With an increased the lift-off distance, the specimen might be out of the range of the probing field, as in lift-off 2 in Figure 4.8. To examine the effect of lift-off distances, the thickness for the specimen was chosen to be 20B- a thickness much bigger than the critical thickness for both of the cases according to the results shown in the previous section. This means the thickness (with and without the grounded substrate) will not have any effect on the probe response in the models. In this case, a non-conducting specimen with its permittivity value to be 4 and a conducting specimen with its surface explicitly grounded were examined, and the results are shown in Figure 4.9.
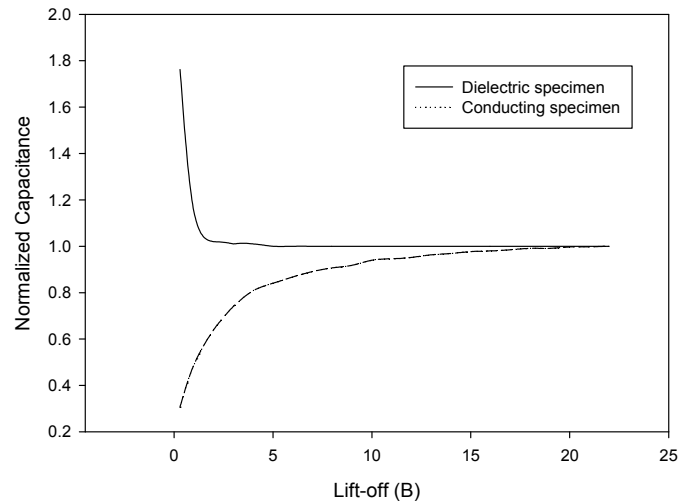
Figure 4.9: *Normalized capacitance against lift-off.*

It can be seen that the trends of the capacitance change are opposite for the two cases: for the non-conducting specimen, the capacitance dropped with the lift-off distance increased to 3B, which indicated the CI probe can reach the specimen at a distance of roughly 3B. For the conducting specimen, the capacitance increased with the lift-off distance increased to 18B. Therefore, it can be concluded that the CI probes operate in an enhancement mode when sensing a dielectric specimen and a depletion mode when sensing a grounded conducting specimen and the measured capacitance saturated quicker in the dielectric case as the lift-off increasing. For both of the cases the absolute values of the tangent slopes of the curves decrease as the lift-off increases, which suggests decreasing measurement sensitivities.

4.3.3.1.3 Effects of relative permittivity values for non-conducting specimens

If the specimen is in direct contact with the electrodes, the capacitance will be proportional to the permittivity value. However, this is rarely the situation in NDE applications as there will always be an air gap between the specimen and the electrodes. Models were thus constructed to find out the relationship between the capacitance of the CI probe and the permittivity value of the specimen with an air gap.

The non-conducting specimen examined in this case was 20B thick and the lift-off distance (air gap) was 0.3B. The relative permittivity values were increased from 1 to 80. Figure 4.10(a) shows the results from the specimen without the grounded substrate

and Figure 4.10(b) shows the results from the specimen with the grounded substrate. It can be seen from Figure 4.10 that the capacitance increases non-linearly with permittivity when the values are low (i.e. < 15 in both figures). When the permittivity is > 15, the capacitances start to decrease with permittivity increases. The reasons are twofold:

(i)   With higher permittivity values, more electric field lines travel along the surface as the deflection of electrical flux at the boundary becomes pronounced and the specimen starts to behave like conductors. As a result, the capacitance between the electrodes will be reduced.

(ii)   For specimens with higher permittivity values, the electric field lines within the specimen tend to be straight and drawn to the ground plane rather than bended back towards the sensing electrode, which again will reduce the capacitance.

Note that in the case without the grounded substrate (shown in Figure 4.10(a)), the ground potential was at the computational domain boundary, so the distance off the grounded plane was literally further, which makes the decrease effect less significant compared to the case shown in Figure 4.10(b).
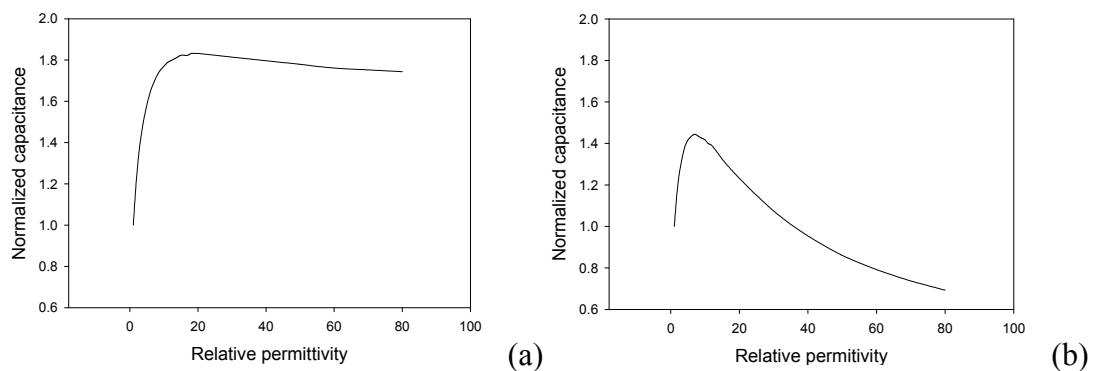
Figure 4.10: *Normalized capacitance against permittivity for a dielectric specimen (a) without grounded substrate and (b) with a grounded substrate.*

4.3.3.2 Applications to flaw detection

The 2D models were used to simulate the process in which the CI probes are scanned over samples with defects. The computational domain was 180B by 120B and the width of the specimens were 60B with their thicknesses of 20B at the unflawed parts. The lift-off distances between the probe surface and unflawed specimen surfaces were set to be 0.5B. Three fundamental flaws were studied, namely step, 7B wide groove and 3B wide groove. The responses for a dielectric specimen (Perspex, ε_1=3.3) and a conducting specimen (aluminium) were studied respectively for each flaw. In the case of dielectric specimens, the dielectric properties were assumed to be ideal: homogeneous, isotropic and lossless. In the case of conducting materials, the specimen was grounded. All the voids were assumed to be filled with air (ε_0=1).

To simulate the signal obtained from scanning the probe over the specimen, the specimen was fixed in the centre of the computational domain and the 2D CI probe was moved across the domain width from left to right, zero position were taken as the step position in the first case and centres of the grooves in the latter two cases.

4.3.3.2.1 Step

The first flaw geometry was a step. The geometry of the probe and the specimen is schematically shown in Figure 4.11.
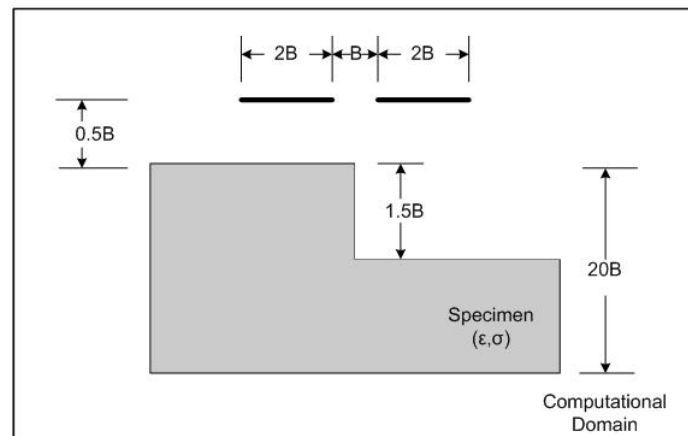
Figure 4.11: *Geometry of the probe and the specimen with a step.*

Figure 4.12(a) shows the electric field for the aluminium specimen when the step is right under the centre of the CI probe. The corresponding plot of the capacitance as a

function of the distance from the central line of the CI probe to the zero position of the scan is shown in Figure 4.12(b).

(a)   (b)
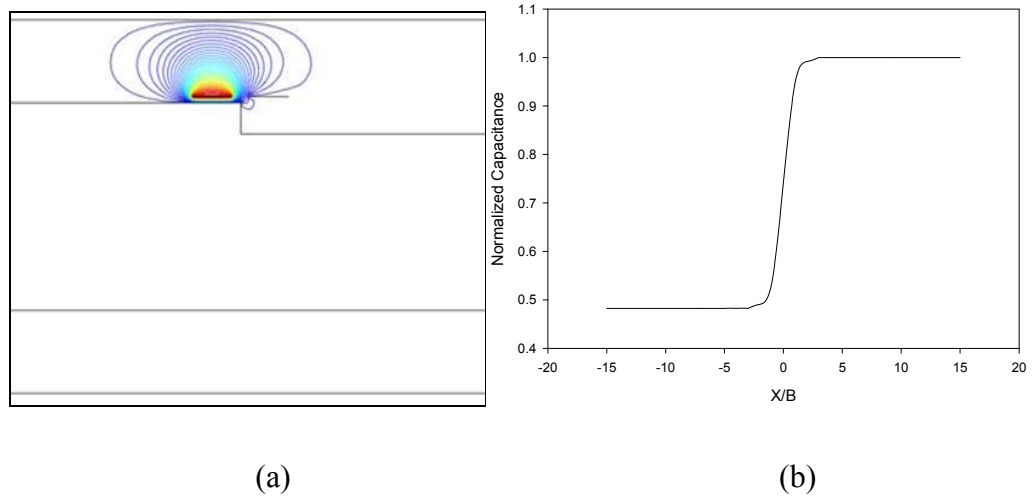
Figure 4.12: *Response for the conducting specimen with a step. (a) Electric potential distribution for a step height of 1.5B, and (b) the predicted change in capacitance.*

The equivalent representations of the electric field and the CI probe's response to the step with the same dimension in a Perspex specimen are shown in Figure 4.13.

(a)   (b)
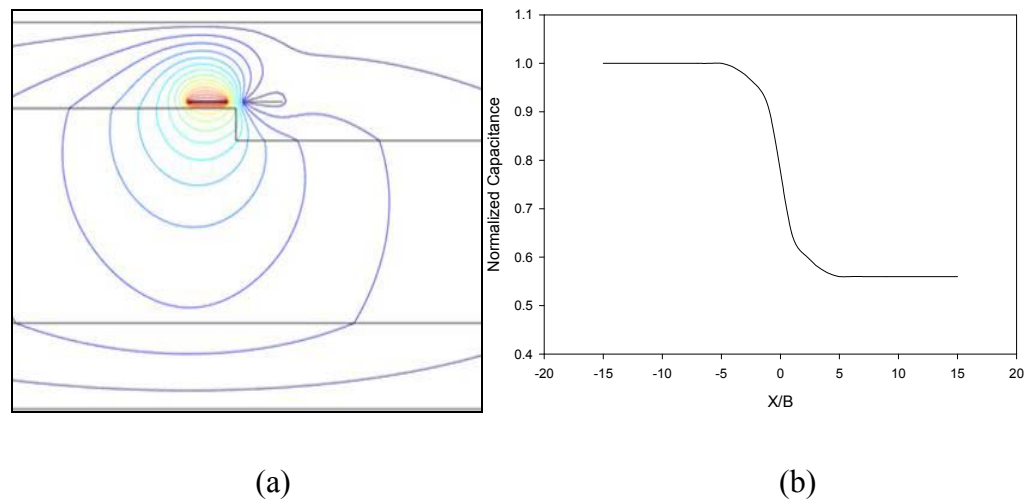
Figure 4.13: *Response for a dielectric specimen (step) (a) electric potential for step of height 1.5B, and (b) the predicted change in capacitance.*

From Figures 4.12 and 4.13 it can be seen than the electric fields were perturbed in both of the cases, but that the step changes in capacitance were in opposite directions. The corners are also sharper in the aluminium case The changes are due to variations in lift-off distance (due to the presence of the step), and the responses of the probe are in good agreement with the results shown in Figure 4.9.

4.3.3.2.2   7B Groove

The second flaw geometry was a rectangular groove with a 7B width, which was wider than the overall width of the probe in the scan direction (5B), The probe and specimen are shown schematically in Figure 4.14.
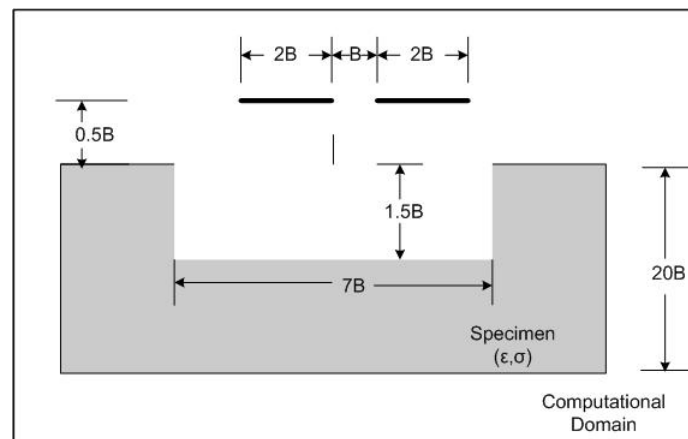
Figure 4.14: *Geometry of probe and specimen with a 7B groove.*

Figure 4.15(a) shows the electric field for the aluminium specimen when the CI probe is centred above the groove. The corresponding plot of the capacitance as a function of the distance from the central line of the probe to the zero position (centre of the groove) is shown in Figure 4.15(b). The equivalent representations of the electric field and the CI probe's response to the same groove in a Perspex specimen are shown in Figure 4.16. Both of the results are symmetric about the zero position, which is to be expected from the geometry of the flaw. The striking difference between the results is that the two curves have opposite polarities - with a peak shown in the aluminium case and a valley in the Perspex case. The dynamic ranges of the results are nearly the same for the corresponding case as shown in Figure 4.13(b) and Figure 4.14(b). This is because the groove is wider than the probe and when the probe is centred above the groove, the probing electric field will not be greatly affected by the edges of the

groove, so that the calculated capacitance will be determined only by the depth of the groove and should nearly the same as in the case with a step shape flaw. The full width half maximum/minimum (FWHM) can also give some indication of the width of the groove.

(a)   (b)
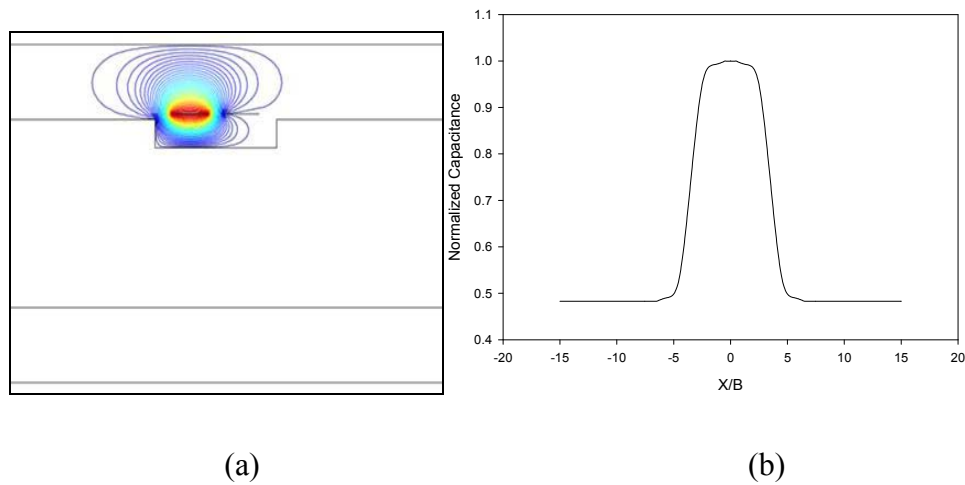
Figure 4.15: *Response for a conducting specimen (7B groove) (a) electric potential for 7B groove (b) change in capacitance.*

(a)   (b)
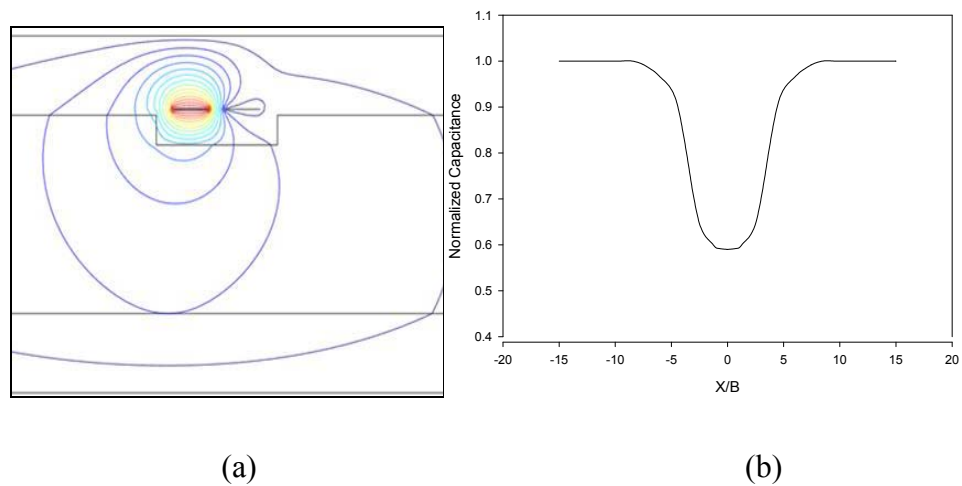
Figure 4.16: *Response for a dielectric specimen (7B groove) (a) electric potential for 7B groove (b) change in capacitance.*

94

4.3.3.2.3   3B Groove

The third flaw geometry studied was with a groove (3B wide) which was narrower than the overall probe width (5B), as shown in Figure 4.17.
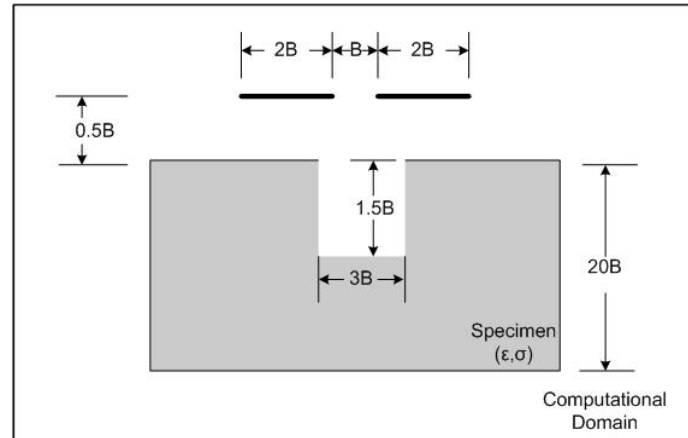
Figure 4.17: *Geometry of probe and specimen with a 3B groove.*

Figure 4.18(a) shows the electric field for the aluminium specimen when the CI probe is centred above the groove. The corresponding plot of the capacitance as function of distance from the central line to the zero position (centre of the groove) is shown in Figure 4.18(b). The result is shown in the same scale as Figure 4.15(b), so that a direct comparison can be made.

(a)   (b)
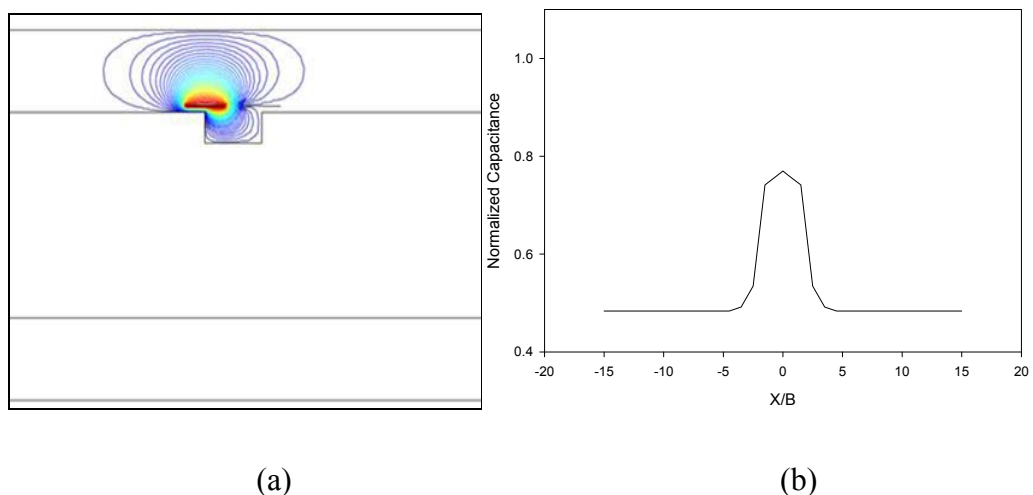
Figure 4.18: *Response for a conducting specimen (3B groove) (a) electric potential for 3B groove (b) change in capacitance.*

95

The equivalent representations of the electric field and the CI probe's response to the same groove in a Perspex specimen are shown in Figure 4.19. The result (Figure 4.19(b)) is presented in the same scale as Figure 4.16(b).

<div align="center">(a)   (b)</div>
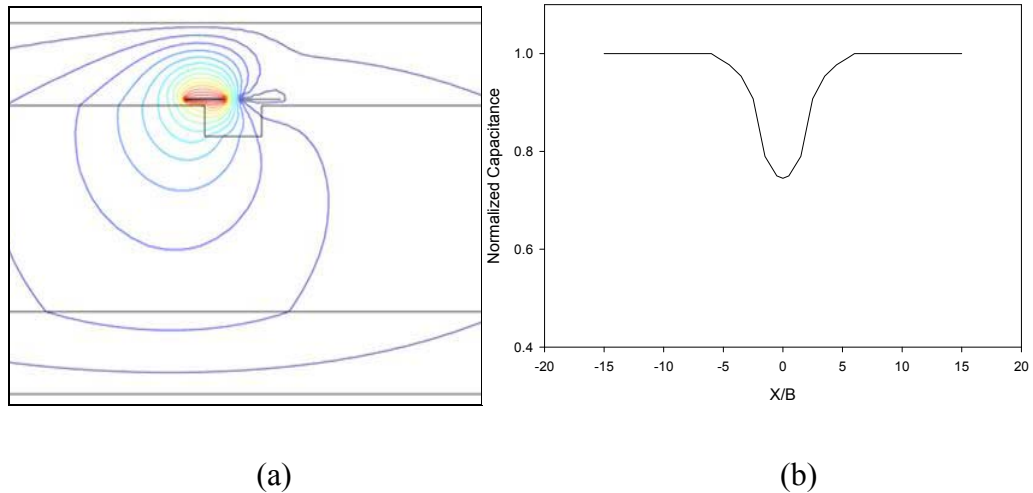
Figure 4.19: *Response for a dielectric specimen (3B groove) (a) electric potential for 3B groove (b) Change in capacitance.*

The 3B groove produced similar results to the 7B groove case for both the aluminium and Perspex samples. However from the simulated electric fields shown in Figure 4.18(a) and Figue 4.19(a), it can be seen that when the probe was centred above the groove, the edges of the narrower groove located in a position where the electric lines are denser compared to the 7B case and took a more significant part in the measurements, which brings extra complication to get the depth information of the groove from such scans. In addition, it is evident that the dynamic ranges of the curves shown in Figure 4.18(b) and Figure 4.19(b) are smaller than the corresponding result in the 7B cases.

4.3.4   Discussion on the 2D model predictions

The 2D theoretical models were constructed to investigate how the electric fields from the CI probe interact with both non-conducting specimen and conducting specimens with an insulation layer. The results suggest a wide application range for this technique.

Non-dimensional 2D models were constructed and influential parameters including the effects of thickness of specimen, lift-off distance and electric properties were studied to evaluate the performance of the CI probes. The fixed probe geometry eliminated the effects of design parameters discussed in Chapter 3 and can be used to demonstrate how the given CI probe responds to the non design-related parameters. The non-dimensional models were then used to predict the probe responses to typical flaws on the two cases representing the two extremes of electric properties, namely conductor (aluminium) and insulator (Perspex). The results from the typical flaws together with the results from the parametric studies give some indications of the probe responses for different defects on different specimens.

It is necessary to emphasize that, the calculated capacitance from the non-dimensional models are affected greatly by the dimension of the computation domain unless the domain is big enough to be considered as infinity or explicitly grounded planes are included. Therefore, the trends of the curves shown in the normalized scale are of more interest than the absolute values.

4.4   3D modelling for probe design and performance evaluation

The 2D models have provided an indication of the way CI probes interact with various specimens in different situations. To characterize the given CI probes with more complex geometries than the simplest rectangular electrode pair (e.g. probes with guard electrode and triangular electrodes), 3D models are needed.

4.4.1   Setting up the 3D models

The 3D models were setup in the "Multiphysics" mode in COMSOL^{TM}, in which one can combine basic modes together. For the 3D models for CI probes, the electrostatic mode and conductive media DC mode are combined. With such combination, models can be constructed and the functions required for capacitance calculation are available in the post processing mode.

The model for a back-to-back triangular probe is described here in detail. A 60 mm x 60 mm x 60 mm block centred at point ($x = 0$, $y = 0$, $z = 0$) was defined to be the computational domain. A 50 mm (x-axis) by 30 mm (y-axis) rectangular was drawn

on the $z = 0$ plane and extruded upwards (positive z direction) to be a 2 mm thick plate as the dielectric substrate of the CI probe, as show in Figure 4.20(b),

(a)   (b)
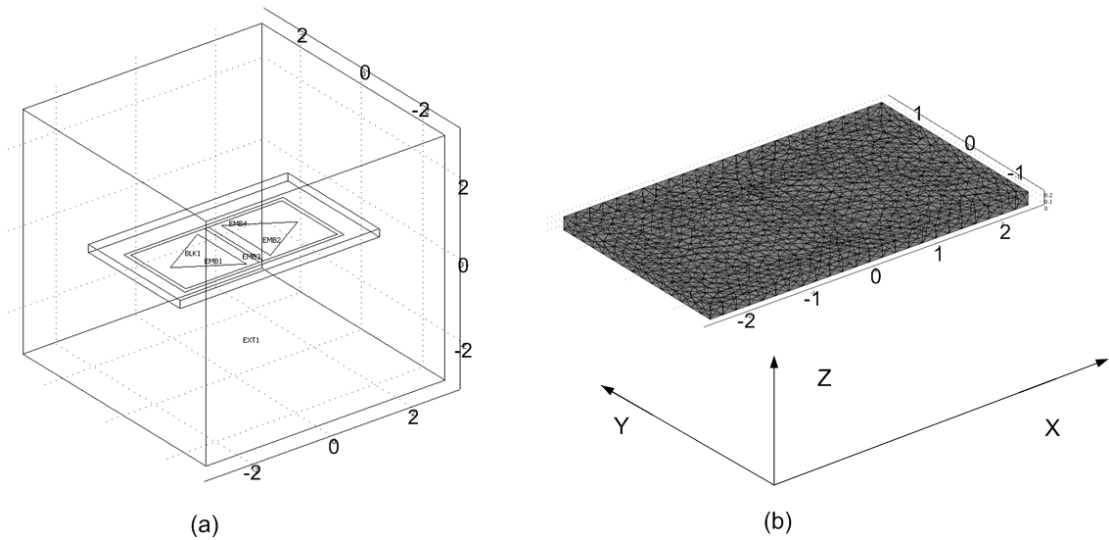
Figure 4.20: *3D model: (a) the computational domain (60 mm x 60 mm x 60 mm) with a CI probe; (b) An example of FE meshing of the CI probe with the coordinate system used hereafter (axes have units of 'cm').*

In the coordinate system shown in Figure 4.20(b), based on which the results will be presented hereafter, the probe surface is centred at ($x = 0$, $y = 0$, $z = 0$). $x = 0$ plane is the cross-sectional plane along the short axis of symmetry of the CI probe, $y = 0$ plane is the cross-sectional plane along the long axis of symmetry of the CI probe, and $z = a$ ($a = -0.2$, -0.5 or -1) planes are the parallel planes under the probe surface at the distances according to the values of a. To clarify the results, the plane coordinate systems for the 3 kinds of cross sections are shown in Figure 4.21 (taking back-to-back triangular probe as an example).

X=0 Plane   Y=0 Plane   Z=a Planes
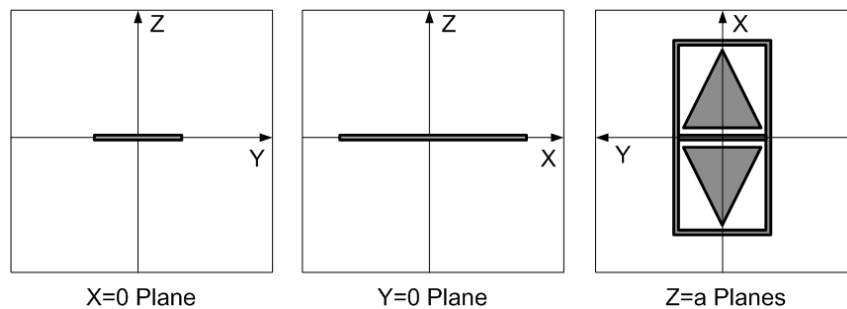
Figure 4.21: *Plane coordinate systems for the 3 kinds of cross sections.*

98

Seven geometries were studied in this work as shown in Figure 4.22, with their specifications shown in Table 4-1.
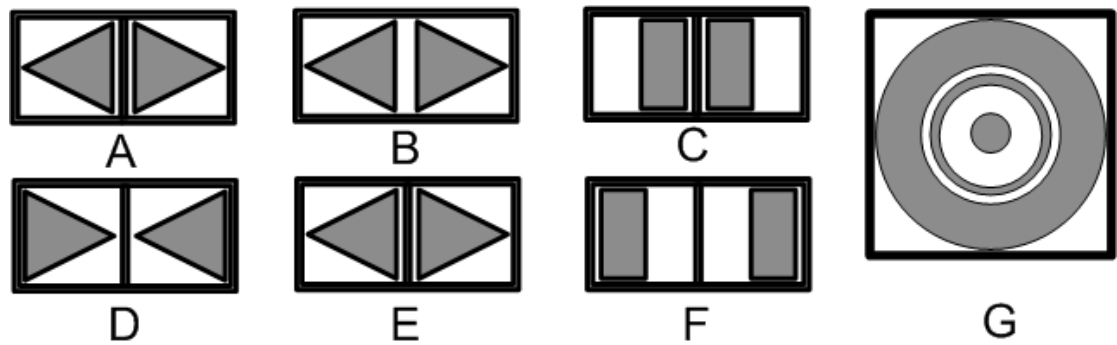
Figure 4.22: *Geometries of the seven probes studied.*

The computational domain for studying probe fields in air only assumed the dielectric constant to be 1. The material of the insulating substrate of the PCB was flame retardant woven glass reinforced epoxy resin (FR-4), and accordingly, the dielectric constant was set to 4.5. Since the electrodes and backplane are very thin copper layers (35 μm), they were treated as boundaries rather than sub-domains. This can reduce the computation complexity to a great extent as very thin sub-domains will require a very fine mesh element and increase the total number of the elements.

All sides of the computational domain except the bottom plane (z=-3 plane was set to be 'ground') have a Neumann boundary condition which can be expressed as

$$\partial \Phi / \partial \vec{n} = 0 , \qquad (4.12)$$

where $\vec{n}$ is the direction perpendicular to the surfaces. The conditions on all internal surfaces apart from the metal parts of the probe were set to 'continuity'. The electric potential of the driving electrode was set to be 1 V and the electric potential of the sensing electrode was set to be 0 V (Dirichlet Boundary condition). Guard electrodes and backplane of the probe were set to 'ground'.

The 'triangle mesh' was used and the number of elements was typically 400,000, which was about the maximum limit the PC (3.0 GHz Intel® CORE™ 2 Duo processor, 2.0 G RAM) could handle.

Table 4-1: *Specifications of probes shown in Figure 4.22*

Probe A: back-to-back triangular electrode probe I	
Overall Area (X-axis by Y-axis)	40 mm by 20 mm
Area of each electrode plate	Triangular- (16 mm x 16 mm)/2=128 mm^2
Distance between the closest electrode edges	6 mm
Substrate thickness	2 mm
Width of guard electrodes	Both surrounding and in between (1mm)
Probe B: back-to-back triangular electrode probe II	
Overall Area (X-axis by Y-axis)	40 mm by 20 mm
Area of each electrode plate	Triangular- (16 mm x 16 mm)/2=128 mm^2
Distance between the closest electrode edges	6 mm
Substrate thickness	2 mm
Width of guard electrodes	Only surrounding (1mm wide)
Probe C: rectangular electrode probe I	
Overall Area (X-axis by Y-axis)	40 mm by 20 mm
Area of each electrode plate	Rectangular- 8 mm x 16 mm=128 mm^2
Distance between the closest electrode edges	6 mm
Substrate thickness	2 mm
Width of guard electrodes	Both surrounding and in between (1mm)
Probe D: point-to-point triangular electrode probe I	
Overall Area (X-axis by Y-axis)	40 mm by 20 mm
Area of each electrode plate	Triangular- (16 mm x 16 mm)/2=128 mm^2
Distance between the closest point	6 mm
Substrate thickness	2 mm
Width of guard electrodes	Both surrounding and in between (1mm)
Probe E: back-to-back triangular electrode probe III	
Overall Area (X-axis by Y-axis)	40 mm by 20 mm
Area of each electrode plate	Triangular- (16 mm x 16 mm)/2=128 mm^2
Distance between the closest electrode edges	6 mm
Substrate thickness	1 mm
Width of guard electrodes	Both surrounding and in between (1mm)
Probe F: rectangular electrode probe II	
Overall Area (X-axis by Y-axis)	40 mm by 20 mm
Area of each electrode plate	Rectangular- 8 mm x 16 mm=128 mm^2
Distance between the closest electrode edges	28 mm
Substrate thickness	2 mm
Width of guard electrodes	Both surrounding and in between (1mm)
Probe G: concentric electrode probe	
Overall Area (X-axis by Y-axis)	40 mm by 40 mm
Radius of the inner disc	Triangular- (16 mm x 16 mm)/2=128 mm^2
Distance between the closest electrode edges	6 mm
Substrate thickness	2 mm
Width of guard electrodes	Both surrounding and in between (1mm)

4.4.2 Sample results

Probe A (see Figure 4.22) was used as an example to demonstrate the kind of results that could be expected from the 3D models. There are two ways of presenting the electric field. The first way is using electric field lines, in which the direction of the electric field is directly shown and the strength is related to the degree of density of the lines. The second way is using electric potential, in which the direction of the electric field is perpendicular to the equal potential surfaces and the strength is related to the degree of density of the equal potential surfaces. Although both of the ways can be used in COMSOL^{TM}, the second way was adopted in this chapter as it can provide a clearer illustration of the factors at work.

Figure 4.23 shows the electric field in the form of electric potential in the planes (a) $y = 0$, (b) $x = 0$, (c) $z = -0.2$ (plane parallel and under probe surface at a distance of 0.2 cm), (d) $z = -0.5$, and (e) $z = -1$. In Figure 4.23(a) the driving electrode is on the left and in Figure 4.23 (c) to Figure 4.23(e) the driving electrode is on the top. All figures are in the same colour scale. Figure 4.23(a) and Figure 4.23(b), provided panoramic views of the electric field distribution and Figure 4.23(c) to Figure 4.23(e) demonstrated the attenuation of the electric field with the increasing distance away from the probe surface. The calculated capacitance for this probe is 1.30×10^{-12} F.

A perturbation was then introduced in this model- a grounded steel sphere (3mm in diameter, centred at ($x = 0$, $y = 0$, $z = -0.5$)), as shown in Figure 4.24. Electric potential distribution in this model geometry was then obtained and plotted in Figure 4.25. Comparing with the corresponding plots in Figure 4.23, the presence of the sphere is clearly seen. The calculated capacitance in the model with the perturbation (the steel sphere) is 4.13×10^{-13} F - a smaller value than in the case without the perturbation.
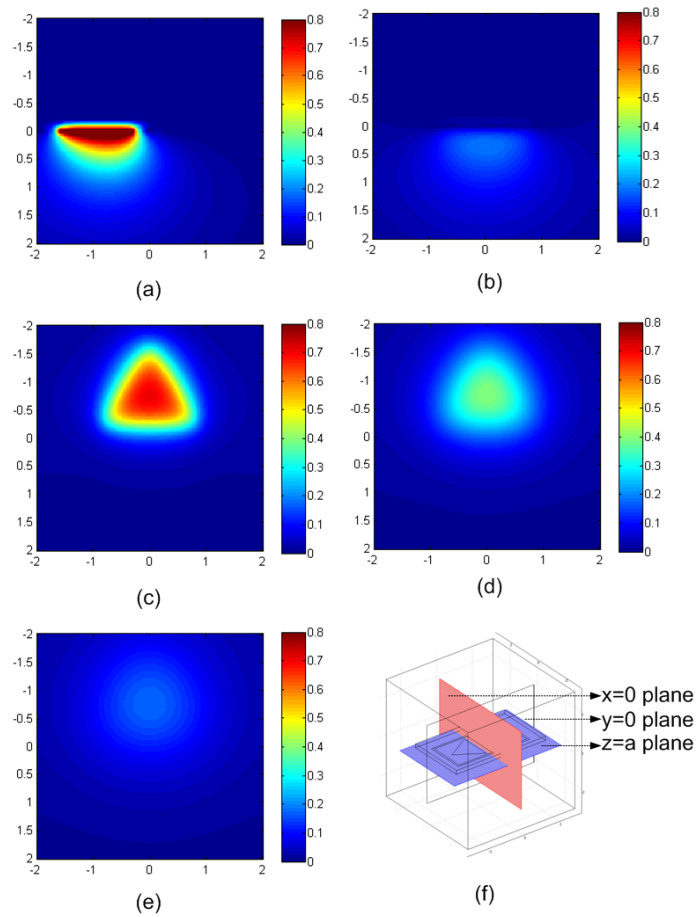
Figure 4.23: *Calculated electric field potentials for (a) the y=0 plane, (b) the x=0 plane, (c) the z=-0.2 plane, (d) the z=-0.5 plane, (e) the z=-1 plane and (f) the planes that the plots were taken.*
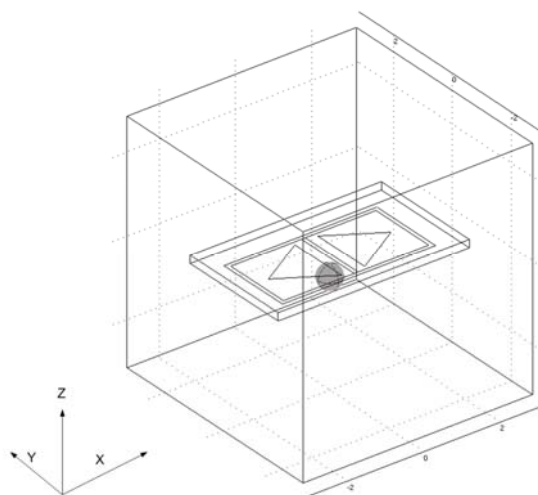
Figure 4.24: *3D model: A back-to-back triangular probe with a grounded steel sphere.*

102
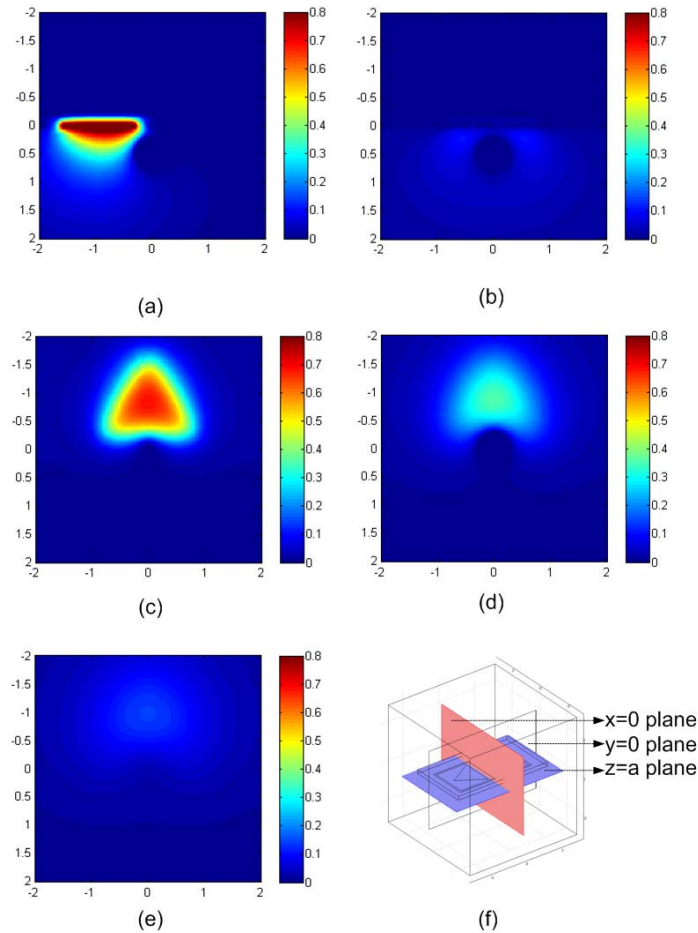
Figure 4.25: *Calculated electric field for the model with perturbation (presented in the form of electric potential) for the (a) y=0 plane, (b) x=0 plane, (c) z=-0.2 plane, (d) z=-0.5 plane, (e) z=-1 plane, and (f) the planes that the plots were taken.*

It is worth mentioning that in addition to the direct visualization feature and calculation functions provided by COMSOL^{TM}, the solved model can be exported to MATLAB^{TM}. Variables, such as the electric field **E**, can be extracted and used for further analysis in a more flexible way.

4.4.3 Discussion on the 3D models

In a similar way to the 2D cases, the effects of specimen thicknesses, lift-off distances and different electrical properties on the calculated capacitance can also be obtained from the 3D models. To avoid repetition, this will not be presented here. It is worth noting that, like the 2D models, the 3D models also approximated infinite space by surrounding the CI probe with a finite domain, which could bring in errors. In

addition, the thickness of the metal electrodes was neglected (modelled as boundaries in models) which would also cause errors.

From the sample results, the penetration depth of a particular CI probe can be obtained from the model using the two methods introduced in Chapter 3 (as mentioned in section 3.2.1) and the design issues discussed in Chapter 3 can also be investigated by changing the model configurations. However, how to determine the imaging ability of a particular CI probe remains unanswered. The sensitivity distributions of CI probes were thus studied and the results are presented in the next section.

4.5 Sensitivity Distribution

The sensitivity distribution, mentioned in Chapter 3, describes how effectively each region in the sensing area is contributing to the measured charge signal on the sensing electrode and it can be used to determine the VOI and the imaging ability of a CI probe. As also mentioned in Chapter 3, due to the non-linearity of the probing electric field, the sensitivity distribution of a capacitive imaging probe is non-uniform and is mostly dependent on the geometry of the probe.

Calculations for the effect of variations in permittivity, voltage and electrode displacement have been reported for capacitive sensors [14, 15], including a discussion on obtaining sensitivity distribution/map for electrical capacitance tomography applications, as the sensitivity is the key for image reconstructions. While the sensitivity distribution for planar capacitive sensors is found sporadically [16], it has not been systematically discussed although it is very important for the CI probe's performance evaluation. Two methods rely on the results from the finite element models are considered here for the calculations of the sensitivity distributions.

4.5.1 Obtaining the sensitivity distribution using the perturbation method

The perturbation method, as the term implies, is a method to evaluate the effects of an introduced perturbation on the resulting capacitance. The sensitivity distribution in a plane parallel to the probe surface was analyzed by placing cube perturbations of size 5 mm x 5mm x 5mm under the CI probe (the distance was 2 mm). Figure 4.26(a)

shows the model for evaluating the sensitivity distribution with 64 perturbations distributed under the CI probe. In order to avoid the necessity to re-mesh the geometry for the perturbations in every position, all 64 perturbations were place in the domain and only the permittivity value of a single perturbation was changed. The background permittivity was set to 1(air) and the perturbation permittivity value was set to be 3.3 (Perspex).
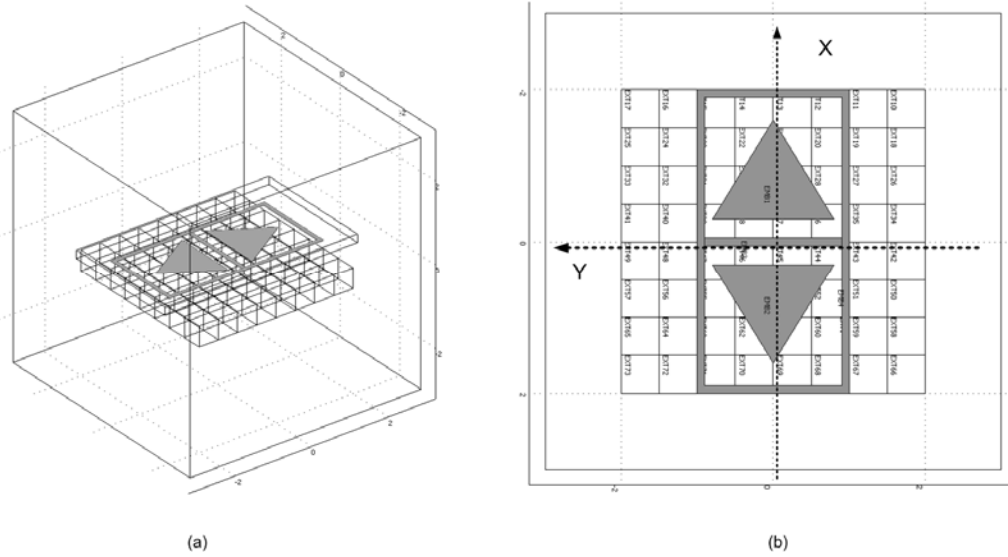
Figure 4.26: *Model for evaluation the sensitivity distribution with 64 perturbations.*
(a) 3D view and (b) 2D view with the coordinate system.

The change in the capacitance ΔC_n due to the presence of one particular perturbation at a position *n* is given by:

$$\Delta C_n = |C_n - C_0| \qquad (4.13)$$

where C_0 is the capacitance for the unperturbed domain. The sensitivity distribution *S* can then be defined as [17]:

$$S = \frac{\Delta C_n}{max(\Delta C_n)}, \qquad (4.14)$$

where *n* =1,…,64 and the *max(ΔC_n)* is the maximum ΔC_n among all perturbations. Thus, the 64 perturbations provided 64 sensitivity values in the corresponding positions.
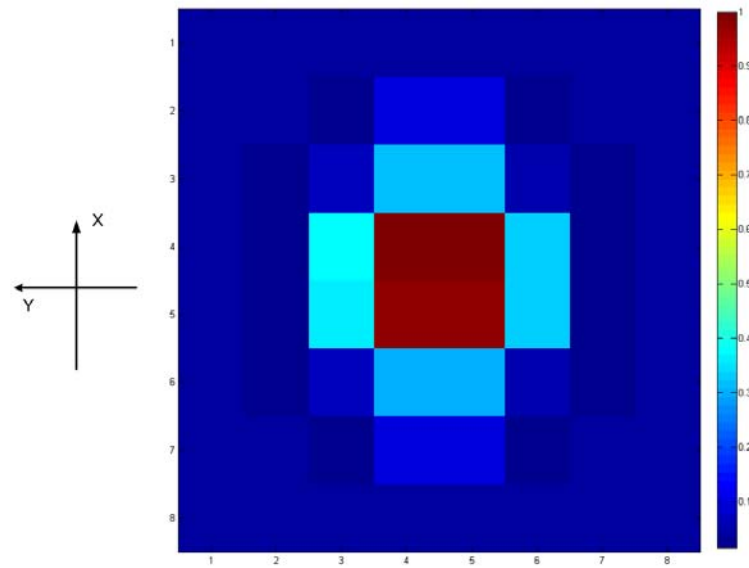
Figure 4.27: *Sensitivity distribution in the z=-0.2 plane.*

Figure 4.27 shows the calculated sensitivity values which are plotted according to the direction of the CI probe shown in Figure 4.26(b). It can be seen from Figure 4.27 that the high sensitivity values are in the middle of the probe and decay quicker in y-axis than x-axis due to the geometry, which implies the back-to-back triangular CI probe will be directional in an X-Y scan.

It is costly in terms of computation to obtain such a sensitivity distribution using perturbation method, as the model had to be solved 64 times to get the all 64 sensitivity values in the plane. In addition, the sensitivity distribution is rather coarse and maybe of little help to provide the information of the CI probe's imaging ability.

4.5.2 Obtaining the Sensitivity distribution from a mathematical model

To avoid repetitive computation, more efficient models are required. A model to compute the sensitivity distribution for a multi-electrode electrical capacitance tomography (ECT) system was developed [18] and the idea is adopted here to construct a similar model to obtain the sensitivity distribution for the planar CI probes.

The model is schematically shown in Figure 4.28. To obtain the sensitivity distribution in the volume of influence (VOI) of a capacitive imaging probe, a small perturbation with high relative permittivity ε_r is introduced into the volume of

influence, as highlighted in the box. The volume of the perturbation is small with respect to the volume of influence so the electric field can be considered as a linear/uniform in the region of the perturbation. To simplify the discussion, the sensitivity distribution is firstly obtained in air and the conclusions will be generalized to the practical cases in the end of this section.
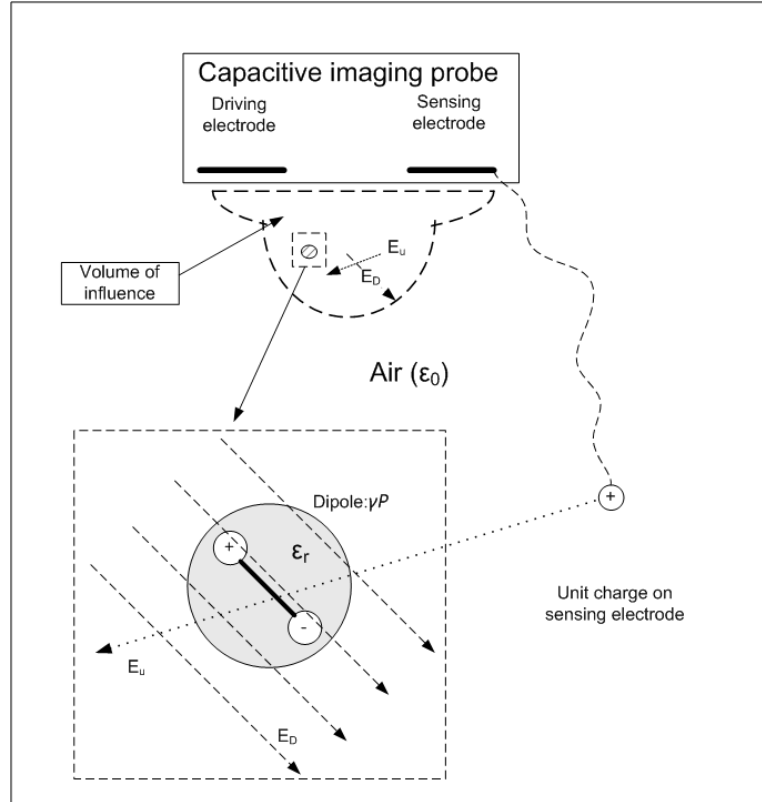
Figure 4.28: *Schematic diagram for the model to obtain the sensitivity distribution.*

The perturbation in the electric field generated by the driving electrode can be modelled as a dipole [14, 15] with an effective moment γP, where γ is the volume of the perturbation and P is the polarization of this perturbation caused by the electric field E_D from the applied voltage V on the driving electrode, as show in the box. The relationship between the dipole polarization P and the unperturbed electric field caused by the electric field from the driving electrode E_D can be written as:

$$\vec{P} = \varepsilon_0 \chi_e \vec{E_D} \tag{4.15}$$

where χ_e is the electric susceptibility of the dipole medium and is related to its relative permittivity ε_r by:

$$\chi_e = \varepsilon_r - 1 \tag{4.16}$$

The presence of the dipole will change the electric field in the volume of influence and cause the signal change on the sensing electrode. The capacitance between driving and sensing electrodes can be defined as:

$$C = \frac{Q_s}{V} \tag{4.17}$$

where Q_s is the charge on the sensing electrode, and V is the voltage applied on the driving electrode. As the potential on the sensing electrode is kept as zero, V is also the potential difference between the driving and sensing electrodes. If the charge Q_s is fixed on the sensing electrode, the dipole perturbation will cause a small potential change on the sensing electrode, denoted ΔV. So the potential difference between the electrodes V becomes $V+\Delta V$, and the capacitance change ΔC caused by the perturbation can be calculated as:

$$\Delta C = \frac{Q_s}{V + \Delta V} - \frac{Q_s}{V} \approx -\frac{Q_s}{V^2} \Delta V , \tag{4.18}$$

where ΔV is assumed to be small with respect to V.

It is complicated to calculate ΔV directly from modelling the electric field caused by the introduced dipole in an arbitrary position, and to evaluate the effect of the dipole in every position in the volume, an iterative procedure which takes a long computation time is required as in the perturbation method discussed in section 4.5.1. Instead of modelling the electric field directly, the reciprocity theorem, initially introduced by Hermann von Helmholtz in connection with bioelectricity, can be used here to predict the potential change on the sensing electrode ΔV due to the perturbation. In brief, the reciprocity theorem indicate that the source and the detector can be swapped without changing the detected signal [19]. In the case of a capacitive imaging probe, because of the reciprocity relationship between the charge and electric potential, the prediction of the potential change ΔV on the sensing electrode caused by the dipole perturbation can be obtained from the consideration of the electric field potential Φ_u at the position of the perturbation caused by a unit charge on the sensing

electrode [18]. Then the contribution of the dipole to the voltage change ΔV can be expressed as [20]:

$$\Delta V = \gamma \vec{P} \bullet \overrightarrow{E_u} , \qquad (4.19)$$

where $\boldsymbol{E_u}$ is the electric field at the position perturbation caused by a unit charge on the sensing electrode. Equation (4.19) was derived by other researchers from lead field theory in [20] and from superposition theory in [18], and the author thinks that for the capacitive imaging probes it is more appropriate to interpret the equation in terms of electric potential energy.

Considering the electric potential energy change for a unit charge on the sensing electrode caused by the dipole perturbation, denoted as U, we get:

$$U = q\Delta V , \qquad (4.20)$$

where in this case q is a unit charge, so we get:

$$U = \Delta V \qquad (4.21)$$

The electric potential energy change of the unit charge, U, should be equal to the electric potential energy of interaction between the unit charge and the dipole perturbation, which can be calculated from the dipole situated in the electric field $\boldsymbol{E_u}$ caused by the unit charge. Based on the assumption that the volume of the dipole is small, $\boldsymbol{E_u}$ can be considered as a uniform electric field in the region of the dipole. Thus U can be calculated as:

$$U = \overrightarrow{P_{dipole}} \bullet \nabla \Phi_u = -\overrightarrow{P_{dipole}} \bullet \vec{E_u} = -\gamma \vec{P} \bullet \vec{E_u} \qquad (4.22)$$

So Equation (4.19) can be obtained from Equations (4.20) (4.21) and(4.22). Substituting Equation (4.19) into Equation(4.18), the capacitance change ΔC can be written as:

$$\Delta C = -\frac{Q_s}{V^2} \gamma \vec{P} \bullet \overrightarrow{E_u} , \qquad (4.23)$$

109

where $Q_s\vec{E_u}$ is equal to the unperturbed electric field caused by the sensing electrode if it is driven by a same voltage V, while the potential on driving electrode is kept at zero (referred to as reciprocal energization) and can be denoted as $\boldsymbol{E_S}$. Substituting Equations (4.15) into (4.23), the capacitance change due to a high permittivity dipole perturbation in the volume of influence can then be written as:

$$\Delta C = -\frac{\varepsilon_0 \chi_e \gamma}{V^2} \overrightarrow{E_D} \bullet \overrightarrow{E_S} \tag{4.24}$$

For a given perturbation and a given voltage applied on the driving electrode, $\frac{\varepsilon_0 \chi_e \gamma}{V^2}$ is a constant and the capacitance change caused by a dipole in an arbitrary position is determined by the dot product of the unperturbed electric fields from the driving electrode ($\boldsymbol{E_D}$) and from sensing electrode ($\boldsymbol{E_S}$) in that position. To simplify the calculation, Equation (4.24) can be rewritten as:

$$\Delta C = -\frac{\varepsilon_0 \chi_e \gamma}{V^2} \overrightarrow{E_D} \bullet \overrightarrow{E_S} = -\varepsilon_0 \chi_e \gamma \frac{\overrightarrow{E_D}}{V} \bullet \frac{\overrightarrow{E_S}}{V} = -\varepsilon_0 \chi_e \gamma \overrightarrow{\xi_D} \bullet \overrightarrow{\xi_S} \tag{4.25}$$

where ξ_D and ξ_S are the electric fields in the position of the dipole perturbation when the driving and sensing electrodes are energised with a unit voltage respectively. The sensitivity distribution can then be defined as:

$$S = \frac{\partial \Delta C}{\partial \varepsilon_0 \chi_e \gamma} = -\overrightarrow{\xi_D} \bullet \overrightarrow{\xi_S} \tag{4.26}$$

This is in the same form for electrical capacitance tomography sensors [21-23], but the derivation process based on dipole perturbation presented in [18] and based on equations expressing electric field energy presented in [24] assumed that all the electrodes in a ECT system were identical, which is not always the case for planar capacitive imaging probes. Similar methods to calculate the sensitivity distribution/map (using dot product of two unperturbed fields) were developed initially for biomedical applications [25, 26], and also widely used in electrical impedance tomography systems [27], electro-magnetic tomography [28, 29], and eddy current coil systems [30].

Depending on the angles of the two electric fields, there can be regions where the sensitivity values are zero, positive or negative. Such situation can be illustrated in Figure 4.29.
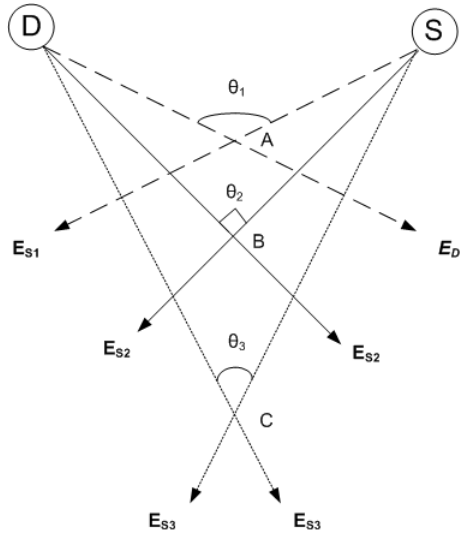
Figure 4.29 : *Distribution of positive, zero and negative sensitivity values.*

Considering the driving electrode D and sensing electrode S as two point charges. As shown in Equation (4.26), the sensitivity at point A, denoted as S_A, is the opposite number of the dot product of the two electric fields $\boldsymbol{E_{S1}}$ and $\boldsymbol{E_{D1}}$. Because the angle θ_1 is greater than 90 degree, S_A is positive. Similarly, with θ_2 being 90 degrees, S_B is equal to zero and with θ_2 being less than 90 degrees, S_C is negative. Note that this is only an illustrative explanation. Due to the complexity of the actual CI probe geometry, and the positions of the grounded electrodes/backplanes, the sensitivity distribution is much more complicated than the case shown in Figure 4.29.

The sensitivity distributions of the back-to-back triangular probe (Probe A) and the concentric probe (Probe G) were firstly studied as examples. According to Equation (4.26), the constructed model needs to be solved twice with the driving and sensing electrode reciprocally energized by the unit voltage (1V). The electric fields from the two solutions can then be exported to MATLAB$^{\text{TM}}$ for the calculation.

Figure 4.30 shows the sensitivity distributions obtained from Equation (4.26) for the back-to-back triangular probe (Probe A), including (a) the $x = 0$ plane plot, (b) the $y = 0$ plane plot, (c) the 3D representation of $y = 0$ plane plot and (d) the 3D

representation of the $z = -0.2$ plane plot. It can be seen from Figure 4.30 that the high sensitivity values are mainly distributed at the adjacent boundaries between the driving and sensing electrode, and generally the sensitivity values decay along the negative z-axis.
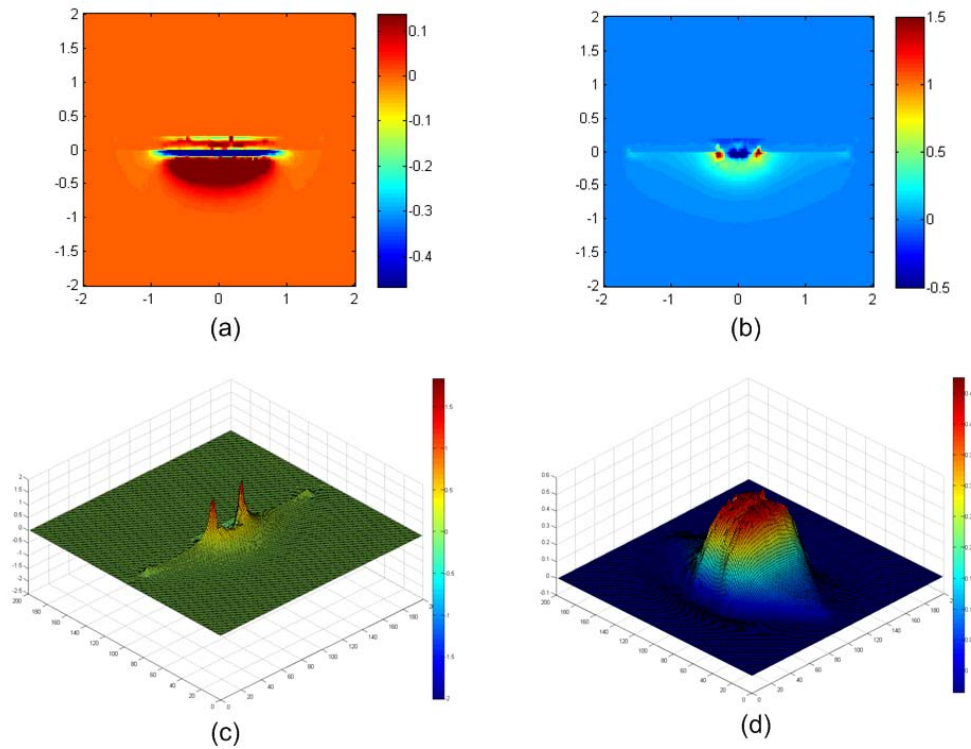
Figure 4.30: *Sensitivity distribution of Probe A. (a) x=0 plane, (b) y=0 plane, (c) 3D representation of y=0 plot and (d) 3D representation of the z=-0.2 plane plot.*

Figure 4.31 shows the results for the concentric probe (Probe G), for (a) the $x = 0$ plane, (b) the $y = 0$ plane, (c) the 3D representation of the $y = 0$ plane and (d) the 3D representation of the $z = -0.2$ plane. Similar results as in Figure 4.30 were obtained, and it can be seen that the sensitivity distributions are the same in both $x = 0$ and $y = 0$ planes, indicating that the concentric probes are non-directional in the X-Y plane.
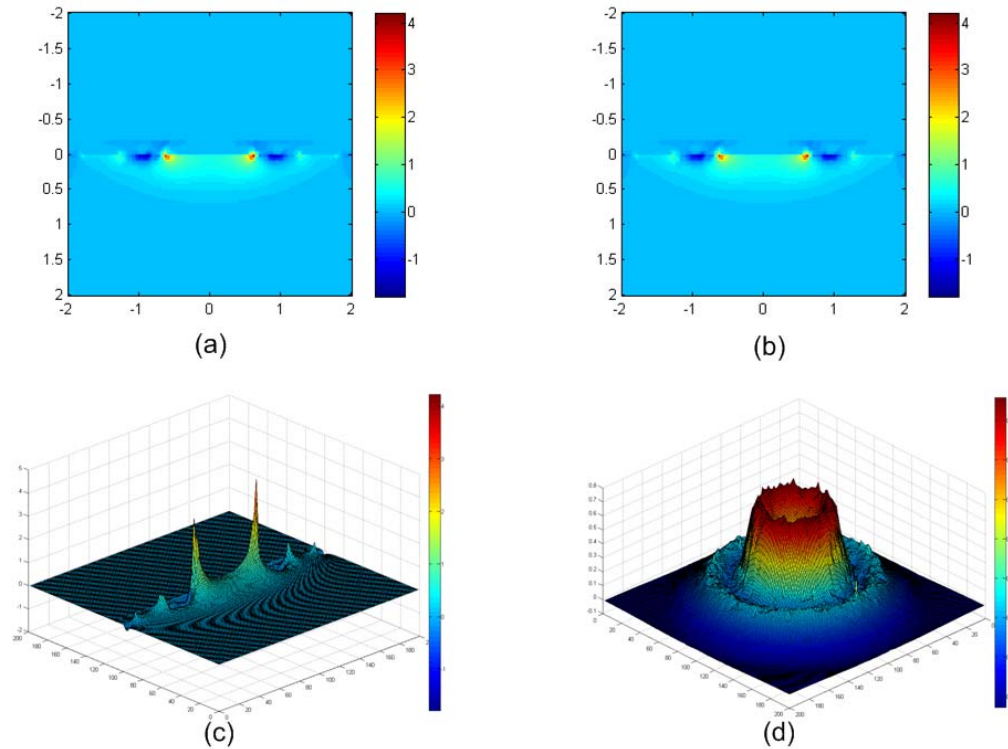
Figure 4.31: *Sensitivity distribution of Probe G. (a) x = 0 plane, (b) y = 0 plane, (c) 3D representation of y = 0 plot and (d) 3D representation of the z = -0.2 plane plot.*

It can be noticed from both of the cases that negative sensitivities were located near the guard electrodes, within the dielectric substrate in the PCB, and in regions relatively far from the probe surfaces. From the derivation process, it can be concluded that, in such regions, increased permittivity values result in a decreasing capacitance. In practical scans, the regions with negative sensitivity values must be dealt with carefully, as will be demonstrated in Chapter 5.

From the derivation process, it can be seen that the sensitivity distribution in a plane describes the responses of the CI probe to a point perturbation, which is practically a point spread function. By analysing the sensitivity distribution, the imaging ability of the probe can be estimated. In addition, the VOI of the CI probe can be defined with a selected threshold value. For instance, if the sensitivity value 0.15 was selected for the back-to-back triangular probe (Probe A) case, the penetration depth can be estimated by assessing the sensitivity values along negative *z*-axis in Figure 4.30(a) and Figure 4.30(b) which is roughly 10 mm. Note that, the selection of threshold value is determined by the signal conditioning circuit connected to the probe, which

determines how small a signal variation can be observed. It is also worth mentioning that the analysis on the imaging resolution of the CI probe using the sensitivity distribution is more complicated than the conventional point spread function method in an optical imaging system, as the sensitivity distributions are different in different planes, so the imaging resolution changes with the distances off the probe surface. However, good approximations can be made by assessing the cross section planes parallel to the probe surfaces ($z = a$ planes).

It is necessary to emphasise that the expression for the sensitivity distribution (Equation(4.26)) is obtained by introducing a high permittivity dipole perturbation in air. However, the results can be generalized, as the calculation of the unperturbed electric field using FEM can take into account the effects of internal inhomogeneities in a sample or boundaries between different materials. In addition, the perturbation is not limited to permittivity changes, as the presence of conducting objects and surface feature changes on conducting samples will also have similar effects to perturbations.

4.5.3   Sensitivity distributions of CI probes

The sensitivity distribution can be used as a useful tool to characterize the CI probe and verify the design principles obtained in Chapter 3, as it provides a panoramic view of the probe performance. Also, by setting the same threshold value for different probes, a comparison of VOIs can be made, and the imaging abilities of the probes can be compared. Note that, in practice, this threshold value is the detecting limit of the measurement circuit, while in this chapter it is determined according to different plots only for optimal visualization.

The sensitivity distributions of Probe C and Probe F were firstly obtained and compared to investigate the effects of electrode separation on the probe performances (see Figure 4.32). Probe C and Probe F are two rectangular electrode probes, and the only difference between them is the electrode separation, being 6 mm in Probe C and 28 mm in Probe F.
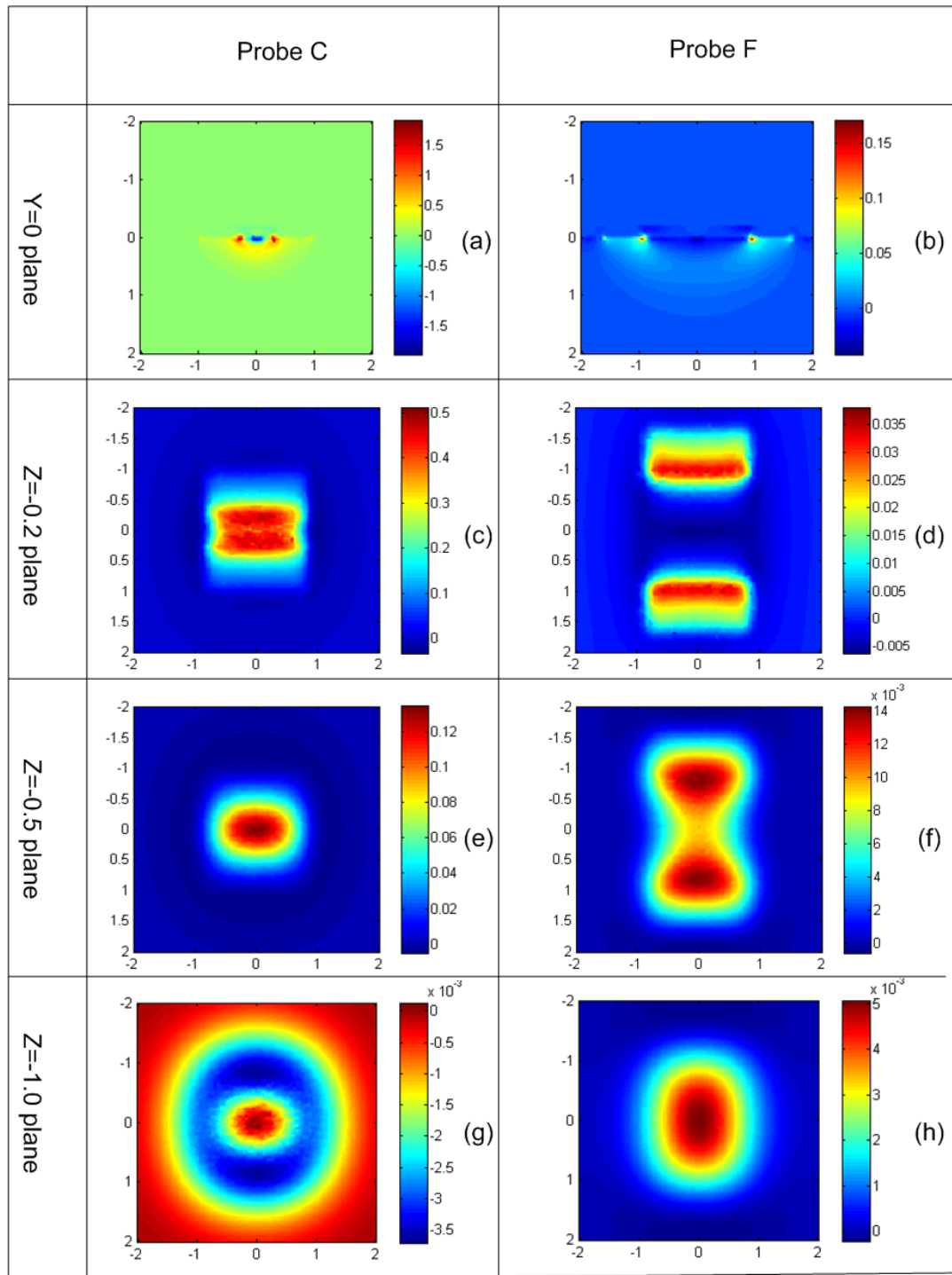
Figure 4.32: *Comparison between the sensitivity distributions of Probes C and F, for. (a) and (b) the y = 0 plane, (c) and (d) the z = -0.2 plane, (e) and (f) the z = -0.5 plane, and (g) and (h) the z = -1.0 plane.*

The colour maps can be forced to have the same scale for the corresponding planes, as shown in Figure 4.33. This is can be considered as setting a threshold to define the VOIs. Although some features are missing (saturated values in the middle as shown in

Figure 4.33(a), (c) and (e) for Probe C) and some features are very fuzzy (Figure 4.33(d) and (e) for Probe F), direct comparison can be made between the two probes. It can be seen that the sensitivity is much higher for Probe C above the $z = -0.5$ planes, but it decays much more quickly for Probe C, as for the $z = -1$ planes there are rarely any separable sensitivity values in Figure 4.33(g) compared to Figure 4.33(h). Based on the comparison, it can be concluded that a smaller electrode separation will increase the signal level but reduce the penetration depth. This agrees with the discussion presented earlier in Chapter 3.

The sensitivity distributions for Probe A (back-to-back triangles) and Probe D (point-to-point triangles) were then compared, as shown in Figure 4.34. The colour maps are in the same scale for same planes in the two cases. Comparing Figure 4.34(a) and Figure 4.34(b), higher sensitivity values were distributed across a bigger volume for Probe A than Probe D. Comparing Figure 4.34(c) and Figure 4.34(d), the volume encircled by the outermost separable isoline (same value for the two cases) is bigger for Probe D in both horizontal and vertical directions, indicating a deeper penetration depth but a lower lateral imaging resolution. Comparing Figure 4.34(e) and (f) with Figure 4.34(g) and (h), it can be seen that the sensitivity distributions differ due to the different geometries. The sensitivity values are higher in the $z = -1$ plane for Probe D.

Comparing Figures 4.33 and 4.34, the sensitivity distribution of the back-to-back triangular probe (Probe A) is similar to the rectangular probe with a smaller electrode separation (Probe C), but it has a bigger penetration depth. The sensitivity distribution of point-to-point triangular probe (Probe D) is likewise similar to that of Probe F, but with a stronger signal strength. It can thus be concluded that the triangular electrode pairs (in both the back-to-back and the point-to-point triangular probes) can have advantages over probes with rectangular electrodes in certain situations.
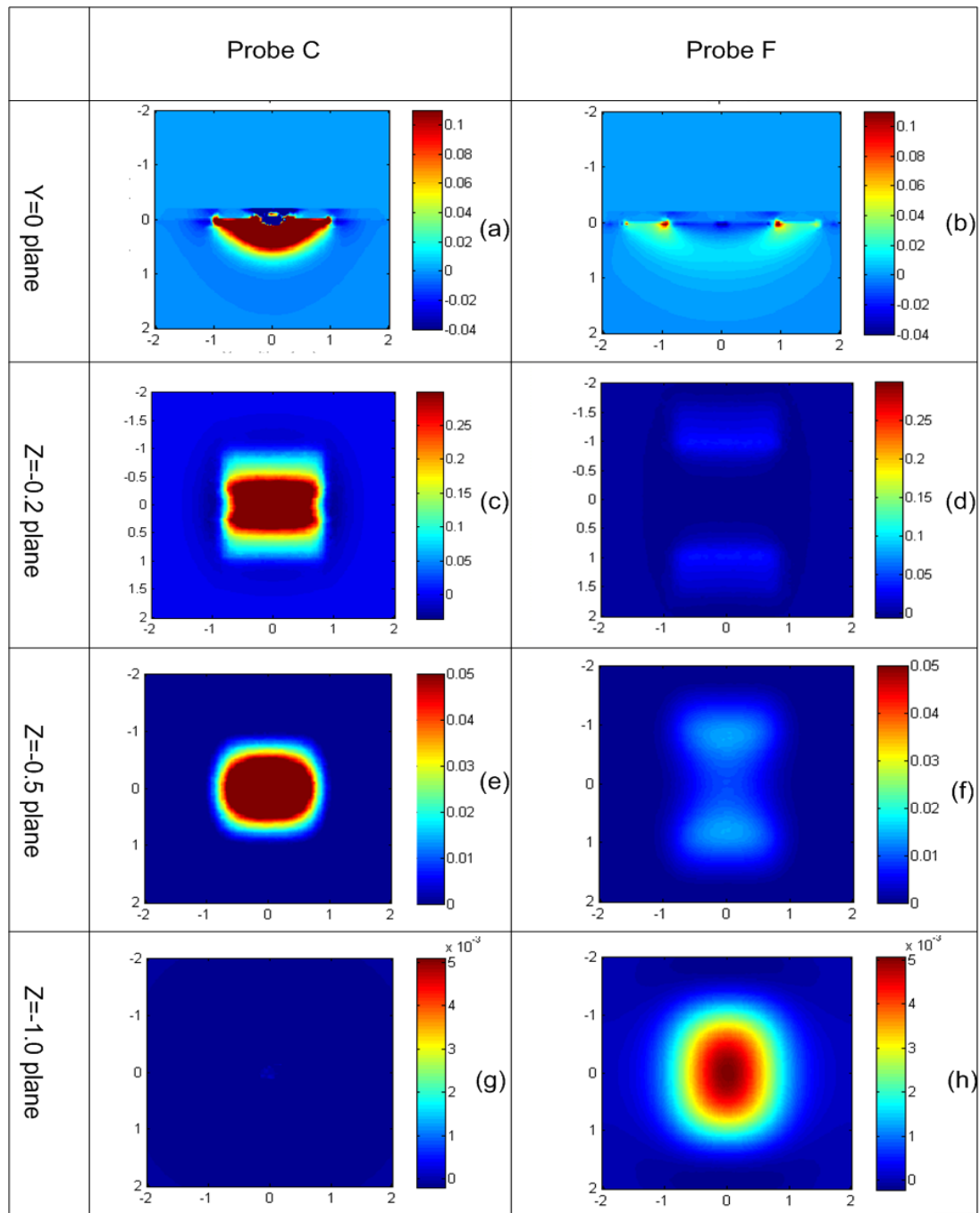
Figure 4.33: *Comparison between the sensitivity distributions of Probe C and Probe F (in the same colour scale). (a) and (b) the y=0 plane, (c) and (d) the z = -0.2 plane, (e) and (f) the z = -0.5 plane and (g) and (h) the z = -1.0 plane.*

117
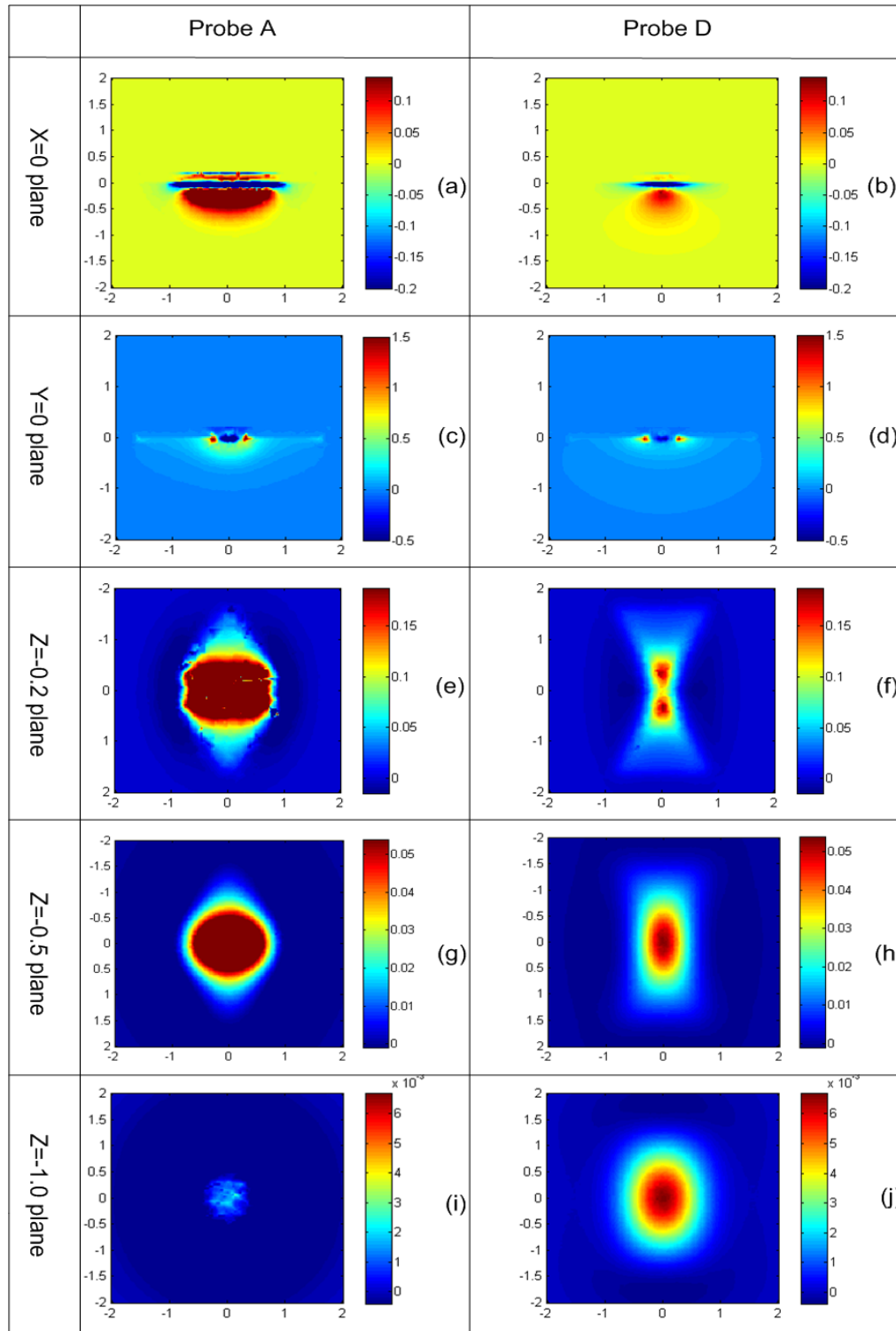
Figure 4.34: *Comparison between the sensitivity distributions of Probe A and Probe D in the same colour scale. (a) and (b) the x = 0 plane, (c) and (d) the y = 0 plane, (e) and (f) the z = -0.2 plane, (g) and (h) the z = -0.5 plane, and (i) and (j) the z = -1.0 plane.*

Some of the design parameters were also investigated from the sensitivity distributions, e.g. guard electrode and thickness of substrate. The back-to-back triangular probe (Probe A), the probe without inner guard electrode (Probe B) and the probe with thinner substrate (Probe E) were studied and the sensitivity distributions are shown in Figure 4.35. Comparing Figure 4.35 (a), (b) and (c) with (j), (k)and (l), it can be seen that Probe A has a deeper penetration depth than Probe B due to the introduced guard electrode, and the penetration depth is further increased by thinning the dielectric substrate.
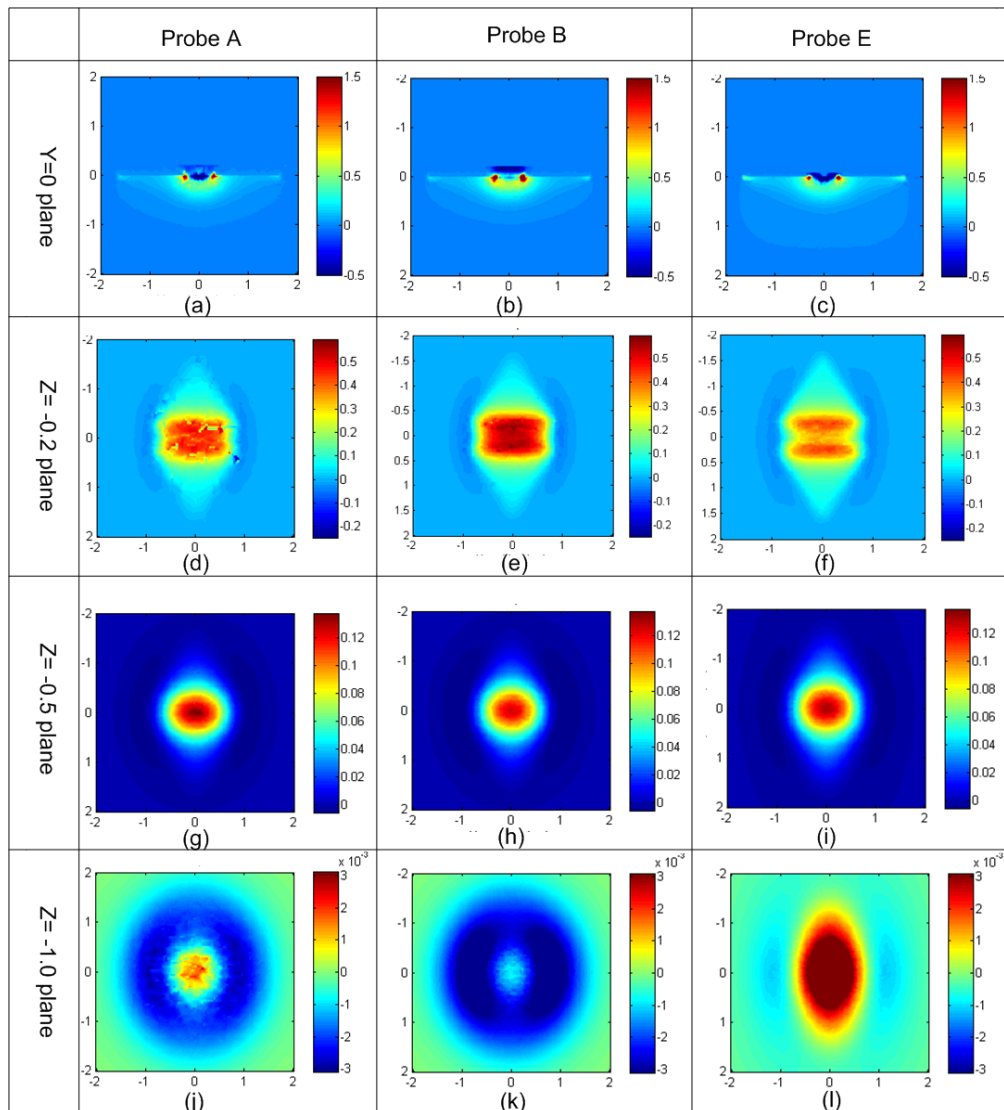
Figure 4.35: *Comparison among the sensitivity distributions of Probe A, Probe B and Probe E (in the same colour scale). (a),(b) and (c) the y = 0 plane, (d),(e) and (f) the z = -0.2 plane, (g),(h) and (i) the z = -0.5 plane and (j),(k) and (l) the z = -1.0 plane.*

4.5.4 Sensitivity distributions with specimens

The sensitivity distributions presented in Section 4.4.3 were obtained in air. However, in practical measurements, the presence of specimens will inevitably change the sensitivity distributions. Sensitivity distributions of CI probes with testing specimens in the sensing areas are discussed in this section.

Figure 4.36 shows the sensitivity distributions of the back-to-back triangular probe (Probe A) in the $y = 0$ plane and the $z = -0.5$ plane with a dielectric sample ($\varepsilon = 4$) situated under the probe at a distance of 20 mm (the $z = -0.2$ plane). They were compared to the sensitivity distributions in air as shown in Figures 4.36(a) and (c) in corresponding planes. It can be seen that the dielectric specimen enhanced the sensitivity in the air gap and depleted the sensitivity in the specimen.
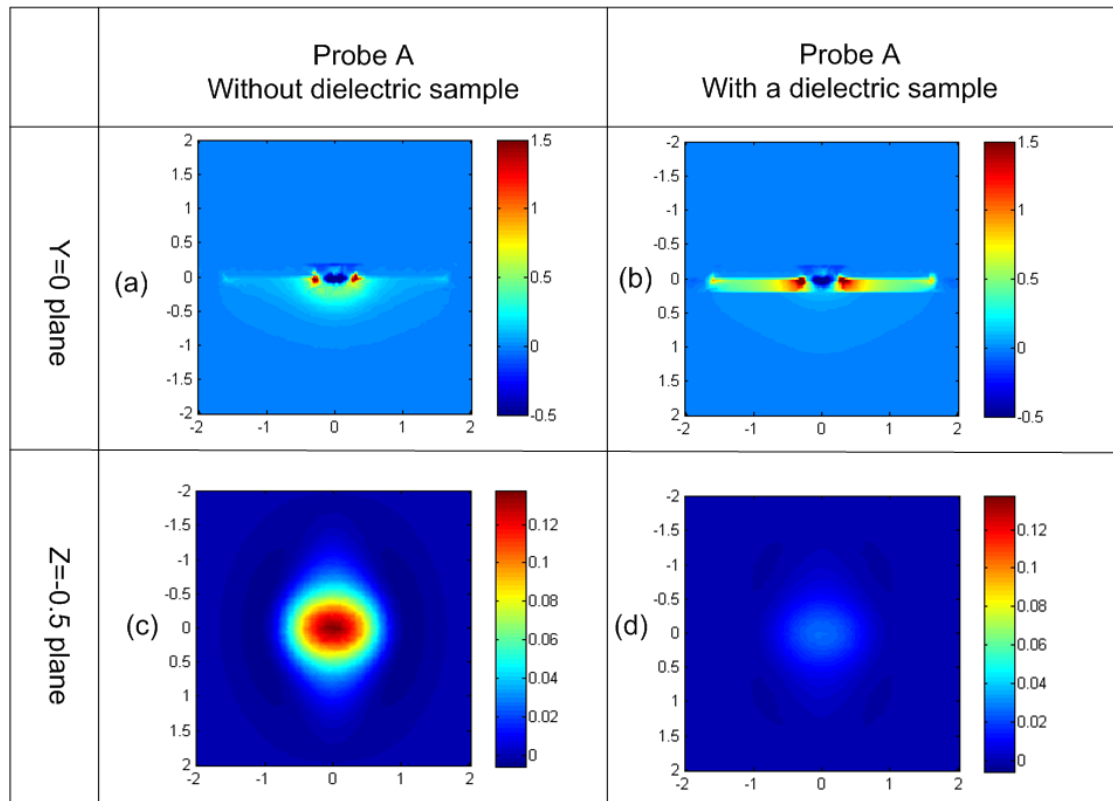
Figure 4.36: *Comparison of the sensitivity distributions of Probe A without and with a dielectric sample. (a) and (b) the y = 0 plane; (c) and (d) the z = -0.5 plane.*

The results of the point-to-point probe (Probe D) were also obtained and are presented accordingly in Figure 4.37.
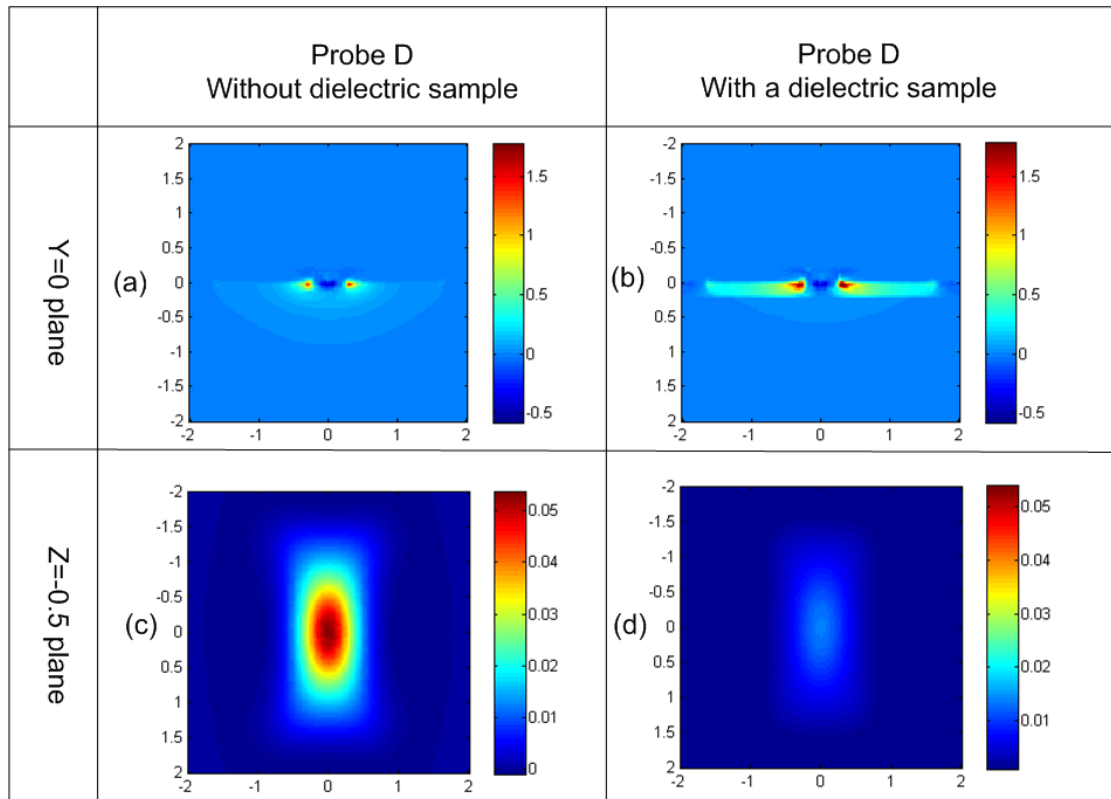
Figure 4.37: *Comparison of the sensitivity distributions of Probe D without and with a dielectric sample. (a) and (b) the y = 0 plane; (c) and (d) the z=-0.5 plane.*

Similarly, the sensitivity distribution for CI probes with a grounded metal can be obtained (the lift-off distance was also 2 mm, which means the metal surface was in the $z = -0.2$ plane). Contrary to the dielectric specimen, the grounded metal will deplete the sensitivity in the air gap. To avoid repetition, the results are not shown here.

Similar models were constructed for the point-to-point probe (Probe D), and direct comparisons can then be made between the sensitivity distributions of the back-to-back and the point-to-point triangular probes with specimens, if the sensitivity distributions with dielectric/conducting specimens are presented in the same colour map for the same planes, as shown in Figure 4.38.

Consider the dielectric specimen in the $z =- 0.5$ plane (a plane within the dielectric specimen). The sensitivity values for the back-to-back triangular probe (Probe A in Figure 4.38(a)) are much higher and are distributed over a smaller area than for the point-to-point probe (Probe D) shown in Figure 4.38(b). This means that the back-to-

back triangular probe is better for imaging defects buried at shallow depths within a dielectric specimen. Note that, if the defect is deeper buried and beyond the reach of a back-to-back triangular probe, a point-to-point one has to be used as the penetration depth is bigger, although it may only provide a fuzzy image with small variations.

For the grounded metal surface, in the $z = -0.1$ plane (a plane near the grounded metal surface in the air gap), the sensitivity values for Probe A (Figure 4.38(c)) are much higher but distributed over a bigger area compared to Figure 4.38(d). This means that the back-to-back triangular probe will not give a sharp image when trying to image small features, because the point spread function in that plane is spatially bigger than the point-to-point probe. Therefore, the point-to-point triangular probe is a better choice for small surface feature on conducting surface if a signal conditioning circuit with high SNR is available.

	Probe A	Probe D
Z= -0.5 plane Dielectric specimen	(a)	(b)
Z= -0.1 plane Grounded conducting specimen	(c)	(d)
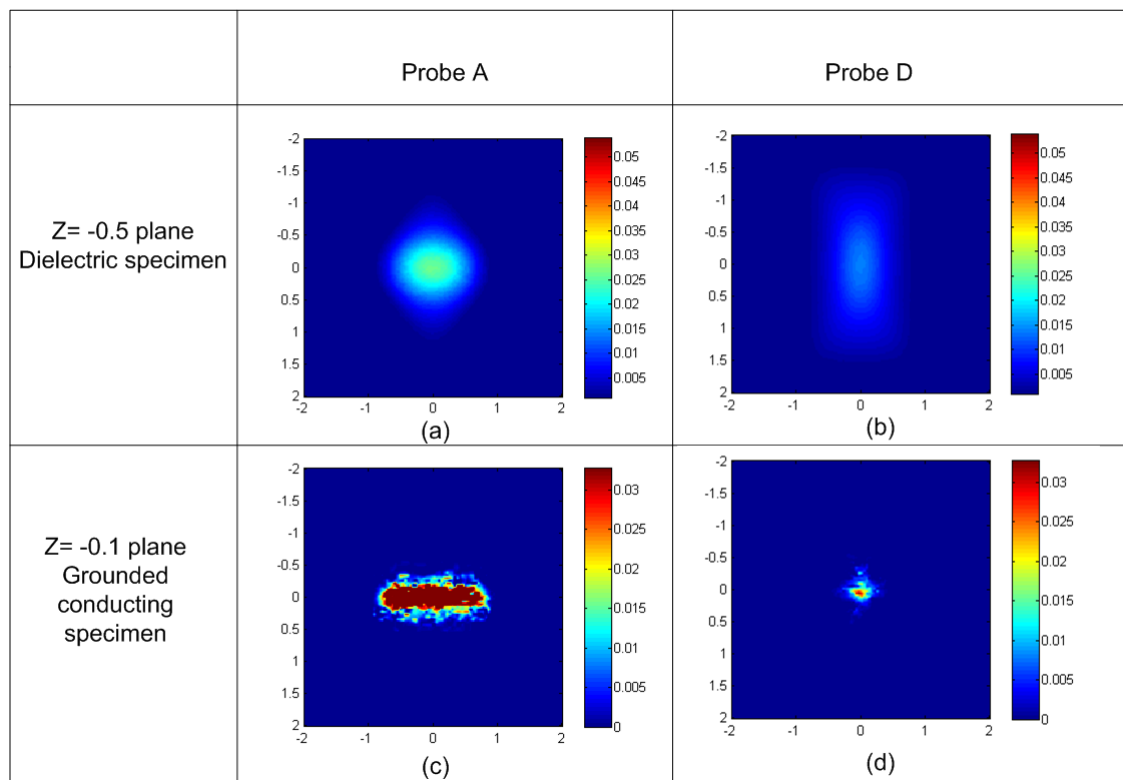
Figure 4.38: *Comparison of the sensitivity distributions of Probe A and Probe D for (a) and (b) the plots of z = -0.5 plane with a dielectric specimen, and (c) and (d) the plots of z = -0.1 plane with a grounded conducting specimen.*

4.6   Conclusions

In this chapter, the use of FE models for the modelling of the fields from CI probes was discussed. Firstly, 2D models were constructed to demonstrate the electric field from the CI probe interacting with both non-conducting specimen and conducting specimen with an insulation layer. It has been demonstrated that the electric field distributions under the CI probe were significantly perturbed by the defects. 2D non-dimensional models were then used to study the effects of specimen thickness, lift-off distance and different electrical properties of the specimen. Those non-design related parameters are difficult to be studied experimentally. It has been revealed that such parameters can affect the measured signal in a complex way and need to be taken into consideration in practical measurements. The 2D models were also used to predict the probe response for three typical flaws, namely step, narrow groove and wide groove, on both insulating and conducting specimens. The results indicated that the presence of the insulating specimens can enhance the output while the conducting specimens deplete the output. In addition, it can be seen from the calculated CI probe responses, the edges of the defects on the conducting specimens were better defined compared to the insulating specimens.

3D models were then constructed in order to characterize CI probes with more complex geometries than the simplest rectangular electrode pair. The 3D models were used to obtain the sensitivity distribution both from a perturbation method and a mathematical approach. In the former method, a small perturbation was introduced in the sensing area, and the changes in the calculated capacitance values were registered to form a relatively coarse sensitivity map. In the latter method, it has been demonstrated that the sensitivity distribution can be expressed as the dot product of the electric fields from the driving and sensing electrodes which were reciprocally energized by a unit voltage.

The sensitivity distributions for various CI probes were then obtained from the mathematical model and studied in detail. The sensitivity distribution can be used to determine the VOI and evaluate the imaging ability of a CI probe. Comparisons were made among the calculated sensitivity distributions from different probes, and some of the design principles raised in Chapter 3 were backed up by the analysis of the

obtained sensitivity distributions. The sensitivity distributions for back-to-back triangular probe and point-to-point triangular probe were studied with specimens presented under the probes. For both probes the presence of the insulating specimen enhances the sensitivity in the air gap and depletes the sensitivity within the specimen, while the presence of the grounded conducting specimen depletes the sensitivity in the air gap (no sensitivity within the conducting specimen). And the results confirmed that the back-to-back triangular probe is advantageous for the imaging of subsurface features in insulating specimens and the point-to-point triangular probe is advantageous for the imaging of surface features on a conducting specimen.

The systematic studies of the influential parameters presented in Chapter 3 and Chapter 4 have provided an assessment of the practicality of the CI technique and it is now possible to anticipate the likely performance of any design.

4.7 References

[1] G. Meng, A. J. Jaworski, and J. C. S. Kimber, "A multi-electrode capacitance probe for phase detection in oil-water separation processes: design, modelling and validation," *Measurement Science and Technology,* vol. 17, pp. 881-894, 2006.

[2] A. J. Jaworski and G. T. Bolton, "The design of an electrical capacitance tomography sensor for use with media of high dielectric permittivity," *Measurement Science and Technology,* vol. 11, pp. 743-757, 2000.

[3] F. Jiang, S. Liu, J. Liu, and X. Wang, "Measurement of ice movement in water using electrical capacitance tomography," *Journal of Thermal Science,* vol. 18, pp. 8-12, 2009.

[4] A. A. Nassr and W. W. El-Dakhakhni, "Non-destructive evaluation of laminated composite plates using dielectrometry sensors," *Smart Materials and Structures,* vol. 18, p. 055014, 2009.

[5] R. Nimmer, J. Osiensky, A. Binley, K. Sprenke, and B. Williams, "Electrical resistivity imaging of conductive plume dilution in fractured rock," *Hydrogeology Journal,* vol. 15, pp. 877-890, 2007.

[6] G. M. Maillet, E. Rizzo, A. Revil, and C. Vella, "High Resolution Electrical Resistivity Tomography (ERT) in a Transition Zone Environment: Application for Detailed Internal Architecture and Infilling Processes Study of a Rhône River Paleo-channel," *Marine Geophysical Researches,* vol. 26, pp. 317-328, 2005.

[7] K. Karhunen, A. Seppanen, A. Lehikoinen, P. J. M. Monteiro, and J. P. Kaipio, "Electrical Resistance Tomography imaging of concrete," *Cement and Concrete Research,* vol. 40, pp. 137-145, 2009.

[8] V. Spitas and P. Michelis, "The Potential Drop Technique for Measuring Crack Growth in Shear," in *Fracture of Nano and Engineering Materials and Structures*, 2006, pp. 463-464.

125

[9]   M. Saka, M. Nakayama, T. Kaneko, and H. Abé, "Measurement of stress-intensity factor by means of a-c potential drop technique," *Experimental Mechanics,* vol. 31, pp. 209-212, 1991.

[10]   S. M. Musa and M. N. O. Sadiku, "Using finite element method to calculate capacitance, inductance, characteristic impedance of open microstrip lines," *Microwave and Optical Technology Letters,* vol. 50, pp. 611-614, 2008.

[11]   E.-W. Bai and K. E. Lonngren, "Capacitors and the method of moments," *Computers & Electrical Engineering,* vol. 30, pp. 223-229, 2004.

[12]   T. Chen and N. Bowler, "Analysis of a concentric coplanar capacitive sensor for nondestructive evaluation of multi-layered dielectric structures," *Dielectrics and Electrical Insulation, IEEE Transactions on,* vol. 17, pp. 1307-1318.

[13]   H. H. Park, J. H. Kwon, J. W. Lee, and H. J. Eom, "Analysis of single-layered multiconductor transmission lines using the Fourier transform and mode-matching techniques," *Microwave and Optical Technology Letters,* vol. 36, pp. 315-317, 2003.

[14]   Jérôme Lucas, Stéphane Holé, and Christophe Bâtis, "Analytical capacitive sensor sensitivity distribution and applications," *Measurement Science and Technology,* vol. 17, pp. 2467-2478, 2006.

[15]   Jérôme Lucas, Stéphane Holé, and Christophe Bâtis, "Simple and direct calculation of capacitive sensor sensitivity map," *COMPEL: The International Journal for Computation and Mathematics in Electrical and Electronic Engineering,* vol. 27, pp. 307-318, 2008.

[16]   Xiaohui Hu and W. Yang, "Planar capacitive sensors -Designs and Applications," *Sensors Review,* vol. 30, pp. 24-39, 2010.

[17]   G. P. Lucas, J. C. Cory, and R. C. Waterfall, "A six-electrode local probe for measuring solids velocity and volume fraction profiles in solids-water flows," *Measurement Science and Technology,* vol. 11, pp. 1498-1509, 2000.

[18]   J. P. Oakley and M. S. Bair, "A mathematical model for the multi-electrode capacitance sensor [and tomographic reconstruction algorithm]," *Measurement Science and Technology,* vol. 6, pp. 1617-1630, 1995.

[19]   M. Jaakko, "Principle of reciprocity solves the most important problems in bioimpedance and in general in bioelectromagnetism," *Journal of Physics: Conference Series,* vol. 224, p. 012001.

[20]   Jaakko Malmivuo and R. Plonsey, *Bioelectromagnetism: Principles and applications of bioelectric and biomagnetic fields*. New York Oxford University Press, 1995.

[21]   W. Q. Yang and S. Liu, "Electrical capacitance tomography with square sensor," *Electronics Letters,* vol. 35, pp. 295-296, 1999.

[22]   J. Mirkowski, W. T. Smolik, M. Yang, T. Olszewski, R. Szabatin, D. S. Radomski, and W. Q. Yang, "A New Forward-Problem Solver Based on a Capacitor-Mesh Model for Electrical Capacitance Tomography," *Instrumentation and Measurement, IEEE Transactions on,* vol. 57, pp. 973-980, 2008.

[23]   R. Banasiak, R. Wajman, J. Betiuk, and M. Soleimani, "Feasibility study of dielectric permittivity inspection using a 3D capacitance CT method," *NDT & E International,* vol. 42, pp. 316-322, 2009.

[24]   R Banasiak, R Wajman, and M. Soleimani, "n efficient nodal Jacobian method for 3D electrical capacitance tomography image reconstruction," *INSIGHT,* vol. 50, pp. 36-38, 2009.

[25]   D. B. Geselowitz, "An Application of Electrocardiographic Lead Theory to Impedance Plethysmography," *Biomedical Engineering, IEEE Transactions on,* vol. BME-18, pp. 38-41, 1971.

[26]   J. R. Mortarelli, "A Generalization of the Geselowitz Relationship Useful in Impedance Plethysmographic Field Calculations," *Biomedical Engineering, IEEE Transactions on,* vol. BME-27, pp. 665-667, 1980.

[27]   P. Kauppinen, J. Hyttinen, and J. Malmivuo, "Sensitivity distribution simulations of impedance tomography electrode combinations," *International Journal of Bioelectromagnetism,* vol. 7, pp. 344-347, 2005.

[28]   Alejandro Gonzalez-Nakazawa, W. Yang, and K. Hennessey, "An analytical approach for modelling electro-magnetic tomography sensors," *Sensors Review,* vol. 28, pp. 212-221, 2008.

[29]   R. Javier and et al., "Sensitivity maps and system requirements for magnetic induction tomography using a planar gradiometer," *Physiological Measurement,* vol. 22, p. 121, 2001.

[30]   Xiaohui Hu and W. Yang, "An imaging system with planar PCB-coil sensor array," in *Imaging Systems and Techniques, 2009. IST '09. IEEE International Workshop on*, 2009, pp. 26-31.

Chapter 5   Experimental validation of the CI technique

5.1   Introduction

In previous chapters, the concept of the CI technique has been established in analytical models and finite element models, and the studies on probe geometries and sensitivity distributions have delivered criteria for probe design. This chapter is dedicated to the experimental validation of the CI concept. Firstly, issues related to instrumentation are addressed. Experiments on typical specimens are then presented to validate the feasibility of the technique on various specimens which were also studied in the FE models. Thirdly, parameters that may have effects on the capacitive images have been studied. A typical image is obtained by scanning the CI probe in a raster pattern with a step size of 1 mm above the test samples at a certain lift-off distance. In a typical signal amplitude plot, lighter areas indicate higher intensity values.

5.2   Instrumentation related issues

As discussed in Chapter 2, the charge signal on the sensing electrode is very small and can be easily buried in noise or disturbed by unwanted sources. Although a charge amplifier and lock in amplifier can be employed to increase the measurement sensitivity and improve the SNR, particular attention is required:

Cabling - Cables and connectors have to be carefully chosen and properly placed as they are typically the weakest part of a measuring system. When the coaxial cables connecting the CI probe, charge amplifier and lock in amplifier are subjected to movement (bending or tension), there may be charge transport, and local changes in capacitance can be generated. The produced charge signal cannot be distinguished from the probe output. This can be troublesome when measuring small features. To minimize this effect, the cables should be as short as possible and relative cable motion apart from the slack to allow free movement of the probe should be avoided. Alternatively, the charge amplifier can be built right on the probe as a unit and this problem can be solved completely.

Probe housing - As mentioned in Chapter 3, shielding is very important for the CI probes. While testing, it is quite noticeable that moving object (*i.e.* hand) near the PCB probe will affect the output voltage. This shows that the conducting back plane is inadequate to shield the electric field, as it is leaking from the sides of the PCB, such situation is illustrated in Figure 5.1:
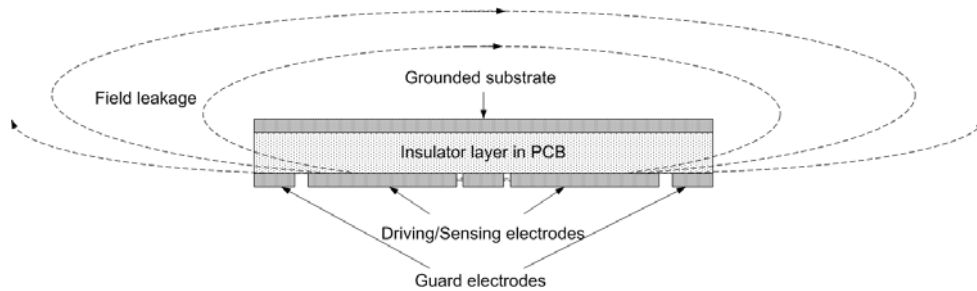
Figure 5.1: *Electric field leakage.*

Therefore, a metal housing is needed for the PCB. In practice, screening metal boxes are used, as shown in Figure 5.2. A hole with the same size of the PCB is machined into the lid of the box and the PCB is forced into the hole with its sides covered by metal. The metal box is then grounded via the BNC connector to effectively prevent field leakage. In addition, a handle can be mounted on the box for the scanning stage to manipulate the probe. An insulation layer is always used to protect the probe surface and prevent the probe from directly contacting with specimens (especially for the conducting ones, which will cause a ground loop if direct contact happened).
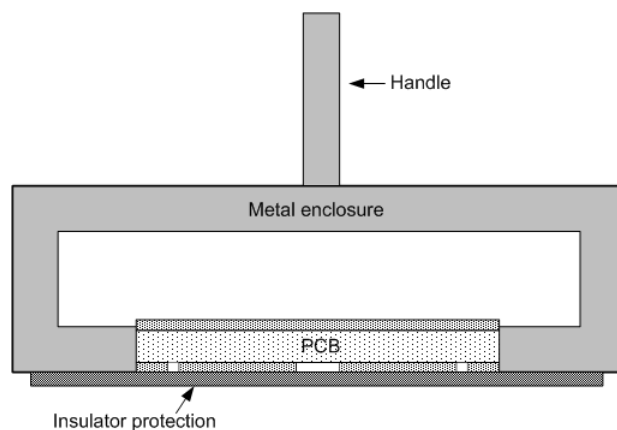
Figure 5.2: *PCB with metal enclosure and insulator protection. This layer was typically made from polyester and was 0.1 mm thick.*

Probe mounting - Choosing the optimum mounting arrangement will significantly improve the measurement accuracy. For best performance, parallelism is crucial. If the specimen has an uneven surface or the probe/target is tilted any significant amount, as shown in Figure 5.3, measurement errors will be introduced.
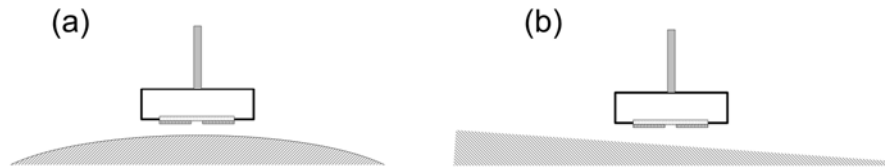
Figure 5.3: *(a) Uneven Surface and (b) lack of parallelism.*

For flat specimens, the probe and specimen are normally positioned with care to ensure the parallelism. However, for specimens with uneven surface, constant lift-off is difficult to achieve. In these cases a spring can be built into the handle, and during the scan process the probe is spring-loaded to keep intimate contact with the specimens.

Specimen surface finish - As mentioned in previous chapters, the CI probes work in a weighted averaging manner. Therefore, when trying to image subsurface features on specimens with rough surfaces, sometimes the measured value can change, even in a position without a hidden defect. The magnitude of this error depends on the nature and symmetry of the surface irregularities.

Edge effects - For both dielectric and conducting specimens, edge effects can cause leakage of the probing electric field which will result in a sudden signal change. This is to do with the probing electric field being partially in the specimen range and partially outside. This effect could be predominant and may blanket the targeting features. One of the possible ways to solve this problem is to reduce electrode size, although trade-offs have to be made accordingly as discussed in Chapter 3.

5.3   Typical results

In Chapter 4, the 2D FE models were constructed to predict the possible response from the CI probe to defects in both insulators (see Figure 4.2) and conductors (see Figure 4.4). In this section, experimentally validation of these 2D models is presented.

5.3.1 Dielectric specimen

Perspex represents an insulating dielectric material, and scans under different conditions have been performed for a 21 mm thick sample containing four 20 mm square depressions of different depths (3 mm, 7 mm, 11 mm and 15 mm), as shown in Figure 5.4 .
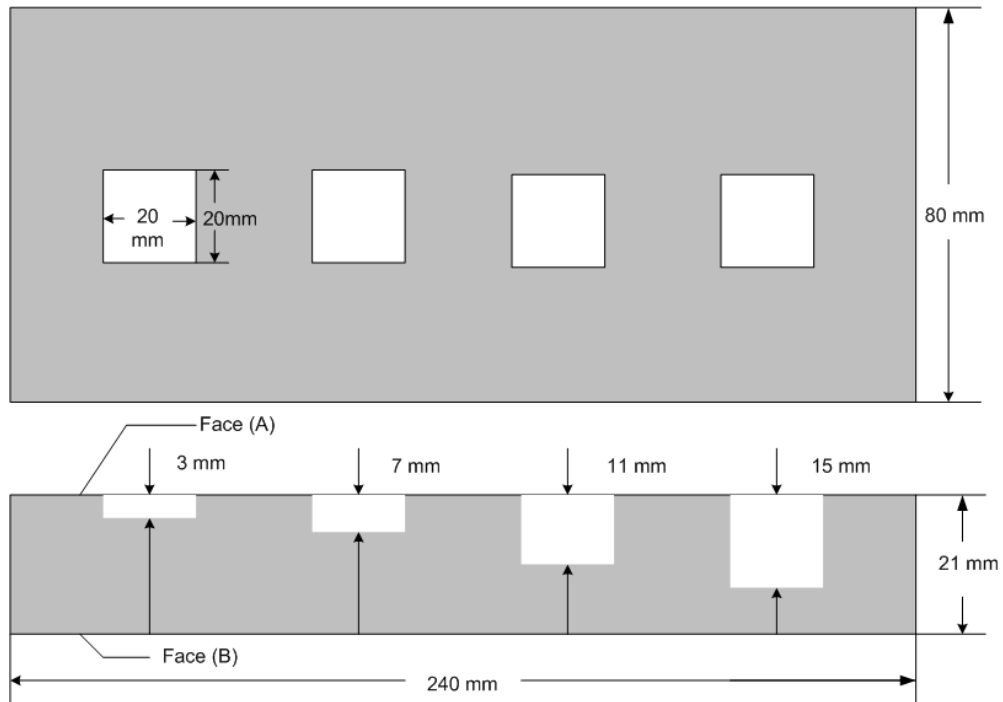
Figure 5.4: *Schematic diagram of a 21mm thick Perspex plate containing flat bottomed holes of depth (from left to right) 3 mm, 7 mm, 11 mm and 15 mm.*

This sample was firstly scanned over a 200 mm by 50 mm area, with the 40 mm by 20 mm back-to-back triangular probe (shown in Figure 3.13(a)) maintained at a distance of 1 mm from the surface containing the flat-bottomed holes (Face A in Figure 5.4). The plate was placed on a grounded platform which acted as a grounded substrate on the far side. The resultant image is shown in Figure 5.5 (a), with the darker areas representing lower values. It can be seen from the intensity variations of the image that the holes in the Perspex plate depleted the measured signal to different extents according to the depths. A second scan from the flat surface (Face B in Figure 5.4) was then performed and the result (Figure 5.5 (b)) shows that the technique has also captured the presence of these holes, but with a lower resolution. It is worth noting that, contrary to the case for surface holes, the hidden holes were actually shown as

132

lighter areas in the image which suggested higher values. This phenomenon will be explained in detail in Section 5.4.
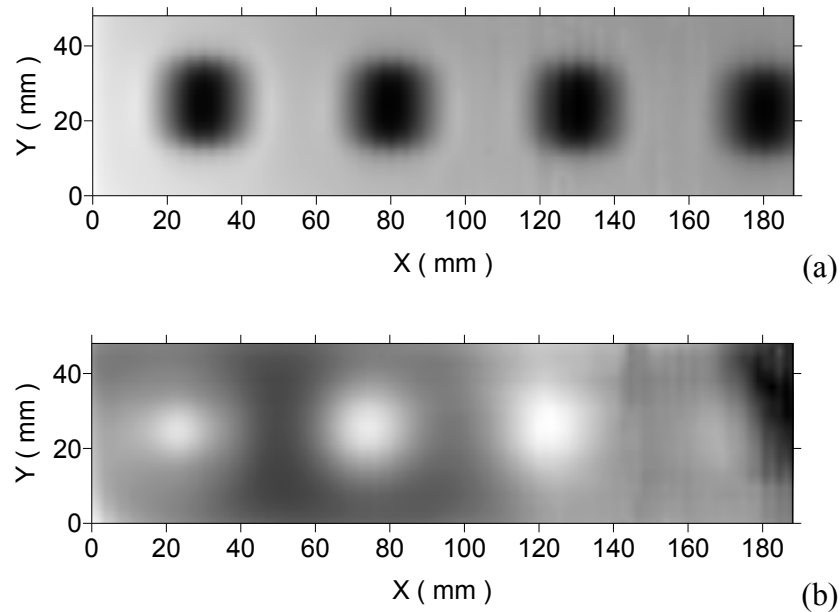
Figure 5.5: *(a) Scan image from the surface containing the flat-bottomed holes. (b) Scan image from the far (flat) surface. The depths of the holes are 15 mm, 11 mm, 7 mm and 3 mm from left to right.*

5.3.2   Conducting specimens

5.3.2.1 Aluminium specimen

Aluminium (conductivity $\sigma_{alu}= 3.5\times 10^7$ S/m) represents a conducting material, and a scan was performed on a 9 mm thick sample containing four 20 mm square holes of different depths (2 mm, 4 mm, 6 mm and 8 mm), as shown in Figure 5.6 . A 40 mm by 200 mm area was scanned. During the scan, the aluminium plate was explicitly grounded and the 40 mm by 20 mm back-to-back triangular probe was maintained at a distance of 1 mm from the surface containing the flat-bottomed holes. The resultant image is shown in Figure 5.7. The holes are clearly imaged and the depth of the hole is related to the intensity of the image, as in the Perspex case. But the presence of the holes resulted in a local signal increment, as indicated by the lighter areas.
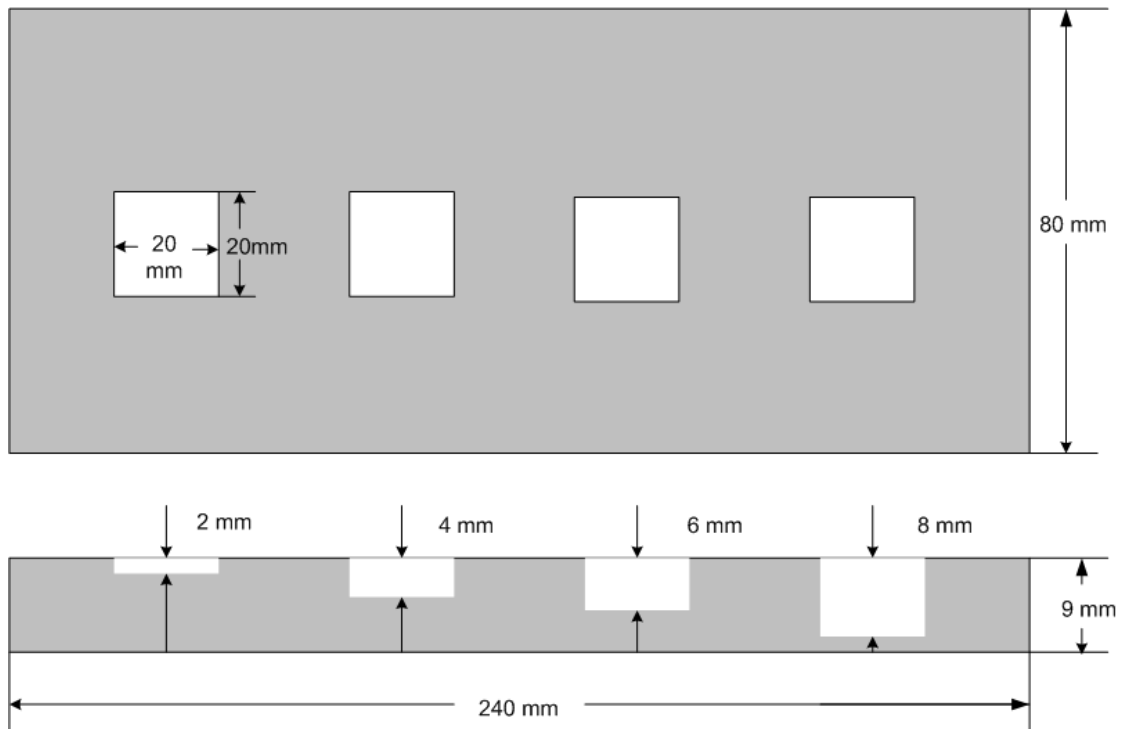
Figure 5.6: *Schematic diagram of a 9 mm thick aluminium plate containing flat bottomed holes of depth (from left to right) 2 mm, 4 mm, 6 mm and 8 mm.*
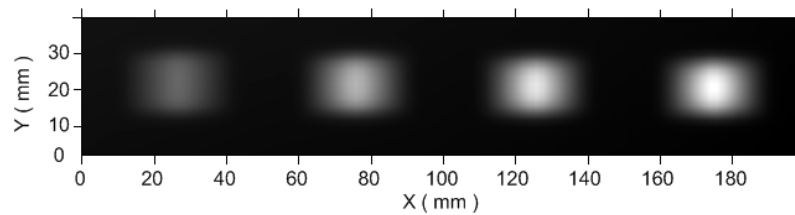
Figure 5.7: *Capacitive image of the aluminium plate containing flat bottomed holes of depth (from left to right) 2 mm, 4 mm, 6 mm and 8 mm.*

5.3.2.2 Steel specimen

A carbon steel (SAE 1045, conductivity $\sigma_{steel}= 6.2 \times 10^6$ S/m) specimen was also investigated to test if the conductivity of a conductor affects the detect ability of the system. The sample was 10 mm thick and contained 4 circular holes of same diameter (20 mm) and different depths (2 mm, 4 mm, 6 mm and 8 mm), as shown in Figure 5.8. A 40 mm by 200 mm area was scanned. During the scan the steel plate was explicitly grounded and the 40 mm by 20 mm back-to-back triangular probe was maintained at a distance of 1 mm from the surface containing the flat-bottomed holes. The resultant image, shown in Figure 5.9, is similar to the aluminium case apart from the shape of

the imaged holes-the circular holes appeared in the image as lighter areas with the intensities related to the depths.
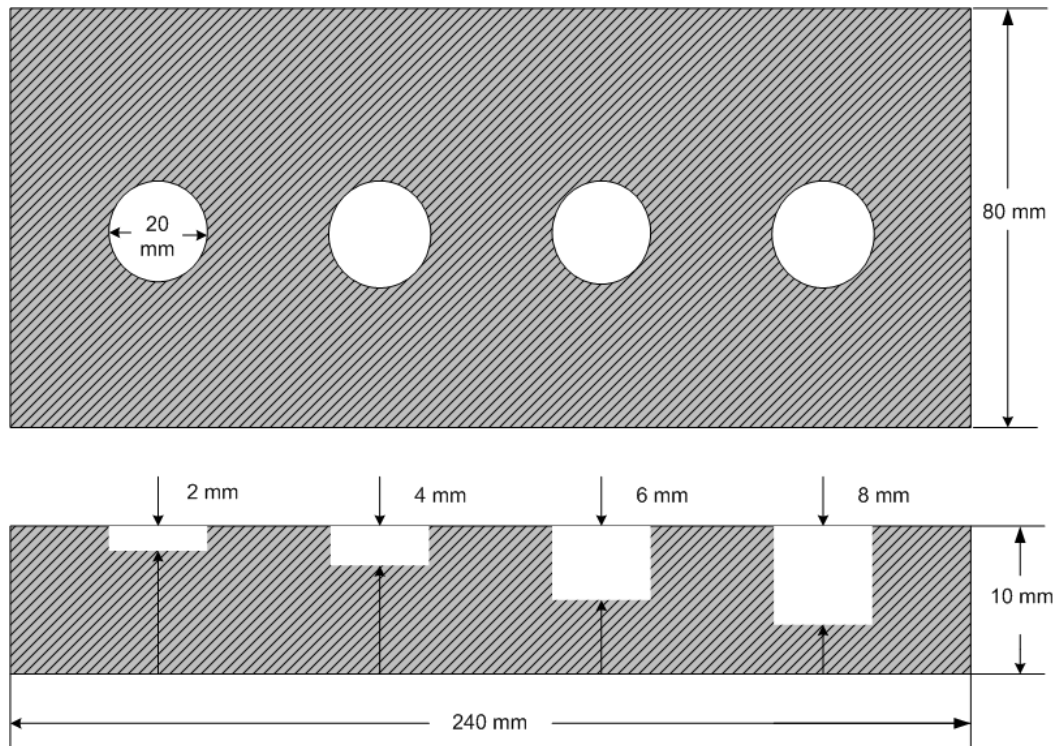
Figure 5.8: *Schematic diagram of a 10mm thick steel plate containing flat bottomed holes of depth (from left to right) 2 mm, 4 mm, 6 mm and 8 mm.*
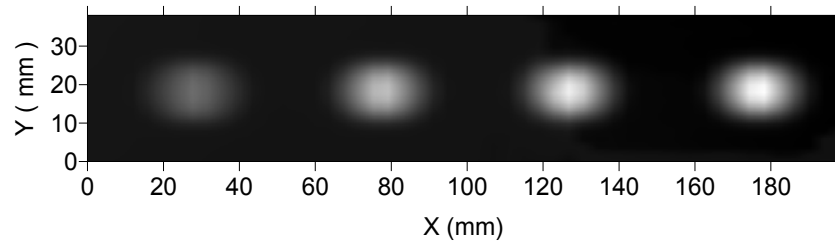
Figure 5.9: *Capacitive image of the steel plate containing flat bottomed holes of depth (from left to right) 2 mm, 4 mm, 6 mm and 8 mm.*

5.3.2.3 Carbon fibre composite specimen

Laminated carbon fibre composite is another example of a conducting material, although the electrical conductivity of the composite can be anisotropic due to good conductivity down the fibres. In fact, the electrical conductivity of the carbon fibre with a 7.5 μm diameter is 6.25×10^4 S/m [1], and the conductivity in directions across

135

the fibres is often lower due to the presence of the epoxy layers. The specimen tested here was a 5 mm thick carbon fibre composite plate with two 20 mm square flat bottomed holes with depth 2 mm and 4 mm respectively, as shown in Figure 5.10.
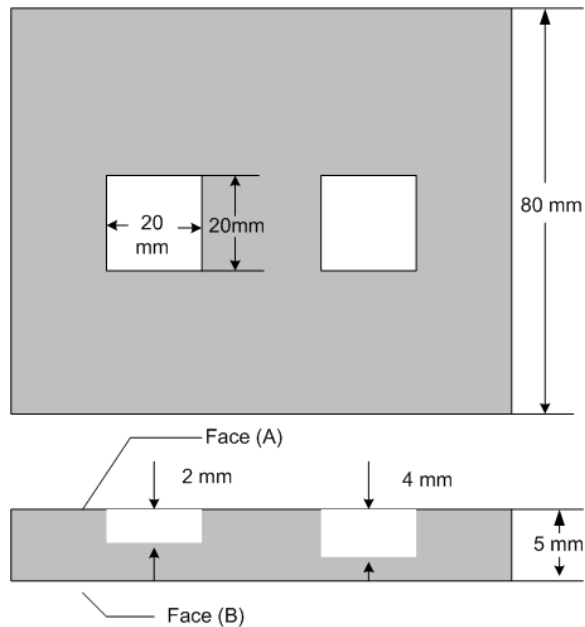
Figure 5.10: *Schematic diagram of a 5 mm laminated carbon fibre composite plate containing two flat bottomed holes of depth 2 mm(left) and 4 mm(right).*

A 40 mm by 100 mm area of Face A (in Figure 5.10) was scanned using the 40 mm by 20 mm back-to-back triangular probe with a 1 mm lift-off. During the scan the all the carbon fibre layers in the plate were grounded. The resultant image, shown in Figure 5.11, is similar to the aluminium case - the square holes appeared in the image as lighter areas with the intensities related to their depths.
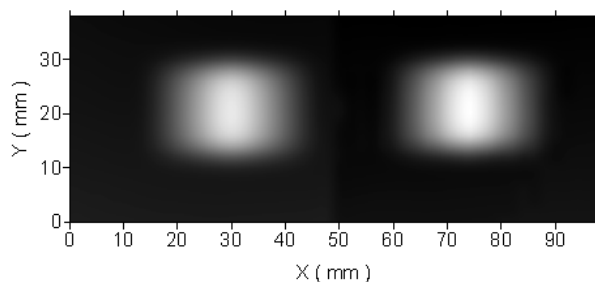
Figure 5.11: *Capacitive image of the laminated carbon fibre composite plate containing two flat bottomed holes of depth 2 mm(left) and 4 mm(right).*

A similar scan was conducted from Face B, but neither of the holes could be detected in this case. Although the conductivity along the thickness of the carbon fibre

136

composite might be low, the high conductivity in the same layers of the carbon fibres will blanket any features underneath them. Therefore, the CI technique is only sensitive to surface features in carbon fibre composite as in the cases of metals. However, if the defects are near the surface and cause changes in the surface, they can be detected by the CI technique, as shall be demonstrated in Chapter 6.

5.3.3 Preliminary conclusions

The expected responses of the CI technique predicted by the 2D FE models were experimentally validated. For dielectric specimens, the probing field is modulated by both the surface and the subsurface features within the VOI of the probe. While for conducting specimens, the probing field is only modulated by the surface features and is insensitive to subsurface features.

For surface features in dielectric specimens and conducting specimens, the responses of the CI probe are in opposite polarities. This is in agreement with the FEM results shown in Chapter 4. It is also worth noting that the CI probes are insensitive to the conductivity variations for specimens with high conductivities, unless these materials are very thin (on the order of microns - a case not examined in this thesis).

5.4 Imaging hidden defects in dielectric specimens

When trying to image subsurface features in dielectric specimens, special attention should be paid as the hidden feature could locate in a region where the sensitivity values are negative.

As mentioned in Chapter 4, in the VOI of a CI probe there are regions where the sensitivity values are negative. In such regions, a perturbation with bigger relative dielectric constant than the ambient material will result in a lower output. Normally, if the sensitivity distribution is calculated without specimens (in air) the influential negative sensitivity values are situated beyond a critical distance (denoted as d_1) from the electrode surface, as shown in Figure 5.12(a). For the cases with specimens, the critical distance (denoted as d_2) will be reduced to a certain extent depending on the electrical properties of the specimen and the lift-off distance, as shown in Figure 5.12(b).
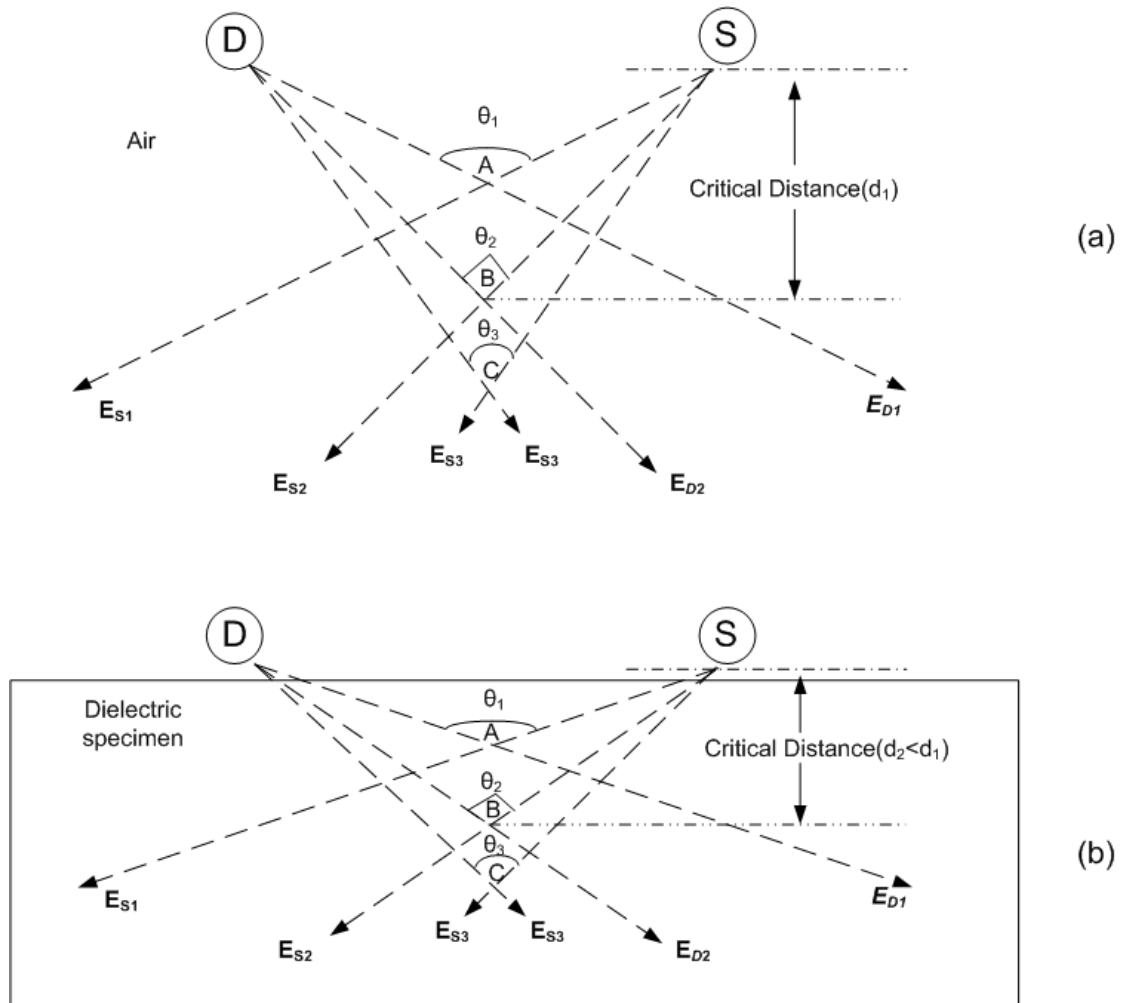
Figure 5.12: *Illustrations of the critical distance for (a) without specimen (in air) and (b) with dielectric specimen.*

When imaging surface features, the distance between the probe surface and the targeting surface is usually smaller than d_1. Therefore, in this case there will be positive sensitivity values along the targeting surface, and the effect caused by the negative values beyond the depth of d_2 are nulled out if the material is homogeneous under the surface. When imaging subsurface features, the situation varies with the buried depth of the targeting features. If the feature is buried at a depth smaller than d_2, the positive sensitivity values will dominate, and the resultant image will be similar to the case with the same features appear on the surface although the contrast will be smaller due to the smaller sensitivity values. If the feature is buried at a depth greater than d_2, the negative sensitivity values will dominate, and the resultant image will be similar to the complementary version of the case with the same features appear on the

138

surface, as the negative sensitivity values imply a reverse relation between the relative dielectric constant change and the output.

The image obtained from the flat face of the Perspex sample, shown in Figure 5.5(b), is an example of targeting features located in negative sensitivity value regions - the holes filled with air which possess a lower relative permittivity value (ε_{air}= 0) than Perspex ($\varepsilon_{perspex}$= 3.3) produced higher values compared to the complete part.

It can be seen from Figure 5.5(b) that even for the deepest hole, the bottom of which was 6mm from the flat side, was in the negative sensitivity value region. To investigate subsurface features in the positive sensitivity value region, a further set of experiments was performed on the same Perspex plate. In these experiments the face with the holes was covered by four pieces of Perspex plates with different thicknesses (2 mm, 3 mm, 4 mm and 5mm) in turn. Four scans were then performed with the 40 mm by 20 mm back-to-back triangular CI probe maintained at a 1 mm distance above each cover and the holes can be considered as hidden defects buried at the depth of 2 mm, 3 mm, 4 mm and 5 mm in the four cases. The results are shown in Figure 5.13. Despite of the interface between the two Perspex plates, the arrangement can be used as good approximations of hidden defects at different depths. It can be seen from the results, with the 2 mm or the 3 mm cover, the holes appeared as darker areas representing lower output values. With the 4 mm or the 5 mm cover, the holes appeared as lighter areas. And it can be seen that the contrast of the image for the 4 mm cover case is small than the 5 mm cover case, which indicates that 3~4 mm is roughly the critical distance and in the regions near this critical distance (*i.e.* the 4 mm case) the CI probe is less sensitive to the permittivity change than other regions (*i.e.* the 2 mm and 5 mm cases).

It should be emphasized that the above mentioned "critical depth" is determined mainly by the probe geometry, the electric properties of the specimen and the lift-off distance between the probe and the specimen.
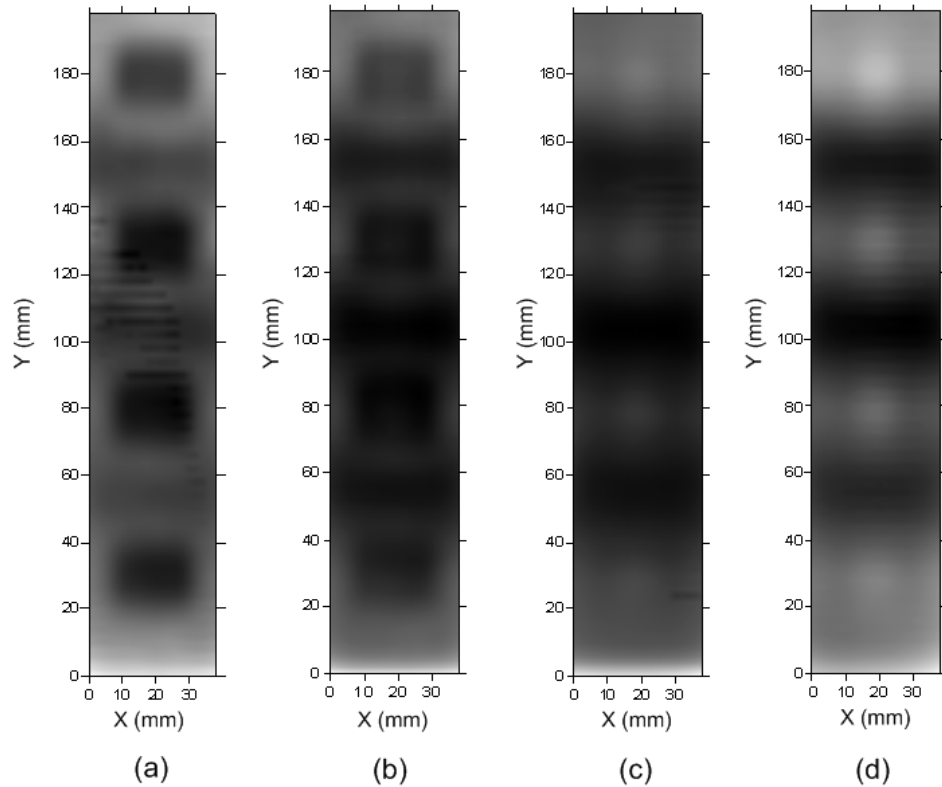
Figure 5.13: *Capacitive images of the Perspex plate, taken with the holes covered by another Perspex plate with thickness (a) 2 mm, (b) 3 mm, (c) 4 mm and (d) 5 mm. The depths of the holes are 15 mm, 11 mm, 7 mm and 3 mm from top to bottom.*

5.5 The effects of grounded substrate under dielectric specimens

In Chapter 4, it was demonstrated by 2D FE models that the grounded substrate under the dielectric specimen will affect the probe responses to specimens with different thicknesses. These effects have been studied experimentally. The specimen was a 5 mm thick Perspex plate with a conical hole (3 mm deep, aperture diameter 10 mm). The 20 mm by 10 mm back-to-back CI probe (a scaled-down version of the back-to-back triangular probe shown in Figure 3.13(a)) was used and maintained at a 1 mm lift-off distance for all the scans. The side with the hole was firstly examined. The Perspex plate was blocked up with a 50 mm air gap under the plate in the targeting area, and the resultant image is shown in Figure 5.14(a). The Perspex plate was then place above a grounded substrate and the same area was scanned, as shown in Figure 5.14(b). The hole was detected in both of cases and no significant differences can be observed. That is because the surface feature modulated the dominant part of the

probing electric field (electric field near the probe surface where the electric lines are more dense), and the effects of the grounded substrate became less significant.
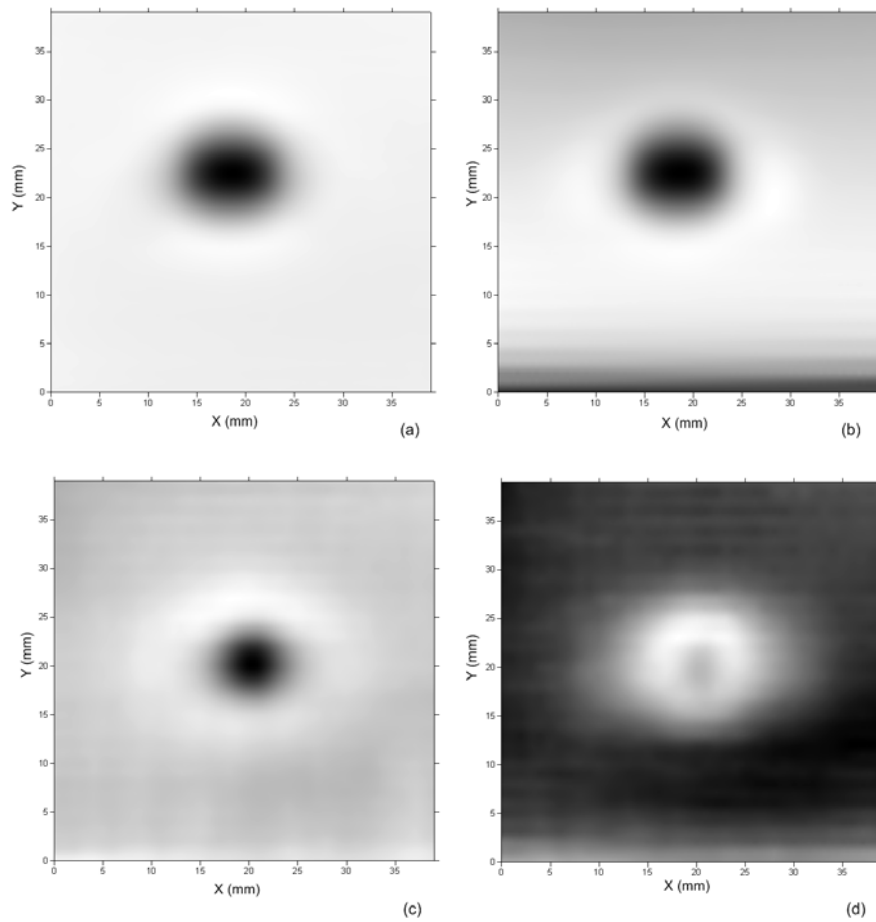
Figure 5.14: *Capacitive images of the Perspex plate taken from the side with the cone-type hole (a) without and (b) with the grounded substrate, and taken from the flat side(c) without and (d) with the grounded substrate.*

The Perspex plate was then imaged from the flat side, both with and without a grounded substrate being in position. The resultant images are shown in Figure 5.14(c) and Figure 5.14(d) respectively. The effects of the grounded substrate can be noticed clearly. In Figure 5.14(c), the hole appeared as a darker shade surrounded by a lighter ring. This is because only the tip part of the cone-typed hole was situated in a region where the sensitivity values are positive (shown as a darker shade in the centre), whereas the other part of the hole was situated in a region where the sensitivity values are negative (shown as the lighter ring). For the case with the grounded substrate, Figure 5.14(d), the outer ring is smaller and brighter, and the inner darker shade is not

141

as obvious as the previous case. Such changes in the image can be explained in terms of probe sensitivity distributions, as the grounded substrate can drag electric lines towards it and change the sensitivity distribution of the CI probe. In this particular case, when the grounded substrate was placed under the plate, the "critical distance" decreased and a bigger part of the cone-type hole was situated in a region of negative sensitivity.

It may seem like the grounded substrate is not particularly beneficial in the above - this is because the plate is relatively thin, and the defects crossed both positive and negative sensitivity value regions. For a deeper buried defect, where the whole defect is in a negative sensitivity region, the advantage of using a grounded substrate would be more obvious. Another scan of the thick Perspex plate with four holes shown in Figure 5.4 from the flat face was thus performed to demonstrate this advantage. Here, the grounded substrate was removed and the specimen was raised up by 50 mm. The resultant image is shown in Figure 5.15(a). The image obtained with grounded substrate added back in is included as Figure 5.15(b) for direct comparison. It can be seen that the contrast is much bigger when the grounded substrate is used.
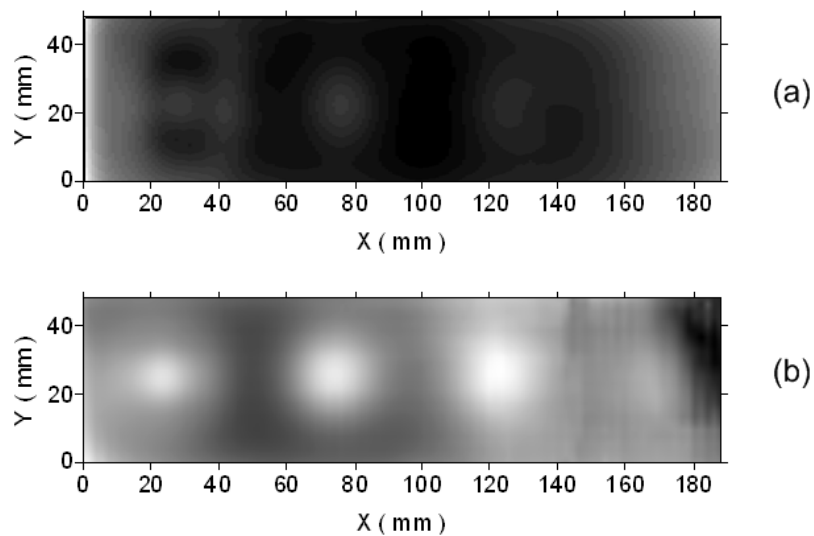
Figure 5.15: *Capacitive images of the Perspex plate containing four flat bottomed holes, taken from the flat side - (a) without and (b) with the grounded substrate. The depths of the holes are 15 mm, 11 mm, 7 mm and 3 mm from left to right.*

5.6 The effects of electrical conditions of conducting specimens

As mentioned in Chapter 2, the equivalent circuit diagrams are different with the specimens being floating or grounded. In principle, when the CI probe is brought near a conductor, free electrons in the conductors are attracted (by the positive charges on driving electrode) to the surface near the probe. For a floating conductor, positive charges are repelled to the opposite surface, while for a grounded conductor the positive charges flow through the connection to ground and the conductor has a net negative charge. In practical application, the potential for errors from a floating specimen is when the specimen is very small or is a significant distance from any other grounded object (*i.e.* it has a small capacitance to ground). A set of experiments were performed to study the effects of electrical conditions of conducting specimens. The steel specimen shown in Figure 5.8 was examined. Firstly, it was supported on a 30 mm thick Perspex plate so it was kept electrically isolated as a floating conductor. The 40 mm by 20 mm back-to-back triangular CI probe was kept at a 1 mm lift-off distance and scanned over the face with the four holes. The results are shown in Figure 5.16(a) with the intensity plot shown of the left and contour plot shown on the right. The four holes appeared as butterfly patterns in the plots.
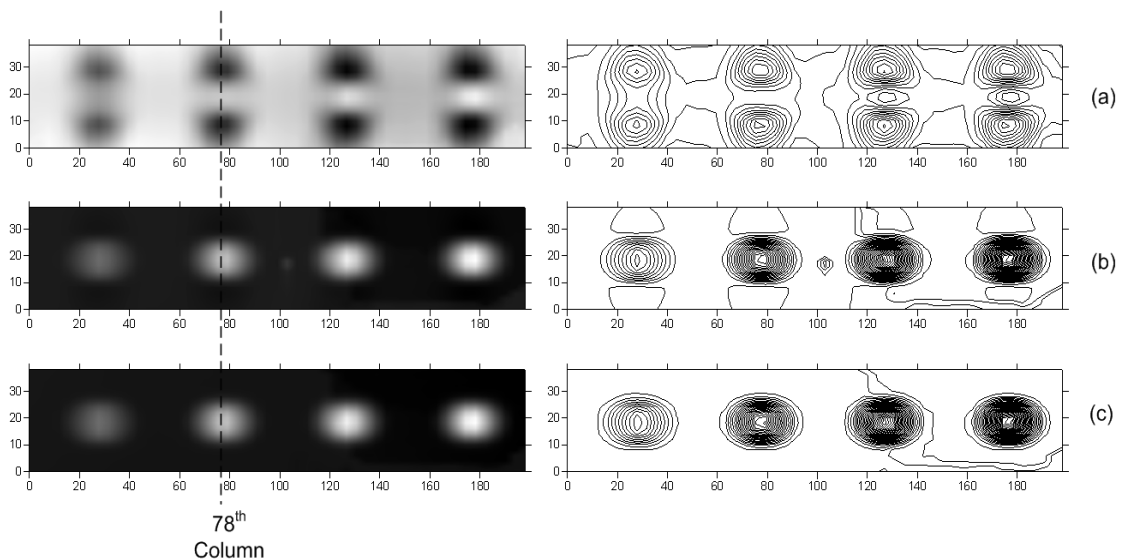
Figure 5.16: *Capacitive images of the steel plate containing flat bottomed circular holes with the specimen (a) floating (b) connected to a second floating conductor and (c) grounded. The of depth of the holes are 2 mm, 4 mm, 6 mm and 8 mm from left to right.*

143

A line scan along the middle line of the second hole (78th column of the image) is plotted in Figure 5.17(a) for a clearer view of the pattern. It is difficult to recognise the real shape of the targeting features (circular holes) from the resultant image, although the depths of the holes are related to the intensity values of the valleys and peaks of the butterfly patterns.

The second scan was performed with a similar arrangement and the only difference was that the steel sample was connected to another piece of metal with the same dimension via a conducting wire. Although the two pieces of metal were both isolated from ground, the capacitance between the testing piece and ground was changed. The results are also shown in two formats in Figure 5.16(b). Compared to Figure 5.16(a), it can be seen from the contour plot that, the valleys were suppressed to a great extent (only one contour line on each side and the valley can hardly be seen from the intensity plot) and the real shape of the features is noticeable. The 78th column was again plotted in Figure 5.17(b), and the dominant feature in the line plot is the peak although small valleys still exist on both sides of the peak. The third scan was performed with the steel sample explicitly grounded. The results are shown in two formats in Figure 5.16(c). Compared to Figure 5.16(a) and (b), it can be seen from the contour plot that, the valleys were suppressed completely (no contour lines on either side of the peak). The 78th column was again plotted in Figure 5.17(c), and it can be seen that the extended lines on both side of the peak are flat.
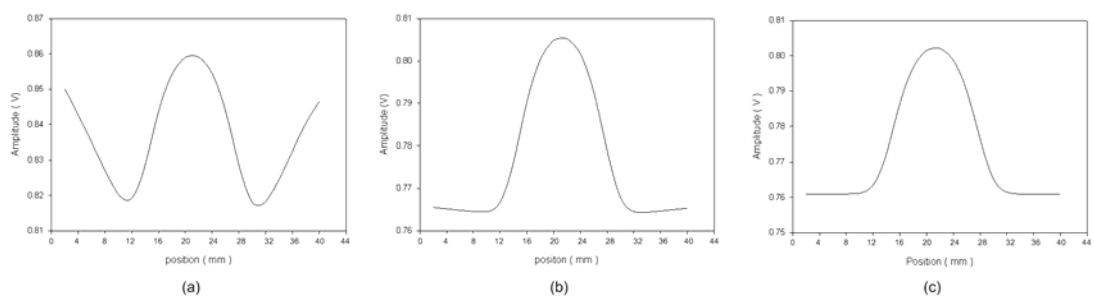
Figure 5.17: *Line plots along the centre of the middle hole with the specimen (a) floating (b) connected to a second floating conductor and (c) grounded.*

For floating conductors, uncertainties were evident. It can be seen from the two line scans in Figure 5.17(a) and (b) that the shapes of the line (especially the valleys on both sides of the peak) vary. Connection to a second floating conductor changed the

144

capacitance between the targeting specimen and the ground. This change could also be achieved by many other situations, such as a nearby ground potential. In addition, the floating conductor can sometimes work as an antenna and make the measurement easily disturbed by ambient electric field. Therefore, for conducting specimen inspections, it is preferable that the specimen is grounded.

5.7 The effects of CI probe geometries

The experiment on the floating steel sample was repeated using a point-to-point triangular CI probe (shown in Figure 3.13(b)) with other arrangements remained unchanged and the results are shown in Figure 5.18. Compared to Figure 5.16(a), the butterfly patterns are different from the ones obtained from the back-to-back CI probe, suggesting a significant influence of probe geometry on resultant images.
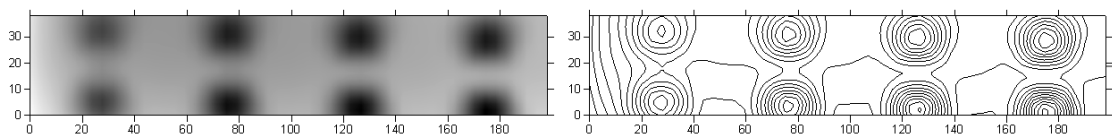
Figure 5.18: *Capacitive image of the steel plate containing flat bottomed circular holes obtained by the point-to-point triangular probe with the specimen floating. The depth of the holes are 2 mm, 4 mm, 6 mm and 8 mm from left to right.*

The effects of probe geometry on obtained images were then studied systematically. The first sample examined was the Perspex plate shown in Figure 5.4. The face with four holes was scanned by the back-to-back triangular probe (shown in Figure 3.13(a)), the point-to-point triangular probe (shown in Figure 3.13(b)) and the concentric probe (shown in Figure 3.15). The scans were 40 mm by 200 mm, and the CI probes were maintained to be 1 mm off the surface. The images are shown in Figure 5.19(a), (b) and (c) respectively, and the probe orientations relative to the corresponding images are also indicated. The three probes responded to the same feature differently. With the same sensing area, the results from the back-to-back probe and the point-to-point probe can be compared directly. In Figure 5.19(a), the darker areas look sharper and are closer in size to the actual holes, while in Figure 5.19(b), the darker areas seem elongated along the long symmetry axis of the probe. For the concentric probe, the holes were detected but the shape of the feature is not

145

recognisable, because the sensing area of the concentric probe is bigger than the symmetric ones, and as a result a bigger area than the targeting features was sampled for each scan step. It is also worth mentioning that, the images obtained from the concentric probe with the inner disc as the driving electrode and the outer ring as the driving electrode were identical.
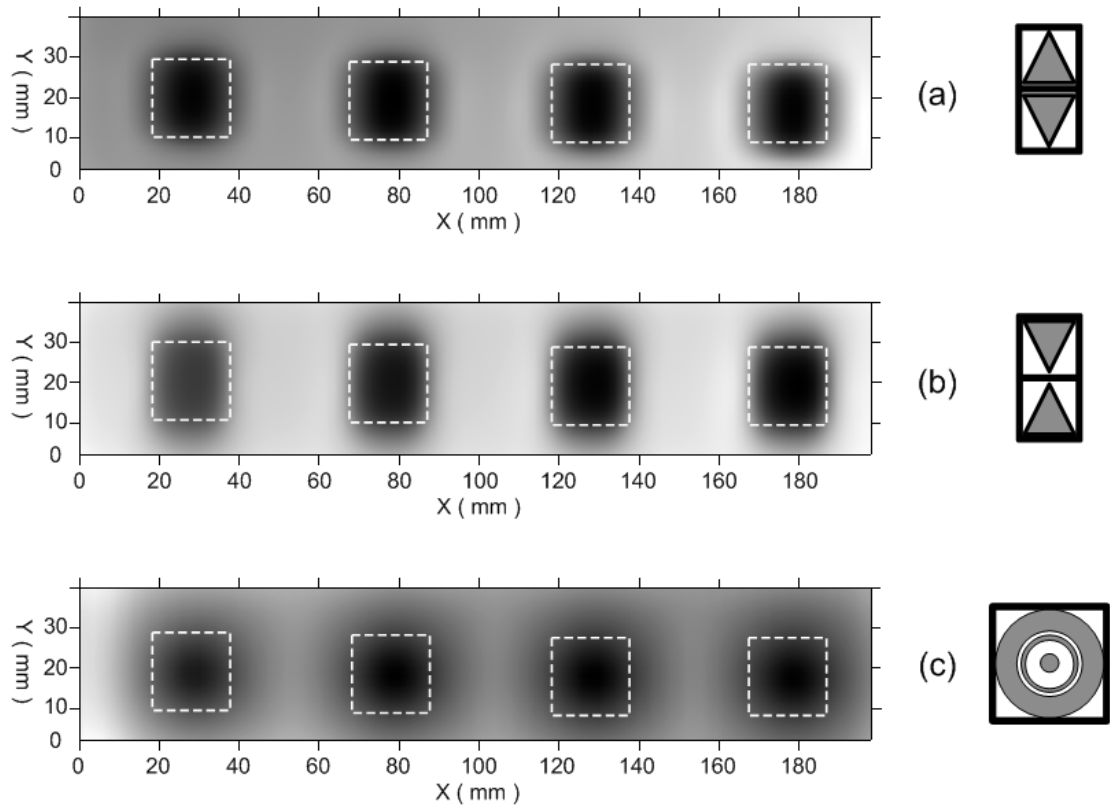
Figure 5.19: *Capacitive images of the Perspex plate, obtained from (a) the back-to-back triangular CI probe (b) the point-to-point triangular CI probe and (c) the concentric CI probe. The depths of the holes are 15 mm, 11 mm, 7 mm and 3 mm from right to left (The size and position of the holes were highlighted).*

The second sample was the aluminium plate shown in Figure 5.6. The face with four holes was scanned by the back-to-back triangular probe, the point-to-point triangular probe and the concentric probe. The scans were 40 mm by 200 mm, and the CI probes were maintained to be 1 mm off the surface. During this set of scans, the aluminium plate was grounded. The images are shown in Figure 5.20(a), (b) and (c) respectively, and the probe orientations relative to the corresponding images are also indicated. Again, the three probes responded to the same feature on a grounded conducting

specimen differently. In Figure 5.20(b), the lighter areas look sharper in and are closer in size to the actual holes, while in Figure 5.20(a), the light areas seem elongated along the short symmetry axis of the probe. It is interesting to note that for the concentric probe, the presence of the holes were detected but as darker discs surrounded by lighter rings, and the depth information can be obtained from the different intensity contrasts of the patterns.
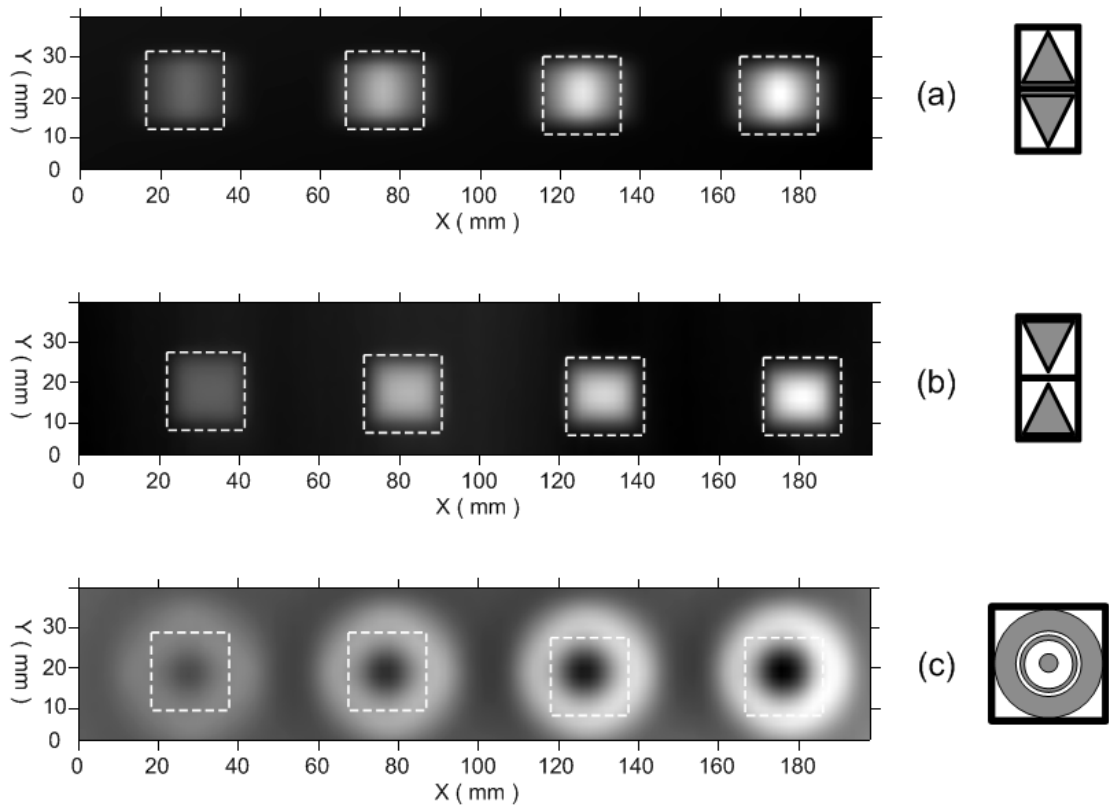
Figure 5.20: *Capacitive images of the aluminium plate, obtained from (a) the back-to-back triangular CI probe (b) the point-to-point triangular CI probe and (c) the concentric CI probe. The depths of the holes are 2 mm, 4 mm, 6 mm and 8 mm from left to right (The size and position of the holes were highlighted).*

The results obtained using the back-to-back triangular probe and point-to-point triangular probe demonstrated that one of the conclusions obtained from FE models in chapter 4 was verified experimentally - that the back-to-back triangular probe is advantageous on dielectric specimens and point-to-point triangular probe is advantageous on conducting specimens. It is also worth noting that the two symmetric probes are directional in the above mentioned scans as the square holes were

147

elongated along one of the symmetry axes of the probes, which suggests that when imaging narrow grooves or cracks a symmetric probe would respond differently with the short symmetry axis being parallel or perpendicular with the targeting feature.

Another variable that might affect image resolution is the size of the electrodes. Thus, the same Perspex plate shown in Figure 5.4 was scanned with two back-to-back triangular probes with different sizes. The results are shown in Figure 5.21. As expected, the larger probe size caused the image resolution to decrease, because of spatial averaging across the probe aperture.
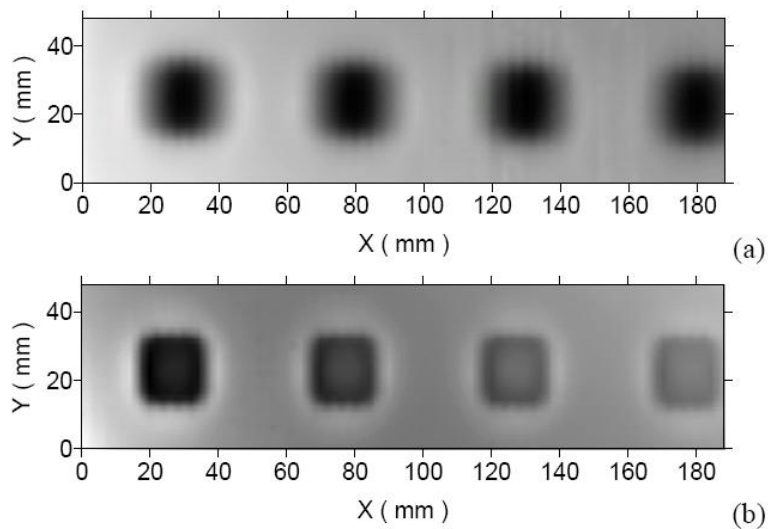
Figure 5.21: *Capacitive scan images obtained of the Perspex sample from back-to-back triangular electrodes of size (a) 40 mm by 20 mm and (b) 20 mm by 10mm. The depths of the holes are 15 mm, 11 mm, 7 mm and 3 mm from left to right.*

5.8   The effects of lift-off distance

The effects of lift-off distance were now examined for the Perspex plate shown in Figure 5.4, with the 40 mm by 200 mm scans above the surface being performed at distances of 1 mm, 3 mm, 5 mm and 7 mm in air. The results are shown in Figure 5.22. It is evident that, as expected, the resolution of the image decreases as the capacitive electrode is moved further away from the sample surface. Note that, for the image obtained with a 7 mm air gap, the holes were detected and appeared as lighter areas in the image. This is caused by the negative sensitivity values at this distance.
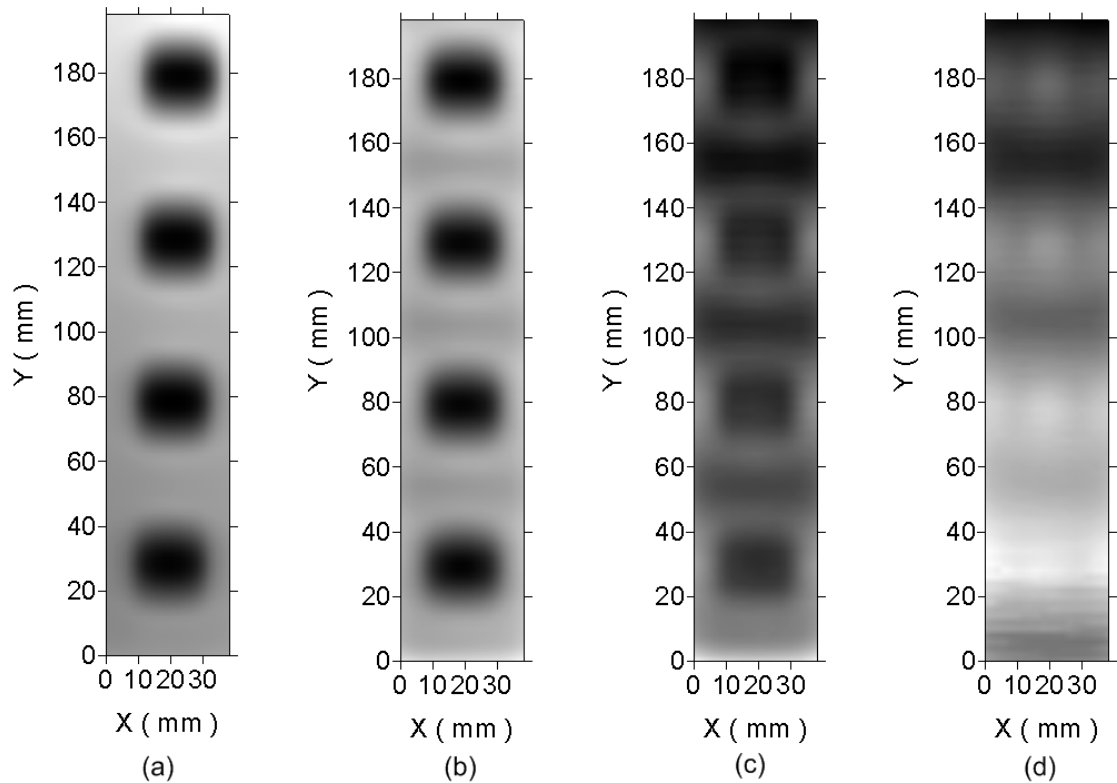
Figure 5.22: *Capacitive images of the Perspex plate, taken at stand-off distances of (a) 1 mm, (b) 3 mm, (c) 5 mm and (d) 7 mm. The scan was performed at the surface containing the flat-bottomed holes.*

The lift-off experiments were also performed on the steel sample shown in Figure 5.8. In this case, measurements were taken at distances of 1 mm, 3 mm, 5 mm, 7 mm, 9 mm, 11 mm and 13 mm in air. The resultant images obtained with the steel plate electrically grounded, are shown in Figure 5.23, and again indicate that the resolution is better at closer distances to the sample. The experiments were then repeated with the steel sample being floating, and the results are shown in Figure 5.24. Now, as expected with a floating conductor, some interesting features appear, involving changes in spatial shape. Thus, for instance, a butterfly pattern is seen when the lift-off distance is less than 5 mm. At a larger stand-off distance of 5 mm, as shown in Figure 5.24(c), the circular shape is shown and signal over the hole is decreasing with the increasing lift-offs. It is worth noting that, for the two sets of experiments on a conducting specimen, even for a 13 mm air gap, the holes on the surface are still detected as lighter areas (increased signal over the holes) indicating that in such cases the sensitivity values are positive at a 13 mm lift-off - a bigger value than in Perspex.

149
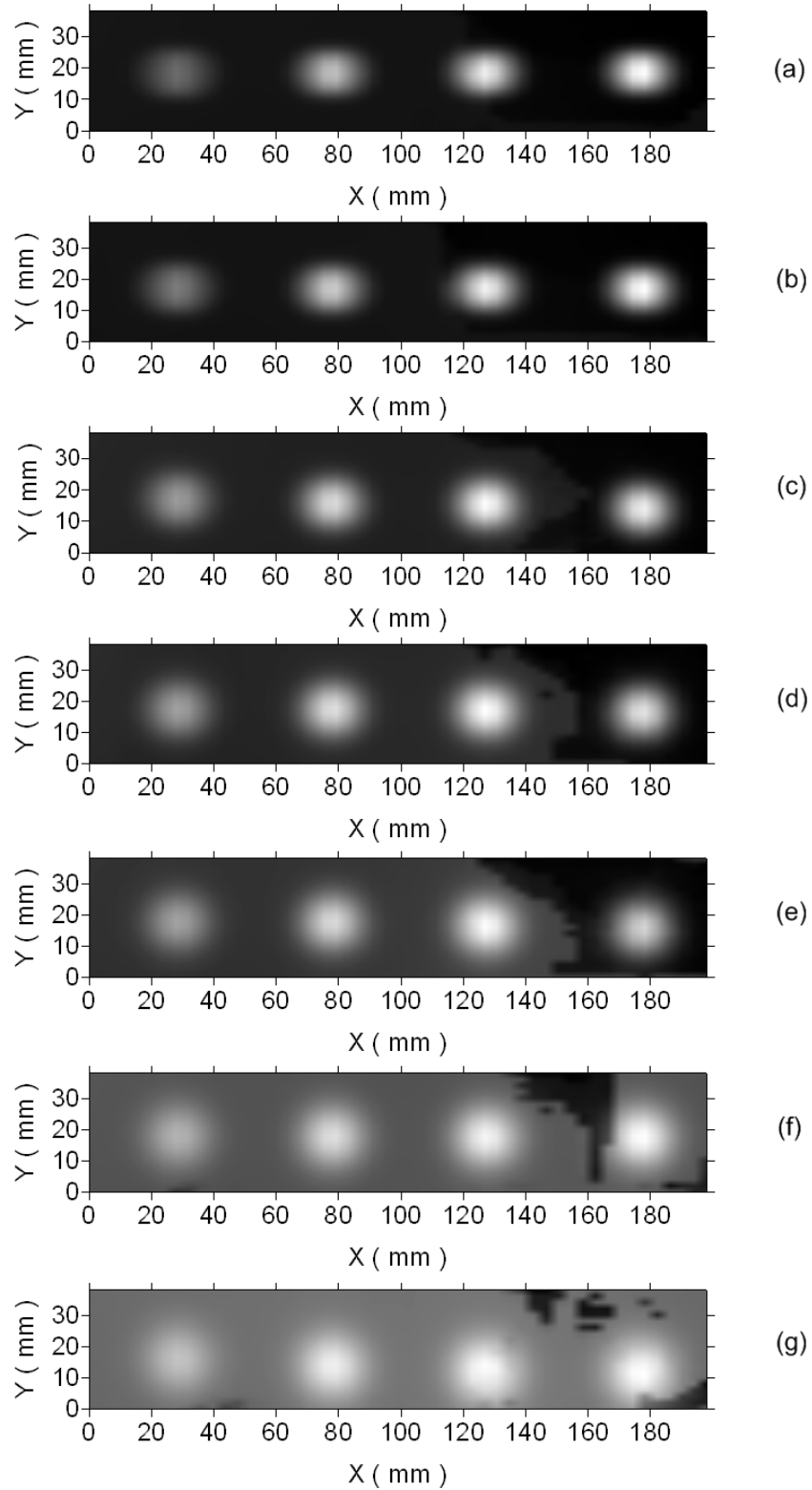
Figure 5.23: *Capacitive images of the steel plate(grounded), taken at stand-off distances of (a) 1 mm, (b) 3 mm, (c) 5 mm, (d) 7 mm, (e) 9 mm, (f) 11 mm, and (g) 13 mm. The scan was performed at the surface containing the flat-bottomed holes.*
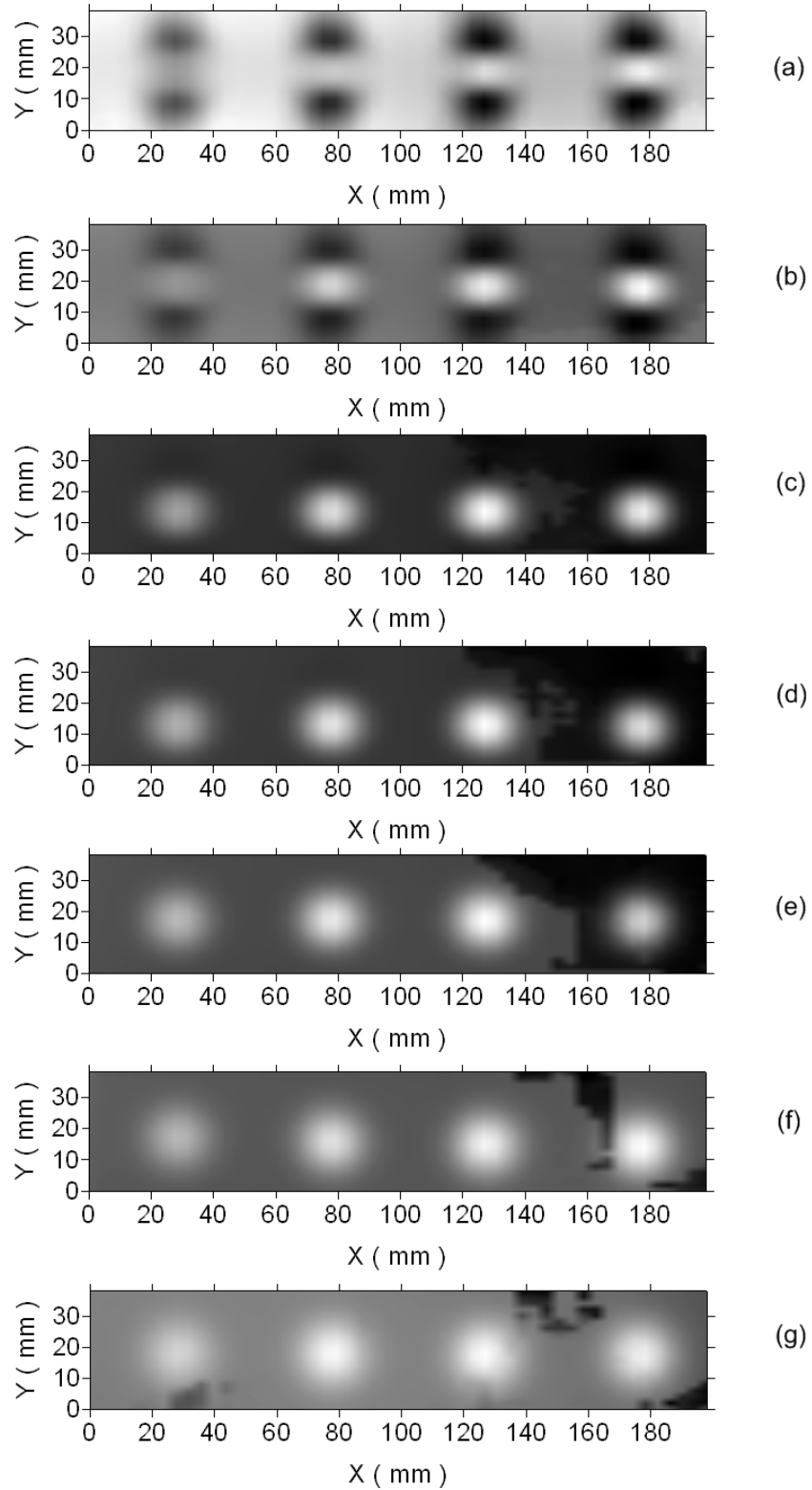
Figure 5.24: *Capacitive images of the steel plate(floating), taken at stand-off distances of (a) 1 mm, (b) 3 mm, (c) 5 mm, (d) 7 mm, (e) 9 mm, (f) 11 mm, and (g) 13 mm. The scan was performed at the surface containing the flat-bottomed holes.*

5.9 Imaging surface features on metal through insulation

The lift-off experiments on metals provided indications that the CI technique is capable of detecting surface features on metal through a significant air gap. In practice, the targeting surface features (e.g., corrosion, pitting) are sometimes hidden under an insulation layer. It was thus thought interesting to embark on a study of how well capacitive imaging could detect the surface features through insulation.

A capacitive imaging scan was performed over a 200 mm by 40 mm scan area on the aluminium sample (shown in Figure 5.6), with the probe assembly maintained at a constant air gap of 6 mm from the surface containing the holes. The aluminium plate was kept grounded during the scan. The resultant image is shown in Figure 5.25(a). The holes are clearly imaged and the depth of hole is related to the intensity of the image, as in the previous cases. The scan was then repeated with the surface coated with a 5 mm layer of insulating foam, and there was a 1 mm lift-off between the probe and the foam. Note now that the resolution of the image has decreased, because of the presence of the foam, but the holes were still detected, with again the detected amplitude being a function of hole depth. This gives encouragement for the detection of surface features in metals under coatings of insulation.
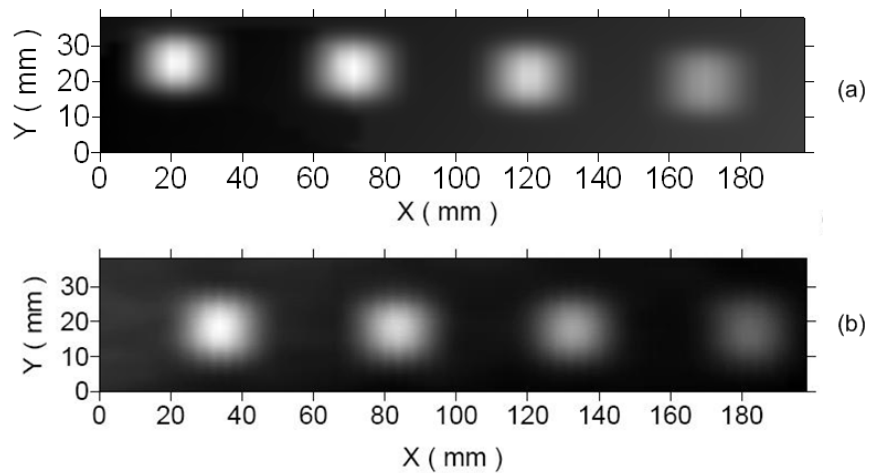
Figure 5.25: *Capacitive images of the aluminium plate containing flat bottomed holes of depth (from left to right) 8 mm, 6 mm, 4 mm and 2 mm. (a) Image obtained for a 6 mm air gap between electrodes and the surface, and (b) result with a 5mm layer of insulating foam between the electrodes and the metal surface.*

152

Further experiments were carried out to explore the ability of CI technique on imaging surface features on metal through insulation. A piece of high density extruded polystyrene (Styrofoam®, relative permittivity value ε_r= 2.5) was machined into a plate with stepped thickness (10 mm, 15 mm, 20 mm and 25 mm) as demonstrated in Figure 5.26(a). The polystyrene plate was placed above the same aluminium plate used in the previous experiments as shown in Figure 5.26(b), to simulate different thickness of insulation coating. Only the 2mm deep hole in the aluminium sample was covered by the plate and examined in this case. 4 line scans were performed over the 2mm deep hole with the thickness of the polystyrene plate changing from 10 mm to 25 mm in turn, and the scan direction is indicated by the arrows, as shown in Figure 5.26(b). The results (line scans of 50 points each) were obtained using the 40 mm by 20mm back-to-back triangular probe with a minimal stand-off between the probe and the polystyrene plate. All the four results were obtained with the aluminium sample grounded.
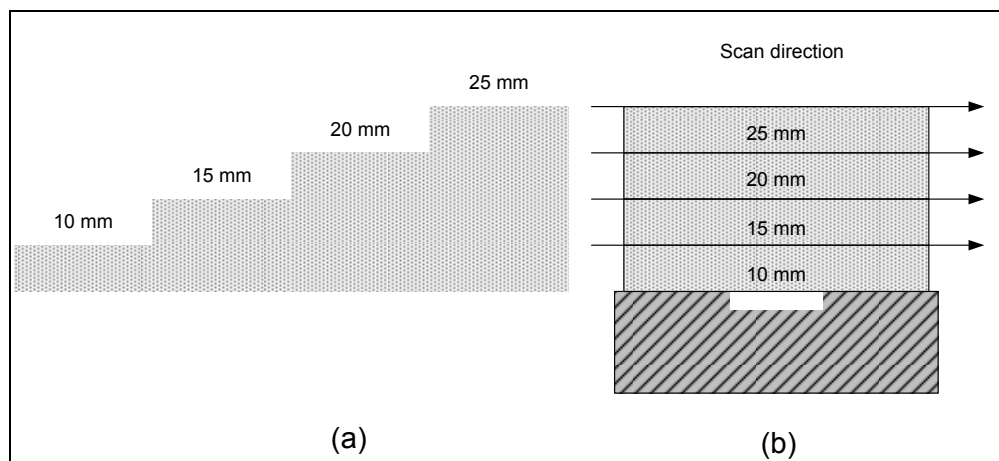
Figure 5.26: *Schematic diagram of (a) a high density extruded polystyrene plate with stepped thickness and (b) sample assembly and scan direction (cross-section view).*

The results are presented in Figure 5.27 with the same scale. It can be seen that each of the four results has a bump in the middle, indicating the successful detection of the hole through the insulation coating of different thicknesses. Comparing the four plots, it can be seen that the height of the bump drops and the width of the bump increases while the coating thickness increases, which suggests an image with lower resolution could be formed by performing a 2D scan. The fact that the 40 mm by 20 mm back-to-back triangular probe could be used to detect surface feature through a 25mm thick

insulation coating indicates the capacitive imaging probe is sensitive to the surface contours on a metal sample even if measured from a big lift-off distance and/or with a thick insulation layer between the probe and metal surface.
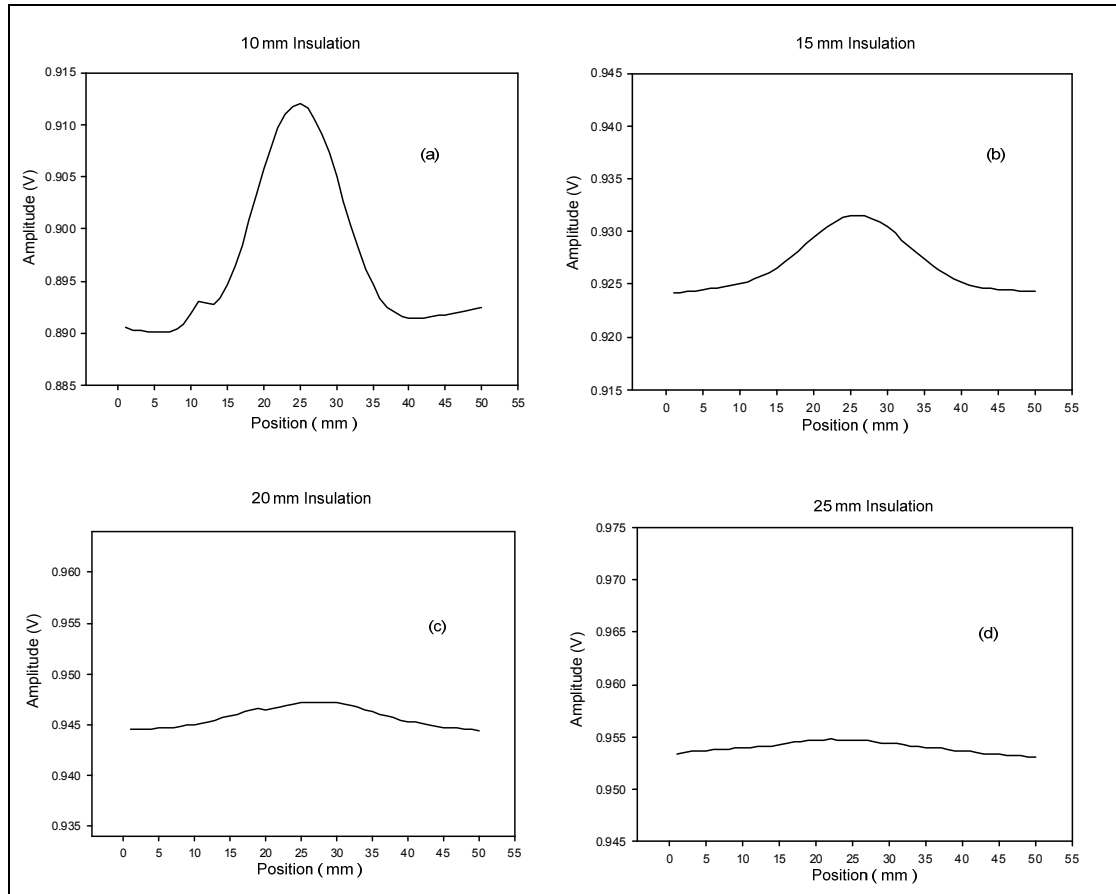
Figure 5.27: *Line scan plots with the machined hole covered by different thicknesses of the polystyrene plate (a) 10mm (b) 15mm (c) 20 mm and (d) 25 mm.*

5.10 Imaging defects of smaller size compared to the CI probe

The above mentioned parameters that can affect the imaging results were studied from the experiments in which the targeting features are comparable in size with the CI probes. It is thus worth investigating the way CI probes responding to features much smaller than their sizes. Experiments were performed to study the probe response to features of smaller size compared to the sensing areas of the CI probes. The CI probes with back-to-back triangular electrodes were used in these experiments.

The first sample was a 25 mm thick Perspex plate. The plate contains six 15 mm deep circular holes of different diameters (ranging from 1-3.5 mm). The 40 mm by 20 mm back-to-back triangular CI probe and the 20 by 10 mm back-to-back triangular CI probe were each scanned over the surface containing the holes with the probes maintained at 1 mm lift-off. The results are shown in Figure 5.28. And the areas for the thinnest hole (highlighted by the dashed boxes in the images) were enlarged as contour plots. The orientation of the probes relative to the images is also indicated. As expected, the bigger probe has a higher degree of spreading of the holes. And from the enlarged contours plots, it can be seen that the thinnest hole is shown clearly in the image obtained by the smaller probe while it only appeared as protuberances of the contour lines in the image obtained by the bigger probe.

It is also worth noting from the results, especially from the results obtained from the 40 mm by 20 mm probe, shown in Figure 5.28(a), the images of the holes were elongated along the short axis of symmetry of the probe to approximately 10 mm (half length of the triangle's back). While along the long axis of symmetry, the images were spread to approximately 4 mm (the distance separating the parallel adjacent edges of the triangles). This provided an indication of the imaging resolutions in both directions of the back-to-back triangular CI probe on non-conducting specimens.
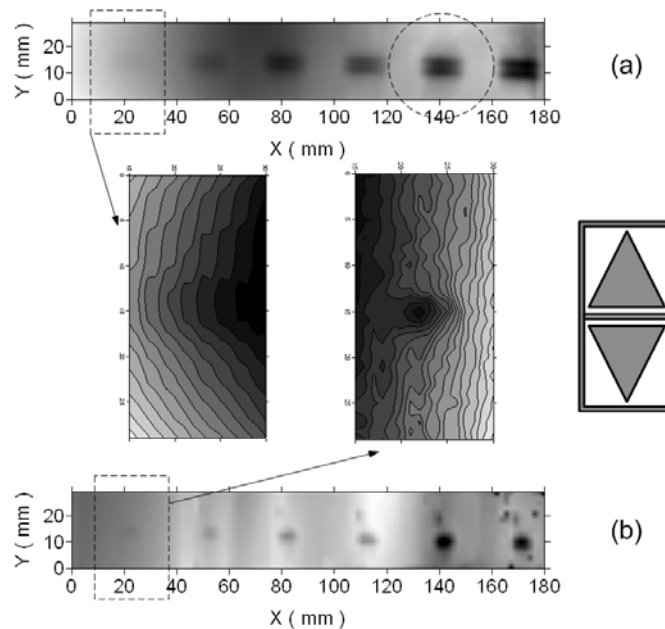
Figure 5.28: *Capacitive images obtained of the Perspex sample with thin holes, using back-to-back triangular probes of size (a) 40 mm by 20 mm and (b) 20 mm by 10mm.*

155

The area highlighted by a circle in Figure 5.28(a), an image of the 3 mm diameter hole, was now studied in more detail. The results obtained from this selected area can be considered as essentially the sensitivity distribution, as it is almost the same process as was used in deriving the equations for sensitivity distribution in Chapter 4. The only difference is that, in the model, the perturbation is of higher permittivity value than its ambient material, while in the experiment the perturbation is air which has a lower permittivity value than Perspex. To make a direct comparison, the effect of perturbation with lower permittivity was reversed. The results are shown in Figure 5.29(a) as an intensity plot (left) and as a 3D plot (right). These results are in good agreement with the results from the FE models, shown in Figure 5.29(b).
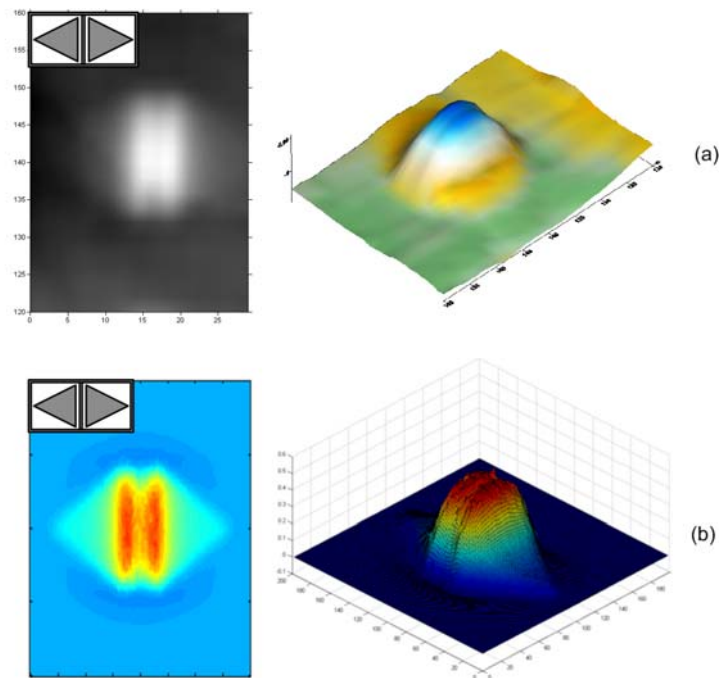
Figure 5.29: *(a) The capacitive image of a hole (3 mm in diameter) on a Perspex plate and (b) the calculated sensitivity distribution.*

A second sample was now studied in the form of a 20 mm thick aluminium plate with a 15 mm deep, 3 mm diameter hole drilled into the surface. The 40 mm by 20 mm back-to-back triangular probe was scanned over a 40 mm by 20 mm area, at a lift-off distance of 1 mm. The scan was repeated three times with the aluminium plate electrically floating, connecting to another floating metal object via a conducting wire and grounded. The resultant images are shown in Figure 5.30. As expected, the probe responded differently with different conditions of the aluminium sample. The hole on

the floating conductor produced an image in which the two metal electrodes of the probe can be recognized, as shown in Figure 5.30(a). This explains why the square holes on the floating aluminium appeared as butterfly patterns in capacitive images and why the patterns are different when obtained from back-to-back or point-to-point triangular probes. A similar result was obtained on connection to another floating metal, but the dark triangular areas in the image that represented the electrodes were less clear, as shown in Figure 5.30(b).
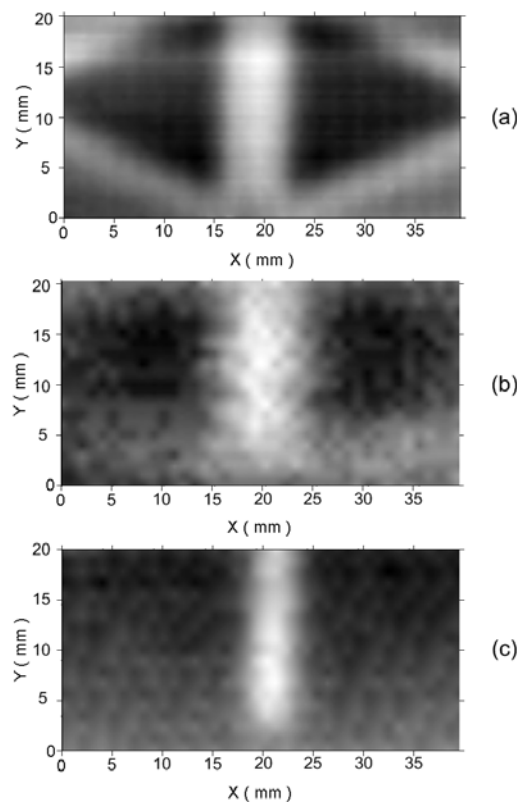
Figure 5.30: *Capacitive images of a hole (3 mm in diameter) on an aluminium plate with the plate (a) floating (b) connected to a second floating conductor and (c) grounded.*

In the case of the grounded plate, Figure 5.30(c), the dominant feature in the image is the lighter strip. Again, this corresponded to the sensitivity distribution of the back-to-back triangular probe in the plane 1 mm below the probe surface. The result shown in Figure 5.30(c) is in good agreement with the result obtained earlier from FE models (shown in Figure 4.38(c)).

Encouraged by the results from small holes in the Perspex and aluminium plates, a second set of experiments was performed. This time, instead of using air filled holes as perturbations, thin testing rods were used, aiming to measure the sensitivity distribution of the CI probe by introducing perturbations with higher permittivity or conductivity values. The first testing rod was a Perspex rod (15 mm long and 3 mm in diameter). The 40 mm by 20 mm back-to-back triangular probe was scanned over a 30 mm by 60 mm area in a plane 1 mm off the tip of the rod. And the result is presented as an intensity plot and a contour plot in Figure 5.31. The probe orientation relative to the image is also indicated in the intensity plot. It can be seen that the rod was detected as an elliptical pattern with high intensity values.

(a)   (b)
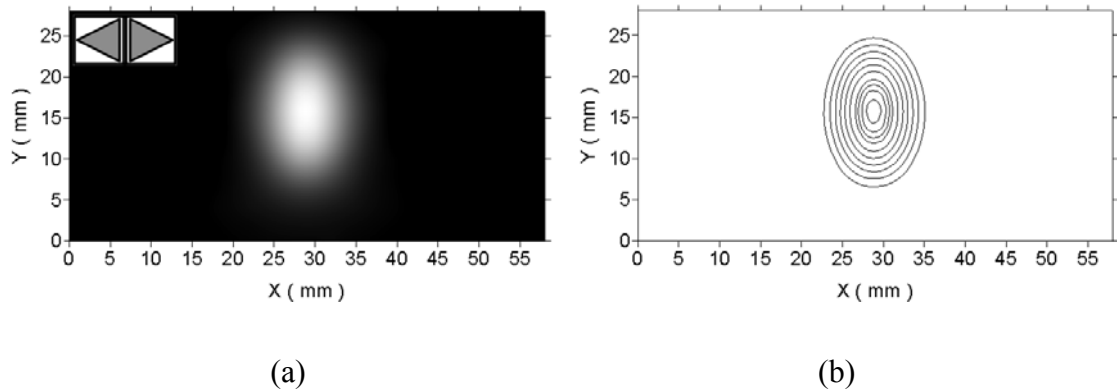
Figure 5.31: *The capacitive image of a Perspex rod. (a) Intensity plot and (b) contour plot.*

The second testing rod was a steel rod (15 mm long and 3 mm in diameter). The 40 mm by 20 mm back-to-back triangular probe was scanned over a 30 mm by 60 mm area in a plane 1 mm off the tip of the rod. The scan was performed twice, firstly with the steel rod being grounded and then floating. The results are shown in Figure 5.30 and as expected the probe responded differently for the two cases. The grounded rod appeared as a circular pattern with low intensity values, and the inner few contour lines were elliptical as in the Perspex case, as shown in figure 5.32(a). The floating rod also appeared as an elliptical pattern as in the Perspex case, but with low intensity values and a higher slope gradient (the contour lines are denser), in addition there were brighter areas on both sides of the darker shade as indicated more clearly by the outer few contour lines protruding towards the middle, as shown in Figure 5.32(b).
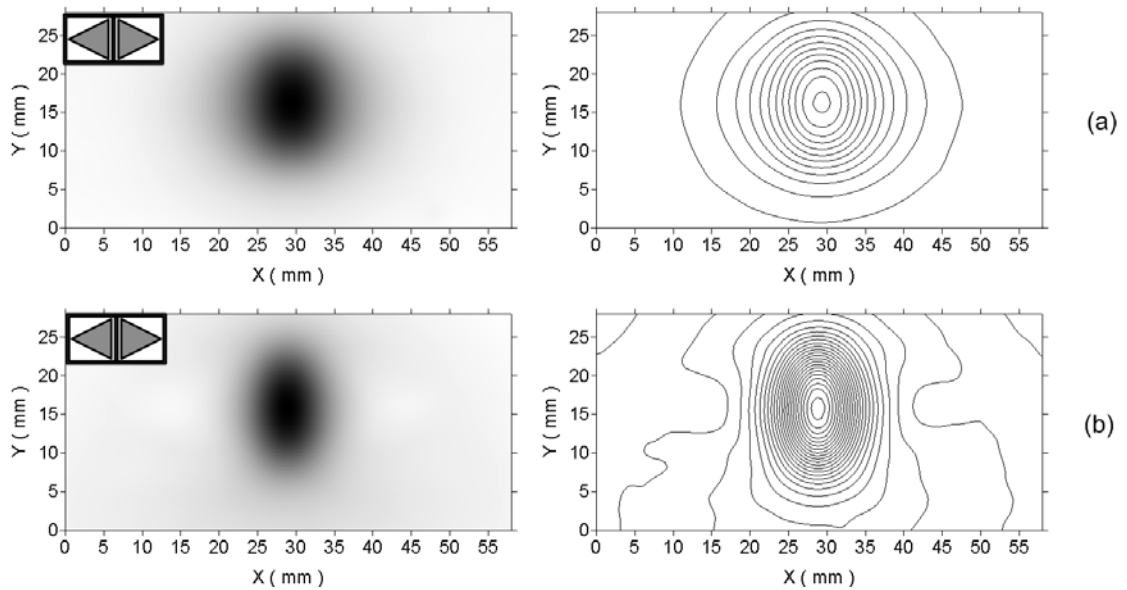
Figure 5.32: *Capacitive image of a Steel rod with the rod: (a) grounded and (b) floating.*

With the same dimension as the air filled holes in the Perspex and aluminium plates, the results obtained from the testing rods are not as well-defined as the ones from the holes. The explanation is that the whole length of the rods took part in the measurements and the sensitivity distributions in different planes were superposed together, while for the holes, only the apertures were effective in the scans. This explanation suggests that the CI probes are less sensitive to the depth information for smaller holes/cracks. This is experimentally confirmed by imaging an aluminium plate with 4 narrow cracks (1mm wide) of different depths (10 mm, 15 mm, 20 mm and 25 mm). The 20 mm by 10 mm back-to-back triangular probe was scanned over a 20 mm by 180 mm area in a plane 1 mm above the plate. The plate was grounded during the scan.

The results are shown in Figure 5.33. The four cracks were detected as four lighter strips in the intensity plot (Figure 5.31(a)) but the depth information cannot be obtained as can be seen from the 3D plot (Figure 5.31(b)) that the four bumps are of similar height.
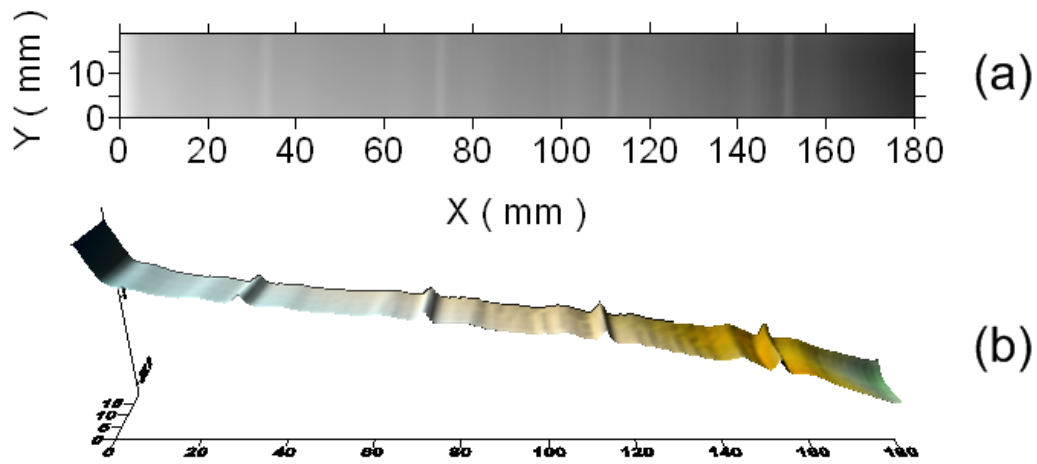
Figure 5.33: *Capacitive images of the aluminium plate containing four narrow cracks.*
(a) Intensity plot and (b) 3D plot.

It will be evident from the above experiments that if a targeting feature is larger than the CI probe, the image obtained by the probe will be a good representation of the defect. However, if the dimensions of the features of interest are smaller than the probe, the resultant image of the feature is not only spread out, but its shape is transformed by the spatial variation of the sensitivity distribution of the CI probe.

To help understanding this, it is appropriate to bring in the concept of "point spread function (PSF)". For an imaging system, the PSF describes the response of the system to a point source or object, and the degree of spreading of the point object is a measure for the quality of the system. For an optical imaging system, if the PSF is available, the quality of an image can be significantly improved by digital deconvolution with the (two-dimensional) point spread function (PSF) of the imaging system [2]. From the discussions in Chapter 4 and the results show in this section, it can be concluded that the calculated sensitivity distribution of a given CI probe can be regarded as the PSF of the CI system. However, it is more complicated to process capacitive images compared to optical ones. The reasons are two-fold. Firstly, the PSF (sensitivity distribution) for a given CI probe varies with different specimens and different testing conditions; also, the sensitivity distributions of the CI probes and the targeting features are both in 3D. Therefore, more than one PSF (sensitivity distributions in different planes), or a 3D deconvolution, may be required.

One practical way round this, when imaging features much smaller than the size of the overall sensing area, is to perform the scan twice with the probe in orthogonal alignment; a final image can then be obtained by combining the two results from the two scans with a thresholding algorithm. Note that, this method is applicable to any CI scans using symmetric CI probes, depending on the different requirements, but is not suitable for concentric probe designs.

5.11 Discussions and conclusions

In this chapter, the validity of the CI technique has been assessed in detail and parameter studies have also been performed to investigate their effects on the resultant capacitive images.

An extensive range of experiments were successfully conducted on various specimens under different conditions using different CI probes. The results of experiments on Perspex, steel, aluminium and carbon fibre composite plates containing machined flat-bottomed holes of various depths gave an indication of the response of the CI approach. In the cases of surface features on both conducting and non conducting specimens, very good surface information was obtained, indicating that the depth of the hole could possibly be determined from such scans. The detection of hidden defects buried at different depths in dielectric specimens was also demonstrated and the results indicated that extra attentions are needed as the hidden defects maybe situated in a negative sensitivity region.

The effects of a grounded substrate on the capacitive images obtained from dielectric specimens were studied. It is also evident that the electrical condition of the conducting specimen can change the capacitive images of the surface features dramatically. CI probes with different geometries were scanned over same specimens to investigate the effects of the probe geometries on capacitive images. In addition, scans with different probe lift-off distances were performed both on a Perspex plate and a steel plate, and the results indicated that a higher resolution image could be obtained with smaller lift-off distances. Surface features on conducting specimens were successfully detected through an insulating covering. This is interesting, as it indicates that the technique may be useful for detecting the presence of pitting caused by corrosion under insulation (CUI). Specimens with smaller defects were scanned,

such scans can be considered as measuring the sensitivity distributions and some of the results are in good agreement with the calculated sensitivity distributions.

On the basis of these results, capacitive imaging would have some specific advantages and benefits if applied to industry. Work has thus been performed to investigate applications of industrial interest (such as corrosion under insulators (CUI), damage in some foam-cored composites, etc.) which are difficult to test with ultrasound due to excessive scattering and attenuation. These are the subject of Chapter 6.

5.12 References

[1]   W. McCarter, G. Starrs, T. Chrisp, and P. Banfill, "Activation energy and conduction in carbon fibre reinforced cement matrices," *Journal of Materials Science,* vol. 42, pp. 2200-2203-2203, 2007.

[2]   G. Dougherty and Z. Kawaf, "The point spread function revisited: image restoration using 2-D deconvolution," *Radiography,* vol. 7, pp. 255-262, 2001.

Chapter 6   Applications of the CI technique to NDE

6.1   Summary

The parameter studies in Chapter 5 have provided an assessment of the practicality of the CI technique. In Sections 6.2 to 6.6 that follow, the CI technique is used as an NDE tool to investigate various samples of industrial interest, including glass fibre laminated composites and sandwich structures, laminated carbon fibre composites, corroded steel plate and other pipework. Section 6.7 then describes a set of preliminary experiments to image buried objects (both conducting and non-conducting) using the CI technique.

6.2   Inspection of laminated glass fibre composites

An increasing amount of glass fibre composite material is being used in aerospace, automotive, architectural and other industrial applications, such as rotor blades of wind-powered devices, radar domes, helmets, pipes, tanks, etc. This is because of their light weight, high strength and excellent corrosion resistance properties. Although the applications of these kinds of composite materials are becoming more extensive, the use of such materials may be accompanied by various types of damage, including foreign material inclusions, delaminations caused by impact or manufacturing imperfections, fibre rupture and cracks. These types of damage can substantially reduce the buckling load capacity and the stiffness, which influence the structure's overall performances [1, 2]. The damage caused by impact *etc* is often either not visible, or is barely visible, to the naked eye, with significant sub-surface damage being present. Therefore, non-destructive evaluation (NDE) techniques for the inspection of these composite materials are required.

Because of the inhomogeneity of composite structures, finding defects in such materials is a challenging task, and many damage detection techniques have been developed to detect defects in composite materials, such as radiography techniques [3-5], ultrasonic scans [6-8], and thermography [9, 10]. In addition, several other

164

techniques, including using microwave [11], and Terahertz (THz) imaging [12], have also been reported.

For glass fibre composites, in spite of the inhomogeneity caused by the innumerable inclusions in filament form and boundary surfaces, the material as a whole is a non-conducting structure, and the presence of damage in the laminated composite plate leads to changes in its dielectric properties. It has been demonstrated in previous chapters that the CI technique is sensitive to such changes, indicating that monitoring the structural integrity of laminated glass fibre composite is a promising application of the CI technique. Research based on capacitance measurements on laminated glass fibre composites for NDE purposes, referred as dielectrometry sensing, is reported elsewhere [1] to detect the presence of delaminations simulated by pre-fabricated slots, but not for imaging applications.

Experiments were conducted on glass fibre composite samples and the experimental arrangement shown earlier in Figure 2.14 was used, with the back-to-back triangular electrodes being scanned over the surface of the composite. The first sample, provided by AIRBUS, was a 2 mm thick laminated glass fibre composite, with a crack (roughly 10 mm long) in the centre, as shown in Figure 6.1. The crack was initiated by external load and the crack area was relatively flat on one side, as shown Figure 6.1(a). The crack was extended through the thickness to the other side of the composite and caused delaminations, as can be seen from Figure 6.1(b). Note that, although damage was visible on the surface, sub-surface damage still needed to be quantified.

(a)   (b)
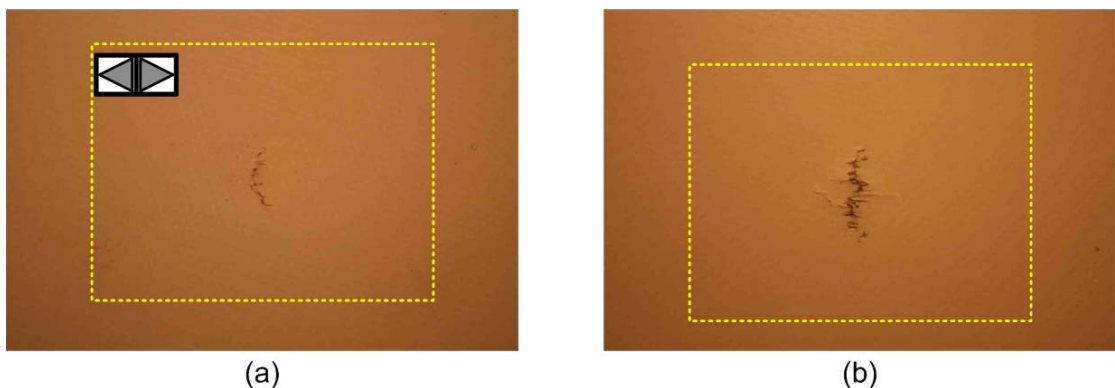
Figure 6.1: *Photographs of the AIRBUS glass fibre sample. (a) Face A, (b) Face B.*

A 20 mm by 10 mm back-to-back triangular CI probe was used at a 1 mm stand-off distance, and the sample placed on a grounded substrate. A 60 mm by 40 mm area, as indicated by the dashed line, was scanned at 1 mm intervals over the surface, with the orientation of the CI probe as illustrated in Figure 6.1(a). The scan was taken from the relatively flat surface, shown in Figure 6.1(a), and the results are shown in Figure 6.2. It can be seen from Figure 6.2 that the extent of delamination within the composite was successfully detected as the darker areas.
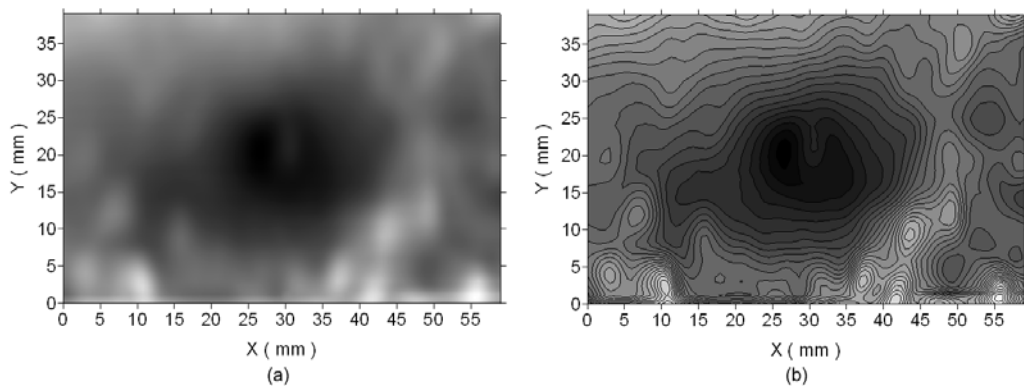
Figure 6.2: *Two representations of the capacitive imaging scan of the Airbus glass fibre sample. (a) Intensity plot and (b) contour plot.*

The second sample investigated was a 5 mm thick EXTREN® pultruded glass-fibre reinforced polymer composite. The specimen was damaged by an impactor with a hemispherical nose. The impact energy was 16 Joules and the impact position is indicated by the red dot (on Face A) shown in Figure 6.3(a). The impact caused internal damage to the panel and the damage extended to Face B, as can be seen from the other side of the panel (Face B) shown in Figure 6.3(b).
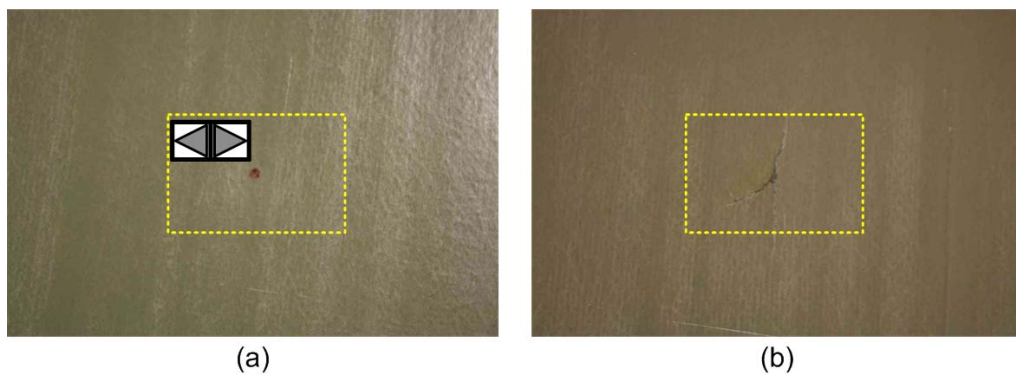
Figure 6.3: *Photographs of the pultruded glass-fibre reinforced polymer composite with impact damage. (a) Face A and (b) Face B.*

The 20 mm by 10 mm back-to-back triangular CI probe was again held 1 mm off the sample surface and a 60 mm by 40 mm area, as indicated by the dashed line, and again scanned over the surface (the orientation of the CI probe is also illustrated in Figure 6.3(a)). The scan was taken from the surface where the impact was applied (as shown in Figure 6.3(a)) and the results are shown in Figure 6.4. It can be seen from Figure 6.4 that the damage extended under the surface, and was successfully detected as the darker areas shown in the plots.
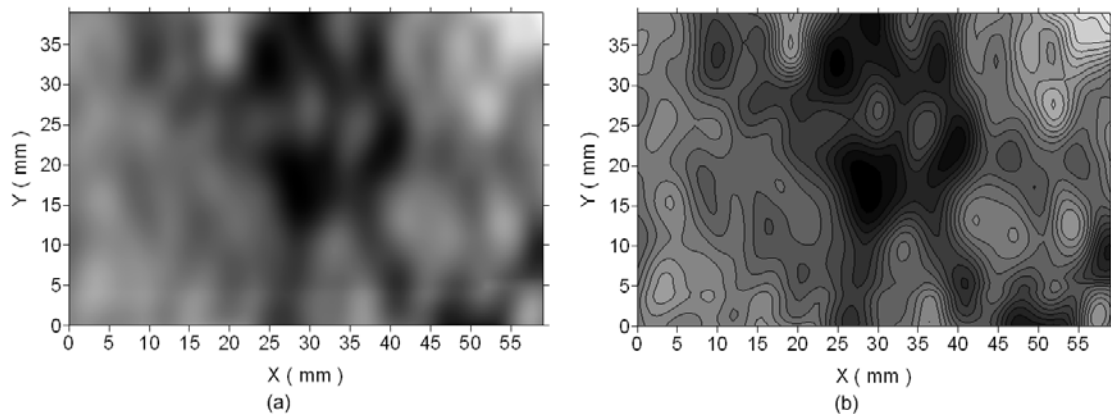
Figure 6.4: *Two representations of the capacitive imaging scan of the glass fibre sample with impact damage. (a) Intensity plot and (b) contour plot.*

6.3   Inspection of glass fibre sandwich structures

In addition to the solid laminated glass fibre composites, bonded sandwich structures are another category of advanced composite materials and have a wide range of applications in the aviation, marine and sports industries. A sandwich structure consists of three main parts: two faces of thin, strong, stiff and relatively dense material (generally called skin faces) separated by a thick core material with low density. Skin faces may consist of metal sheets or of composite materials laminates. The most common used core materials are honeycomb cores and polymer foam cores [13]. Due to both differences between sandwich structure components properties and the complexity of the manufacturing process of a sandwich construction, detection of defects can be challenging. Defects of interest within such sandwich structures include core-to-face sheet disband and damage in the face sheets and cores. Beyond visual inspection and manual tap tests, many NDE techniques have been studied to assess the sandwich structure, including ultrasonics [14-16], thermography [13, 17],

acoustic emission [18], and radiography [19]. All the technique mentioned above are reported to be capable of detecting defects in the sandwich structure, although some of them possess limitations. For instance, in the ultrasound techniques, the received signal is usually greatly attenuated and in the contact approaches the couplant may contaminate the perforated face sheets.

The CI technique has thus been applied to the inspections of the sandwich structures. Note that, due to the capacitive nature of the technique, the probing electric field will not penetrate well through conducting faces (such as those made from aluminium and carbon fibre). Therefore, the CI technique is only applicable to the sandwich structures with non-conducting face sheets (usually glass fibre).

The first sandwich structure investigated was provided by HEXCEL. The sandwich structure was fabricated with PVC foam core and glass fibre sheet faces. Face A was 1 mm thick glass fibre laminates covered with 0.5 mm coating as shown in Figure 6.5(a). Face B was 3 mm thick glass fibre laminates, as shown in Figure 6.5(c). The thickest part of the foam core was 20 mm as shown in Figure 6.5(b). Four artificial defects were introduced during fabrication in the highlighted area of Figure 6.5(a).
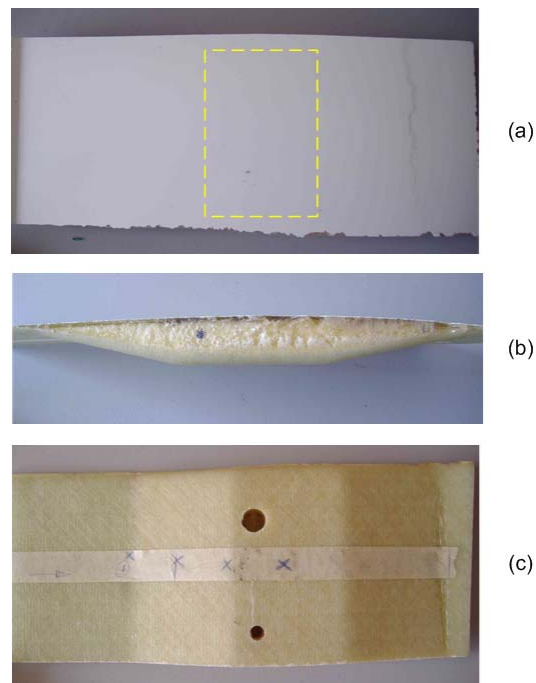
Figure 6.5: *Photographs of the HEXCEL foam core sandwich structure. (a) Top view-Face A, (b) side view, and (c) bottom view-Face B.*

The relative positions of the defects from a top view are shown schematically in Figure 6.6(a). Defects 1 and 4 were two flat bottomed holes drilled from Face B, which are visible from Face B, as shown in Figure 6.5(c). Defect 1 was 12 mm in diameter and was drilled through Face B and the foam core, so that the bottom of the hole was approximately 1.5 mm from the white surface. Defect 4 was 6 mm in diameter and was drilled through Face B and half way through the foam core, so that the bottom of the hole is approximately 11.5 mm from the white surface. Defect 2 and 3 were two identical cylindrical voids within the foam core. The base of the cylindrical void was 6 mm in diameter, and the height of the cylinder was 5 mm. Defect 2 was located 3 mm below Face A (4.5 mm from the white surface) and Defect 3 was 3 mm above Face B (11.5 mm from Face A). The relative positions of the defects in a projection view from a cross section indicated by the dashed line shown in Figure 6.6 (a) are schematically shown in Figure 6.6 (b).
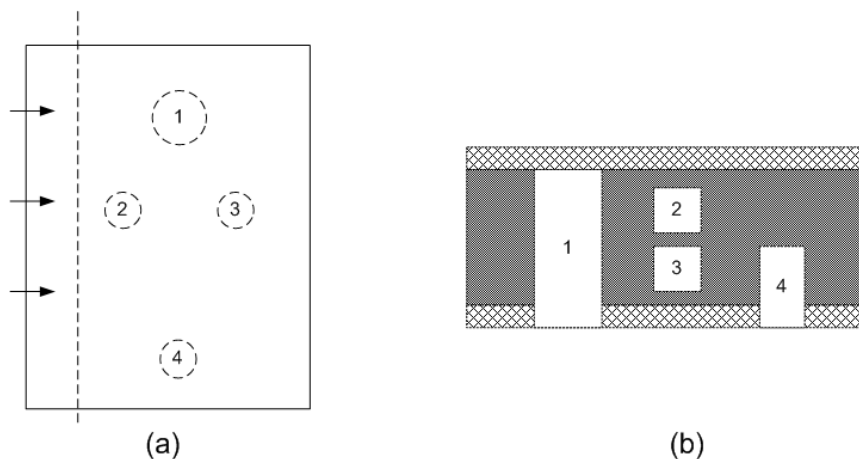
Figure 6.6: *Schematic diagrams of the relative positions of the defects. (a) Top view and (b) projection view from the cross section.*

The 40 mm by 20 mm back to back triangular CI probe was scanned over the white surface (Face A). Due to the uneven surface, the spring loaded handle was used to ensure an intimate contact with the surface. The resultant images are shown in Figure 6.7. It can be seen that Defects 1 and 2 were successfully detected as lighter areas shown in the intensity plot. Defects 3 and 4 were not detected, because they were buried beyond the penetration depth of the CI probe employed, penetration being adversely affected by the multilayer structure of the sandwich panel.
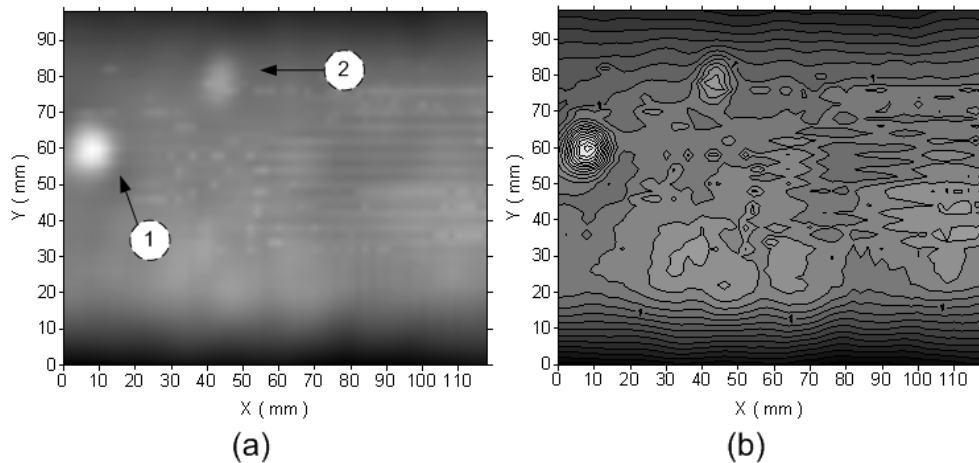
Figure 6.7: *Two representations of the capacitive imaging scan of the form core sandwich structure. (a) Intensity plot and (b) contour plot.*

A second set of experiments was designed to demonstrate the feasibility of the CI technique for the inspection of sandwich structures with a honeycomb core. A piece of 0.5 mm thick glass fibre composite panel was placed on top of a piece of aluminium honeycomb structure, shown in Figure 6.8, to simulate the glass fibre sandwich structure with aluminium honeycomb core. The honeycomb structure was 15 mm thick, the cell size was 6.4 mm and the cell wall was 0.7 mm thick.
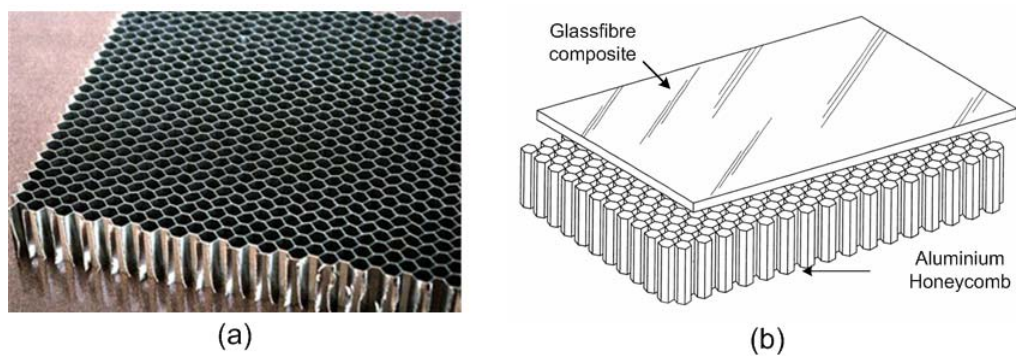
Figure 6.8: *(a) Photograph of the aluminium honeycomb structure and (b) schematic diagram of the simulated glass fibre sandwich structure with an aluminium honeycomb core.*

Given the size of the cell, a smaller version of the back-to-back triangular CI probe, 10 mm by 5 mm in this case, was used. The CI probe was kept at a minimal lift-off distance during the scan. The scan was 40 mm by 30 mm with a step size of 0.5 mm. The results are shown in Figure 6.9. It can be seen that the honeycomb structure is clearly imaged. It is worth mentioning that this result is a proof-of-concept as the

170

specimen was prepared in the favour of demonstrating the feasibility of the CI technique - the cell wall is relatively thick and the simulated glass fibre face is thin. In practice, the cell wall of the aluminium core is usually very thin (less than 0.1 mm) and sometimes the cell size is small compared to the thickness of the glass fibre face sheets. However, the image demonstrates that such measurements are possible. Fortunately, in many cases, the structural failures usually occur in more than one cell - hence, the failures are sometimes detectable even in smaller diameter honeycomb patters where individual cells may not be imaged properly.
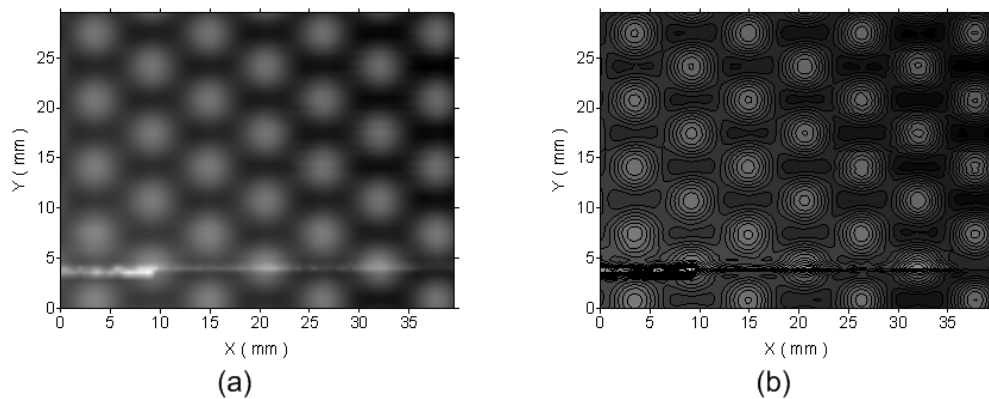
Figure 6.9: *Two representations of the capacitive imaging of the aluminium honeycomb structure. (a) Intensity plot and (b) contour plot.*

An experiment was also conducted to detect structural failures in the aluminium honeycomb structure. The aluminium honeycomb structure used in this experiment was 15 mm thick. The cell size was 3.2 mm and the cell wall was 0.07 mm thick. A folding failure was introduced on the top surface of the honeycomb structure, as shown in Figure 6.10. The aluminium honeycomb structure was covered by a 0.5 mm glass fibre composite to simulate the face sheet and a CI scan was performed with the 10 mm by 5 mm back-to-back triangular probe. The results are shown in Figure 6.11. It can be seen that the honeycomb structure is not recognizable from the resultant image due to the small cell size and thin cell wall. The folding failure was successfully detected though, appearing as a lighter area in the image.
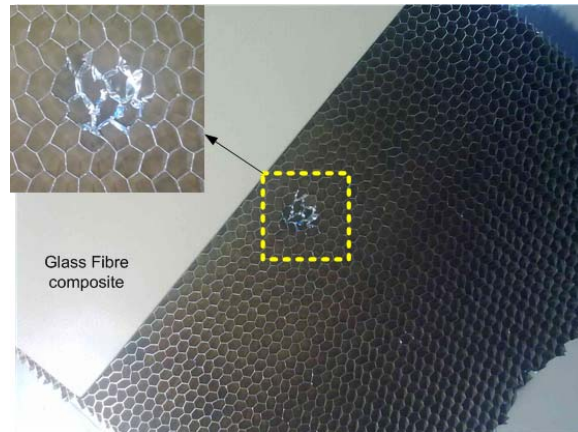
Figure 6.10: *Photograph of the aluminium honeycomb with folding failure covered by glass fibre composite.*
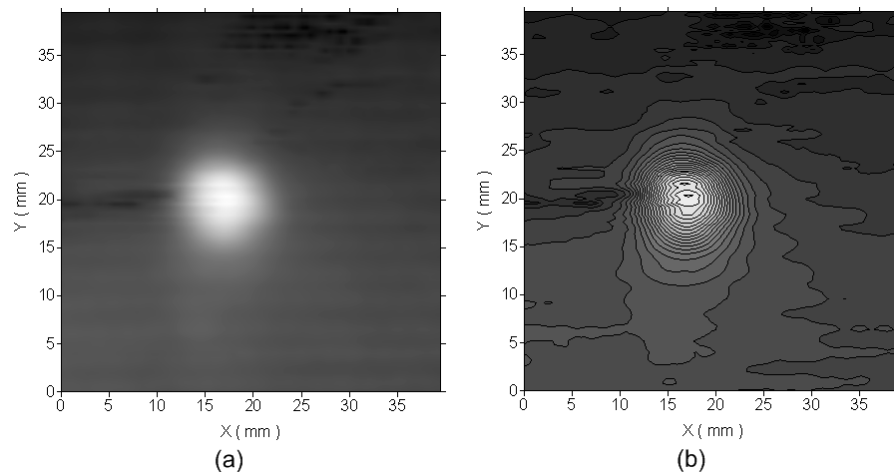
Figure 6.11: *Two representations of the capacitive imaging scan of the simulated sandwich structure with folding structure in the aluminium core. (a) Intensity plot and (b) contour plot.*

A further experiment was conducted using the same aluminium core as the previous experiment. This time, some of the cells were filled with oil and water, as shown in Figure 6.12. It can be seen from Figure 6.12 that nine cells were filled with oil and fifteen cells were filled with water. The honeycomb core was then covered by a 1 mm thick glass fibre composite to simulate the face sheet and a CI scan was performed with the 10 mm by 5 mm back-to-back triangular probe. This setting is an approximation to the problem of water/oil intrusion into the sandwich structures.
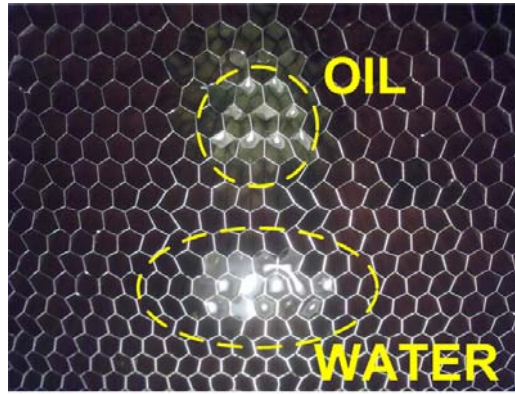
Figure 6.12: *Photograph of the aluminium honeycomb with some of the cells filled with oil and water.*

The results are shown in Figure 6.13. The honeycomb structure is not directly imaged due to the small cell size and thin cell wall compared to the electrode size, but the cells filled with fluid were successfully detected with the oil intrusion appearing as a darker area and the water intrusion appearing as a lighter area in the image. Although such a measurement could be made using X-ray and through transmission ultrasound [20], CI is a useful additional technique for finding such fluid intrusion, without the need for contact or contamination, and can be achieved from one surface.
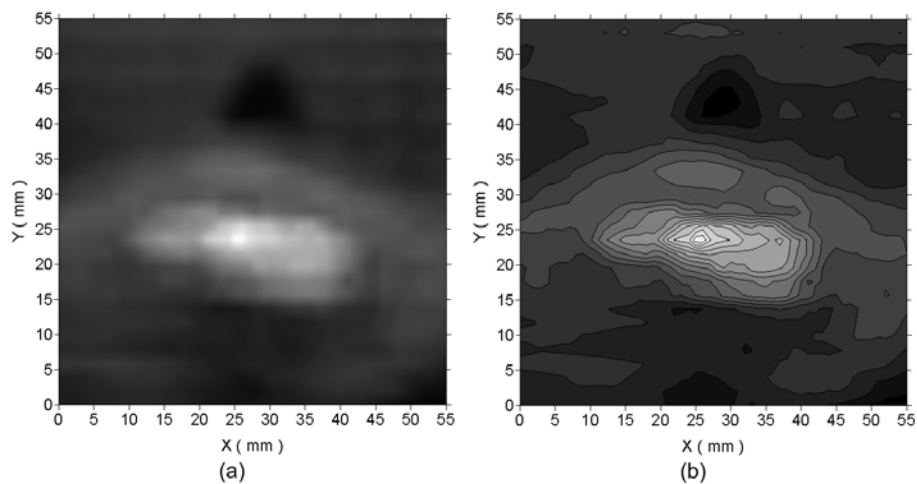
Figure 6.13: *Two representations of the capacitive imaging scan of the simulated sandwich structure with oil and water in the aluminium core. (a) Intensity plot and (b) contour plot.*

The CI technique was now applied to an industrial sample in the form of a panel, provided by AIRBUS, as shown in Figure 6.14. The panel was a sandwich structure

containing both glass fibre and carbon fibre face sheets. The details of the materials and lay up are shown in Figure 6.15.

Figure 6.14: *Photograph of the AIRBUS panel.*
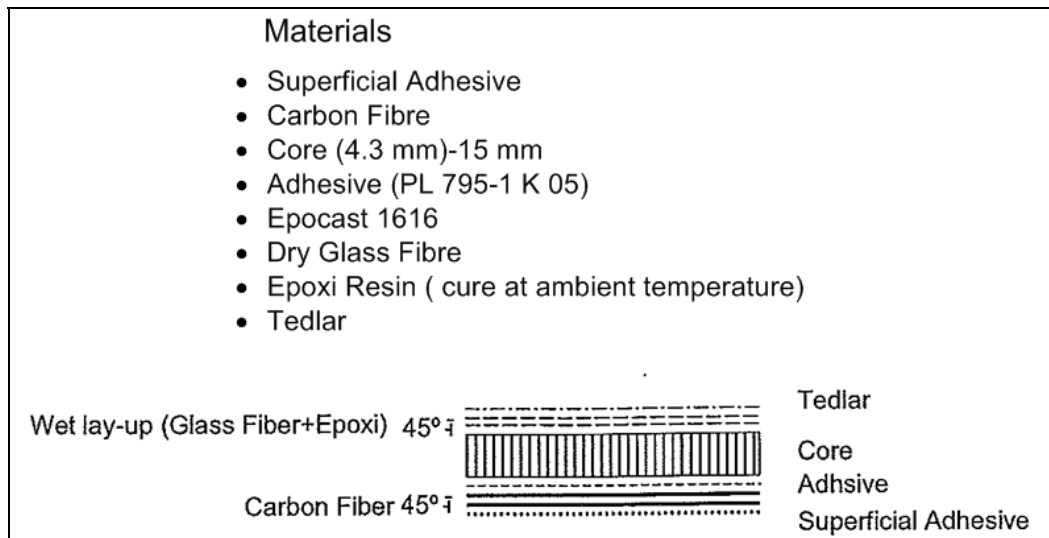
Figure 6.15: *Materials and lay up of the AIRBUS panel.*

Defects were also introduced during fabrication. Details and distributions of the defects are shown in Figure 6.16.

- File A: 10 % of the core cells height filled with adhesive
- File B: 50 % of the core cells height filled with adhesive
- File C: 90 % of the core cells height filled with adhesive
- File D: Core cells, filled with water. With different heights, column 1 and 4 90%, column 2 and 5 50% and column 3 and 6 10%.

- Defects size 240 mm2 (12 cells): Columns 1, 2 and 3
- Defects size 120 mm2 (6 cells): Columns 4, 5 and 6
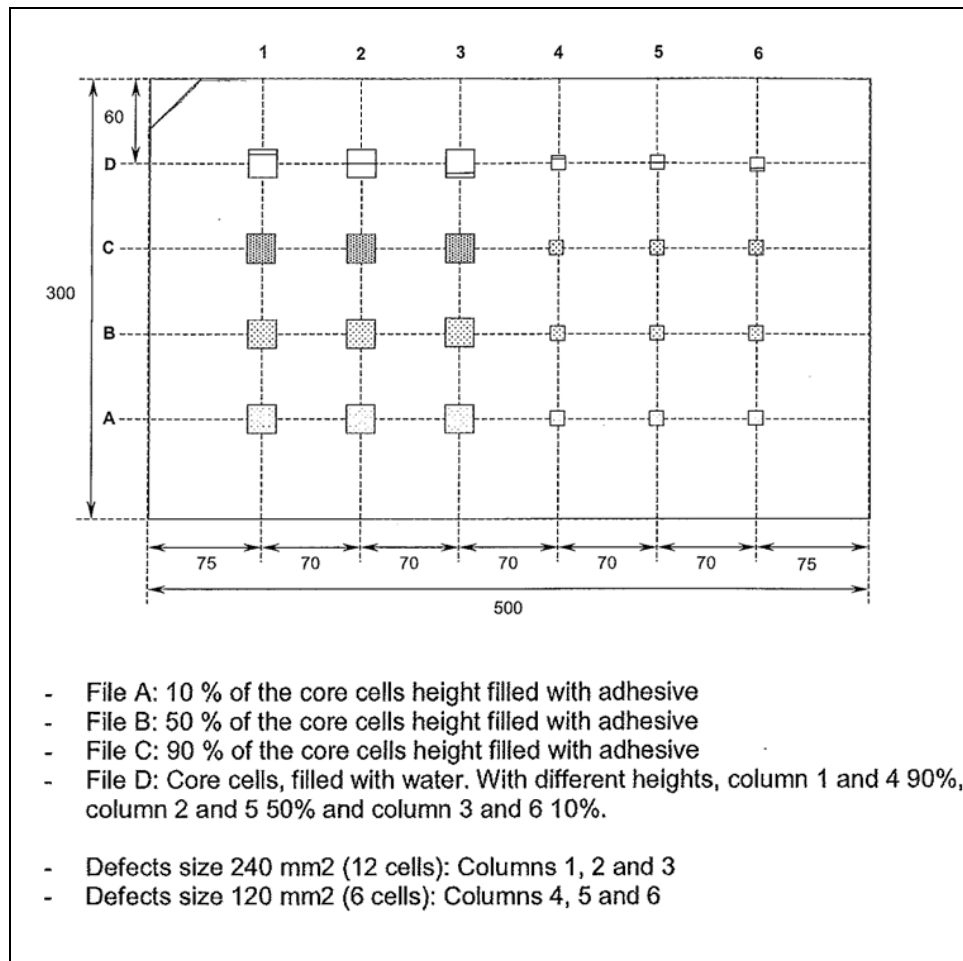
Figure 6.16: *Schematic diagram of the distributions of defects in the AIRBUS panel.*

The 40 mm by 20 mm back-to-back triangular CI probe was scanned over a 450 mm by 260 mm area, from the glass fibre side of the panel, and the results are shown in Figure 6.17. The results from File C (the location of which is shown in Figure 6.16 above) are plotted separately in Figure 6.18, as they are not very obvious in Figure 6.15 due to the image contrast. It is evident that the features have been identified, and that certain defects are more easily detected than others. Comparison of the results obtained from defects filled with adhesive (Files A, B and C), the contrast was seen to decrease as the percentage of the filled adhesive increased. This is because the permittivity value of the adhesive (~2.3) is similar to the Nomex core (~2.6). For defects filled with water (File D), the defects filled with more water (columns 1 and 4) are less obvious than the ones with less water (columns 2, 3 and 6).
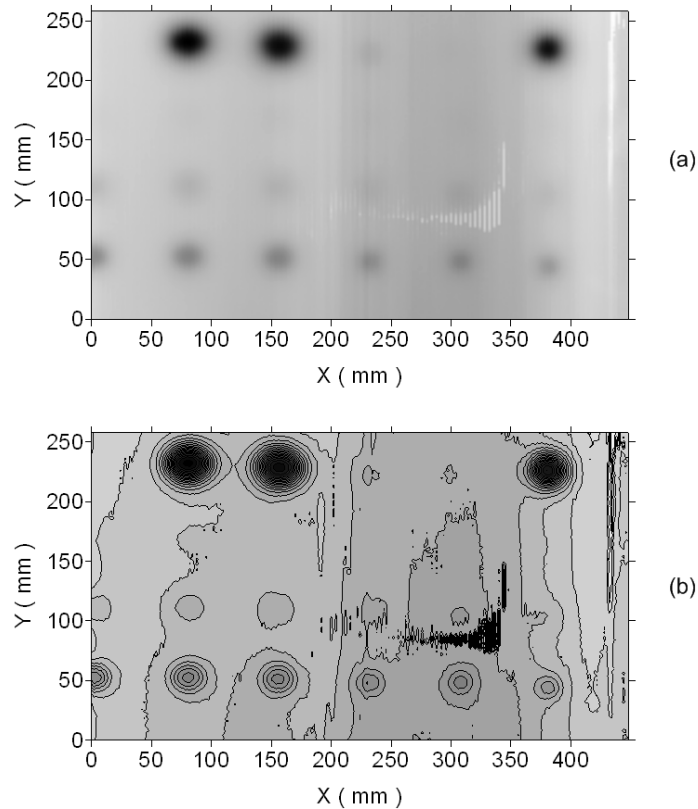
Figure 6.17: *Two representations of the capacitive imaging scan of the AIRBUS panel with defects. (a) Intensity plot and (b) contour plot.*
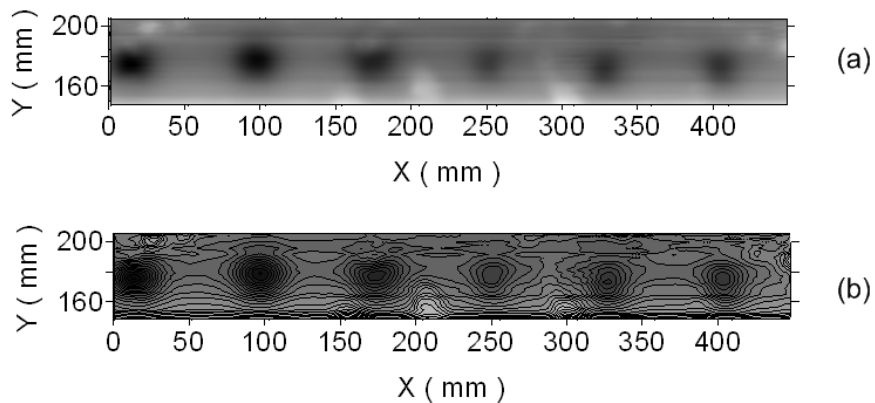
Figure 6.18: *Replot of the capacitive imaging scan along file C on the AIRBUS panel in two representations. (a) Intensity plot and (b) contour plot.*

It is worth mentioning that, in this section, only the inspection of core damage in a sandwich structure has been demonstrated, and the ability to non-destructively detect the core-to-face disbond will be studied in future work.

176

6.4 Inspection of carbon fibre composites

Carbon fibre composite materials also have wide applications in industry because of its high strength-to-weight ratio. Presently, there are various NDE methods that could be used for the assessment of the damage on carbon fibre composite. Most NDE techniques applicable to glass fibre composite materials, such as ultrasonics [6, 21], X-Ray [22] and thermography [23, 24], can be used to carbon fibre composite materials. In addition, many techniques relying on the electrical conductive characteristics of carbon fibres have also been studied, including eddy current [25], resistance measurement [26], and non-contact electric potential measurement [27].

As has been detailed in earlier chapters, the probing electric field from the CI probes cannot penetrate through significant thicknesses of carbon fibre composites due to the high electrical conductivity of the carbon fibres. Thus, in this case, the CI technique is most sensitive to surface features, as was observed in the inspection of metals.

The CI probe responses to surface features on carbon fibre composite samples are studied here. The first sample studied was a 5 mm thick laminated carbon fibre composite panel with damage initiated from one side (Face A), shown in Figure 6.19(a), and extended to the other side (face B), shown in Figure 6.19(b). The 20 mm by 10 mm back-to-back triangular probe was scanned over the highlighted area (60 mm by 50 mm) 1mm above Face B.

(a) (b)
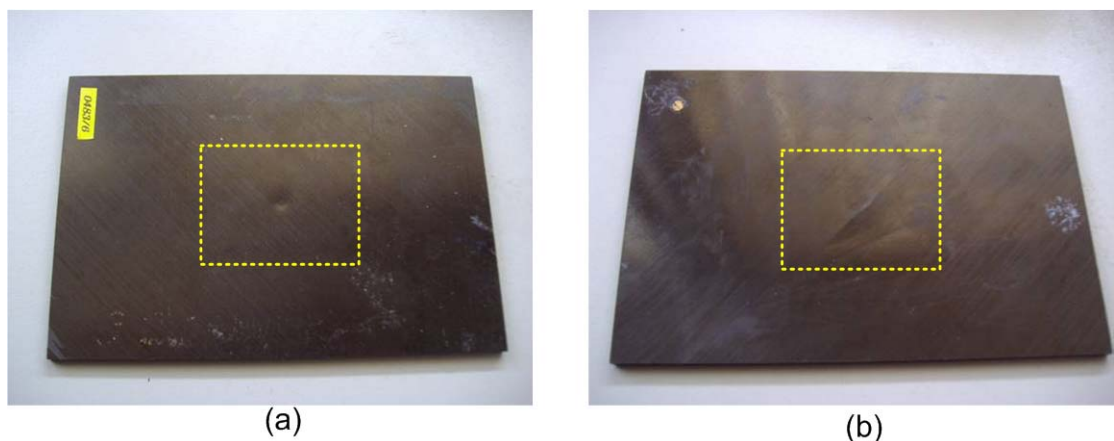
Figure 6.19: *Photographs of the carbon fibre composite with impact damage. (a) Front face (Face A) with the impact and (b) reverse face (Face B).*

The results are shown in Figure 6.20. The extent of the impact damage was clearly imaged. Although the CI technique is less sensitive to sub-surface features, it still detects an area of damage. This is probably due partially to lift-off distance changes caused by the presence of impact damage, but there may also be a small contribution from the change in conductivity across a large area cause by damaged fibred due to impact. A scan using an air-coupled ultrasound transducer pair in through-transmission mode was also conducted on the same sample, so as to image internal structural changes. The resultant image formed from the peak transmitted amplitude, obtained using a chirp signal swept from 200-800 kHz and pulse compression processing, is presented in Figure 6.21 for comparison. It is evident that the areas identified in the ultrasonic scans show good correlation to the impact damage areas identified from CI scans.
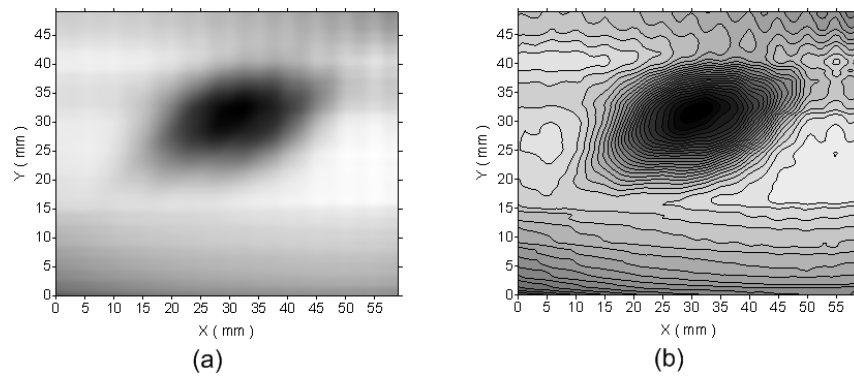
Figure 6.20: *Two representations of the capacitive imaging scan of the carbon fibre composite with impact damage. (a) Intensity plot and (b) contour plot.*
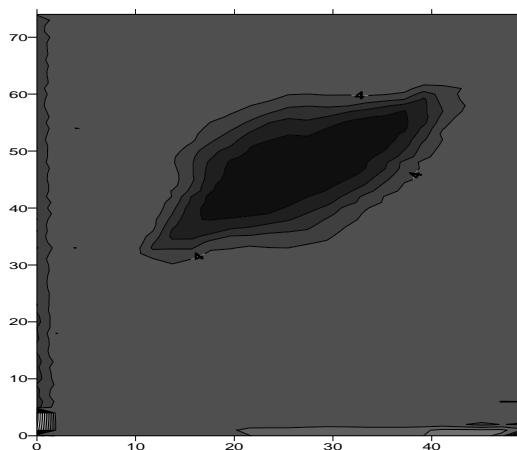
Figure 6.21: *Amplitude plot of the carbon fibre composite with impact damage obtained from air-coupled ultrasound scan.*

The second sample studied was a 3 mm thick laminated carbon fibre composite panel with superficial burn damage, shown in Figure 6.22(a), and the size of the damage can be compared to a 5 pence coin. The 20 mm by 10 mm back-to-back triangular probe was scanned over the highlighted area 1mm above the surface, and the result is shown in Figure 6.22(b). The burn damage was detected as darker area in the image. This is almost certainly due to the change in electrical properties of the area (oxygenization and breakage of the fibres).

(a)

(b)
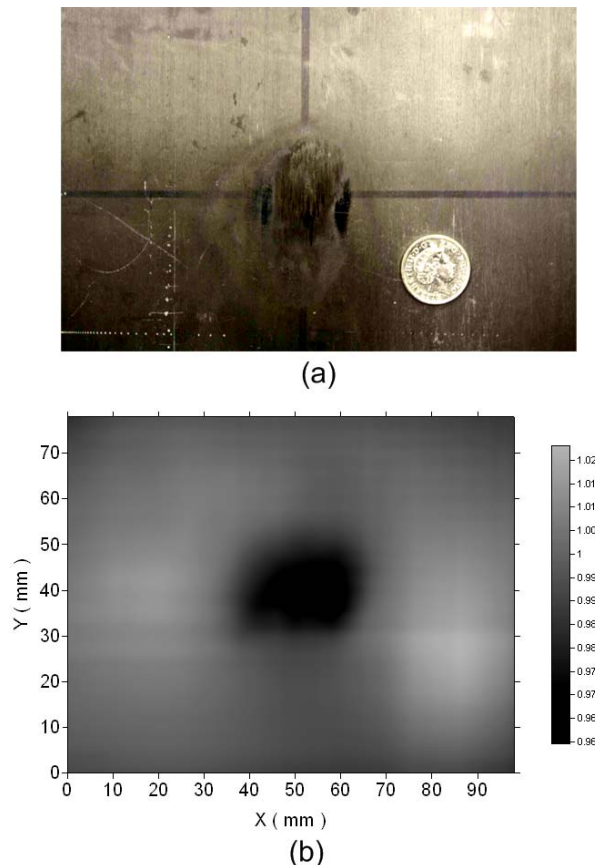
Figure 6.22: *(a) Photograph of the carbon fibre composite panel with superficial burn damage and (b) the intensity plot of the capacitive image.*

The third sample was a carbon fibre woven fabric sample. This sample was coated with epoxy filler and the aligned carbon fibre mats had been woven in an alternate, cross-ply (0°/90°) arrangement, as shown in Figure 6.23. There was also a fracture along the sample caused by bending.

179
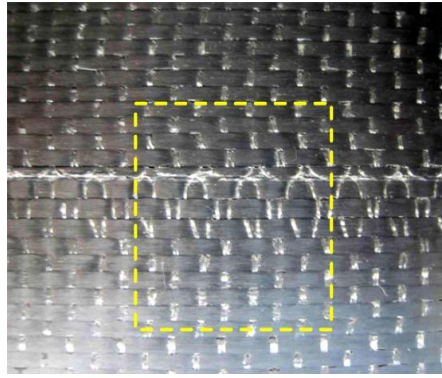
Figure 6.23: *Photographs of the carbon fibre woven sample with the area to be scanned highlighted.*

The 10 mm by 5 mm back-to-back triangular probe was scanned over the highlighted area 1 mm above the surface and the results were shown in Figure 6.24.
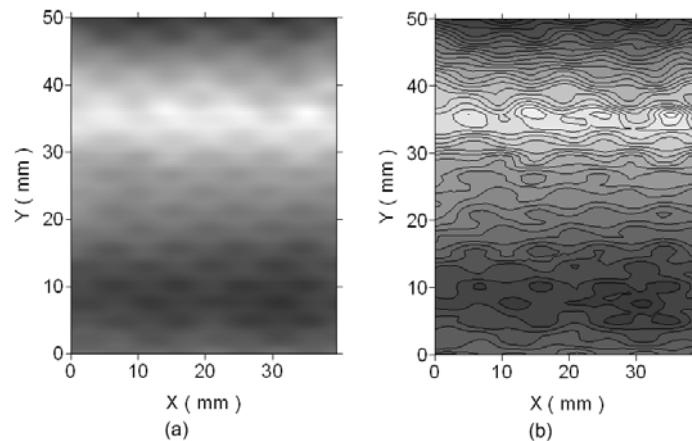
Figure 6.24: *Two representations of the capacitive imaging scan of the carbon fibre woven sample. (a) Intensity plot and (b) contour plot.*

It can be seen that the texture and pattern of the woven carbon fibre are apparent and the fracture was also detected as the lighter area across the image.

6.5   Detection of Corrosion Under Insulation (CUI)

Corrosion under insulation is a big problem that destroys expensive industrial infrastructure, often steel pipe-work. To inspect and maintain these pipes in a cost-effective manner, NDE techniques that do not require removal of the insulation are needed. Techniques such as radiography [28], eddy current [29] and magnetostrictive sensor techniques [30] have shown some promise in meeting this objective.

The results presented earlier in section 5.9 indicated that the CI technique is sensitive to surface features on a steel specimen covered by a significant insulation layer. It was thus thought interesting to embark on a study of how well capacitive imaging could detect the presence of surface rust on mild steel. Figure 6.25(a) shows a photograph of a plate which was immersed into brine to half its depth and held at a high temperature for 10 days. There are various areas of rusting visible within the lower half of the plate. The upper section is, in fact, anodized, so that rusting is inhibited. A capacitive imaging scan using the 20 mm by 10 mm back-to-back triangular CI probe was then performed, and the main areas of rust were detected, as shown in Figure 6.25(b). This is almost certainly due to the change in electrical properties of the oxide layers, and the fact that the lift-off distance has changed due to the presence of oxide. Both factors are likely to cause a change in signal. In the present case, this shows up as a darker shade on the grey scale image. Figure 6.25(c) is a scan with the sample covered in a 5 mm thick layer of foam insulation. Again the main rusted areas are identified, but with a lower resolution due to the increased lift-off distance to the metal surface.

(a) (b) (c)
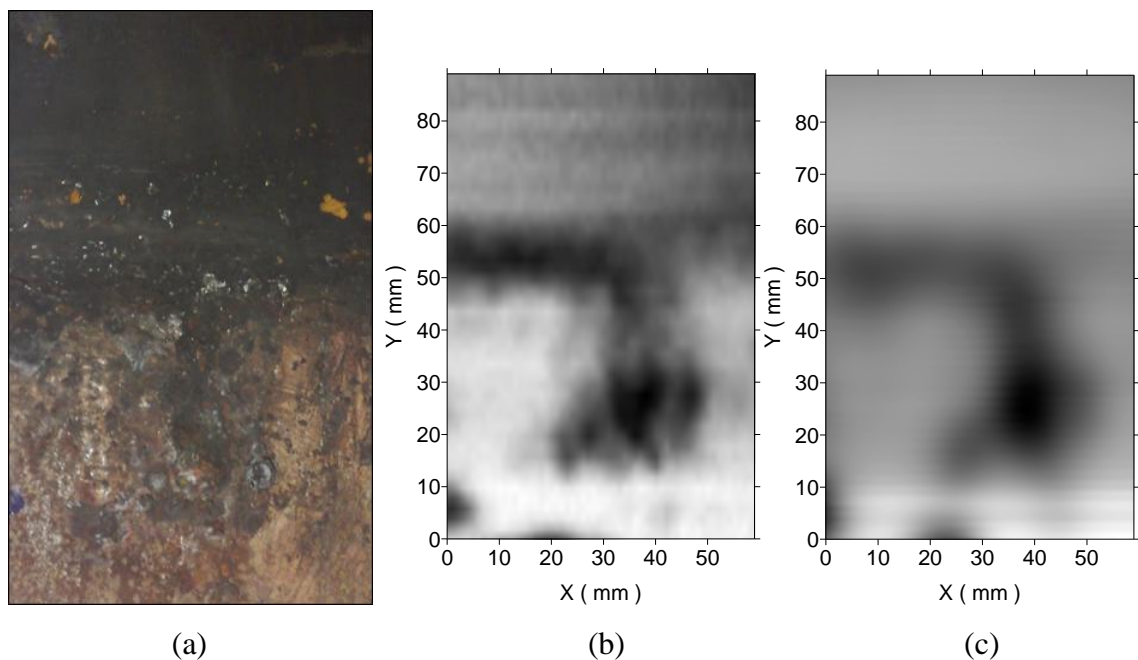
Figure 6.25: *(a) Photograph of a steel plate, immersed in brine for 10 days to cause accelerated rusting in the lower section shown. (b) Capacitive image taken in air, highlighting the main areas of rusting, and (c) a similar image taken through a 5 mm thick insulating polymer foam coating.*

6.6 Inspection of pipe samples

Steel pipeline is usually vulnerable to attack by corrosion, cracking, thermal damage and manufacturing flaws. A preliminary experiment using capacitive imaging technique was designed and performed to detect defects on the external surface of a steel pipe specimen. The experiment setup is shown in Figure 6.26. The steel pipe was held by the rotational stage and the centre of the pipe was aligned with the rotation axis. The capacitive imaging probe, in this case the 20 mm by 10 mm back-to-back triangular CI probe, was held at a certain height and kept a 5mm distance away from the pipe surface during the scan.

Rotational stage

Steel Pipe

CI Probe
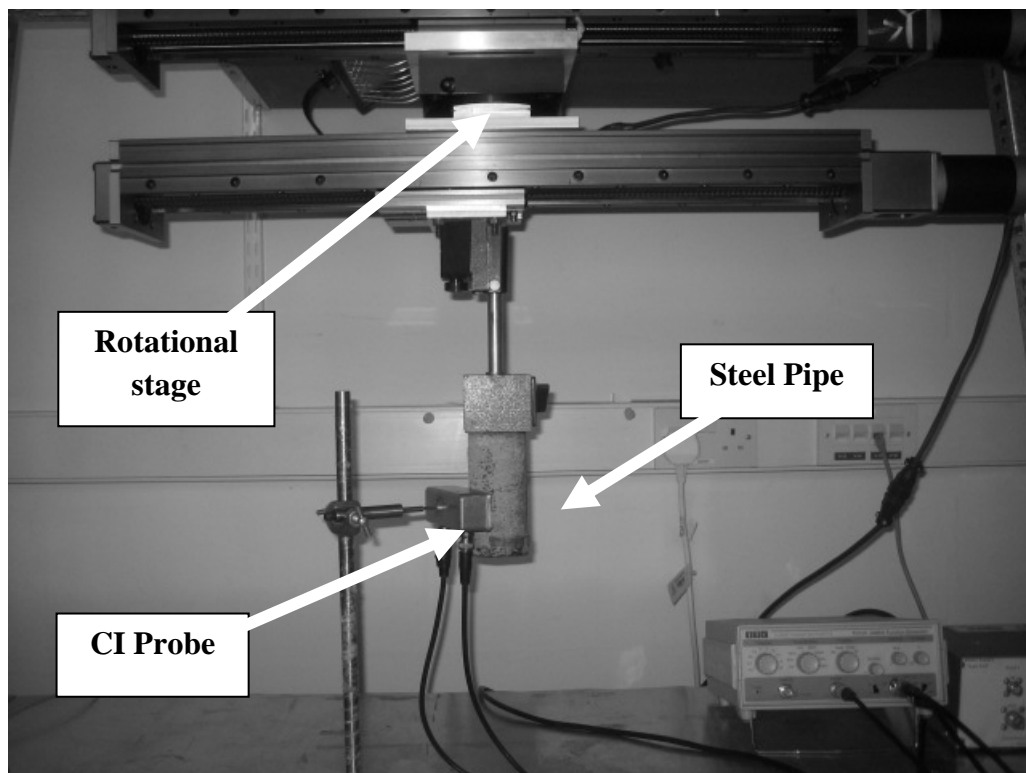
Figure 6.26: *Experiment setup for pipe inspection.*

A cross-sectional view of the pipe along the scan line is sketched based on the real situation in Figure 6.27(a). The pipe, with a grinding defect and a highly rusted area, was rotated over 360 degrees with a one degree step size to complete a circular scan along its external surface. The dashed line in Figure 6.27(a) represents a pipe surface without any defect. The obtained line scan data was presented in a polar plot as show in Figure 6.27(b) to directly describe the pipe surface profile. The radius for each

angle in the polar plot is related to each of the lift-off distance between the probe and the pipe surface for that particular measuring point. Any defect (corrosion, crack and rust) will change the lift-off distance and the measured signal. Comparing Figures 6.27(a) and (b), it can be seen that the experiment result is in agreement with the real situation- the grinding defect (shown as a concave off the baseline) and the highly rusted area (shown as a convex off the base line) were detected.
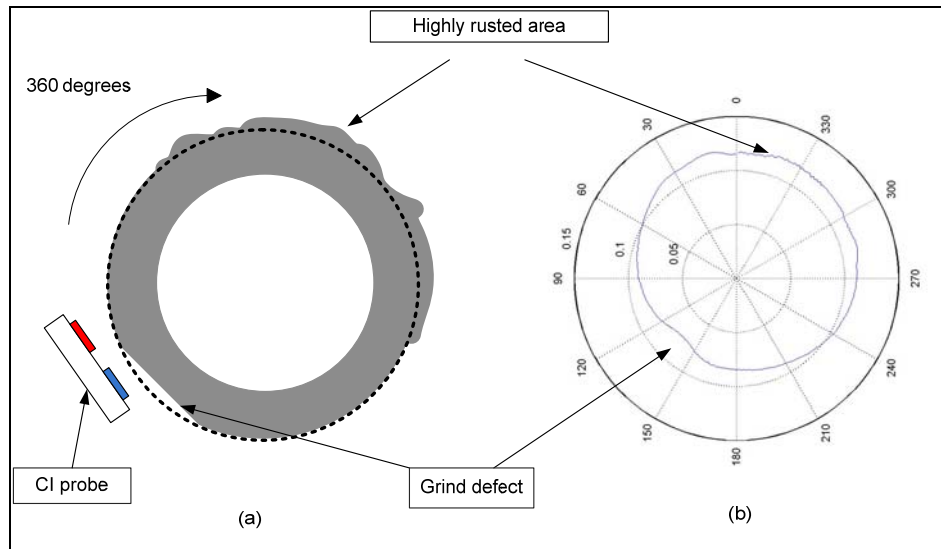
Figure 6.27: *Comparison between the pipe cross-session profile (a) and CI result (b).*

6.7 Detection of buried objects

The exploration of the ground's subsurface to detect and identify buried objects is an important task in various applications, and many techniques have been studied, including Ground Penetrating Radar (GPR) [31], metal detectors [32, 33], capacitive resistivity techniques [34] and the use of inductive and capacitive arrays [35].

Experiments were conducted to demonstrate the feasibility of using the CI technique to detect buried objects. The first experiment was aiming to detect buried metal objects. A sandbox filled with fine sand was prepared and two metal objects, shown in Figure 6.28(b) were buried in sand. The diameter of the steel ball was 10 mm and the length of the screw was approximately 20 mm. The sand layer was about 25 mm thick and the buried metal objects were about 15 mm from the surface. The surface of the sand layer was made flat.

Figure 6.28: *Photographs of (a) the sandbox and (b) the metal objects (a steel ball and a screw) to be buried.*

The 40 mm by 20 mm back-to-back triangular CI probe was scanned over a 70 mm by 60 mm area 1mm above the sand surface, and the results are shown in Figure 6.29. It is evident that the two metal objects were detected as darker areas shown in the image.
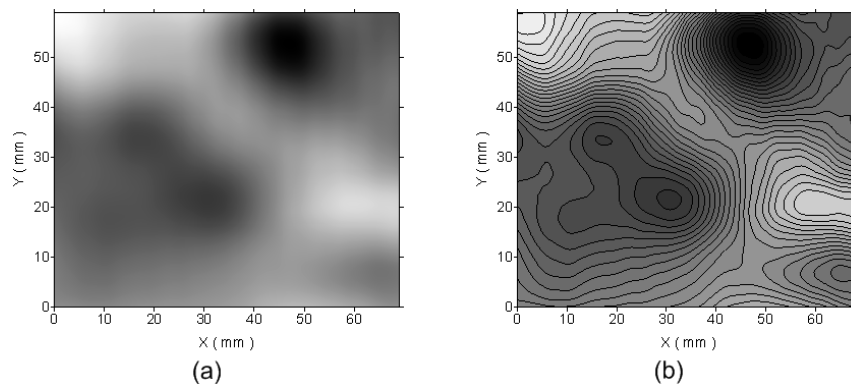
Figure 6.29: *Two representations of the capacitive imaging scan of the sandbox with buried objects (a steel ball and a screw). (a) Intensity plot and (b) contour plot.*

The second experiment was aimed at detecting buried non-conducting objects. The same sandbox was used and this time a plastic pen cap was buried in sand, as shown in Figure 6.30. Again, the surface of the sand layer was flattened to allow easy scanning of the probe over the surface. The 40 mm by 20 mm back-to-back triangular CI probe was again scanned over a 70 mm by 60 mm area 1mm above the sand surface, and the results are shown in Figure 6.31. It is evident that the pen cap was detected as lighter area shown in the image.

(a)   (b)

Figure 6.30: *Photographs of (a) the sandbox and (b) the non-conducting object (plastic pen cap) to be buried.*

(a)   (b)
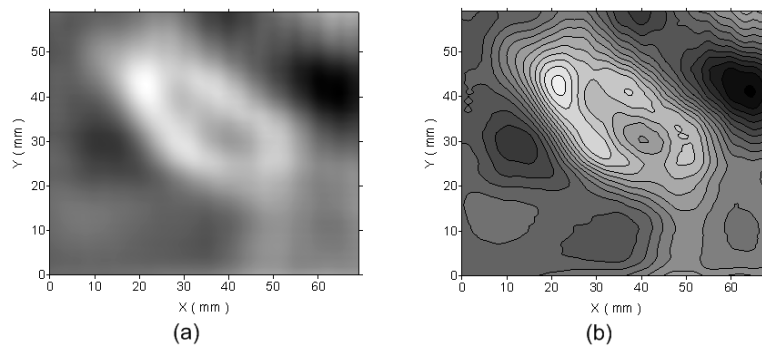
Figure 6.31: *Two representations of the capacitive imaging scan of the sandbox with buried objects (plastic pen cap). (a) Intensity plot and (b) contour plot.*

From the two sandbox experiments, it can be seen that the CI technique is a promising technique for detecting both conducting and non-conducting objects buried under the surface of sand, although in practical field experiments, design concerns must be addressed to cope with more complicated situations (uneven surfaces, and the inhomogeneous and partially conducting nature of some soils).

It is also worth mentioning that the images obtained from the sandbox experiments were not very sharp. This is partially because of the moisture content in sand, which makes the sand layer have a higher permittivity and conductivity values than dry sand [36, 37]. Despite the negative influence on the resultant images, the inclusion of the moisture content in sand provides indication that the CI technique can be used to detect subsurface features in materials with low electrical conductivity. Research on

concrete specimens, which have similar conductivity as humid sand, was conducted and the results will be presented in Chapter 7.

6.8 Conclusions

In this chapter, the CI technique has been tested on some samples of practical interest. The CI technique was used as a NDE tool to investigate an extensive range of specimens. CI probes with different sizes were used in different experiments depending on the nature of the specimens and the defects in them. Both surface crack and delaminations under the surface in glass fibre composites were successfully detected. Defects within the foam core of the glass fibre sandwich structure were detected. The honeycomb pattern of the aluminium core structure, the folding failures and fluid intrusion in the aluminium honeycomb core were imaged through a thin glass fibre composite to demonstrate the feasibility of the CI technique on the inspection of such sandwich panels. This has been further confirmed by the experiment on the sandwich panel provided by AIRBUS. Surface defects including a crack caused by impact damage and superficial burn damage were detected on carbon fibre composites and the texture and pattern of the woven carbon fibre were imaged. Detection of the CUI was also demonstrated by scanning a steel plate with highly rusted areas. External profiling of a pipe with defects (rust and grinding defect) was obtained from a CI line scan. The ability of detecting buried objects was demonstrated by two sandbox experiments involving both a conductor and insulator.

6.9   References

[1]   A. A. Nassr and W. W. El-Dakhakhni, "Non-destructive evaluation of laminated composite plates using dielectrometry sensors," *Smart Materials and Structures,* vol. 18, p. 055014, 2009.

[2]   A. A. Nassr, W. H. Ahmed, and W. W. El-Dakhakhni, "Coplanar capacitance sensors for detecting water intrusion in composite structures," *Measurement Science and Technology,* vol. 19, p. 075702, 2008.

[3]   H. E. M. A. Jama H A and L.-S. P, "Detection of debonding in composite-aluminum joints using gamma-ray Compton scattering," vol. 31, p. 99, 1998.

[4]   C. J. C. Chang F H, Eisenmann J R, Yee B G W, "Application of a special x-ray nondestructive testing technique for monitoring damage zone growth in composite laminates," p. 176, 1975.

[5]   C. Sauerwein, M. Simon, and J. T. Rheinländer, "Inspection of Fibre Based Technical Composites by Radioscopy and Computed Tomography," in *15th World Conference on NDT* Roma, 2000.

[6]   K. Imielinska, M. Castaings, R. Wojtyra, J. Haras, E. L. Clezio, and B. Hosten, "Air-coupled ultrasonic C-scan technique in impact response testing of carbon fibre and hybrid: glass, carbon and Kevlar/epoxy composites," *Journal of Materials Processing Technology,* vol. 157-158, pp. 513-522, 2004.

[7]   A. D. W. McKie and R. C. Addison Jr, "Practical considerations for the rapid inspection of composite materials using laser-based ultrasound," *Ultrasonics,* vol. 32, pp. 333-345, 1994.

[8]   R. Hosseinzadeh, M. M. Shokrieh, and L. Lessard, "Damage behavior of fiber reinforced composite plates subjected to drop weight impacts," *Composites Science and Technology,* vol. 66, pp. 61-68, 2006.

[9]   C. N. J. Starnes M A and K. E. A, "Preliminary thermography studies for quality control of concrete structures strengthened with fiber-reinforced polymer composites," vol. 15, p. 266, 2003.

[10]   J. R. Krishnapillai M, Marshall I H, Bannister M and R. N, "Thermography as a tool for damage assessment," vol. 67, p. 149, 2005.

[11]   Y.-H. Teo, X. Wang, and W.-K. Chiu, "Simulations of microwave propagation in delaminated unidirectional glass-epoxy laminate," *Composite Structures,* vol. 75, pp. 422-427, 2006.

[12]   C. Jordens, M. Scheller, S. Wietzke, D. Romeike, C. Jansen, T. Zentgraf, K. Wiesauer, V. Reisecker, and M. Koch, "Terahertz spectroscopy to study the orientation of glass fibres in reinforced plastics," *Composites Science and Technology,* vol. 70, pp. 472-477.

[13]   V. Dattoma, R. Marcuccio, C. Pappalettere, and G. M. Smith, "Thermographic investigation of sandwich structure made of composite material," *NDT & E International,* vol. 34, pp. 515-520, 2001.

[14]   C. V. Subramanian, M. Thavasimuthu, P. Palanichamy, D. K. Bhattacharya, and B. Raj, "Evaluation of bond integrity in sandwiched structures by dry couplant ultrasonic technique," *NDT & E International,* vol. 24, pp. 29-31, 1991.

[15]   D. K. Hsu, "Nondestructive testing using air-borne ultrasound," *Ultrasonics,* vol. 44, pp. e1019-e1024, 2006.

[16]   P. A. Fomitchov, A. K. Kromin, S. Krishnaswamy, and J. D. Achenbach, "Imaging of damage in sandwich composite structures using a scanning laser source technique," *Composites Part B: Engineering,* vol. 35, pp. 557-562, 2004.

[17]   M. Vikstrom, J. Backlund, and K. A. Olsson, "Non-destructive testing of sandwich constructions using thermography," *Composite Structures,* vol. 13, pp. 49-65, 1989.

[18] A. Quispitupa, B. Shafiq, F. Just, and D. Serrano, "Acoustic emission based tensile characteristics of sandwich composites," *Composites Part B: Engineering,* vol. 35, pp. 563-571, 2004/12.

[19] J. S. Giguere, "Damage Mechanisms and Non-Destructive Testing in the Case of Water Ingress in CF-18 Flight Control Surfaces," 2000.

[20] A. B. Doyum and M. Dürer., "Defect Characterization of Composite Honeycomb Panels by Non-Destructive Inspection Methods " in *DGZfP-JAHRESTAGUNG*, 2002.

[21] K. Maslov, R. Y. Kim, V. K. Kinra, and N. J. Pagano, "A new technique for the ultrasonic detection of internal transverse cracks in carbon-fibre/bismaleimide composite laminates," *Composites Science and Technology,* vol. 60, pp. 2185-2190, 2000.

[22] L. Dobiaova, V. Star, P. Glogar, and V. Valvoda, "Analysis of carbon fibers and carbon composites by asymmetric X-ray diffraction technique," *Carbon,* vol. 37, pp. 421-425, 1999.

[23] R. J. Ball and D. P. Almond, "The detection and measurement of impact damage in thick carbon fibre reinforced laminates by transient thermography," *NDT & E International,* vol. 31, pp. 165-173, 1998.

[24] N. P. Avdelidis, D. P. Almond, A. Dobbinson, B. C. Hawtin, C. Ibarra-Castanedo, and X. Maldague, "Aircraft composites assessment by means of transient thermal NDT," *Progress in Aerospace Sciences,* vol. 40, pp. 143-162, 2004.

[25] M. P. De Goeje and K. E. D. Wapenaar, "Non-destructive inspection of carbon fibre-reinforced plastics using eddy current methods," *Composites,* vol. 23, pp. 147-157, 1992.

[26] J. Wen, Z. Xia, and F. Choy, "Damage detection of carbon fiber reinforced polymer composites via electrical resistance measurement," *Composites Part B: Engineering,* vol. In Press, Corrected Proof.

[27]   W. Gebrial and et al., "Non-contact imaging of carbon composite structures using electric potential (displacement current) sensors," *Measurement Science and Technology,* vol. 17, p. 1470, 2006.

[28]   P. Ong, V. Patel, and A. Balasubramanyan, "Quantitative characterization of corrosion under insulation," *Journal of Nondestructive Evaluation,* vol. 16, pp. 135-146, 1997.

[29]   R. S. M.A. Robers, "Pulsed Eddy Current in Corrosion Detection," in *8th RCNDE* Barcelona, 2002.

[30]   H. Kwun and A. E. Holt, "Feasibility of under-lagging corrosion detection in steel pipe using the magnetostrictive sensor technique," *NDT & E International,* vol. 28, pp. 211-214, 1995.

[31]   J. Lester and L. E. Bernold, "Innovative process to characterize buried utilities using Ground Penetrating Radar," *Automation in Construction,* vol. 16, pp. 546-555, 2007.

[32]   M. M. Rezos, J. J. Schultz, R. A. Murdock Ii, and S. A. Smith, "Controlled research utilizing a basic all-metal detector in the search for buried firearms and miscellaneous weapons," *Forensic Science International,* vol. 195, pp. 121-127.

[33]   S. Tyagi, A. E. Lord Jr, and R. M. Koerner, "Use of a metal detector to detect buried drums in sandy soil," *Journal of Hazardous Materials,* vol. 7, pp. 375-381, 1983.

[34]   O. Kuras, "The capacitive resistivity technique for electrical imaging of the shallow subsurface," The university of Nottingham, 2002.

[35]   SCHLICKER, D., WASHABAUGH, A., SHAY, I., GOLDFINE, and N., *Inductive and capacitive array imaging of buried objects* vol. 48. Northampton, ROYAUME-UNI: British Institute of Non-Destructive Testing, 2006.

[36]   M. Shahidi, J. B. Hasted, and A. K. Jonscher, "Electrical properties of dry and humid sand," *Nature,* vol. 258, pp. 595-597, 1975.

[37]   J. O. Curtis, "Moisture effects on the dielectric properties of soils," *Geoscience and Remote Sensing, IEEE Transactions on,* vol. 39, pp. 125-128, 2001.

Chapter 7   Non-destructive evaluation of concrete using the CI technique

7.1   Introduction

The work described in previous chapters has investigated various types of specimens, which can have a range of conductivities ranging from an insulator to a metal. For insulators (air, Perspex, glass fibre, air-filled polymer foam, etc.), the conductivity is usually less than 10^{-14} S/m [1], and for good conductors (some forms of carbon, aluminium, steel, etc.), the conductivity is usually higher than 10^4 S/m [1]. Concrete has a typical conductivity in the 10^{-2} S/m range - a value situated between the above values. As demonstrated in Chapters 5 and 6, the CI technique can be used to detect both surface and hidden defects in dielectric specimens (insulator) and to detect surface features predominantly on conducting specimens. How the CI technique would respond to surface and hidden features in concrete specimens has not yet been discussed in this thesis, even though it could be a major area of application. This led to an investigation of the feasibility of the CI technique for concrete inspection. This Chapter describes the NDE of concrete using the CI technique in detail. Note that a research paper has been published based on the work in this chapter [2].

7.2   Background to the inspection of concrete

Reinforced concrete is one of the most important construction materials because it is economical, durable and has the ability to be cast into any shape. In most cases reinforced concrete is reliable and strong throughout its service life. However, factors such as poor design, bad workmanship and a harsh environment can combine to cause deterioration within a concrete structure. This may induce failure of the structure by causing visually unacceptable surface cracking or spalling of the layer of concrete 'cover' that protects the steel reinforcement. This may in turn pose a safety risk to

passing pedestrian or motor traffic owing to falling debris, and ultimately lead to further corrosion and structural failure. Unfortunately, more often than not, this deterioration may not become apparent at the surface until major damage has already occurred. Similarly, in assessing heritage concrete structures, poor record keeping may prevent an accurate knowledge of the quantity and architecture of the internal steel reinforcement being known in advance. Thus non-destructive evaluation (NDE) techniques are very useful for condition assessment of concrete structures, so as to provide information concerning structural conditions within the material. These include:

- Cracks caused by shrinkage of concrete or repetitive freeze-thaw cycles;
- Corrosion of reinforcing steel caused by an ingress of chloride ions (e.g. from sea water or de-icing salt) and/or loss of steel passivity owing to neutralization of the normal alkaline environment provided by the concrete cover by reaction with atmospheric carbon dioxide;
- Weak areas of concrete and/or discrete defects caused by poor quality control in the mixing and placing of concrete (*e.g*. poor curing, incorrect mix design, air voids *etc.*);
- The size, depth and distribution of steel reinforcement bars (rebars) and their condition with respect to corrosion *etc*.

There is a range of techniques used conventionally to inspect concrete structures. They are all designed to detect only a single type of artefact (e.g. rebar, void, corrosion etc). Perhaps the most common is the cover meter [3]. This operates by creating eddy currents within the rebars, and measuring the resultant magnetic field at the concrete surface to gain diagnostic information. This approach is used to estimate cover depth and to give some idea of rebar position, but is difficult to use beyond a certain cover depth or in areas of congested reinforcement and does not easily provide an imaging capability [4]. Ultrasonic techniques are also used to assess concrete

structures, using various transducer technologies and frequencies, including relatively simple, low-frequency piezoelectric systems such as the PUNDIT[TM] [5], more advanced piezoelectric transducer designs [6-8] and the use of air-coupling [9, 10]. However, this approach has yet to receive widespread use for rebar and void characterization because of uncertainties introduced by the significant ultrasonic scattering encountered [11, 12], which is a manifestation of the mismatch in acoustic impedance between aggregates and the cement paste matrix. In many cases, surface preparation is also required.

The half-cell potentiometer can be used to infer the probability of corrosion of the steel rebar from the surface of the concrete [13, 14] by measuring the electrochemical potential between the rebars and a reference 'half-cell' electrode at the surface. Areas of high potential gradient are more likely to be undergoing corrosion. This approach must be combined with other techniques (e.g. resistivity surveys) in order to obtain quantitative results. It sometimes also requires a complicated statistical analysis to retrieve useful data [15] or to predict service life [16]. It also requires that an electrical connection be made to the rebar, which normally entails breaking or cutting out a section of concrete. Ground Penetrating Radar (GPR) has also been proposed for the inspection of concrete structures [17, 18]. The resolution of GPR system is limited to 100 mm for commercial systems owing to the wavelength used [19, 20] which is not really suitable for the majority of artefacts of interest in structural assessment. Other electromagnetic techniques, such as electrical resistance measurement [21, 22], impedance spectroscopy [23] and electrical resistance tomography [24] are reported to be used for inspection and evaluation of concrete structures, but they all require a perfect electrical contact between the electrode and the target surface.

The CI technique aims to offer a possible route to overcoming some of the limitations imposed by existing NDE techniques on the inspection of concrete structures [25]. For example, the technique should be able to recognize both rebars and air voids within a

concrete structure. Other work has described capacitive approaches to measure cover depth and water content, in conjunction with GPR [26].

This Chapter describes the results from both finite element modelling and physical experiments to investigate the usefulness of the CI technique for concrete inspection and imaging. It should be noted that the intention is to demonstrate the potential of capacitive techniques to, in principal, detect artefacts within concrete samples. Thus, the artificial artefacts introduced in the samples, and the conditions under which they were tested, were designed to provide clear results rather than exactly simulate in-service situations. The concomitant limitations of the CI technique on concrete inspection are discussed in section 7.5.

7.3   Two-dimensional Finite Element (FE) modelling

In Chapter 4, the electric field distributions produced by the CI probes, and how they may interact with the dielectric and conducting specimens, were presented. It was felt important to model the probing electric field behaviour for concrete, because of its different electrical properties when compared to an insulator or conductor. Using the quasi-static assumption mentioned in Chapter 4, it is possible to use a Finite Element (FE) technique to predict the electric field from the CI probes within the concrete specimens, using the COMSOL^{TM} Multiphysics FE package. To simplify the models, simulations were restricted to two dimensions as before. The quasi-static mode was again used within COMSOL^{TM}.

The concrete considered in this model is assumed to be a non-magnetic material. As such, the magnetic permeability of concrete (assuming rebars are not present) is deemed equal to that of free space. In terms of the electrical properties, in practice the permittivity and conductivity will depend on the frequency used to drive the electrodes, the moisture content and the thickness of the concrete material, as well as other factors such as the mix used etc. As the main purpose of the FE modelling here

is to demonstrate the possibility of imaging surface and sub-surface features, hidden defects and steel rebars – i.e., we are only interested in demonstrating that the contrast in electrical properties between the various materials (concrete, steel, air/water voids) gives rise to measurable signals – simplifications can be made. Thus, it has been assumed that the permittivity and conductivity of concrete samples can be assumed to have a nominal value, apart from defects or other features that can deviate from this. In addition, these values are assumed to be frequency independent. In the theoretical model, the relative permittivity was set to a value of 6, and the conductivity to 0.02 s m^{-1}, a value used in other published work [27].

The model geometry is shown in Figure 7.1. This represents a slab of concrete containing regions of discontinuity in electric properties. The electrodes were modelled at the relative sizes shown in the figure. Note that the field distribution predicted by these models is determined primarily by these geometric factors in the quasi-static model.
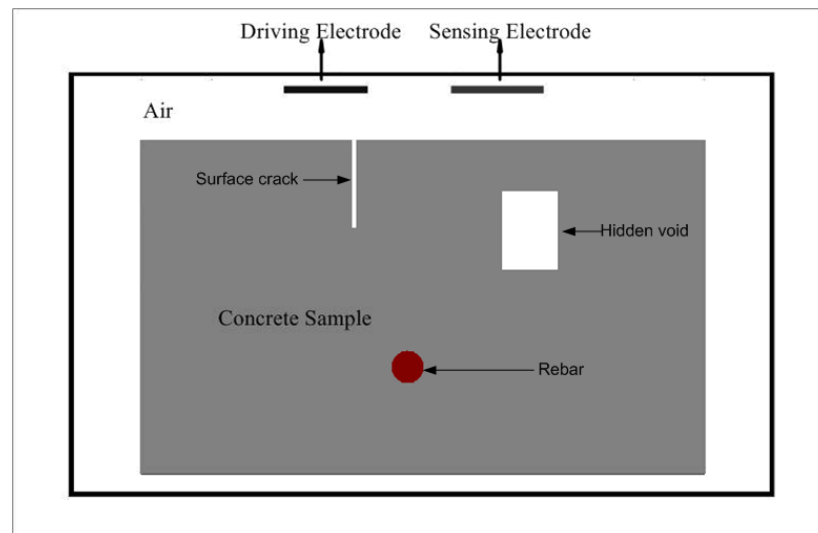
Figure 7.1: *Model used for FE simulation of CI for concrete sample.*

Assuming the geometry of Figure 7.1, the FE model can be used to predict the equipotential lines within the resultant electric field distribution. These are shown in

Figure 7.2 for (a) a uniform concrete sample (b) a sample with a narrow crack on the surface, (c) a simulated void under the surface and (d) a steel rebar in concrete.
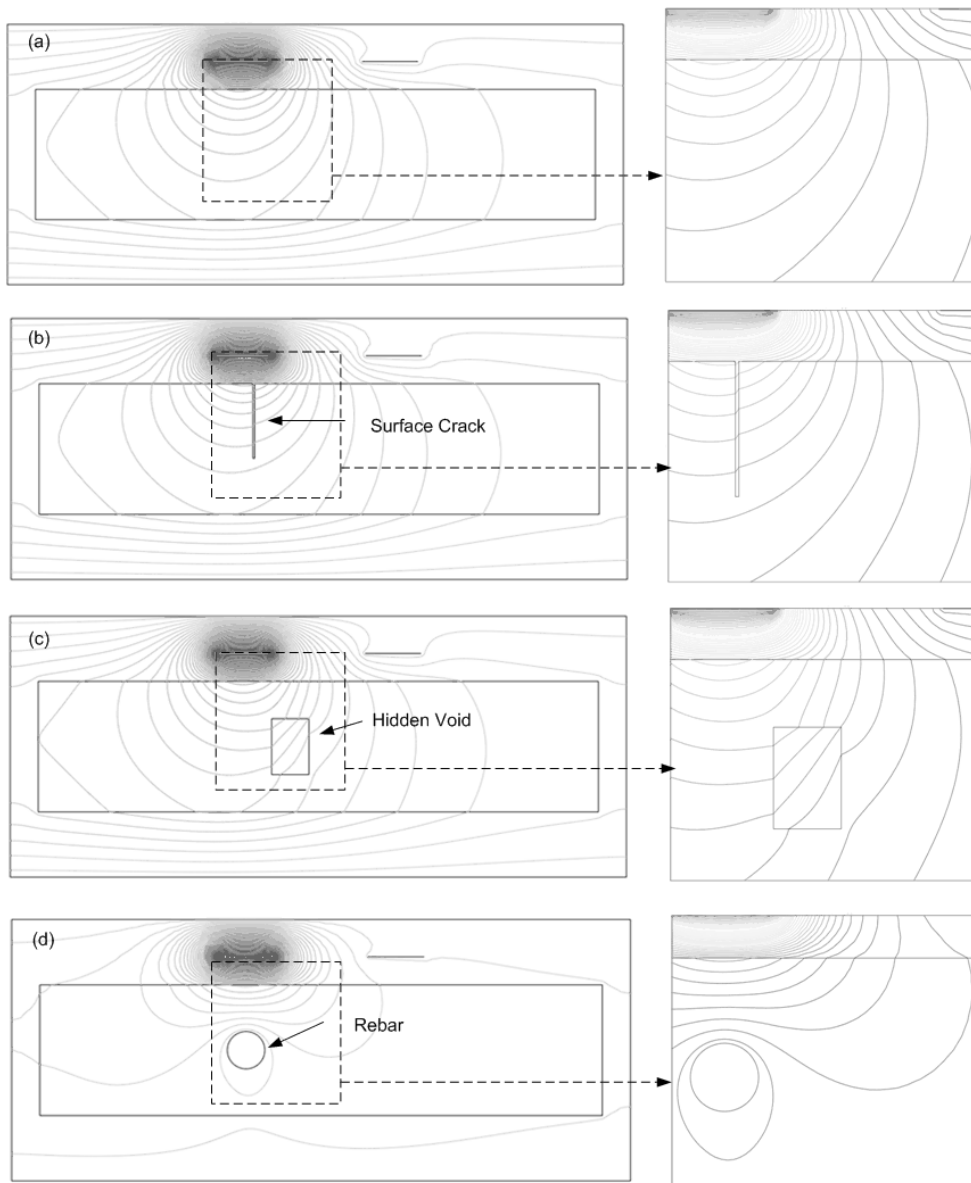
Figure 7.2: *Simulations of the electric field distribution for a concrete sample. Results are shown for (a) a uniform sample (b) a sample with a narrow crack on the surface, (c) a simulated void under the surface and (d) a steel rebar in the location shown.*

The areas in the dashed boxes of each model are expanded to show the distributions of the electric field, and the capacitance recorded by the capacitive probe in each case was calculated and is shown in Table 7-1.

Table 7-1: *Calculated capacitance value from the FE models*

Model	Calculated Capacitance
Capacitive imaging probe above a complete sample	7.319×10^{-13}(F)
Capacitive imaging probe above a sample with a surface crack	6.998×10^{-13}(F)
Capacitive imaging probe above a sample with a hidden void	7.526×10^{-13}(F)
Capacitive imaging probe above a sample with a rebar	2.427×10^{-13}(F)

As can be seen in the latter three cases, the electric field distribution becomes distorted within and around the regions of discontinuity in the dielectric properties within the sample (i.e. the presence of crack, void or rebar). This is a result of the very different electrical properties of concrete compared to either air or steel. The distorted electric field causes a capacitance change of the capacitive imaging probe, as shown in Table 7-1, which leads to a detectable signal change on the sensing electrode. It is also worth noting that the surface crack caused a lower capacitance, while the hidden void caused a higher capacitance. This is a situation very similar to some of the insulator cases. The results from the models give some indication that capacitive imaging is capable of forming the basis for a novel NDE system for concrete. This is confirmed by the experimental results below.

7.4   Experimental results

The apparatus shown in Figure 2.14 was used on the concrete specimens. For an accurate evaluation of concrete, the electrode geometry of the CI probe must be designed with some care. Probes of various geometries have already been investigated in previous chapters, and the results have indicated that it is important to optimise the

electrode geometry for each application. Generally, a wider electrode assembly will provide a deeper depth of penetration into the sample, but this will be traded off against a reduced spatial resolution at the surface. The FE results shown in section 7.3 suggest that concrete behaves similarly as the dielectric specimens, and thus the back-to-back triangular probe was thought to be a good choice. In this work, experimental results were obtained using the back-to-back triangular electrodes such as those shown in Figure 3.13(a), but with different sizes to suit each application.

The concrete samples used in this work were fabricated from a C40 mix (relative proportions by mass 2.55:1.7:1:0.6 of 20 mm limestone aggregate:sand:CEM1 cement: water) unless otherwise specified. After 28 days of moist curing, the samples were aged for a minimum of 12 months (for small samples) and >2 years (for large samples) in ambient laboratory conditions, so that they could be considered to be reasonably stable in terms of their electrical properties and internal moisture distribution. Various concrete samples had been prepared so as to contain certain features of interest. These included surface cracking, changes in thickness and the presence of rebars. Note that, because the air gap between the electrodes and the sample can be quite large (on the order of millimetres), sample surface preparation was not required.

The first sample that was investigated was a mortar block with dimensions 180 (length) x 120 (width) x 30 mm (depth), with no coarse aggregate. A surface crack initiated by impact was present on the upper surface, as shown in the photograph of Figure 7.3(a). This has been cleaned to show the presence of the crack more clearly. The 40 mm by 20 mm back-to-back triangular probe was scanned over a 100 mm x 50 mm area, as highlighted by the dotted line in Figure 7.3(a), with a 1 mm step size and 1 mm stand-off distance (the gap between the probe and the sample surface). The excitation frequency was 1 MHz.

(a)   (b)
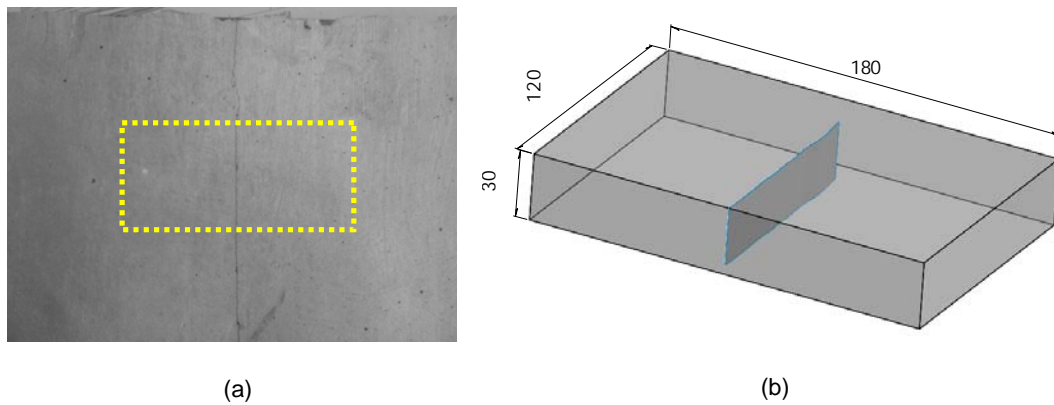
Figure 7.3: *Concrete specimen with a crack on the surface. (a) Photograph of top surface containing the crack, and (b) schematic diagram of the crack geometry.*

The image resulting from this scan is shown in Figure 7.4, where the amplitude of the signal output from the sensing electrode has been plotted against position across the sample surface. It can be seen that there was an obvious discontinuity in the image caused by the presence of the surface crack.
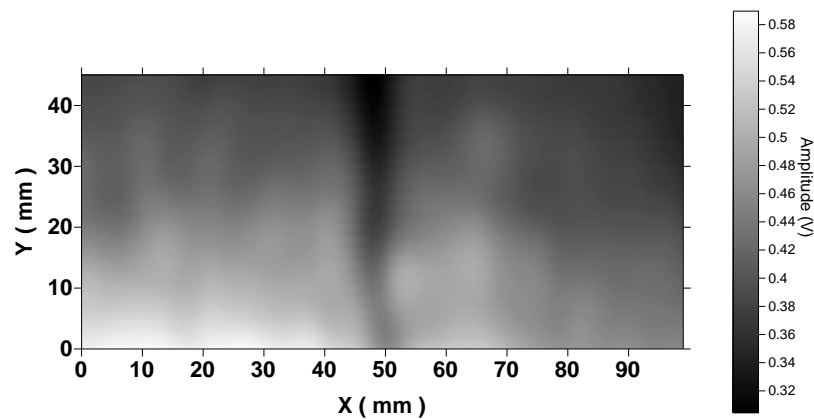
Figure 7.4: *Capacitive imaging results for concrete sample with a crack on the surface.*

A second concrete specimen with dimensions 980 mm (length) x 860 mm (width) x 125 mm (depth) was also fabricated, containing a stepped air-filled channel running through the centre to simulate a local change in thickness. The channel had two depth

values, 30 mm and 60 mm, so that the cover thickness over the void had values of 125 mm (full sample thickness), 95 mm and 65 mm respectively, as shown in figure 7.5.

(a)   (b)
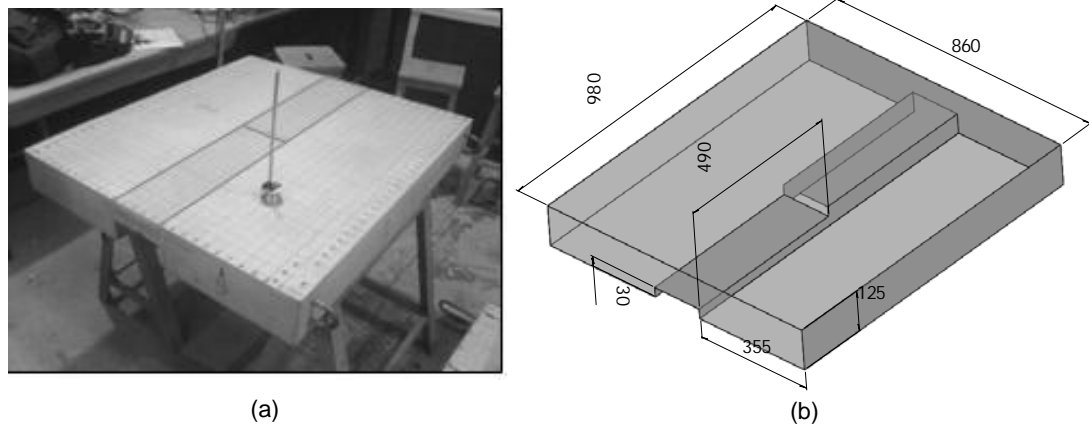
Figure 7.5: *(a) Photograph and (b) schematic diagram of a concrete sample with a hidden channel of two different depths (30 mm and 60 mm).*

The thickness of this sample and the width of the channels meant that a larger pair of electrodes shown earlier in Figure 3.13(a). In this case, the triangular electrodes were each 150 mm wide in the horizontal direction, and the sensing area was 320 mm by 160 mm. A scan at a frequency of 1 MHz was performed, over a 540 mm x 600 mm area, with a 30 mm step size and 1 mm stand-off distance. The result is shown in Figure 7.6. The lighter area indicates the presence of both the shallow void and the deep void, as indicated by the dotted lines which represent the actual positions of the channel. It can also be seen that the shallower channel (with the greater cover depth of 95 mm) produced a lower output than that region containing the smaller cover depth of 65 mm. Hence, it seems that some depth information is available from such scans.
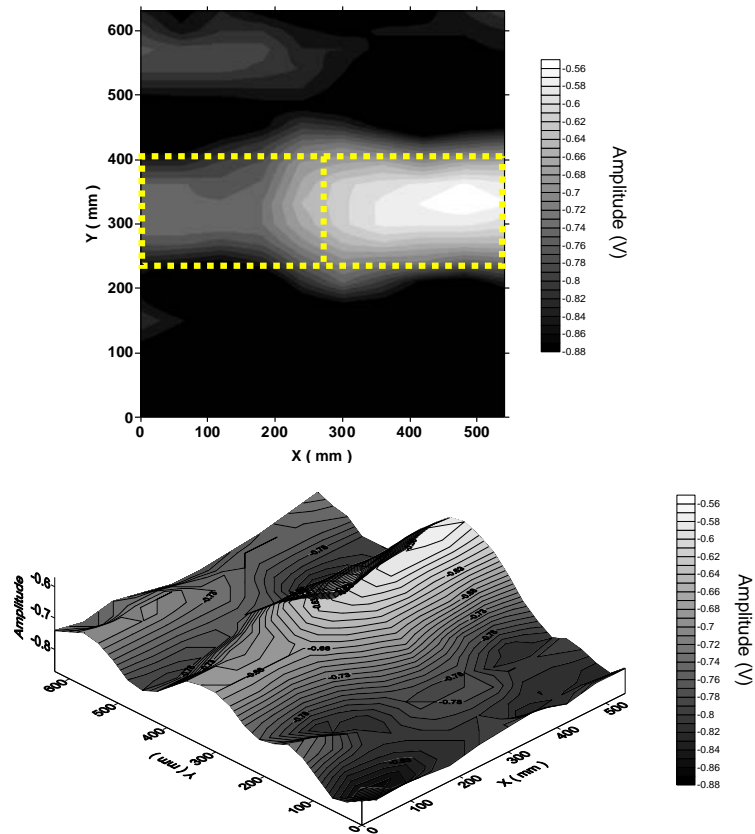
Figure 7.6: *Capacitive imaging results for concrete sample with a hidden stepped channel.*

A further set of experiments was now performed, to indicate the presence of rebars. The first test sample, shown in Figure 7.7, contained a single 10 mm diameter rebar located at a cover depth of 10 mm. The concrete sample itself was of dimensions 300mm (length) x 150 mm (width) x 30 mm (depth) and in this case, 10mm aggregate was included in the mix. The rebar was equidistant from the top and bottom surfaces and parallel to them. The rebar and the scanned area are highlighted on the surface of the photograph shown in Figure 7.7(a).
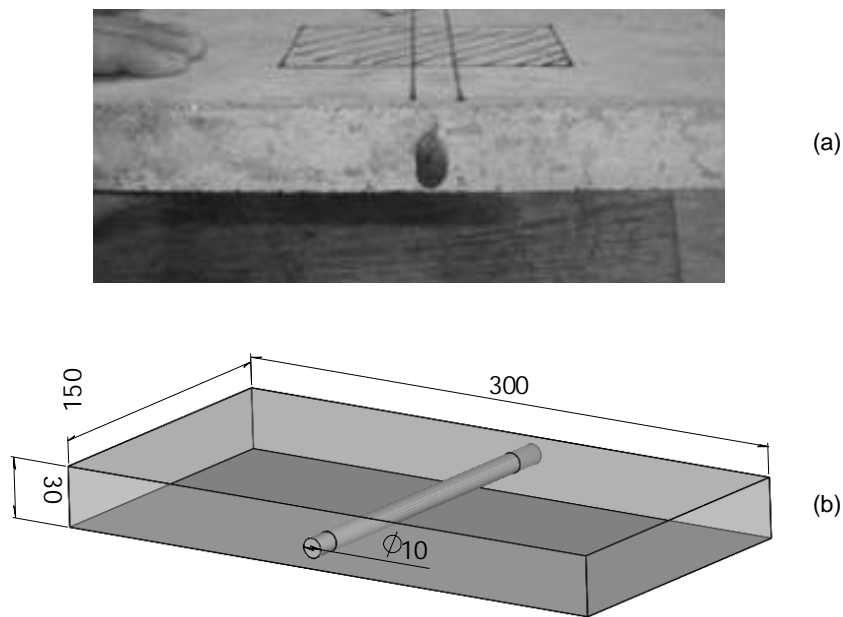
Figure 7.7: *Concrete sample with a single rebar of 10 mm diameter placed symmetrically within the thickness of a 30 mm thick concrete sample. (a) Photograph of sample, and (b) schematic diagram.*

An 80mm x 60 mm area was scanned using the 40 mm by 20 mm back-to-back triangular probe shown in Figure 3.13(a) with a 1 mm step size and a 1mm stand-off distance, using a 1 MHz driving signal. The resulting image is show in Figure 7.8(a). The rebar can be seen as the darker vertical strip in the centre of the image, which indicates that the capacitive imaging technique was sensitive to the hidden rebar and had detected it successfully. During the scan, the rebar was grounded using a conducting wire with a crocodile clip to enhance the contrast of the image (analogous to similar practice in half-cell potentiometer surveys). Note however that detection of the rebar is also possible with the rebar floating (i.e. not grounded) but the obtained image will have less contrast, as shown in Figure 7.8 (b).
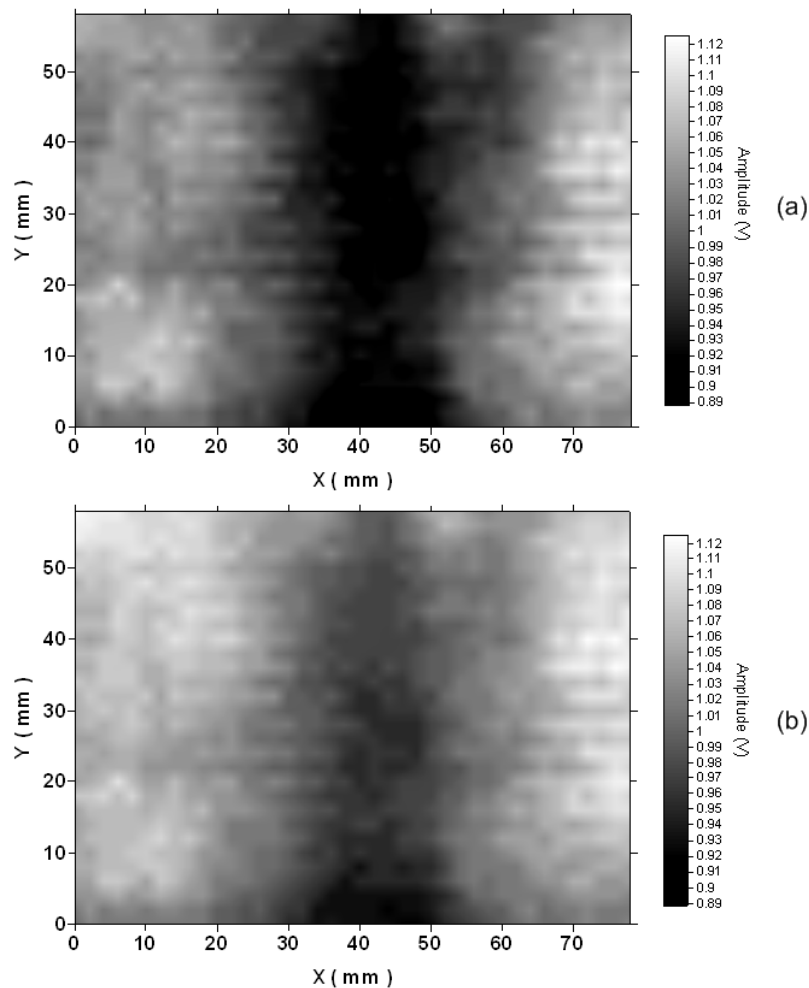
Figure 7.8: *Capacitive imaging results for the concrete sample of Figure 9, containing a single rebar. (a) Grounded rebar and (b) electrically-floating rebar.*

A further sample was now prepared containing multiple rebars, and is shown in Figure 7.9. It was of 1000 (length) x 1000 (width) x 150 mm (depth), with two sets of rebars of 10 mm diameter passing through the concrete slab and parallel to the top and bottom surfaces. The first set of rebars (two parallel rebars with a 300mm spacing between their centres) was buried at a depth of 100mm from the top surface to their centres, and the second set (also two parallel rebars with a 300mm spacing between the centres), were oriented perpendicular to the first set were buried at a depth of 120 mm from the top surface to their centres. This sample provided a more complex scanning environment, such as that likely to be met in practice, with sets of rebars at different depths and orientation.

(a)   (b)
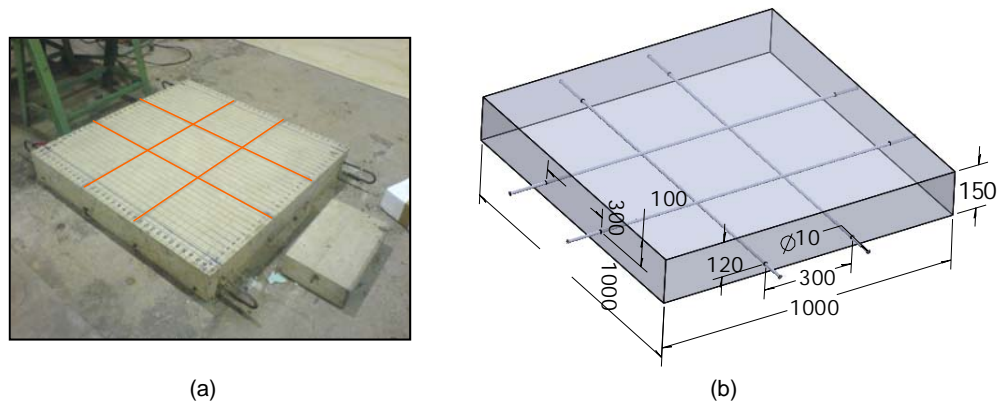
Figure 7.9: *Concrete sample with rebars (a) Photograph of sample, and (b) schematic diagram.*

A 780mm x 690 mm area was scanned using the larger probe, using a 1MHz driving signal. A 30mm step size and 1mm stand-off distance were used for the scan, with the rebars again grounded. The result is shown in Figure 7.10. The rebars can be seen clearly as the darker areas in the image. Note that the two horizontal features are darker than the two vertical ones; this is because the former represent the two parallel rebars located closest to the scan surface.
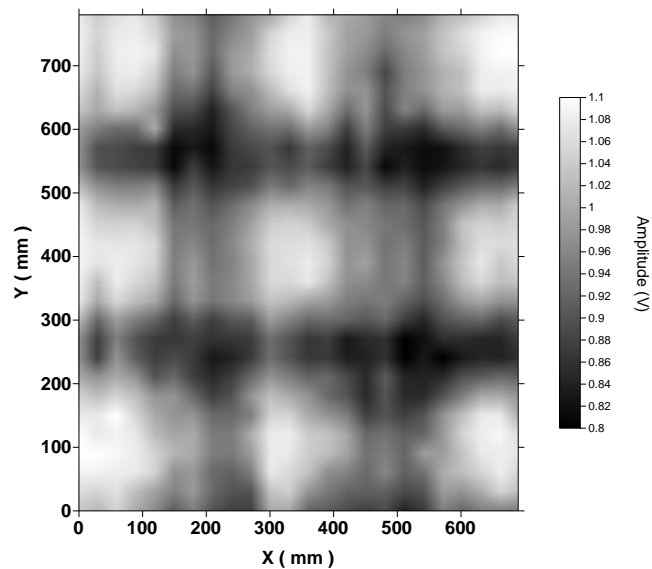
Figure 7.10: *Capacitive imaging results for the concrete sample shown in Figure 7.9.*

7.5 Discussion

It can be seen from the preliminary results that the capacitive imaging technique is sensitive to the presence of surface crack, hidden sub-surface changes in thickness (e.g. voids) and rebars. However, due to the co-planar shape of the capacitive imaging probe, which forms a non-linear fringing electric field, there is no analytical formulation to precisely define the measurement volume and penetration depth. This, together with the fact that different kinds of defects could change the local electric properties to the same extent, make the characterization of the crack (width and depth), void (location and size) and rebar (depth and diameter) very difficult by performing one scan using a typical capacitive imaging probe which only has one pair of electrodes. This could be addressed in more advanced systems by using pulsed signals on arrays of multiple electrodes, rather than single pairs, since modelling and experiments in other materials [28] suggests that effective penetration depth is related to electrode spacing. By analysing changes in the relationship between capacitance and electrode spacing caused by artefacts, their depth should be able to be estimated.

As indicated by the FE models, the electric field lines are denser in the vicinity of the electrode pair, so the capacitive imaging probe is sensitive to the surface features of the concrete specimen and the lift-off distance between the probe and the surface. This sometimes causes confusion in the obtained image, e.g. in Figure 7.4 the gradient along the Y-axis in the image is caused by a lack of parallelism between the probe and the sample surface and in Figure 7.6, the lighter area on the upper-left part of the image is caused by a pitted area on the surface which may be misinterpreted as a hidden void. More sophisticated signal processing and analysis should be able to distinguish between stray signals caused by such effects and 'real' diagnostic information, perhaps by using the arrays mentioned above.

7.6 Conclusions

In previous chapters, it has been confirmed that the probe size and geometry are the key factors for penetration depth and image resolution in specimens for the capacitive imaging technique. This is also true for the inspection of concrete specimens. Discussions in Chapter 3 and 4 have identified the triangular electrodes as a good general purpose design for preliminary inspections. However, as a general rule, the use of smaller electrodes will allow a better resolution of near-surface defects, whereas greater penetration comes from larger electrodes for a given electrode geometry. Accordingly, to image the crack on the surface and shallowly buried rebar, a 40 mm by 20 mm triangular electrode probe was used in this paper, whereas for imaging deeper features, a 320 mm by 160 mm triangular electrode probe was used.

The predictions of FE modelling and the results of preliminary experiments both indicate that the capacitive imaging system has the potential to simultaneously detect surface features, changes in thickness to an air void and cover depth and position of rebars in concrete samples. Thus, the technique has the potential to be developed into a single compact device to detect many different features within concrete samples, providing indications of possible defects in concrete samples to guide more comprehensive NDE surveys of a concrete structure is performed by specialised devices. Note that, unlike ultrasound and some other techniques, there is no need for specific surface preparation, and no couplant is required. The technique works in a non-contact and a non-invasive manner, and only requires single-side access to the sample. In addition, the difference in electric properties between details of interest (crack, void and rebar) and concrete is much larger than that between cement paste and aggregate and so the scattering effect encountered in ultrasonic imaging is absent. The transducers are very simple and cheap – effectively, just copper plates – in contrast to complex and expensive piezoelectric or electromagnetic transducers,

which means that a wide range of probe geometries and thus assessment applications could be available to practitioners at little added cost.

In practice the situation is usually rather more complicated compared to the samples interrogated in this work. Defect types and sizes will be unknown, moisture conditions may be inhomogenous, and voids may be poorly defined (e.g. by honeycombing). Further development of the capacitive imaging probe is required to meet different practical requirements and provide enhanced diagnostic information, e.g. systematic identification and characterisation of defects. Electrode arrays or multi-electrode probes with flexible combinations of electrode size/shape could help obtain the depth and size information of a subsurface void/rebar. Advanced signal processing algorithms can filter out stray signals from e.g. changes in surface roughness. Nonetheless, capacitive imaging shows considerable promise for NDE of concrete.

7.7 References

[1]   T. H. L. George William C. Kaye, John G. Noyes , Geoffrey F. Phillips, Owen Jones, Jim Asher, *Tables of Physical and Chemical Constants (Kaye & Laby)*, 16 ed.: Longman, 1995.

[2]   X. Yin, D. A. Hutchins, G. G. Diamond, and P. Purnell, "Non-destructive evaluation of concrete using a capacitive imaging technique: Preliminary modelling and experiments," *Cement and Concrete Research,* vol. 40, pp. 1734-1743, 2010.

[3]   S. Rostam, "High performance concrete cover--why it is needed, and how to achieve it in practice," *Construction and Building Materials,* vol. 10, pp. 407-421, 1996.

[4]   X. Derobert, C. Aubagnac, and O. Abraham, "Comparison of NDT techniques on a post-tensioned beam before its autopsy," *NDT and E International,* vol. 35, pp. 541-548, 2002.

[5]   "Ultrasonic tester for concrete," *Ultrasonics,* vol. 9, pp. 71-71, 1971.

[6]   K. Warnemuende and H.-C. Wu, "Actively modulated acoustic nondestructive evaluation of concrete," *Cement and Concrete Research,* vol. 34, pp. 563-570, 2004.

[7]   P. Antonaci, C. L. E. Bruno, P. G. Bocca, M. Scalerandi, and A. S. Gliozzi, "Nonlinear ultrasonic evaluation of load effects on discontinuities in concrete," *Cement and Concrete Research,* vol. 40, pp. 340-346, 2009.

[8]   M. Saafi and T. Sayyah, "Health monitoring of concrete structures strengthened with advanced composite materials using piezoelectric transducers," *Composites Part B: Engineering,* vol. 32, pp. 333-342, 2001.

[9]   J. R. Berriman, D. A. Hutchins, A. Neild, T. H. Gan, and P. Purnell, "The application of time-frequency analysis to the air-coupled ultrasonic testing of concrete," *Ultrasonics, Ferroelectrics and Frequency Control, IEEE Transactions on,* vol. 53, pp. 768-776, 2006.

[10]   P. Purnell, T. H. Gan, D. A. Hutchins, and J. Berriman, "Noncontact ultrasonic diagnostics in concrete: A preliminary investigation," *Cement and Concrete Research,* vol. 34, pp. 1185-1188, 2004.

[11]   M. Schickert, "Ultrasonic NDE of concrete," in *Ultrasonics Symposium, 2002. Proceedings. 2002 IEEE*, 2002, pp. 739-748 vol.1.

[12]   S. A. Abo-Qudais, "Effect of concrete mixing parameters on propagation of ultrasonic waves," *Construction and Building Materials,* vol. 19, pp. 257-263, 2005.

[13]   R. K. Dhir, M. R. Jones, and M. J. McCarthy, "Quantifying chloride-induced corrosion from half-cell potential," *Cement and Concrete Research,* vol. 23, pp. 1443-1454, 1993.

[14]   V. Leelalerkiet, J.-W. Kyung, M. Ohtsu, and M. Yokota, "Analysis of half-cell potential measurement for corrosion of reinforced concrete," *Construction and Building Materials,* vol. 18, pp. 155-162, 2004.

[15]   M. Ohtsu and T. Yamamoto, "Compensation procedure for half-cell potential measurement," *Construction and Building Materials,* vol. 11, pp. 395-402, 1997.

[16]   S. Ahmad, "Reinforcement corrosion in concrete structures, its monitoring and service life prediction--a review," *Cement and Concrete Composites,* vol. 25, pp. 459-471, 2003.

[17]   G. Klysz and J. P. Balayssac, "Determination of volumetric water content of concrete using ground-penetrating radar," *Cement and Concrete Research,* vol. 37, pp. 1164-1171, 2007.

[18]   W. L. Lai, S. C. Kou, W. F. Tsang, and C. S. Poon, "Characterization of concrete properties from dielectric properties using ground penetrating radar," *Cement and Concrete Research,* vol. 39, pp. 687-695, 2009.

[19]   V. Barrile and R. Pucinotti, "Application of radar technology to reinforced concrete structures: a case study," *NDT & E International,* vol. 38, pp. 596-604, 2005.

[20]   J. H. Bungey, "Sub-surface radar testing of concrete: a review," *Construction and Building Materials,* vol. 18, pp. 1-8, 2004.

[21]   D.-M. Bontea, D. D. L. Chung, and G. C. Lee, "Damage in carbon fiber-reinforced concrete, monitored by electrical resistance measurement," *Cement and Concrete Research,* vol. 30, pp. 651-659, 2000.

[22]   J. F. Lataste, C. Sirieix, D. Breysse, and M. Frappa, "Electrical resistivity measurement applied to cracking assessment on reinforced concrete structures in civil engineering," *NDT & E International,* vol. 36, pp. 383-394, 2003.

[23]   N. Ozyurt, T. O. Mason, and S. P. Shah, "Non-destructive monitoring of fiber orientation using AC-IS: An industrial-scale application," *Cement and Concrete Research,* vol. 36, pp. 1653-1660, 2006.

[24]   K. Karhunen, A. Seppanen, A. Lehikoinen, P. J. M. Monteiro, and J. P. Kaipio, "Electrical Resistance Tomography imaging of concrete," *Cement and Concrete Research,* vol. 40, pp. 137-145, 2009.

[25]   P. Purnell, G. G. Diamond, D. A. Hutchins, T. H. Gan, and K. K. Leong, "Capacitive internal imaging technique for concrete," *Abstracts: Cement and Concrete Science,* pp. 41-44, 15-16th September 2005.

[26]   X. Derobert, J. Iaquinta, G. Klysz, and J.-P. Balayssac, "Use of capacitive and GPR techniques for the non-destructive evaluation of cover concrete," *NDT & E International,* vol. 41, pp. 44-52, 2008.

[27]   J. Davis, Y. Huang, S. G. Millard, and J. H. Bungey, "Determination of dielectric properties of insitu concrete at radar frequencies," in *International Symposium* Berlin, Germany: DGZfP, 2003.

[28]   A. A. Nassr and W. W. El-Dakhakhni, "Non-destructive evaluation of laminated composite plates using dielectrometry sensors," *Smart Materials and Structures,* vol. 18, p. 055014, 2009.

Chapter 8   Further measurements using modified CI Probes

8.1   Background

In previous chapters, CI probes with electrodes etched onto PCBs were fabricated and tested under various situations. In addition to these conventional coplanar PCB probes, modified geometries can be made and they can lead to different applications. A brief overview of these modified probes is presented in this chapter, and the potential applications brought by these probes are also discussed.

8.2   High resolution surface imaging

It has been revealed in previous chapters that the design parameters and the selection of the CI probes are primarily determined by the nature of the specimen and the feature to be detected. In this section, a special CI probe was designed and constructed with the specific aim of providing high resolution surface imaging. The CI probe used pins as both the driving and sensing electrodes, and the tips of the pins were made very close to each other, as shown in Figure 8.1. The pins were 0.5 mm in diameter and 11 mm long. The tips were 0.1 mm in diameter and the separation between the tips was 0.2 mm.

Figure 8.1: *Photograph of the CI probe comprises two pins as active electrodes.*

It can be infered from the discussions on the sensitivity distribution of the CI probe presented in chapter 4 that the high sensitivity values of such a CI probe will be in a small area in the vicinity of the two tips. In other words, the VOI of this probe is small and the imaging resolution should be high.

The equipment shown in Figure 2.14 was used to scan the probe in plane above the surface of the rear side of a two pence coin, as show in Figure 8.2 (a). A 30mm by 30 mm scan was performed with a step size of 300 μm. During the scan the coin was grounded via the grounded lifting support and a minimal lift-off distance between the probe and the coin was maintained. Figure 8.2 (b) shows this data plotted as a greyscale image, where lighter areas represent higher values. It can be seen that the image is reasonably clear, with the head and facial features on the coin being recognisable. However, not all the lettering on the coin is legible.

(a)

(b)
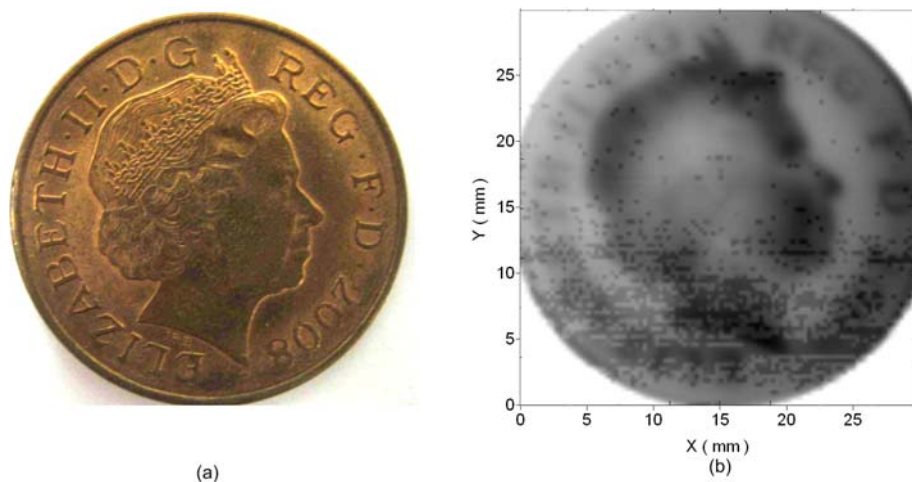
Figure 8.2: *(a) Photograph of a two pence coin and (b) the capacitive imge of the coin shown in gray scale.*

The characteristics of the the pin CI probes depend largely on the sharpness of the pins and the distance between the tips, as they correspond to the electrode size and separation respectively in the normal metal plate electrode probe. Therefore, higher

imaging resolution could be achieved by using smaller tips and closer inter-tip spacings.

8.3 A combined CI/eddy current technique

Comparisons have been made between the proposed CI technique and the conventional eddy current approach in Chapter 2, and it can be seen from the discussions that each technique represents a unique blend of advantages for a variety of applications. For instance, the CI technique can be used on non-conducting specimens and the eddy current approach can be used to detect subsurface features in conducting specimens. It is thus interesting to see if the two techniques can be combined together.

A pair of coils initially designed for eddy current inspections were used as the two active electrodes (driving/sensing) in the CI technique to explore the possibility of combining the two techniques together. Each coil was 1 mm in diameter and contained three layers of 25 turn wire wound onto a ferrite core. The photograph and the cross-sectional view of the coils are shown in Figure 8.3, with the two separate drive and receive coils shown in (b) being hidden behind a coating in the photograph in (a).
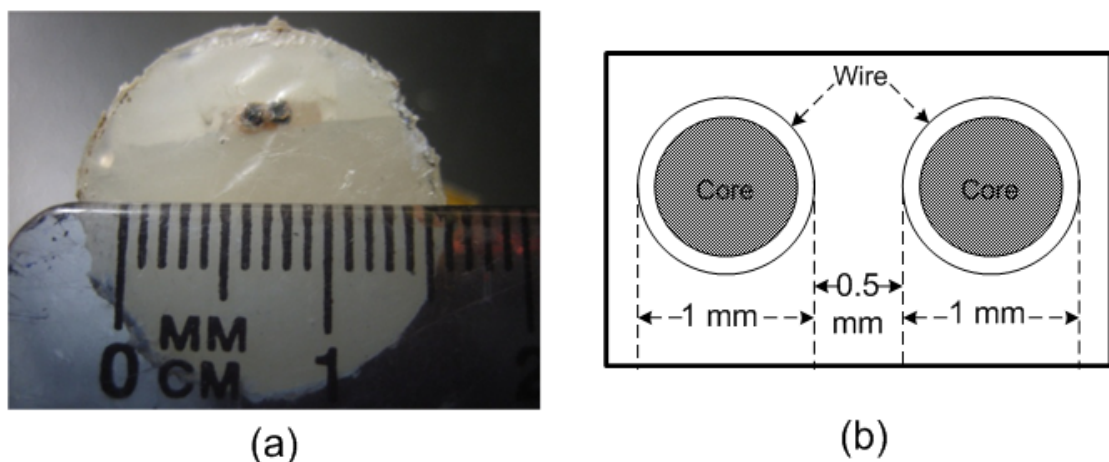
Figure 8.3: *(a) Photograph of the coils and (b) the cross-sectional view.*

In the eddy current mode, one of the coil was drivien by an alternating current (100 mA rms, 2.5 MHz) and the voltage across the other coil was measured and used to form images. The equivalent circuit for the eddy current mode is shown in Figure 8.4.
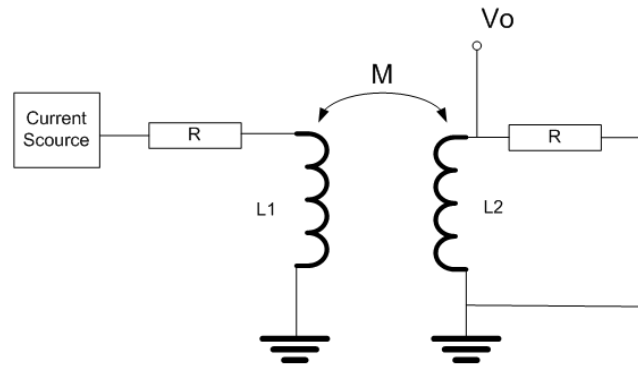
Figure 8.4: *Equivalent circuit of the eddy current mode.*

An eddy current scan was performed on a steel plate with a flat-bottomed hole (20 mm in diameter and 4 mm deep). The coil shown in Figure 8.3 was scanned over a 25 mm by 25 mm area with a minimal lift-off distance, and the results are shown in Figure 8.5 (courtesy of Dr. Y Fan from the Department of Physics, University of Warwick).
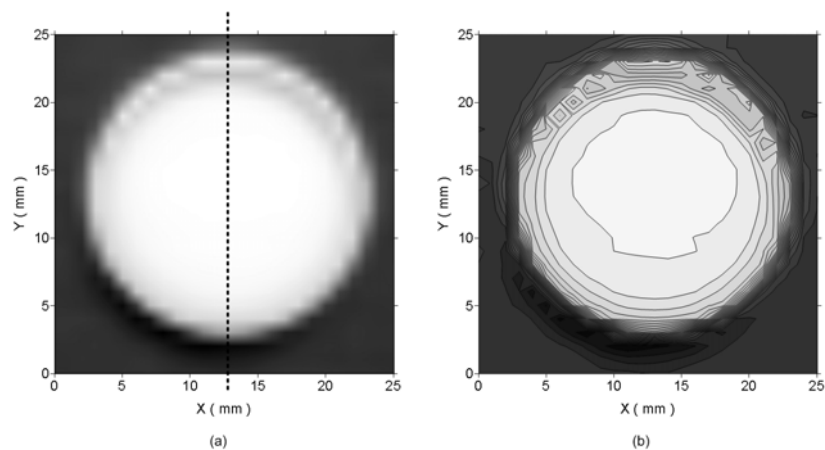
Figure 8.5: *Results of the flat bottomed hole on a steel plate obtained from the eddy current mode.(a) An intensity plot and (b) a contour plot.*

The coils were then used as a CI probe. For the driving coil, one end was connected to the voltage source (20 V pk-pk, 10 kHz) and the other end was left empty. For the sensing coil, one end was connected to the measurement circuit of the CI system and the other was also left empty. The schematic diagram of the instrument is shown in Figure 8.6
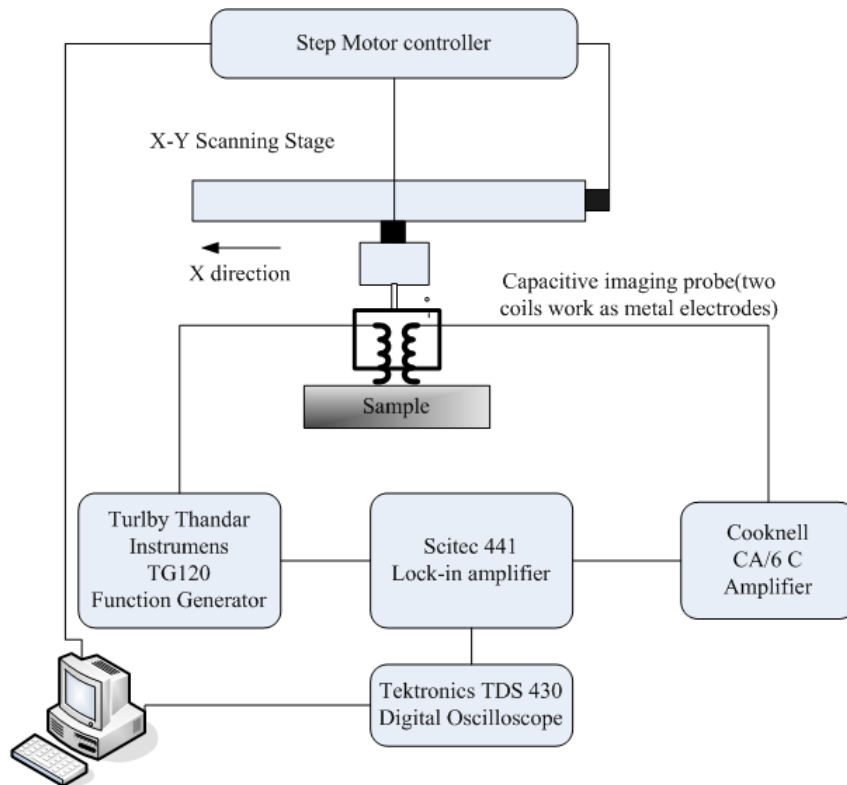
Figure 8.6: *Schematic diagram of the system using coils in the capacitive image mode.*

The coils were scanned over the same area of the above mentioned steel plate at a 1 mm lift-off distance. The results were shown in Figure 8.7. It can be seen that the hole was detected as lighter areas in both of the two modes.
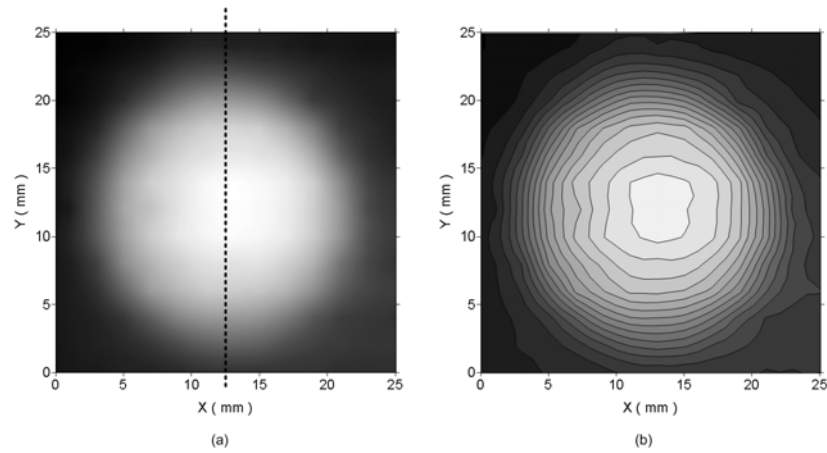
Figure 8.7: *Results of the flat bottomed hole on a steel plate obtained from the capacitive imaging mode.(a)The intensity plot and (b) the contour plot.*

To compare the two sets of results, the data of the dotted line in each image were extracted and plotted in Figure 8.8.
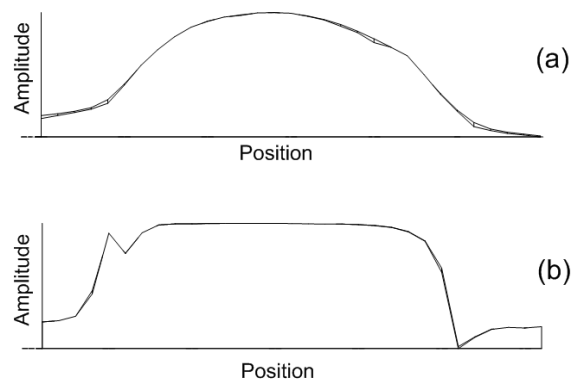
Figure 8.8: *Line plots from images obtained from (a) the capacitive imaging mode and (b)the eddy current mode.*

It can be seen that, for the line plot from the capacitive image (Figure 8.8(a)), the signal transitions at the edges of the hole are relatively smooth and axially symmetric, while for the line plot from the eddy current image (Figure 8.8(b)), the transitions at the edges are abrupt and are asymmetric due to the nature of the induced eddy current in the steel sample.

In terms of image resolution for the same feature on the steel specimen, the image obtained from the CI mode is not as sharp as the one obtained from the eddy current mode. The reasons are twofold: The lift-off distance for the CI scan was bigger; the coils were designed for the eddy current inspection and the capacitive coupling between the two coils was suppressed. In addition, the coil mechanism was not properly shielded for capacitive imaging.

The two images obtained in the eddy current mode (shown in Figure 8.5) and the CI mode (shown in Figure 8.7) were now normalized and superposed to simulate a combined scan, as shown in Figure 8.9.
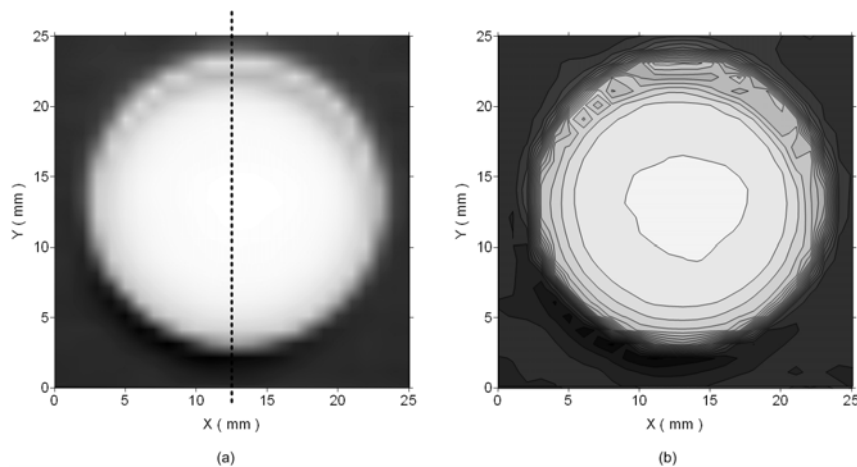
Figure 8.9: *Combinting the images obtained from the eddy current mode and the capacitive imaging mode.(a)The intensity plot and (b)the contour plot.*

As can be seen, the combined image differs to the image from either the eddy current mode or the capacitive imaging mode, and seems to give a clearer representation of the defect. This is further demonstrated by plotting the data extracted along the dotted line, as shown in Figure 8.10. The top of the scan is flatter, and the sides more steep and defined, when compared to single scans using either technique.
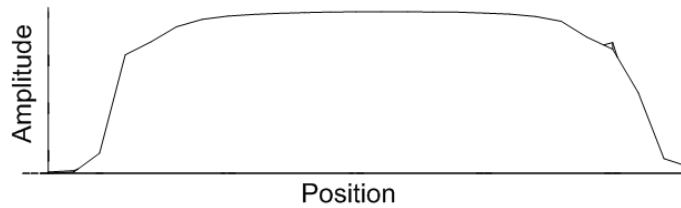
Figure 8.10: *Line plot from the combined image.*

The coils were now used in the capacitive imaging mode only on a Perspex specimen- a Perspex plate with a 20 mm square flat bottomed hole (4 mm deep). The coils were scanned over a 25 mm by 25 mm area from the surface with the hole at a 1 mm lift-off distance, and the results are shown in Figure 8.11.
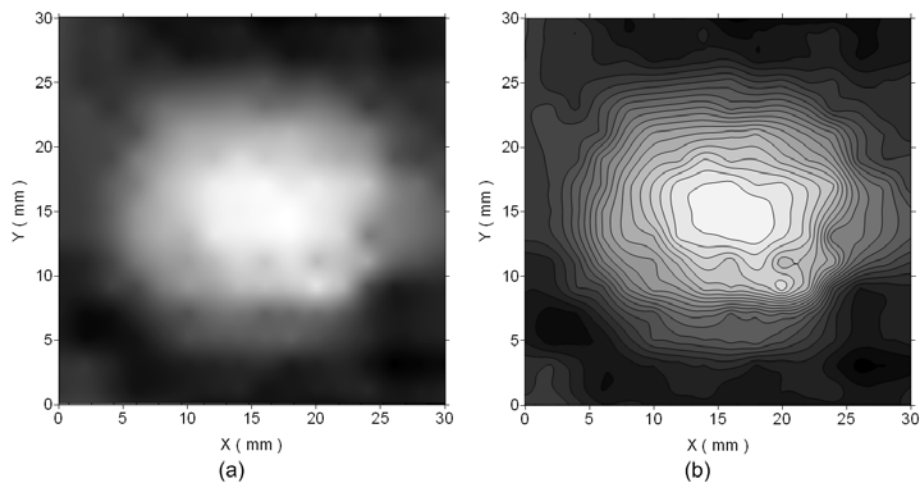
Figure 8.11: *Results of the flat bottomed hole on a Perspex plate obtained from the capacitive imaging mode.(a) The intensity plot and (b) the contour plot.*

The presence of the hole was detected as a lighter area. Note that the eddy current mode would not work on such non-conducting specimens. Note that the hole was detected as lighter area (higher output) because of the negative sensitivity values of the coil pair at the surface of the specimen.

This set of proof-of-concept experiments indicated that, with the high measurement sensitivity provided by the measurement circuit in the CI system, the coils for eddy

current inspections can be used in a CI mode, leading to a possible combination of the two techniques. In addition, planar eddy current sensors manufactured using PCB have been reported in literature [1-3]. Therefore, design principles for CI probes can be easily taken into consideration when manufacturing such planar coils to make the final product suitable for both CI mode and eddy current mode. For instance, the coplanar spiral coil pair fabricated on a PCB board can be made in to the back-to-back or the point-to-point triangular shapes.

8.4 Using an oscilloscope probe as the sensing electrode

In Chapters 3 and 5, probes with concentric geometry have been studied and the results have shown that, the concentric geometry has the advantage of rotational symmetry, but at the same time it brings in complication in the resultant image due to the cup-shape sensitivity distribution near the probe surface (shown in Figure 4. 31 (d)). A modified version of the concentric CI probe was thus designed aiming to overcome the weaknesses that normal concentric probes may have. The photograph of the modified concentric probe is show in Figure 8.12.

Figure 8.12: *Photograph of modified concentric electrode design. The outer annular electrode had inner and outer diameters of 32mm and 48 mm respectively, and the inner disc electrode (before the hole was drilled) was 16 mm in diameter.*

The original PCB was a concentric probe without guard electrode between the inner disc and the outer ring and the overall sensing area was 50 mm by 50 mm. A hole was

drilled in the inner disk and an oscilloscope voltage probe (Tektronix P6139 passive voltage probe, input impedance 10MΩ 8pF) was fitted into the hole (the tip of the voltage probe was in the same plane as the PCB surface). In practical scans, the outer ring works as the driving electrode, the inner ring (derived from the inner disc) is grounded as the guard electrode and the oscilloscope probe works as the sensing electrode. The diagram of the CI system with the modified concentric probe is shown in Figure 8.13.
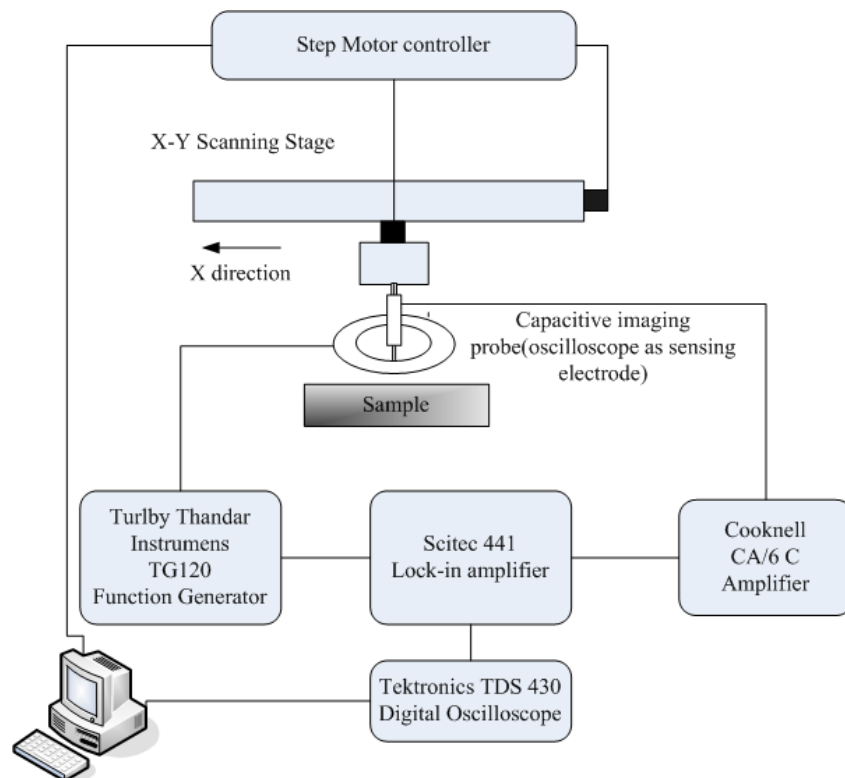
Figure 8.13: *Schematic diagram of the system using the modified concentric CI probe.*

The Perspex plate with four square holes (show in Figure 5.4) and the aluminium plate with four square holes (shown in Figure 5.6) were scanned by this modified concentric probe. The scans were 55 mm by 180 mm at a 1 mm lift-off distance, and the aluminium plate was grounded during the scan. The results are shown in Figure 8.14.

222
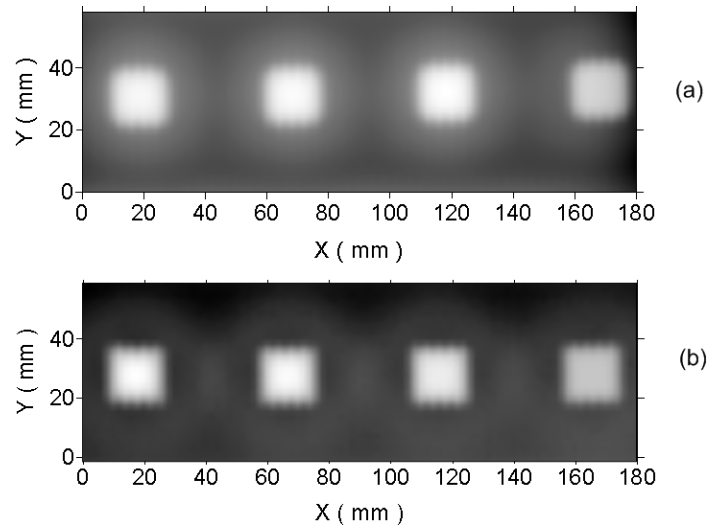
Figure 8.14: *Results for (a) the Perspex plate and (b) the aluminium plate.*

It can be seen that the holes on both the Perspex plate and the aluminium plate were detected as lighter squares in the images and the depth information can be obtained from the intensity value variations of the lighter squares.

The modified concentric probe used here has the same sensing area as the normal concentric probe used in Chapter 5, and thus direct comparison can be made between the results obtained by the two probes. For the Perspex plate, comparing the image obtained by the modified probe (Figure 8.14(a)) with the image obtained by the normal concentric probe (Figure 5.17(c)), it is evident that the modified concentric probe provided a sharper image and the square shapes can be clearly seen in the image while in the normal concentric probe case, only the presence of the holes were detected but the shape and size were not distinguishable. It is also worth noting that instead of appearing as darker areas obtained by the normal concentric probes, the holes on the Perspex plate were detected as lighter areas (higher values). This can be explained by the negative sensitivity values on the surface of the Perspex plate.

For the aluminium plate, the image obtained by the modified probe (shown in Figure 8.14(b)) clearly shown the square shapes and their sizes, while in the image obtained by the normal concentric probe (shown in Figure 5.18(c)), complicated features can

be observed, involving changes in spatial shape of the response as the electrodes were scanned over each hole.

The lift-off experiments were also conducted with the modified concentric probe on the Perspex plate (shown in Figure 5.4), with the 55 mm by 200 mm scans above the surface being performed at distances of 1 mm, 3 mm, 5 mm and 7 mm in air. The results are shown in Figure 8.15. It is evident that, as expected, the resolution of the image decreases as the capacitive electrode is moved further away from the sample surface.
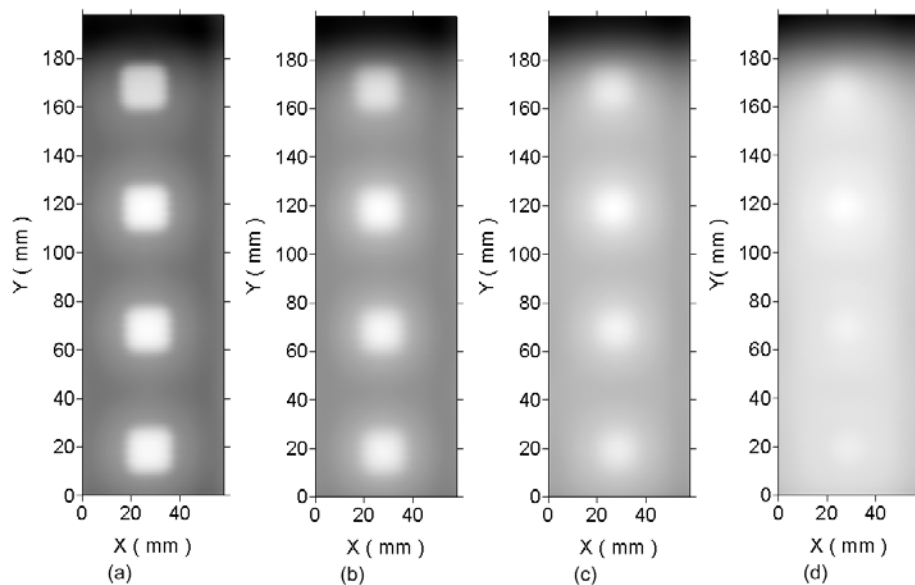
Figure 8.15: *Capacitive images of the Perspex plate, taken at lift-off distances of (a) 1 mm, (b) 3 mm, (c) 5 mm and (d) 7 mm. The scan was performed at the surface containing the flat-bottomed holes.*

The second set of lift-off experiments using the modified concentric probe was performed on the aluminium plate (shown in Figure 5.6). In this case, measurements were taken at distances of 1 mm, 3 mm, 5 mm, 7 mm, and 9 mm in air. The resultant images obtained with the steel plate electrically grounded, are shown in Figure 8.16. It can be seen from the results that, only in the case when the probe was close to the aluminium plate (1 mm lift-off) the sensitivity values on the surface were positive and

the holes were detected as lighter areas. At the 3 mm lift-off, shown in figure 8.16(b), the holes appeared as Mexican-hat shaped patterns (if shown in 3D), with the dimensions of the central peaks varied with the depths of the holes. At lift-offs bigger than 5 mm, the holes were detected as darker areas due to the negative sensitivity values.
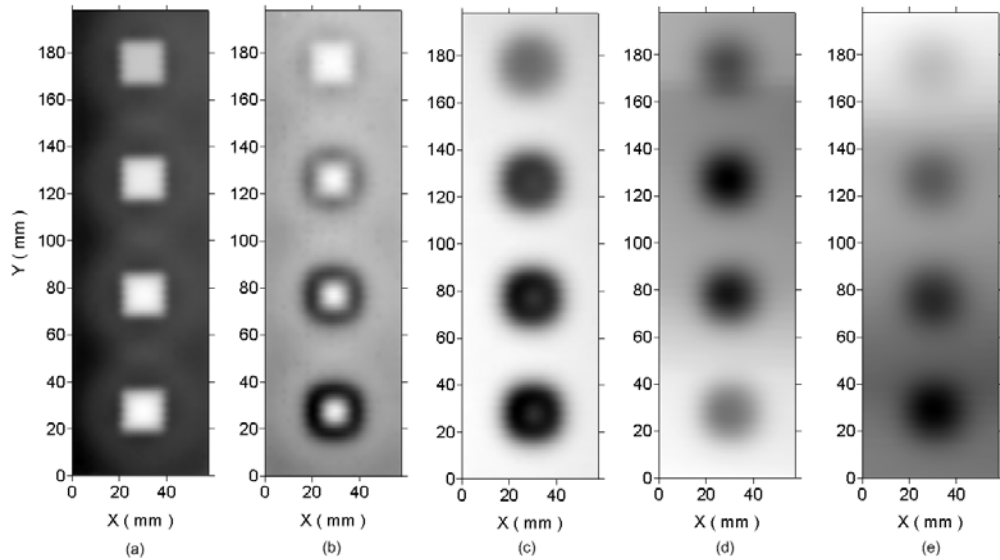
Figure 8.16: *Capacitive images of the aluminium plate (grounded), taken at stand-off distances of (a) 1 mm, (b) 3 mm, (c) 5 mm, (d) 7 mm and (e) 9 mm. The scan was performed at the surface containing the flat-bottomed holes.*

It is necessary to emphasize that, strictly speaking, the modified concentric probe does not work in a capacitive way, although capacitive coupling still exists between the outer ring (driving electrode) and the voltage probe tip. This is because the voltage probe has very high input impedance and it measures the potential in the vicinity of the tip rather than the charge induced on the tip. The sensing mechanism is similar to the reported electric potential (displacement current) sensors [4-6] and the difference is in their applications an external electric field has to be applied to the specimen, thus they are only applicable to conducting specimens. While for the above mentioned modified concentric probe, the field is provided by the outer ring electrode and it works on both dielectric specimens and conducting specimens

225

8.5 Conclusions

In this chapter, modified CI probes were made and tested. The two pins with their tips close to each other provided a high resolution image of the surface features on a two pence coin. The eddy current coils were used in the capacitive imaging mode and results obtained from both conducting specimen (steel) and non-conducting specimen (Perspex) were presented. A passive voltage probe was used as a sensing electrode in a concentric probe and the results indicated that such probe had a better performance compared to the normal concentric probe with the same sensing area.

226

8.6   References

[1]   R. J. Ditchburn and S. K. Burke, "Planar rectangular spiral coils in eddy-current non-destructive inspection," *NDT & E International,* vol. 38, pp. 690-700, 2005.

[2]   J. O. Fava, L. Lanzani, and M. C. Ruch, "Multilayer planar rectangular coils for eddy current testing: Design considerations," *NDT & E International,* vol. 42, pp. 713-720, 2009.

[3]   H. Xiaohui and Y. Wuqiang, "An imaging system with planar PCB-coil sensor array," in *Imaging Systems and Techniques, 2009. IST '09. IEEE International Workshop on*, 2009, pp. 26-31.

[4]   W. Gebrial and et al., "Non-contact imaging of carbon composite structures using electric potential (displacement current) sensors," *Measurement Science and Technology,* vol. 17, p. 1470, 2006.

[5]   A. Aydin and et al., "A high sensitivity calibrated electric field meter based on the electric potential sensor," *Measurement Science and Technology,* vol. 21, p. 125901.

[6]   S. T. Beardsmore-Rust and et al., "Imaging of charge spatial density on insulating materials," *Measurement Science and Technology,* vol. 20, p. 095711, 2009.

Chapter 9   Conclusions and future work

9.1   Conclusions

Although the concept of using the capacitive coupling to measure properties of specimens has been known for some time, previous research has been focusing on using capacitive sensors to characterise materials or measure distance/thickness, and the imaging ability of the planar capacitive sensors hasn't been systematically studied. This thesis has been primarily concerned with this issue by considering the probe design principles, the characterization of the probes and the applications of the proposed capacitive imaging (CI) technique.

9.1.1   The Capacitive Imaging (CI) technique

The Capacitive imaging (CI) technique discussed in this thesis is a novel imaging technique capable of detecting surface and hidden defects in specimens that are dielectric or poorly conducting and detecting surface features on conducting surfaces through a significant air gap or insulation layer. The CI probe usually comprises two metal electrodes and uses the fringing electric field established between the electrodes as the probing field. The probing electric field samples a local volume of the specimen, and the electric field distribution can be modulated by defects within the sampled volume. The result is that the charges induced at the sensing electrode will vary. This change in signal can be detected, and used to create a map of changes in electrical properties within the specimen after a raster pattern scan. This approach is a non-contact technique and the air gap between the electrodes and the sample can be quite large (on the order of millimetres). Thus, sample surface preparation is often not required. In addition, the approach only requires single-sided access to the specimens. The CI technique is also advantageous for its capacitive nature which allows the technique to work on a wide variety of material properties, without the restrictions encountered by eddy current and potential drop methods. Furthermore, the CI probes work in a volume averaging manner and the scattering problem associate with ultrasound method in some of the materials is absent.

228

9.1.2 Theoretical formulations of the CI technique and the quasi-static approximation

The work described in this thesis provided a systematic study of the physical principles of the CI technique and their theoretical descriptions, thus delivering a full account of all relevant aspects of the technique. It was shown that in the operating frequency range (10 kHz to 1 MHz), the quasi-static approximation applies and the Maxwell's equations can be simplified. The electrostatic formalism which is based on electrostatic theory was thus found to be suitable for the analysis of the CI system. Instead of using conventional conformal mapping methods or green function methods, the capacitance of the coplanar CI probes are obtained by calculating the amount of charge on the sensing electrode using Gauss's Law after the electric potential is obtained via the Laplace's equation. However, this is not accomplished analytically due to the computation complexity, and instead the Finite Element modelling was employed. COMSOL^{TM} Multiphysics was found to be a suitable PC-based package for this type of FE modelling work.

Finite element modelling was used to predict the electric field distribution between the electrodes, calculate the capacitance and evaluate the probe performance. The 2D FE models have indicated that the electric field distribution from a selected electrode pair can penetrate into dielectric materials, and can be used to detect the presence of defects in terms of air voids. In metals, the electric fields do not penetrate the surface in the quasi-static model, but interact strongly with surface features. The 2D models were also used to investigate the effects of thicknesses of dielectric specimens, lift-off distances and relative permittivity values on the probes' response. The feasibility of the CI technique on flaw detection was also demonstrated by the 2D models. 3D models were also constructed and used to obtain the sensitivity distributions of CI probes both from a perturbation method and a mathematical approach. The equation for sensitivity distribution is a dot product of two vectors (the electric fields from reciprocity energization). Thus, depending on the orientations of the two vectors, there are regions with positive, null and negative sensitivity values. As a signature feature of a CI probe, the calculated sensitivity distribution can be used to determine the VOI and evaluate the imaging ability. With the sensitivity distribution, it is possible to anticipate the likely performance of any design. Design parameters were

also studied using the FE models and the results correlated well with the conclusions obtained experimentally.

9.1.3   Measurement method and practical implementation

There are four basic modes of operations of the CI technique: a poorly-conducting sample either with or without a grounded substrate being present, a grounded conductor, and finally a conductor which is floating (i.e. non-grounded). Although the four modes lead to different equivalent circuits, the sensing mechanisms can be treated as variable capacitors. As an instantaneous reflection of the local electrical properties, the capacitance of each variable capacitor can change with scan position. According to the basic circuit theory, this capacitance variation results in an amplitude and phase angle variation of the current (charge flow) from the sensing electrode. The charge signal on the sensing electrode was measured through a charge amplifier which convert the charge signal on the sensing electrode to an AC voltage signal, and a lock-in amplifier which converts the AC voltage signal into a DC voltage proportional to either the amplitude of the received AC signal or the phase difference between the received signal and the reference. The DC output was then recorded using an oscilloscope, and transferred to the PC for storage. The PC also controlled an X–Y scanning stage, which could be used to translate the capacitive imaging electrodes across the sample surface, and the signal recorded in specified locations so as to build up an image. Both the amplitude and phase difference were used to from images and it was shown that the amplitude plots provided higher contrast and were used in most of the scans in this thesis.

As an important variable, the CI probes were designed with care. In this thesis, the measures for the evaluation of the CI probe performance, including penetration depth, measurement sensitivity, imaging resolution and signal to noise ratio (SNR), were discussed. The concept of the volume of influence (VOI) was defined to provide a panoramic view of the imaging ability of a given CI probe. Two types of CI probes were studied as examples to derive the general principles for the CI probe design. It was shown that with frequency not being a major factor, the performance of CI probes depends largely on the geometry of the electrodes. The optimal probe design can be achieved by a proper selection of the electrode size, shape and arrangement depending on the application. Generally, a wider electrode assembly will provide a deeper depth

of penetration into the sample, but this will be traded off against a reduced spatial resolution at the surface. It was also found that the probes with triangular electrodes can balance the tradeoffs to a certain extent and can be used as general purpose probes. Grounded guard electrodes, back plane, thinner PCB substrate and metal enclosure were proved to be beneficial to the overall performance. Modified CI probes were also made and tested. This includes using two pins with their tips close to each other or two eddy current coils as the active electrode pair, and using a passive voltage probe as a sensing electrode in a concentric probe. The results obtained using such modified probes suggested that the CI technique could be used for high resolution surface imaging or combined with the eddy current technique.

In this thesis, the fundamental concept of the CI technique has been validated by scanning two specimens representing the two extremes of electrical properties, namely Perspex and aluminium. The results of experiments on Perspex and aluminium plates containing machined flat-bottomed holes of various depths gave an indication of the response of the CI approach. In addition, in the cases of surface features on both non-conducting (Perspex) and conducting (aluminium) specimens, very good surface information was obtained, indicating that the depth of the hole could possibly be determined from such scans. It was also shown that the holes on the Perspex plate depleted the output while the wholes on the aluminium plate enhanced the output. It was also evident that extra attention was required when trying to image hidden features in non-conducting specimens as they might situate in a region where the sensitivity values are negative. A comprehensive parameter study, including the investigations of the effects of grounded substrate, the electrical conditions of conducting specimen, the CI probe geometries and the lift-off distances, has revealed that such parameters should be considered and determined carefully to achieve optimum results in practical scans. In addition, surface features on conducting specimens were successfully detected through an insulating layer, indicating a possible application of detecting the presence of pitting caused by corrosion under insulation (CUI). It was also evident that, the targeting features were spread by the CI probe in the resultant images. This effect is problematic when trying to image features much smaller than the probe, as the resultant image will appear as a blurred version of the sensitivity map and the targeting feature will be difficult to be recognized.

9.1.4 Applications

It was shown in the thesis that, with a careful design and selection of the probes according to the nature of the specimens and the defects in them, the CI technique can be successfully used as an NDE tool to investigate an extensive range of specimens.

Consider first fibre-reinforced polymer composites. Both surface cracks and sub-surface delaminations were successfully detected in glass fibre composites. Defects within the foam core of a glass-fibre sandwich structure were detected. The honeycomb pattern of the aluminium core structure, folding failures and fluid intrusion into the aluminium honeycomb core were imaged through a thin glass fibre composite surface layer to demonstrate the feasibility of the CI technique to the inspection of such sandwich panels. The detection of such defects is difficult by other NDE techniques, especially if access is required from one side and contact has to be minimised. Surface defects including a crack caused by impact damage and superficial burn damage were detected on carbon fibre composites and the texture and pattern of the woven carbon fibre were imaged.

Experiment to simulate the effects that might be expected from corrosion under insulation (CUI) was also performed, by scanning a steel plate with highly rusted areas. The external profile of a pipe with defects (rust and an area changed by grinding) was obtained from a CI line scan. Both these applications are important in the oil industry. The ability to detect buried objects was demonstrated by two sandbox experiments, containing a buried conductor and insulator respectively. This suggests that, with modification, the detection of buried objects such as pipelines (metallic or polymer) might be achievable.

The feasibility of the CI technique for the NDE of concrete specimens was also demonstrated by the successful detections of surface cracks, hidden voids and rebars within concrete specimens.

It can be inferred from the experimental results that the detection ability of the CI technique is determined by the geometry of the selected CI probe and the properties of both the specimen under test and the defect. It is felt that the 40 mm by 20 mm back-to-back triangular probe should be able to detect a spherical air void (relative permittivity $\varepsilon_r=1$) 20 mm in diameter with its centre 20 mm from the top surface of an

insulating material (*e.g.* the relative permittivity $\varepsilon_r=3$), providing a minimal lift-off distance is maintained during the inspection. Note that, the minimum detectable defect dimension will be reduced with a reduced buried depth and the whole situation can also be affected by the electric property difference (*e.g.* difference in relative permittivity values) between the defect and the specimen. For conducting specimens, the same 40 mm by 20 mm back-to-back triangular probe should be capable of detecting a hemispherical dent 20 mm in diameter with a 20 mm thick insulation layer between the conducting surface and the probe surface. Again, this detection ability could vary with different insulation material.

The estimated detection ability only provided an indication of the potential applications of this CI technique. Experiments for the Probability of Detection (PoD) data acquisition are required in future work to quantify the performance capability of different CI probes in different applications.

9.2 Main contributions

The tasks that have been accomplished during the course of the research described in this thesis are highlighted in this section.

9.2.1 CI experiments and Probe design

The design parameters required for the CI probes have been investigated, and several capacitive imaging probes have been designed and fabricated. A set of measurements have been presented, which have demonstrated for the first time that CI techniques can be used over a broad range of materials for the detection of surface and sub-surface features. Unlike conventional capacitive sensors in which the electrodes (or electrode fingers in the case of interdigital sensors) are usually in a rectangular shape, triangular shape electrodes are used in the proposed CI technique (Section 3.4(c)). The advantages of the probes with triangular-shaped electrodes have been discussed (Section 4.5.3) and such probes have been used successfully in many applications (Chapter 5, 6 and 7). Modified CI probes, such as the CI probe using two pins with the tips close to each other (section 8.2), the CI probe using coils as electrodes (section 8.3), and the concentric CI probe using high impedance oscilloscope probe as sensing electrode (section 8.4), have also been designed to address specific inspection problems.

The use of a combined CI/eddy-current probe is worthy of special mention. This particular combination does not seem to have been applied before to the NDE of materials. It has certain attractions, in that CI works well for insulators and eddy currents for conductors; hence the use of a coil to detect both simultaneously may have many future applications.

9.2.2   Modelling

The 3D measurement sensitivity distributions have been obtained using COMSOL^{TM} through a derived equation (section 4.5.2). For the first time, the measurement sensitivity is used as a tool to evaluate the imaging ability of planar capacitive probes with different design parameters and optimise the probe design (section 4.5.3). The concept of VOI was introduced, to demonstrate the likely volume over which the capacitive probe was likely to be effective. This is a major contribution, as it details the range of applications of the techniques within a particular material. Different types of specimens have also been taken into account during the calculation of the sensitivity distributions of various CI probes, providing indications of the expected resultant images (section 4.5.4).

The concept of negative sensitivity has also been introduced, a phenomenon that is neglected in most of the applications described in the literature, and one that has never been discussed for planar capacitive sensor. In this work, this gap has been filled (Section 4.5.2) and some experiments performed so as to verify the existence of negative sensitivity (Sections 5.4 and 5.5).

9.2.3   New areas of application

Based on the analysis of the sensitivity distributions, the imaging ability of capacitive sensors has been explored and the results suggested the CI technique would be useful in many NDE applications. New areas of applications have thus been investigated (in Chapter 6 and 7), including the inspection of laminated glass fibre composites, and honeycomb sandwich structures with glass fibre reinforced polymer skins. Such scanning has not been demonstrate before, and shows an application where other methods may have difficulty in the detection of anomalous areas. The application to the detection corrosion under insulation, and buried conducting and non-conducting

objects, was also demonstrated. Both of these are important to the oil and gas industries.

The detection of both air voids and rebars in concrete specimens is also an important application area. The detection of rebars in particular in real outdoor environments is a critical issue in older buildings and concrete structures (e.g. overhead roadways, bridges etc) where salt-induced corrosion is a major concern. The ability to detect both rebars and voids has been demonstrated in this work, and is a major advantage over more traditional cover meters and ultrasonic methods.

9.3 Future work

The results presented in the thesis indicated that the CI technique is promising in many NDE applications. It is hoped that it will prove useful in the development of future NDE systems using the CI technique. However, the work could be extended in several ways.

The CI technique is defined by its VOI, as detailed in previous Chapters. Hence, different probes have a different volume in which they operate. It would therefore be of great interest to investigate a multi-electrode probe (probes with flexible combinations of electrode size/shape/separation), which would be able to provide a set of electrode shapes simply by switching smaller elements which make up a bigger electrode. This would allow the depth profile of defects to be investigated in a more quantitative manner. In addition, to speed up the scan process, an array of CI probes could be constructed which, together with appropriate multiplexing equipment, could be used to scan large areas automatically. This could be held within a single unit, and placed against a surface. It could then be moved over a large surface area, such as an aircraft wing, and a large area scan produced. Defects detected could then be examined by other means if required. The image could be obtained in real time.

In practice the situation is usually rather more complicated than those examined in this thesis. For instance, defect types and sizes will be unknown and often poorly defined. At this early stage of development, the aim was to determine the main properties of the technique, and to establish the range of materials in which it might be used. It is proposed that further benchmark experiments can be undertaken, in

which standard defects in various targeting specimens can be systematically identified and characterised by the CI technique.

It is also thought that the use of non-standard electrodes could lead to interesting results. Examples would include curved electrodes for pipes, contoured electrodes for turbine blades etc. Note also that a coil was successfully used as a capacitive electrode in this work in Section 8.3, where eddy current operation with the same probe was demonstrated. It is felt that additional sensing modalities could be introduced into the CI system. For example, a triple-mode capacitive/eddy current/ magnetic sensor head could be developed, using shaped planar coils which would also be sensitive to magnetic fields. This could be very useful as a new approach to NDE, using three coincident measurements via a single probe geometry.

Finally, there are many applications in NDE to which the capacitive approach might be useful. For instance, it is sensitive to surface features on metals, but is very simple in construction and can be easily constructed from heat-proof materials. Being non-contact, it might be possible to develop a version which is useful in rolling mills for hot, moving metal. It is also a type of technique which might be useful for radioactive sights, where the use of a couplant is not possible due to radioactive contamination. These and other examples where the rugged nature of the technique, and its non-contact nature, might give it an advantage over more established NDE techniques.

236

Publications arising from the research

[1]. X. Yin, G. G. Diamond, and D. A. Hutchins, "Further investigations into capacitive imaging for NDE," *BINDT Insight,* vol. 51, pp. 484-490, 2009

[2]. X. Yin, D. A. Hutchins, G. G. Diamond, and P. Purnell, "Non-destructive evaluation of concrete using a capacitive imaging technique: Preliminary modelling and experiments," *Cement and Concrete Research,* vol. 40, pp. 1734-1743, 2010

[3]. X. Yin and D. A. Hutchins，"Capacitive imaging technique for condition monitoring," presented in *The seventh International Conference on Condition Monitoring and Machinery Failure Prevention Technologies*, Stratford-upon-Avon, UK, 22-24 Jun.2010 (also submitted to *International Journal of Condition Monitoring*)

[4]. X. Yin and D. A. Hutchins，"Capacitive imaging technique for NDE," presented in *the* 37th *Annual Review of Progress in Quantitative Nondestructive Evaluation (QNDE) conference,* San Diego,US,18-23 Jul.2010

Appendix- Equipment Specifications

Scitec Analogue OEM Lock-In Amplifier (441)

Input channel

Input:	Differential or single ended voltage via SMB socket
Input Gain:	x 0.1 to x330 in 1, 3.3, 10 steps
Input Impedance:	10^{12} // 1 nF, dc coupled
Frequency:	10 Hz to 100 kHz
Maximum Inputs:	±10 V before saturation occurs
Gain Accuracy:	1%
Gain Stability:	200ppm/°C
Dynamic Reserve:	0dB to 80dB

Output channel

Output Gain:	x1, x10, x100, x1000
Low Pass Filter Time Constants:	100 μs to 30 s in 1, 3, 10 steps
Outputs:	SMB connectors: +/-100 mV to +/-10 V full scale

Reference channel

Frequency:	10 Hz to 100 kHz
Trigger:	Standard TTL, Rising edge triggered.
Acquisition Time:	10 s max
Phase Control:	90° steps + fine shift of 0° - 150°
Phase Drift:	0.1°/C

SR850 Digital Lock-in Amplifier

Input channel

Voltage Input:	Single-ended or differential
Sensitivity:	2 nV to 1 V
Current input:	106 or 108 V/A
Input impedance (voltage):	10 MΩ + 25 pF, AC or DC coupled
Input impedance (current):	1 kΩ to virtual ground

Gain Accuracy:	±1 % (±0.2 % typ.)
	6 nV/√Hz at 1 kHz
Noise (typ.)	0.13 pA/√Hz at 1 kHz (106 V/A)
	0.013 pA/√Hz at 100 Hz (108 V/A)
Line filters CMRR:	50/60 Hz and 100/120 Hz (Q=5) 100 dB at 10 kHz, decreasing by 6 dB/oct above 10 kHz
Dynamic reserve:	>100 dB (without prefilters)

Reference channel

Frequency range:	0.001 Hz to 102.4 kHz
Reference input:	TTL or sine (400 mVpp min.)
Input impedance:	1 MΩ, 25 pF
Phase resolution:	0.001°
Absolute phase error:	<1°
Relative phase error:	<0.001°
Orthogonality:	90° ± 0.001°
Phase noise (Int. reference):	<0.0001° rms at 1 kHz
Phase noise (Ext. reference):	0.005° rms at 1 kHz, 100 ms, 12 dB/oct
Phase drift:	<0.01°/°C below 10 kHz
	<0.1°/°C, 10 kHz to 100 kHz
Acquisition time:	(2 cycles + 5 ms) or 40 ms, whichever is greater

Demodulator

Stability (digital output):	No drift
Stability (analogue output):	<5 ppm/°C for all dynamic reserves
Harmonic rejection:	-90 dB
Offset/Expand:	±100 % offset, expand up to 256×
Time constants:	10 μs to 30 ks (6, 12, 18, 24 dB/oct rolloff)

Internal oscillator

Range:	1 mHz to 102.4 kHz
Accuracy:	25 ppm + 30 μHz
Resolution:	0.01 % or 0.1 mHz (whichever is greater)
Distortion:	−80 dBc (f < 10 kHz)

−80 dBc (f < 10 kHz)

Amplitude:	0.004 to 5 Vrms into 10 kΩ (2mV resolution)
Output impedance:	50 Ω
Amplitude accuracy:	1%
Amplitude stability:	50 ppm/°C
Output:	Sine and TTL
Sweeps:	Linear and log

Output

X, Y outputs:	±10 V, updated at 256 ksamples/s
CH1 output:	±10 V output of X, R or Trace 1 to 4
CH2 output:	±10 V output of X, R or Trace 1 to 4
Aux. D/A outputs:	4 BNC outputs, 1 mV resolution, ±10 V (fixed or swept amplitude)

Cooknell CA6/C charge amplifier

Input impedance:	100Ω above 10kHz
Sensitivity:	250mV/pC
Series noise voltage generator:	0.6nV//Hz typical
Parallel noise current generator:	4×10^{-14}A//Hz typical
Bandwidth:	<10kHz to > 10Mhz
Max output level:	1V rms into 50Ω

Computer controlled scanning stage

Motor steps per revolution:	400
Motor steps per mm:	80
Maximum stroke:	526mm
Accuracy:	0.023mm per 300mm of travel
Repeatability:	0.005mm